

DISS. ETH NO. 26709

# **Adaptive Learning Control for Thermal Error Compensation**

A thesis submitted to attain the degree of  
DOCTOR OF SCIENCES of ETH ZURICH  
(Dr. sc. ETH Zurich)

presented by  
PHILIP BLASER

MSc ETH ME

born on 12.10.1987  
citizen of Walkringen (BE)

accepted on the recommendation of  
Prof. Dr. K. Wegener, examiner  
Prof. Dr. M. Soshi, co-examiner

2020



*füre Papi.*



# Acknowledgements

This thesis was realized during my time as a research associate at the Institute of Machine Tools and Manufacturing (IWF) of ETH Zurich. Therefore I would like to express my gratitude towards the people who supported me during the course of my studies.

I would like to thank Prof. Dr. Konrad Wegener, head of the institute and supervisor of this thesis for the opportunity to do a doctorate at his renowned institute. I would like to thank him for his support, constructive advice and his trust in me and my work. Dr. Josef Mayr, leader of the group thermal simulations, contributed to this work with his profound understanding of thermal issues in machine tools and a special thank to Dr. Sascha Weikert for his precise comments. I would also like to thank Prof. Dr. Masakazu Soshi, from the ARMS Laboratory of the University of California Davis, for co-supervising this thesis.

I am very grateful for the excellent work of my students, who allowed me to supervise their Bachelor Theses, Semester Projects and Master Theses: Christian Hauschel, Oliver Jaussi, Kotaro Mori, Roman Rüttimann, Adrian Ryser, Philip Satz and Sven Schmid. Their invaluable contributions laid the profound basis for this work.

I would like to thank Dr. Michael Gebhardt, my former supervisor and the reason I applied for this PhD position in the first place and Moritz Wiessner who developed the thermal test piece and who supported me throughout the further development.

Special thanks goes to Pablo Hernández Becerro my office colleague and friend. He always supported me during my time and helped me through challenging industrial projects. He was always a great listener whenever I had a problem. Without those helpful discussions this thesis would not be the same.

My time at the institute was enriched by all the support of my colleagues and friends at IWF and inspire AG. A special thanks goes to Daniel Spescha, Natanael Lanz, Titus Haas, Michal Kuffa, Florentina Pavliček, Nico Zimmermann, Joel Purtschert and Nino Ceresa.

One last and very meaningful thanks goes to my beloved wife Una and my son Liam who supported me throughout this time and who always believed in me and my success.

Philip Blaser  
February 2020

# Contents

<b>1</b>	<b>Introduction</b>	<b>1</b>
<b>2</b>	<b>State of the Art</b>	<b>3</b>
2.1	Thermal Influences on Machine Tools . . . . .	3
2.1.1	Internal Influences . . . . .	4
2.1.2	External Influences . . . . .	6
2.1.3	ISO Standards . . . . .	7
2.2	Metrological Investigation of Thermo-Mechanical Behavior . . . . .	7
2.2.1	Direct Measurement of Thermo-Mechanical Deviations . . . . .	9
2.2.2	Indirect Measurement of Thermo-Mechanical Deviations . . . . .	11
2.3	Modeling and Compensation of Thermo-Mechanical Errors of Machine Tools	21
2.3.1	Physical Modeling and Compensation of Thermo-Mechanical Errors of Machine Tools . . . . .	23
2.3.2	Empirical Modeling and Compensation of Thermo-Mechanical Er- rors of Machine Tools . . . . .	24
2.4	Discussion of the State of the Art . . . . .	30
2.5	Research Gap . . . . .	31
2.6	Outline of the Thesis . . . . .	32
<b>3</b>	<b>Fundamentals of Dynamics of Thermo-Mechanical Systems</b>	<b>33</b>
3.1	The 1D Heat Equation . . . . .	34
3.1.1	Non-dimensionalization . . . . .	34
3.1.2	Periodic Boundary Conditions . . . . .	35

3.1.3	Solution of Heat Equation . . . . .	35
3.1.4	Analysis of the Heat Equation Solution . . . . .	39
3.2	The 1D Thermal Elongation . . . . .	41
3.2.1	The Pseudo-Hysteresis Effect . . . . .	41
3.2.2	Discrete Time-Series Modeling . . . . .	44
<b>4</b>	<b>Dynamic Thermal Error Modeling Methodology for Machine Tools</b>	<b>47</b>
4.1	Models of Time-Invariant Systems . . . . .	47
4.1.1	Autoregressive Model with Exogenous Inputs . . . . .	48
4.1.2	Linear Regression of ARX Models . . . . .	49
4.1.3	MIMO System Identification . . . . .	51
4.2	Simulation . . . . .	52
4.2.1	Static Modeling . . . . .	54
4.2.2	Dynamic Modeling . . . . .	56
4.2.3	Comparison . . . . .	61
<b>5</b>	<b>On-machine Measurements for Thermal Error Characterization</b>	<b>65</b>
5.1	Utilized machine tool and equipment . . . . .	65
5.1.1	Machine tool . . . . .	66
5.1.2	Touch probe . . . . .	66
5.1.3	Temperature sensors . . . . .	67
5.2	On-machine Measurement Cycle . . . . .	68
5.3	Uncertainty of On-machine Measurement Cycle . . . . .	71
5.3.1	Uncertainty of a Sphere Measurement . . . . .	71
5.3.2	Uncertainty of Thermal Error Measurement Cycle . . . . .	72
5.4	Thermal Error Measurement with On-machine Measurement Cycle . . . . .	75
<b>6</b>	<b>Thermal Adaptive Learning Control</b>	<b>79</b>
6.1	Methodology . . . . .	80
6.2	Adaptive ARX Model Estimation . . . . .	82
6.2.1	Calibration Phase . . . . .	82



6.2.2	Start of Compensation . . . . .	83
6.2.3	No-Good Phase . . . . .	83
6.2.4	ARX Model Parameter Update . . . . .	84
6.3	Sensitivity Analysis . . . . .	84
6.3.1	Experiments . . . . .	85
6.3.2	Quality Indicators . . . . .	90
6.3.3	Results . . . . .	90
6.3.4	Optimal Parameter Estimation . . . . .	93
6.3.5	Discussion . . . . .	95
6.4	Thermal Error Compensation with TALC . . . . .	96
6.4.1	Axes Offsets . . . . .	96
6.4.2	Long-Term Compensation . . . . .	97
6.4.3	Compensation of Fast Boundary Condition Changes . . . . .	106
<b>7</b>	<b>Thermal Test Piece</b>	<b>117</b>
7.1	Design of Test Piece . . . . .	117
7.1.1	Pre-machining . . . . .	119
7.1.2	Test Cycle . . . . .	121
7.2	Measurement Procedure . . . . .	124
7.2.1	CMM Inspection . . . . .	124
7.2.2	On-Machine Inspection . . . . .	127
7.2.3	Manual Inspection . . . . .	128
7.3	Validation of Thermal Test Piece . . . . .	130
7.4	Compensation with TALC . . . . .	132
<b>8</b>	<b>Conclusion and Outlook</b>	<b>137</b>

# Symbols and Abbreviations

## Notations

Generally, vectors are represented by underlined small letters—e.g.  $\underline{a}$ . Matrices are represented by double-underlined capital letters—e.g.  $\underline{\underline{A}}$ . The mean value is represented by a overline—e.g.  $\bar{a}$ . Time discrete variables are represented by letters followed by square brackets—e.g.  $a[k]$ , where  $k$  is an integer.

## Latin Symbols

$A$	Amplitude
$a$	Parameter for the shifted outputs
$b$	Parameter for the shifted inputs
$B$	B-axis position
$\hat{B}$	Nominal B-axis position
$c$	Specific heat capacity
$C_1$	Integration constant
$C_2$	Integration constant
$C$	C-axis position
$\hat{C}$	Nominal C-axis position
$d/2$	Eccentric distance between sphere and the center of rotation
$d_{Xj}$	Distance of the X-facets to the origin of the thermal test piece
$d_{Yj}$	Distance of the Y-facets to the origin of the thermal test piece
$d_{Zj}$	Distance of the Z-surface to the origin of the coordinate system of the thermal test piece
$e$	Disturbance
$E$	Thermal elongation
$\hat{E}$	Modeled thermal elongation
$E_X$	Thermal error in X-direction of the thermal test piece

$E_Y$	Thermal error in Y-direction of the thermal test piece
$E_Z$	Thermal error in Z-direction of the thermal test piece
$E_B$	Thermal angular error around the Y-direction of the thermal test piece
$E_{TTP}$	Radial growth of the thermal test piece
$E_{RMS}$	Root mean square error
$E_{SMAP}$	Symmetric mean absolute percentage error
$E_{PV}$	Peak to peak improvement
$E_{X0C}$	Error of the position of C in X-axis direction
$E_{Y0C}$	Error of the position of C in Y-axis direction
$E_{Z0T}$	Position error of the table surface in Z-axis direction
$E_{ROT}$	Radial error of the functional surface table
$E_{A0C}$	Error of the orientation of C in A-axis direction; squareness of C to Y
$E_{B0C}$	Error of the orientation of C in B-axis direction; squareness of C to X
$E_{C0C}$	Zero position error of C-axis
$Env_{RT}$	Environmental temperature during the R-Test measurement
$Env_{TP}$	Environmental temperature during the thermal test piece cycle
$g_{Xj}$	Distance of the X-facets to the corresponding reference facet in each segment
$g_{Yj}$	Distance of the Y-facets to the corresponding reference facet in each segment
$h$	Convection coefficient
$k$	Thermal conductivity
$L$	Length of rod
$L_*$	Characteristic length
$l_X$	Distance from one X-facet to the opposite facet of the thermal test piece
$l_Y$	Distance from one Y-facet to the opposite facet of the thermal test piece
$n_a$	Output order
$n_b$	Input order
$N$	Total number of measurements
$\underline{p}_{nom}$	Nominal position vector
$\underline{p}_{act}$	Actual position vector
$\underline{\underline{p}}_{act}$	Actual position matrix of measurement cycle
$q$	Time shift operator
$Q_{Prod}$	Quality indicator productivity
$r_{xy}$	Pearson correlation coefficient
$R$	Radius of thermal test piece
$t$	Time
$t_{total}$	Duration of experiment

$t_M$	Duration of on-machine measurement
$\hat{t}$	dimensionless time
$T_*$	Characteristic time
$T_{Env}$	Environmental temperature
$u$	Temperature distribution
$u_n$	$n^{th}$ system input
$\hat{u}$	Dimensionless temperature distribution
$U_*$	Characteristic temperature
$U(k = 2)$	Extended uncertainty with a confidence interval of 95%
$x$	Position along the X-axis
$\hat{x}$	Dimensionless position on the X-axis
$X$	X-axis position
$\hat{X}$	Nominal X-axis position
$Y$	Y-axis position
$\hat{Y}$	Nominal Y-axis position
$Z$	Z-axis position
$\hat{Z}$	Nominal Z-axis position

## Greek Symbols

$\alpha$	Thermal expansion coefficient
$\beta$	Angle of the Z-surfaces in the thermal test piece coordinate system
$\kappa$	Thermal diffusivity
$\omega$	Angular frequency
$\phi$	Phase
$\varphi$	Phase shift
$\rho$	Density

## Mathematical Definitions

$\text{Re}\{z\}$	Real part of the complex number $z$
$\text{Im}\{z\}$	Imaginary part of the complex number $z$
$\frac{\partial}{\partial a}$	First derivative
$\frac{\partial^2}{\partial a^2}$	Second derivative
$i$	Imaginary number
$[a]$	Floor function to bring $a$ down to a round figure
$a\%1$	Modulus function to represent the remainder of $a$ after division by 1

## Abbreviations

ANN	Artificial Neural Networks
API	Automated Precision
ARX	Autoregressive with Exogenous Input
ASAP	As Soon As Possible
ATC	Automated Tool Change
BC	Boundary Conditions
CFRP	Carbon Fiber Reinforced Plastic
CMM	Coordinate Measuring Machine
CNC	Computer Numerical Control
CP	Calibration Phase
DCG	Drive in Center of Gravity
DFG	Deutsche Forschungsgemeinschaft
DVM	Differential Vector Method
ENV	Environment
ETH	Eidgenössische Technische Hochschule
ETVE	Environmental Temperature Variation Error
FDEM	Finite Differences Element Method
FDM	Finite Difference Method
FEM	Finite Element Method
FIR	Finite Impulse Response
FL	Fuzzy Logic
FOCAS2	Fanuc Open CNC API Specification Version 2
GUM	Guide to the Expression of Uncertainty in Measurement
HSS	High Speed Steel
HTM	Homogeneous Transformation Matrix
IC	Initial Condition
LSE	Least-Squares Estimate
MDL	Minimum Description Length
MIMO	Multiple Input Multiple Output
MISO	Multiple Input Single Output
MOR	Model Order Reduction
MPE	Maximal Permissible Error
MWF	Metal Working Fluid
NG	No-Good
ODE	Ordinary Differential Equation
OE	Output Error

OM	On-Machine Measurement
P99	99 <sup>th</sup> Percentile
PCC	Pearson Correlation Coefficient
PDE	Partial Differential Equation
Post CP	Compensation Phase
PT1	First Order Time Delay Element
PT2	Second Order Time Delay Element
TALC	Thermal Adaptive Learning Control
TCP	Tool Center Point
TF	Transfer Function
VDI	Association of German Engineers
WLSE	Weighted Least-Squares Estimate
WS	Workspace

# Abstract

Precision manufacturing processes are strongly connected to the accuracy of machine tools. There is an increasing demand for high precision workpieces, since the quality of the functional surfaces can be linked to efficiencies of the parts during its operational phase. One of the largest contributors to errors on machined workpieces are thermal influences of the used machine tools.

Therefore the following thesis deals with the development of an on-machine measurement cycle, that captures the most dominant thermal errors in a timely manner and the design of a self-learning adaptive thermal error modeling methodology, which is based on the system identification theory, in order to resolve the most common problems of thermo-mechanical error compensation, including model inaccuracy, non-robustness and long-term instability, model calibration difficulties, lengthy experiments and model adaptation problems. The developed model is then used to compensate the occurring thermal errors of a 5-axis machine tool by correcting the axis movements utilizing the numerical control.

The developed on-machine measurement cycle is capable of measuring the five thermal position and orientation errors of an axis of rotation, as well as the two thermal errors of the functional table surface. As a measurement instrument a touch trigger probe is used. Under the given circumstances an extended uncertainty of maximum  $0.6 \mu\text{m}$  respectively  $2.6 \mu\text{m}/\text{m}$  is achieved. The validation measurements showed, that the thermal behavior can be captured and a minimal process intrusion is caused. The measurement cycle also shows reliable results, when the machine tool is running with metal working fluid and no significant increase in measurement uncertainty is observed.

A common and effective method to model thermal errors on machine tools is the phenomenological model analysis, which captures the correlation between the observed thermally induced errors and the thermal and losses related information. Preferably, the residual errors between the prediction model and the actual machine tool deviations will

approach zero. However, the actual machining conditions may not be identical to the machining conditions used to derive the model, which leads to model uncertainties. This can cause complications, especially for small batch productions, where the sequence of manufacturing processes changes repeatedly as do the direction and rate of change of thermal effects. Due to statistical uncertainties, assumptions in the model and the ever-changing boundary conditions, the error models derived from pre-process calibration are not necessarily accurate enough in the long term. They need to be verified and updated recurrently as the machine tool is continually used. Therefore an adaptive learning control for thermal error compensation is developed, that combines the functionality of a dynamic thermo-mechanical model, with fully automatized on-machine measurements of the thermal errors. This enables self-learning and self-adaptation of the compensation model to the current thermal state of the machine tool. Therefore a long-term stability and robustness can be ensured and a minimum of machine downtime due to measurements is ensured.

Experiments on a 5-axis machine tool show, that over the period of 178 hours a reduction of up to 80 % of the thermal errors of a rotary axis C, are achieved. Furthermore is shown, that the presented approach is capable of handling fast boundary condition changes, such as fast fluctuations in the environment as well as switching conditions such as the metal working fluid supply. In such an experiment a reduction of the occurring errors of up to 88 % is achieved, which corresponds to an absolute reduction of almost  $40 \mu\text{m}$ .

To demonstrate the reduction capabilities of the thermal adaptive learning control on an actual machined workpiece a thermal test piece is developed. The thermal test piece offers the possibility to evaluate the thermal deviations in all three spatial directions, one angular deviation, as well as the distortion of the workpiece itself. The test piece is designed to be measured directly on the machine tool, which enables a fully automatized evaluation of the thermal errors of a machine tool and to monitor the thermal error compensation quality. Two experiments are conducted, one with and one without active thermal adaptive learning control. The deviations in the first hour of the heating up phase are reduced by up to 97 % and a reduction of up to 91 % over the whole 8 hours of the experiment is achieved.



# Zusammenfassung

Die Produktion von hochpräzisen Teilen, Apparaten und Maschinen ist stark mit der Fertigungsgenauigkeit von Werkzeugmaschinen verbunden. Es besteht ein zunehmender Bedarf an hochpräzisen Werkstücken, da die Qualität der Funktionsflächen mit der Effizienz der Teile in der Betriebsphase verknüpft werden kann. Einer der größten Fehlerquellen an bearbeiteten Werkstücken sind thermische Fehler von Werkzeugmaschinen.

Daher beschäftigt sich die folgende Arbeit mit der Entwicklung eines On-Machine-Messzyklusses, der die dominierenden thermischen Fehler zeitnah erfassen kann, und dem Entwurf einer selbstlernenden adaptiven thermischen Fehlermodellierungsmethodik, die auf der Theorie der Systemidentifikation basiert. Damit können die häufigsten Probleme der thermomechanischen Fehlerkompensation gelöst werden, einschliesslich Modellgenauigkeit, Robustheit, Langzeitstabilität, Modellkalibrierungsschwierigkeiten, langwierige Experimente und Modelladaptionsprobleme. Das entwickelte Modell wird dazu verwendet, die auftretenden thermischen Fehler einer 5-Achs-Werkzeugmaschine durch Korrektur der Achsbewegungen mit Hilfe der numerischen Steuerung zu kompensieren.

Der entwickelte On-Machine-Messzyklus ist in der Lage, die fünf thermischen Positions- und Orientierungsfehler einer Drehachse sowie die zwei thermischen Fehler der funktionalen Tischoberfläche zu messen. Als Messinstrument wird ein schaltender Messtaster verwendet. Unter den gegebenen Umständen wird eine erweiterte Unsicherheit von maximal  $0.6\ \mu\text{m}$  bzw.  $2.6\ \mu\text{m}/\text{m}$  erreicht. Die Validierungsmessungen zeigen, dass das thermische Verhalten erfasst werden kann und ein Minimum an Prozessunterbrüchen verursacht wird. Der Messzyklus zeigt auch dann zuverlässige Ergebnisse, wenn die Werkzeugmaschine mit Kühlschmiermittel betrieben wird. Es wird keine signifikante Erhöhung der Messunsicherheit beobachtet.

Eine gängige und effektive Methode zur Modellierung thermischer Fehler an Werkzeugmaschinen ist die phänomenologische Modellanalyse, die die Korrelation zwischen den

beobachteten thermisch induzierten Fehlern und den thermischen und verlustbezogenen Informationen erfasst. Theoretisch sollten die Restfehler zwischen dem Vorhersagemodell und den tatsächlichen Werkzeugmaschinenabweichungen gegen Null gehen. Die tatsächlichen Bearbeitungsbedingungen sind jedoch möglicherweise nicht identisch mit den zur Ableitung des Modells verwendeten Gegebenheiten, was zu Modellunsicherheiten führt. Dies kann zu Komplikationen führen, insbesondere bei Kleinserien, bei denen sich die Reihenfolge der Fertigungsprozesse sowie Richtung und Geschwindigkeit der Änderung der thermischen Effekte wiederholt ändern. Aufgrund der statistischen Unsicherheiten, der Annahmen im Modell und der sich ständig ändernden Randbedingungen sind die aus der Vorprozesskalibrierung abgeleiteten Fehlermodelle auf Dauer nicht genau genug. Sie müssen im Zuge der kontinuierlichen Nutzung der Werkzeugmaschine immer wieder verifiziert und aktualisiert werden. Daher wird eine adaptive lernende Regelung zur thermischen Fehlerkompensation entwickelt, die die Funktionalität eines dynamischen thermo-mechanischen Modells mit einer vollautomatischen Messung der thermischen Fehler auf der Maschine kombiniert. Dies ermöglicht eine selbstlernende und selbstanpassende Anwendung des Kompensationsmodells an den aktuellen thermischen Zustand der Werkzeugmaschine. Somit kann eine Langzeitstabilität und Robustheit gewährleistet werden und ein Minimum an messtechnisch bedingten Maschinenstillstandszeiten ist gewährleistet.

An einer 5-Achs-Werkzeugmaschine wird gezeigt, dass über den Zeitraum von 178 Stunden eine Reduzierung der thermischen Fehler der Rotationsachse um bis zu 80 % erreicht wird. Weiterhin kann gezeigt werden, dass der vorgestellte Ansatz in der Lage ist, schnelle Randbedingungsänderungen, wie z.B. rasche Schwankungen in der Umgebung sowie Schaltzustände wie z.B. die Zuführung von Kühlschmierstoff zu beherrschen. In einem solchen Experiment wird eine Reduktion der auftretenden Fehler von bis zu 88 % erreicht, was einer absoluten Reduktion von fast  $40\ \mu\text{m}$  entspricht.

Um die Kompensationsfähigkeit der thermisch adaptiven Lernkontrolle an einem tatsächlich bearbeiteten Werkstück zu demonstrieren, wird ein thermisches Prüfwerkstück entwickelt. Das thermische Prüfwerkstück bietet die Möglichkeit, die thermischen Abweichungen in allen drei Raumrichtungen, eine Winkelabweichung sowie die Verformung des Werkstücks selbst zu erfassen. Das Prüfwerkstück ist so konzipiert, dass es direkt auf der Werkzeugmaschine vermessen werden kann, was eine vollautomatische Auswertung der thermischen Fehler einer Werkzeugmaschine und die Überwachung der Kompensationsqualität ermöglicht. Zwei Experimente, eines mit und eines ohne thermisch adaptive Lernkontrolle, wurden durchgeführt. Dabei kann gezeigt werden, dass in der ersten Stunde der Aufwärmphase eine Reduktion der auftretenden thermischen Werkstückfehler von bis zu 97 % erreicht wird. Über die gesamte Dauer des Experiments, 8 Stunden, kann eine Fehlerreduktion von bis zu 91 % erreicht werden kann.

## Chapter 1

# Introduction

Productivity and accuracy of machine tools are important competitive aspects. As advances in precision manufacturing require repeatable functionality of multi-axis machines, tremendous efforts have been made to ensure process stability and accuracy of machine tools.

Because machine inaccuracy is a major source of dimensional errors of workpieces, the control of machine tool errors and error sources is important. In general, machine errors consist of kinematic errors, thermo-mechanical errors, motion control errors, static errors due to load changes, dynamic geometric errors due to excitation by time-variant load changes and errors due to wear of components. Among them, thermally induced errors are known to be key contributors to the dimensional workpiece error, as stated by Mayr et al. [80]. In a recent study Putz et al. [94] conclude that the thermal error attributes to half of the total machining error. In a survey published by Bryan [22], the expert J. Peklenik insinuates, based on his own experience, that the influence of thermal errors may lie between 40 % and 70 % of the overall machining error. The ultimate magnitude of the thermally induced errors depends on the machine tool itself, the measurement system, the machined workpiece, the process, the machining conditions as well as the environmental conditions. Nevertheless, it is safe to say that thermal errors affect the accuracy of machine tools considerably.

The issue of thermal deformations in machine tools has received considerable attention since it first gained greater recognition in the 1960s, when the field of thermal error research was established due to closer manufacturing tolerances and the distribution of computerized numerical control (CNC) technology. Since the very first keynote paper by Bryan in 1968 [22] substantial amount of research has been conducted to minimize thermally induced workpiece errors. A major share of this research is summarized by the CIRP keynote papers of Bryan in 1990 [23], Weck et al. in 1995 [116] and Mayr et al. in 2012 [78]. The importance of the topic is reflected in the fact that in Germany more

than 30 researchers are funded directly by the Deutsche Forschungsgemeinschaft (DFG) for the research in thermo-energetic design of machine tools. The research project is called CRC/TR96 and was started in 2011 with its first funding period and will end with the completed third period in 2023.

Since the thermal behavior of machine tools is affected by a variety of factors, reducing thermal errors is a complex process. As both internal and external influences affect the thermal behavior of a machine tool, it is not possible to avoid the occurrence of thermal errors solely by design measures of the machine structure in an acceptable economical effort. To reduce undesirable errors through thermal deformations of the machine tool the development of CNC based compensation methods is an effective and economical way. The ability to compute the occurring thermal errors of machine tools is one of the most promising procedures to improve the accuracy of machine tools and meets the accuracy requirements for future high precision machine tools, as stated by McKeown [85].

Due to the advances in sensing, modeling, and computer techniques, software based error compensation approaches have received wide attention in cost-effectively improving the machining accuracy. These techniques have achieved great success in compensating geometric errors of machine tools. Nevertheless, they are not as effective in the long-term when applied to thermally induced errors. This results from the fact that the thermal issues in machines, which are caused by time-variant changes of the temperature field according to the working cycle and the environmental conditions, are more complex than geometric problems. The effectiveness of thermal error compensation largely relies on the accuracy of prediction of the spatial and time-variant thermo-mechanical errors during machining. Despite extensive research in the field over the last decades, Yang [127] states that major barriers still exist that prevent the practical implementation of thermal error compensation in real industrial production, mainly:

- The process of characterizing thermal machine tool errors is difficult and costly
- Insufficient accuracy and robustness of the thermal error estimation model
- Lack of efficient thermal error calibration methodology
- Lack of model self-adaptation capability under working condition changes

In order to resolve the aforementioned problems, including model inaccuracy and non-robustness, model calibration difficulties, lengthy experiments and model adaptation problems, the goal of this thesis is to develop a self-learning and self-adapting dynamic thermal error modeling methodology.

## Chapter 2

# State of the Art

The thermal influences on machine tools are chronologically summarized in topic related Keynote papers of the CIRP Annals by Bryan in 1968 [22] respectively in 1990 [23], by Weck et al. in 1995 [116] and Mayr et al. [80] in 2012. These four keynote papers conclude that the thermo-mechanical behavior of machine tools can be the most dominant error source of machined workpieces and that the relationship between the thermal load acting on the machine and the thermal displacement at the tool center point (TCP) is complex. Due to the inaccurate knowledge of the heat losses, thermal boundary conditions, mechanisms of heat transfer, material properties and many more factors, a precise prediction of the thermal behavior is difficult.

This chapter describes the thermo-mechanical behavior of machine tools and the state of the art in regards of metrological investigation, modeling and compensation with a special focus on empirical modeling techniques.

## 2.1 Thermal Influences on Machine Tools

Bryan [23] summarized the thermal influences on the machined workpieces in his “thermal effects diagram”. The mentioned sources that can cause thermal errors are:

- Environmental influences
- Cutting process
- Power losses of machine components
- Tempering devices
- Metal working fluid
- People
- Thermal memory from previous environments

In Figure 2.1, a subdivision of the causes in external and internal influences according to Mayr et al. [83] is shown and the chain of effects that result in thermal errors at the TCP is illustrated as well as the possibilities for thermal error reduction of machine tools. The figure shows that power losses, e.g. in the drives and pumps caused by friction and energy dissipation, are transferred to the machine tool structure either by conduction, convection or radiation. This leads to a mostly nonhomogeneous temperature field of the machine tool and a corresponding deformation of the structure due to the temperature dependent elongation of the different structural materials. These effects can be reduced by minimization of the causes when designing or retrofitting the machine tool. Additionally the resulting TCP errors, due to the deformation of the structure, can be compensated by using the machine tool axes and the numerical control. The following sections, Section 2.1.1 and Section 2.1.2 discuss the subdivision in internal and external influences in more detail.

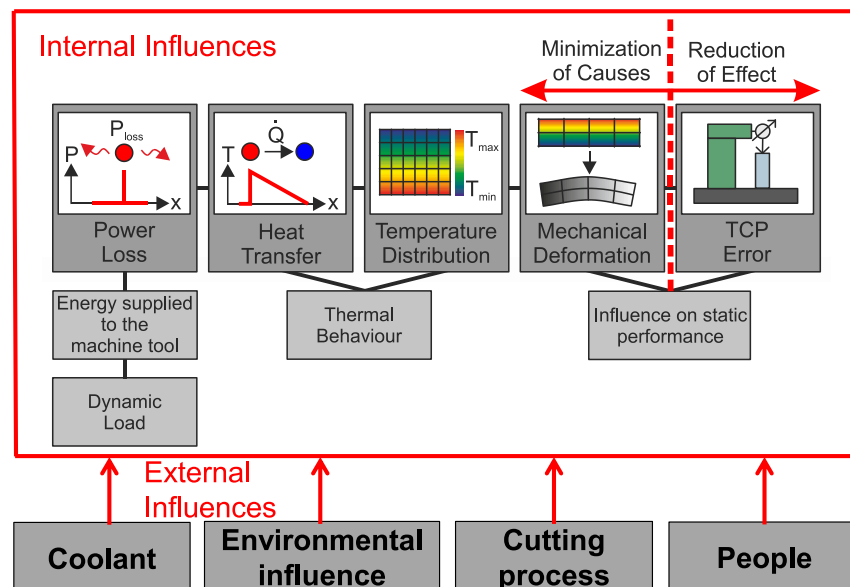


Figure 2.1: Thermal chain of causes and TCP errors [83]

### 2.1.1 Internal Influences

Machine tools have many internal heat sources - spindle motors, drive motors, hydraulic and pneumatic pumps, etc. These internal heat sources conduct the generated heat directly into the machine structure or the surrounding environment. Understanding the effects of these sources is of high importance for the general analytical description of the thermal behavior of machine tools.

As stated by Li et al. [76] and Weck et al. [116] the spindle system and its bearings, as one of the core elements of a machine tool, are one of the main heat sources in terms of its contribution to the total heat generation and resulting deformations. The influence of the spindle depends on various factors, such as spindle type, the type of bearings and the spindle diameter. Bossmanns and Tu [8] investigated the heat losses of a high speed motorized spindle. The spindle is rated at 32 kW maximum power and 25 000 rpm maximum speed. They computed that such a spindle, while running at 250 000 rpm, is producing 2.4 kW heat losses, of which 80 % is produced by the motor itself and around 20 % is generated in the preloaded bearings. The remaining amount of the spindle power is converted into heat due to the cutting process itself.

Additional internal heat sources are the feed drive systems due to friction losses and therefore causing a considerable thermal drift either directly by elongation of the ball screw or at the linear encoder systems of the machine and the underlying TCP. In an experimental setup, where the guideway, the ball screws and the nut are taken into account, Schmitt and Schulz [102] discovered that the nut generates up to 190 W of heating power for feed rates of 25 m/min, which results in a steady state temperature increase of 75 °C for a feed rate of 25 m/min and up to 82 °C for a 30 m/min feed rate.

Züst [130] developed a model based characterization and optimization of machine tool internal heat sources, in order to contribute to the improvement of the machine's precision and energy efficiency. The author states, that parametrizable models of the main spindle, the feed axes, the cooling system and the hydraulic system are sufficient to characterize the thermo-energetic machine behavior. For the characterization of those component's internal heat sources, Züst presents a set of generic models of thermo-energetic machine tool components. This generic models define the interfaces of a component model and enable the combination of different component models according to the investigated machine's topology. The focus is set on thermo-energetic relevant components. This kind of component is characterized by a significant heat input in combination with a thermal contact to the machine's structure or to a cooling circuit. The work presents a new simulation approach for the evaluation of the thermo-energetic dynamics of components in machine tools.

Less considered and researched internal heat sources are the rotary and swiveling axes of 5-axis machine tools, which are most likely driven by direct drive motors integrated into the structure, so that the heat directly conducts into the machine tool frame. Gebhardt [40] characterized the thermal behavior of rotary axes in 5-axis machine tools. He presents temperature measurements during different operational states of the rotary axes and shows, that due to the power supply to the axis drives, a significant change in the temperature distribution of the machine tool structure is induced. This temporal and spatial temperature change causes significant errors between tool and workpiece of the machine

tool.

The research of internal heat sources is of fundamental importance to minimize the occurring thermal workpiece errors. The focus of most papers lays on the reduction of the heat input into the structure, either by the means of design improvements or by novel cooling strategies.

### 2.1.2 External Influences

A major external heat source is the process itself, which warms up the tool, tool holder, workpiece and clamping device. A part of the heat generated by the process is also conducted into the chips. Therefore, the machine table, the structure and other components heat up indirectly by hot chips. An analytical analysis of the heat generation during the cutting process is performed by Klocke et al. [74] in 2015 and extended by Abouridouane et al. [1] in 2016. A verification due to experimental results is performed by Augspurger [3] et al. in 2016. The authors conclude that due to the difficulties in measuring the temperature field of the process zone and the formed chips, an adequate numerical model is needed to accurately predict the heat generated by the cutting process.

Most cutting processes are performed with metal working fluid (MWF) to lubricate the process zone, to dissipate the heat from the process and to evacuate the chips from the working space. According to Mayr et al. [83] the MWF is considered an external influence as well. In 2014 Mayr et al. [81] investigated the MWF influences on the overall thermal behavior of a 5-axis machine tool. The authors show that the MWF has a strong influence on the temperature distribution as well as on the occurring thermal deviations. They stress that especially the change from dry to wet cut or vice versa has a very negative influence on the accuracy of the machine tool. Brecher et al. [14] discussed the issue of non-temperature controlled MWF and concluded that the MWF can have a major impact on machining accuracy and therefore should be investigated in more detail. In 2017 Wegener et al. [118] published a keynote paper about fluid elements in machine tools and devoted one chapter to the research activities in the field of energy efficiency and thermal behavior of machine tools. This overview showed, that the importance of the fluid supplied to a machine tool is widely recognized by the research community. Nevertheless the amount of research conducted on the thermal influences is still very limited.

Another dominant external influence is the environment surrounding the machine tool. The dominant heat exchange mechanism is convection or radiation. A temporal or spatial environmental temperature change, both in vertical as well as in horizontal direction, cause thermo-mechanical deformations at the TCP and prevent a steady-state. As stated by Weck et al. [116] the amplitude of the environmental temperature will vary with the geographical location, the season and the thermal characteristic of the machine shop.



In normal job-shop conditions spatial temperature differences of more than 5 °C can be observed. Additionally the machine enclosures is causing micro-climates, that cause locally different thermal convection coefficients and therefore different heat fluxes from the structure to the environment or vice versa. These effects have been studied in detail by Pavliček [93]. She developed meta models based on the simplified geometrical shapes of the enclosure and temperature measurements of the internal heat source as well as the surrounding temperature to estimate the conductive heat transfer coefficients of the specific wall segments.

### 2.1.3 ISO Standards

The standardized determination of thermal effects on machine tools is explained in three ISO standards. ISO 230-3:2007 [64] is the most general standard concerning thermal effects on machine tools, which deals with thermal distortions caused by either changing environmental temperatures, rotating the spindle or linear motions of components. The same tests are included in ISO 10791-10:2007 [56] for machining centers and in ISO 13041-8:2004 [61] for turning centers.

The underlying description of error motions, positioning errors and axis shifts of linear and rotary axes are stated in ISO 230-1:2012 [62]. In ISO 230-2:2014 [63], specifications and test procedures regarding the evaluation of the geometrical accuracy of linear axes are defined. The equivalent for rotary axes is defined in ISO 230-7:2015 [67]. The determination of thermal effects of rotary axes is not yet included in any international standards and can only be partly derived from the specifications and tests in ISO 230-3:2007. Currently ISO 230-3 is under review and will be extended with specifications of thermal effects of rotary axes in a future version.

The measurement strategies and setups are explained in more detail in the next section.

## 2.2 Metrological Investigation of Thermo-Mechanical Behavior

In this section the investigation of cause-effect relationships of the thermo-mechanical behavior of machine tools is covered. The metrological investigation of measurement machines and machine tools refers to the deviations between the TCP and the nominal contact point on a workpiece. The TCP is defined as a virtual point fixed on the tool. In milling machines, the TCP is always located on the spindle axis, in ball end mills for example it is the center of the ball, as illustrated in Figure 2.2.

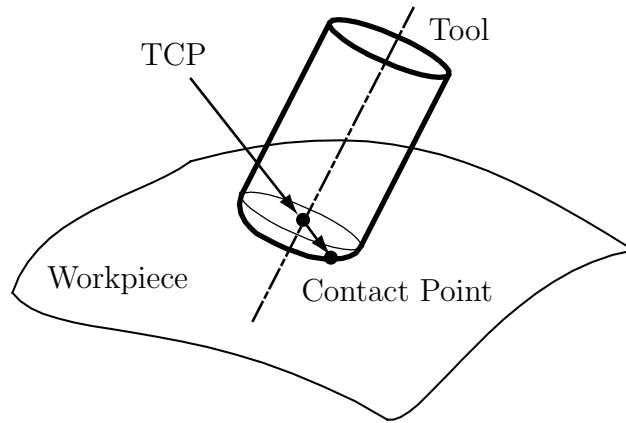


**Figure 2.2:** Illustration of the Tool Center Point (TCP) definition.

Machine tool errors can be divided into two groups: quasi-static errors and dynamic errors. Dynamic errors result from machine tool vibration, tool chatter, and spindle vibration. Quasi-static errors are composed of the geometric error of the machine, influence of static loading, and thermal effects on the machine structure. Static loading and thermal effects change the accuracy of the machine tool by altering the geometric error.

The tests in the aforementioned standard ISO 230-3:2007 [64] are designed to measure the relative displacements between the component that holds the tool and the component that holds the workpiece as a result of thermal expansion or contraction of relevant structural elements under representative load cases. Additionally the temperature of relevant structural parts and the environment have to be recorded to understand the relationship between TCP displacement and the heat flux brought into the machine structure. According to Wennemer [121] all measurement devices used for geometric error estimation can usually be utilized for thermo-mechanical investigations. An essential requirement is the measurement time, to minimize the transient thermal behavior during the measurement itself the time spent for measuring has to be minimized. Due to the superposition of geometrical and thermo-mechanical deformations, the thermal displacements can be decomposed from the geometrical deviations by subtraction of a reference state. Therefore only the relative change due to thermal effects is considered dominant for all the subsequent measurements.

Schwenke et al. [105] categorizes the different measurement methods in direct and indirect methods. Direct measurements allow the measurement of mechanical errors for a single machine axis without the influence of other axes. Direct measurements can be classified in three separate subgroups based on their metrological reference: the material-based methods use artifacts, such as straightedges, line scales or step gauges. The laser-based methods use the laser light's linear propagation and its wavelength as a reference. The gravity-based methods measure in reference to the gravity field of the earth. According

to Ibaraki and Knapp [49], the key of a direct measurement is to set up the measuring instrument so that only the targeted error motion influences the measurement results. On the other hand indirect measurements require multi-axes motion of the machine tool under investigation, e.g. movements to measure positions at different X, Y and Z positions, simultaneous movements of two linear axes, simultaneous movement of linear and rotary axes or machining of a workpiece with several machine axes moved simultaneously. These measurements focus on the TCP position as the superposition of single axis errors. The application of indirect measurements is mostly used to design a kinematic model or to identify geometric error parameters. A typical example of indirect measurements widely done by machine tool builders is the circular test using the double ball bar test, described in ISO 230-4:2005 [65]. Ibaraki and Knapp [49] explain, that in a circular test, measured contour error profiles are influenced by many error motions of two linear axes, e.g., the positioning and straightness error of each axis and the squareness error between both axes. By best-fitting the machine's kinematic model to measured trajectories, many error motions can be estimated and assigned to the specific axis by a single circular test.

### 2.2.1 Direct Measurement of Thermo-Mechanical Deviations

The most popular measurement setup to measure thermal deformations at a single point in the working space is presented in ISO 230-3:2007 [64]. It consists of five linear displacement sensors measuring against a precision mandrel, see Figure 2.3. With this setup three translational and two rotational errors between the TCP and the workpiece coordinate system can be measured. Typical investigations with this setup are the environmental temperature variation error (ETVE) test and thermal distortions caused by rotating spindle and by moving linear axis. Unfortunately, only a superposition of position independent and dependent errors can be measured with this setup at a single point in the whole working space, as shown e.g. by Horejš et al. [45], Mayr et al. [82] and Fujishima et al. [36]. An extension of this setup is presented by Brecher et al. [18], where five mandrels are mounted on a rotary table of a 5-axis machine tool and the probe fixture is clamped into the spindle. This advanced setup allows to estimate the thermal behavior of the spindle and the table at different points in the working space.

To directly measure the position dependent geometric errors of linear axes ISO 230-1:2012 [62] offers several recommendations of measurement setups and measurement devices. The laser interferometer has made its mark as the most accurate means of measuring one degree of freedom in machine tool building, stated by Bleicher et al. [7]. Taking into account the parameters air pressure, temperature and humidity, which have a strong bearing on the quality of measurements, manufacturers state accuracies of up to  $\pm 0.7 \mu\text{m}/\text{m}$  and a

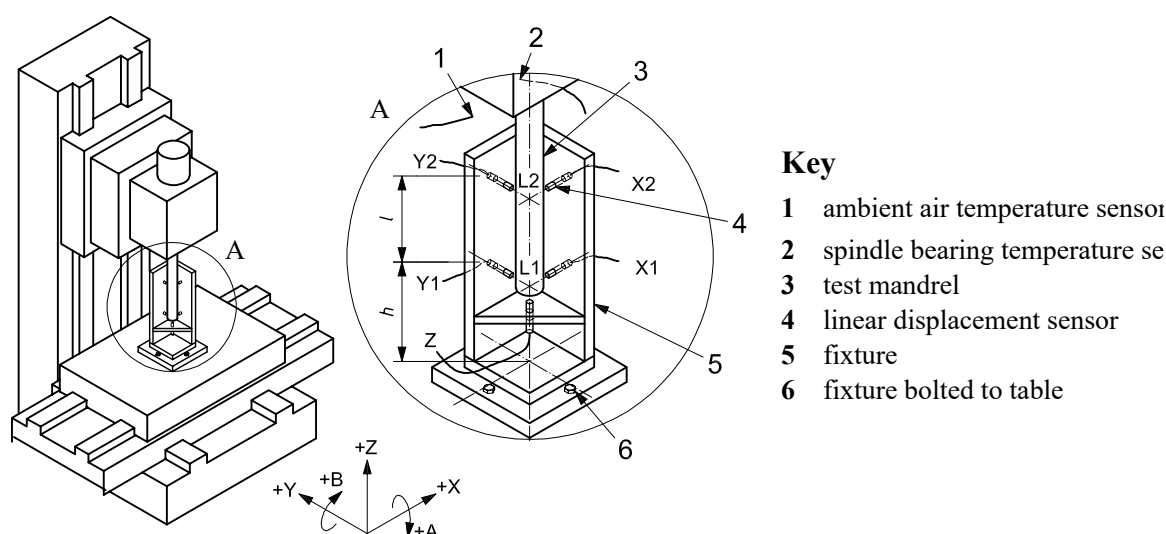


**Figure 2.3:** Typical set-up for testing environmental temperature variation error (ETVE) and thermal distortion of structure caused by rotating spindle and by moving linear axis on vertical spindle machining center [64]

resolution of 1 nm. According to Ibaraki and Knapp [49] the linear positioning error of a linear axis is typically measured by using a laser interferometer. Nevertheless, the laser interferometer is also capable of sequentially measuring the straightness and tilt error motions of linear axis. The change of the positioning error over time, mostly due to thermal influences, is investigated by many researchers. For example Shi et al. [107], Fines and Arvin [32] and Kim et al. [72] used a laser interferometer to measure the thermal positioning error distribution at discrete times and positions under different thermal load cases of the moving linear axis.

Based on a patented technology by Lau and Liu [75] in 1997, the companies Renishaw and Automated Precision (API) offer commercial devices using optical principles for simultaneous calibration of linear axes in six degrees of freedom. The system developed by Renishaw is called XM-60 [98] and the XD-Laser is distributed by API [2]. Yang et al. [126] showed that such devices can be used to efficiently measure all six error movements of a linear axis.

As pointed out by Rahman et al. [95] other means of direct measuring systems exist as well, for example the linear comparator, that is based on an interferential cross grid encoder. The comparator can determine the linear and non-linear curves as well as the reversal errors of machine axes according to ISO 230-2 [63]. In addition to determining the positioning errors, the comparator also measures guideway errors perpendicular to the traversal direction of the machine axes. Such a comparator is for example industrialized by the company Heidenhain under the name VM 182 [43] and consists of a glass scale with

a highly accurate graduation glued on a steel frame and a scanning head that moves over the graduation without mechanical contact, see Figure 2.4.

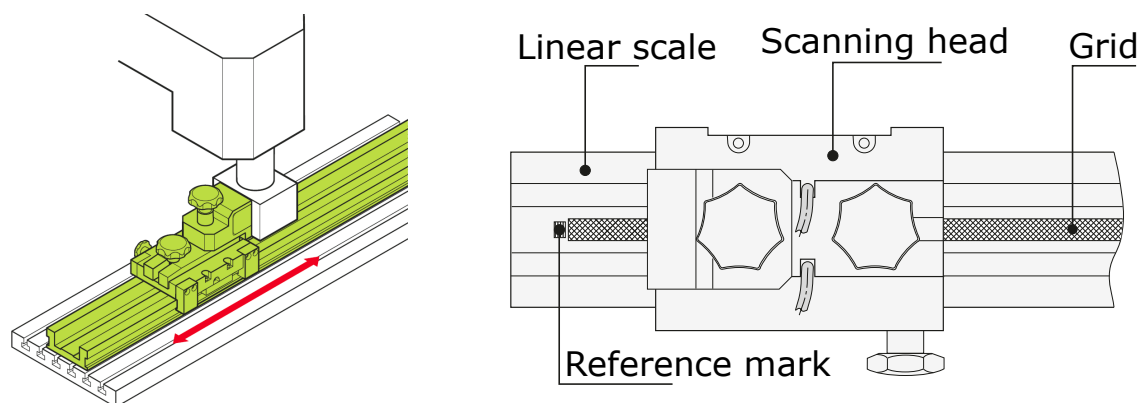


**Figure 2.4:** Illustration of components and installation of the exposed linear comparator (Heidenhain VM 182) [43]

In ISO 230-3:2007 [64] a very simple alternative measurement setup to measure the spatial thermo-mechanical deviations is presented. The setup consist of five measurement points arranged only at the beginning and the end of the axis stroke. This results in the fact, that non-linearities of the thermal errors over the axis position cannot be detected.

The direct measurement of one or more deviations allows a systematic measurement of individual measurands. The direct measurements always record the deviations in relation to the selected axis position, which must always be documented in accordance with ISO 230-3:2007 [64]. Axis dependencies therefore cannot be recorded directly, but only in connection with interim assembly operations. This results in measuring times of several hours. A comprehensive analysis of the thermo-mechanical behavior of machine tools is hardly feasible on this basis, since a stationary geometric machine condition can no longer be assumed after just a few minutes.

Indirect measuring methods offer a solution, which enables comparatively fast volumetric detection of machine deviations in the entire working space.

## 2.2.2 Indirect Measurement of Thermo-Mechanical Deviations

As stated by Ibaraki and Knapp [49] for volumetric error compensation, the efficiency of the direct measurement method can be a critical issue. For orthogonal 3-axis machines, 3 positioning errors, e.g.  $E_{XX}$ ,  $E_{YY}$ ,  $E_{ZZ}$ , 6 straightness errors, e.g.  $E_{XY}$ ,  $E_{XZ}$ ,  $E_{YX}$ ,  $E_{YZ}$ ,  $E_{ZX}$ ,  $E_{ZY}$ , 3 squareness errors, e.g.  $E_{C0X}$ ,  $E_{A0Z}$ ,  $E_{B0Z}$ , and 6 angular errors, e.g.  $E_{AX}$ ,  $E_{AY}$ ,  $E_{BX}$ ,  $E_{BY}$ ,  $E_{CX}$ ,  $E_{CY}$ , must be measured by different setups to construct the

machine's kinematic model. Indirect measurements focus on the tool tip location as the superposition of these single errors and thereby increase the efficiency of the measurement. Most of the volumetric measurement strategies mentioned by Ibaraki and Knapp can be used for the measurement of thermo-mechanical deviations, if they are long-term stable under workshop conditions and fast enough to capture the quasi static errors.

For a better overview Wennemer [121] categorized the indirect measurement methods as follows:

- Measurement artifacts
- Differential vector method
- Diagonal and Step-Diagonal Tests
- Laser tracker/tracer
- Test pieces

In the subsequent sections an overview of the most commonly used indirect measurement methods for the assessment of thermo-mechanical deviations of machine tools is given.

### **Measurement Artifacts**

As defined in ISO 1 [60] the standard reference temperature value for the specification of geometrical and dimensional properties is fixed at 20 °C. Unless otherwise explicitly specified, the reference temperature for geometrical and dimensional properties of workpieces shall be the standard reference temperature.

Artifacts whose dimensional properties are calibrated at 20 °C can be used for thermo-mechanical measurements of measurement machines and machine tools. By comparison of the dimensional measurements of the artifact to its calibrated properties or to its initial dimensions the displacement at the TCP can be evaluated at different points in time or at different thermal states. The thermal elongation of the artifact itself has either to be taken into account by means of temperature measurements or the material of the artifact has to have a sufficiently low thermal expansion coefficient. As stated by Sartori and Zhang [100] the uncertainty of the magnitude of thermal expansion coefficients can only be estimated in the range of  $\pm 10\%$  up to  $\pm 25\%$  for different types of alloys and heat treatment of nominally the same material. Therefore every artifact's thermal expansion coefficient needs to be estimated separately. Additionally the environmental temperature

varies in time and space, so that a homogeneous temperature field of the artifact cannot be ensured. Due to those uncertainties, most measurement artifacts are made out of materials with a sufficiently low thermal expansion coefficient. Commonly used materials are Invar, Zerodur<sup>®</sup> or carbon fiber reinforced plastics (CFRP).

On the other hand it is also possible to not compensate for the thermal expansion of the measurement artifact, so that the artifact mimics the thermal behavior of a potential workpiece. This approach has some restrictions, mainly that the thermal behavior of the machine is only tested for one certain workpiece material and that the dimensions of the artifact have to roughly reflect the final shape of the machined workpiece. Additionally, the workpiece shows a non-homogeneous temperature field due to the heat dissipation of the process itself, which leads to local distortions that cannot be reflected by the artifact. Due to those limitations it is common to assess the thermal behavior of the measurement machines or machine tools isolated from the workpiece behavior.

To estimate the thermal behavior of a machine tool the calibrated artifact is placed inside the machine tool and measured with a touch trigger probe at different thermal states, as presented by Mou and Liu [90]. As the authors explain, reference parts representing the actual geometric shapes and weights of workpieces are used as the metrology standards for machine error characterization. With the difference between the measured and the referred dimensions of the reference parts, the machine errors can be characterized and modeled. The models are used to compensate the positioning errors of a 3-axis machine tool and to increase the accuracy of process-intermittent probing. A similar approach but with a 3D measurement artifact made out of Invar is presented by Kim and Chung [70, 71]. The artifact covers an area of 470 mm × 330 mm × 240 mm and can be measured within four minutes. In combination with a kinematic machine model, the thermo-mechanical deviations, measured along a diagonal, can be reduced below 10 μm.

In contrast to the previous artifacts, ball bars or grids are also frequently used, which can offer a higher measuring accuracy compared to the previously used milled surfaces due to the higher form accuracy and surface quality of the balls (form deviation <0.4 μm). Yang and Lee [122] arranged two spheres diagonally in a plane (X-Y) so that the expansion in two directions (X and Y) and the translational displacement can be measured in less than a minute using analytical equations. For a volumetric analysis, however, significantly more measuring points are required.

Therefore Bringmann [21] developed a flat ball standard which is positioned on the machine table at multiple heights by means of spacers. The ball plate offers together with

the spacers and the used measurement method, a measurement uncertainty of  $\sigma_{k=2} \leq 5 \mu\text{m}$  in the relative position determination of the spheres, in a measuring volume of  $500 \text{ mm} \times 500 \text{ mm} \times 320 \text{ mm}$  and a nominal ball spacing of  $100 \text{ mm}$  under shop floor conditions. In combination with a kinematic model, the geometric errors of a 3-axis machine tool can be identified in about 45 minutes except for the rotational errors of the last axis and the yaw of the second last axis in the kinematic chain. The high number of measuring points makes it possible to speak of a complete volumetric displacement measurement for the first time. However, this method is not used for thermo-mechanical displacement measurements. A measurement time of 45 minutes is still a long time when used for modeling transient thermo-mechanical displacements.

Gomez-Acedo [41] used a flat spherical standard with 16 measuring points made from CFRP in a size of  $500 \text{ mm} \times 1400 \text{ mm}$  with a minimum ball spacing of  $200 \text{ mm}$  for the thermo-mechanical analysis and correction of a portal machine. At a feed rate of  $5000 \text{ mm/min}$ , the measurement is performed within 2 minutes. On the basis of a Kalman filter, Cartesian errors in space can be reduced by an average of 68% without the use of a kinematic machine model. The advantages of a volumetric analysis based on individual axis errors remain unused due to the low number of measuring points.

In summary, measurement artifacts, in particular spherical ball bars and grids, make volumetric measurement of machine tools possible. If available, a 3D probe, such as used by Bringmann [21] or Weikert [120], should be used. The necessary multiple probing of a simple touch trigger probe to determine the center of the sphere would considerably increase the measuring time, so that disturbing thermo-mechanical displacements are to be expected. However, according to Wennemer [121] even when 3D probes are used, long measurement times are to be expected, so that measurement artifacts in conjunction with an indirect volumetric measurement approach cannot be used for thermo-mechanical analysis of machine tools.

### Differential Vector Method

Another group of measuring instruments for checking the geometric accuracy of machine tools can be summarized as Differential Vector Method (DVM). Here, the relative displacement between a fixed point on the machine tool table and the TCP for different axis positions in the machine volume is recorded.

A planar variant of the DVM is the circular test according to ISO 230-4[65]. The 2D circular test can be used to analyze the perpendicularity of axes as well as kinematic deviations. If the 2D surface of the circular test is extended into the third dimension by a spherical surface, all 21 volumetric deviations of a 3-axis machine tool can be recorded



with a conventional double ball bar test, as shown by Spaan [108]. The major disadvantage of a double ball bar is its limited range. Therefore, like the ball plate, several experiments have to be carried out to cover the whole working space of the machine tool. Based on the work of Spaan, Florussen [34] extended the approach and selected 19 partial sphere surfaces with a measuring time of approximately three hours to record all 21 error parameters. Due to the long measuring time, the transient thermo-mechanical machine behavior is analyzed in a simplified variant with only one partial sphere surface with 17 measuring points and two minutes measuring time by Florussen et al. [33]. With the measurement point reduction, however, the application of a kinematic model is omitted and only the Cartesian deviations at the 17 measuring points are evaluated. The advantages of the indirect volumetric method are eliminated.

Yang [125] used a similar measurement technique for thermo-mechanical analysis. In contrast to the previous sequential methods, however, a continuous measurement is performed with a trajectory in the form of a helix. Due to the low measuring point density, purely Cartesian deviations in the machine volume are recorded. However, the potential of a continuous measurement to reduce the measuring time should not be underestimated.

Boye et al. [10] developed a comparable process based on a cross grid from the company Heidenhain. This optical 2D standard offers a measurement accuracy of less than  $1\ \mu\text{m}$  over a circular measuring surface with a diameter of 250 mm. In a total of six measuring setups the deviations are recorded for each setup along a path in the form of a spiral. A kinematic machine model enables the calculation of all 21 error parameters of a 3-axis machine tool. In this method, the measuring sequence consists of six individual measurements, each of which contains a manual mounting and alignment of the device. Unfortunately, there is no information in the paper about the entire measuring period. However, with an estimated time expenditure of five minutes per measurement run including installation, a total measurement time of 30 minutes must be expected. Transient thermo-mechanical displacements can therefore only be recorded to a limited extent on the basis of a rigid body model.

The additional position and orientation errors of the rotational axes of a five-axis machine tool can be measured and the performance can be tested with the R-Test. Firstly introduced by Weikert [120] and included in ISO 230-1 [62] and ISO 10791-6 [58]. Further executions of the R-Test and the underlying kinematic models are published by Bringmann and Knapp [20] and Ibaraki et al. [53]. A ball is fixed onto the machine table and a 3D probe is clamped in the tool holder, or vice versa. During measurement, the rotary axes of the machine table carry out a simultaneous movement with the linear axes. This

would result in a non measurable relative movement between ball and 3D probe in an ideal kinematics, in spite of the motion of all machine axes. The existing axis deviations, however, lead to errors of the TCP relative to the machine table, which can be recorded as difference vectors and converted into the position and orientation errors of the rotary axes.

The R-Test is a very common measurement device used for thermo-mechanical displacement measurements. Firstly used by Mayr et al. [79] in 2009 to measure the thermal displacements of a tool-sided A-axis in different indexations while running the main spindle. Ess et al. [29] later developed the discrete R-Test, which enables to measure the thermal displacements of rotary and swiveling axes of a 5-axis machine tool. With the discrete R-test, the position errors (e.g.  $E_{X0C}$  and  $E_{Y0C}$ ), the perpendicularity deviations to the linear axes (e.g.  $E_{B0C}$ ,  $E_{A0C}$ ) as well as the positioning accuracy (e.g.  $E_{C0C}$ ) can be measured within one minute. The measuring procedure is therefore sufficiently fast for a thermo-mechanical analysis of the mentioned deviations. Gebhardt et al. [37] extended the thermal error description for rotational axes by including the axial and the radial growth (e.g.  $E_{Z0T}$  and  $E_{R0T}$ ) of the functional table surface and showed the feasibility of measuring these additional errors in the same setup as described by Ess et al. [29]. These seven thermal errors allow a complete description of the thermal position and orientation errors of an axes of rotation.

The R-Test measurement concept and especially the chase-the-ball approach of Bringmann and Knapp [20] is further expanded by Bitar-Nehme and Mayer [6] to measure the thermal volumetric errors of a 5-axis machine tool at discrete points in the whole working space in under 3 minutes. The authors measure at 160 points and evaluate the Cartesian displacements over time, the application of a kinematic model is omitted and the benefits of indirect volumetric methods are not further exploited. Brecher et al. [17] applied this concept on the indirect volumetric method with the help of a kinematic model using B-Splines to model the error motions. The drawback is, that the procedure takes up to 2 hours and is so not applicable for thermal error measurements. Therefore Brecher et al. [16] presented a dynamic R-Test procedure to measure the volumetric errors of a 5-axis machine tool in under 10 minutes, with similar uncertainties as the discrete approach. Brecher et al. [19] also use this approach to measure thermo-mechanical deviations for all 5 axes. The enabling technology behind this advanced R-Test setup is the possibility to simultaneously record machine tool data and displacement sensor values with very little latency.

With the difference vector method, the 21 error parameters of 3-axis machine tools (double ball-bar) as well as the additional position and orientation errors of the rotary axes of 5-axis machine tools (R-Test) can be recorded. These methods can also be applied to a thermo-mechanical deviation analysis. In particular, however, the methods utilizing the double ball-bar must be reduced due to long measurement times in conjunction with the stationary rigid-body model, so that up to now only Cartesian displacements of the measurement points can be recorded. The R-Test, on the other hand, permits the use of rigid-body models with a measurement duration of 1 minute for the analysis of transient thermo-mechanical displacements of the position and alignment errors of rotary and swivel axes. The extension of the R-Test device to simultaneously measure machine tool data allows for dynamic measurements of both linear as well as rotary axes error motions as well as position and orientation errors. Nevertheless this approach can only be used for machine tools with accurate enough dynamic behavior to fulfill the measurement quality and an existing interface for data collection is mandatory.

### **Diagonal and Step-Diagonal Tests**

The international standard ISO 230-6 [66] provides a standardized rapid test, initially developed for coordinate measuring machines, see ISO 10360 [55], for checking the volumetric accuracy of machine tools [66]. According to the standard, the method is not suitable for determining the individual error components, but merely a method for estimating the volumetric accuracy [66]. In a diagonal test, the relative distances of measuring points along the body and face diagonals are measured with a standard or laser interferometer. The measuring time is shortened by only four setups in comparison to a complete single axis measurement with a simple laser interferometer.

To estimate the volumetric accuracy, the maximum length measurement deviation along the measuring lines can be used. However, the transfer from the maximum length error to the geometric accuracy is left to the user. In contrast, a standardized procedure exists in coordinate metrology in which the manufacturer supplies this for each machine type in the form of accuracy data sheets, following the acceptance test of ISO 10360 [55]. With machine tools, however, this transfer is not trivial due to the more complex thermo-mechanical displacements and their more frequent transient fluctuations. On the basis of the diagonal test and in conjunction with a kinematic model, the Cartesian deviations of the three linear axes of a 3-axis machine tool can be determined, as explained by Morris [88]. Straightness and angle deviations are not separated, but perpendicularity deviations can be recorded. Morris concludes that body diagonals often provide a quick substitute for full volumetric tests, because maximum errors tend naturally to occur at the extremities

and the face diagonals provide a measure of planar accuracy, which finds application in the work place.

A modification is the step-diagonal test, in which the individual machine axes do not move simultaneously but sequentially. A measured value is recorded at the end of each movement. The method for determining all error parameters introduced by Wang [114] is, however, controversial due to high measurement uncertainties, as pointed out by Chapman [24] and later investigated in depth by Ibaraki et al. [51]. Ibaraki et al. also introduce a new formulation of the laser step-diagonal test, that takes into account the setup errors and even show a possible solution by measuring the linear positioning errors beforehand. Firstly Ibaraki et al. show the procedure for the 2D example [52] and later also for the 3D case [48].

Despite Ibaraki's scientifically proven doubts, Wang [115] uses the simple diagonal test under determination of perpendicularities for the thermo-mechanical analysis of a 3-axis machine tool with a machine volume of  $500 \text{ mm} \times 400 \text{ mm} \times 320 \text{ mm}$ . Zhang et al. [129] uses the critically viewed stepwise diagonal test for thermo-mechanical analysis. The measurement of all four diagonals, however, requires a time-consuming conversion, but the exact measurement duration is concealed in both cases. Displacements during the measurement time are not taken into account and measurement uncertainty considerations are missing.

In conclusion, it can be said that the diagonal test is a comparatively fast measuring method for checking the machine geometry in the entire machine volume. However, a detailed analysis of thermo-mechanical displacements is critical due to the measurement uncertainties. Furthermore, it must also be clarified to what extent the measurement lines of the diagonal test reflect the total working volume.

### **Laser Tracker/Tracer**

The preferred instrument for collecting 3D displacement data in a spatial grid is a laser tracker. Commercial laser trackers are optimized for angular, azimuth and elevation, and displacement measurements and form a spherical coordinate system. Although the measurement uncertainty in direction of the beam is much lower than the angular uncertainty, the displacement measurement is still limited by the precision of the point of rotation. According to Schwenke et al. [104] measurement uncertainties better than  $3 \mu\text{m}$  cannot be achieved. A tracking interferometer is developed by Hughes et al. [46] that employs a high

accuracy sphere as the optical reference for the interferometric measurement. The novel design was named LaserTRACER to differentiate it from the conventional laser trackers. This device is commercially available by the company Etalon AG.

The Etalon LaserTRACER is a self-tracking laser interferometer that automatically tracks a reflector, and hence allows for the identification of geometrical deviations with highest precision. In contrast to conventional measurement devices, the LaserTRACER features an unprecedented accuracy of the center of rotation thanks to a novel measurement technique: A sphere with a form deviation of just 50 nm is used as an optical reference for the interferometer. As a consequence, the mechanical errors of the rotation and swivel axes are fully compensated. For measurement execution, the LaserTRACER is stationary placed at several different positions inside the working volume of the machine. Then, the reflector is mounted to the tool or probe. In the following automated measuring process, the LaserTRACER tracks the actual path of the machine in its entire working volume [31]. The uncertainty of the length measurements is stated as  $0.2\ \mu\text{m} + 0.3\ \mu\text{m}/\text{m}$  what means, that the uncertainty strongly depends on the actual measured distance between tracker and target.

The position of the reflector can be determined by trilateration using the angle information or as introduced by Schwenke et al. [104] by multilateration based on the pure length information. Evaluation by multilateration in conjunction with a high length measurement accuracy offers the advantage of excluding the limited accuracy of the angle encoders from the measurement uncertainty assessment.

As patented by Schwenke et al. [103] a volumetric measurement with tracking interferometers can be performed simultaneously with several measuring instruments or sequentially with only one measuring instrument. Several positions of the tracking interferometer on the machine table and at least one reflector position on the spindle are required. For each position there are previously defined measurement positions of the TCP or reflector, which are traversed in the measurement. When multilateration is used, the measured relative length differences of the interferometers from their position to the individual measuring positions and not the position of the angle encoders form the measured measurement quantities are utilized for the calculation of the volumetric errors.

The measurement of all 21 errors of a 3-axis machine tool requires at least five reflector positions relative to the TCP and six positions of the LaserTRACER. These are required to detect the deviations of the last axis or the yaw of the penultimate axis in the kinematic

chain via the different level arms [31]. The different reflector positions are also required for other measuring methods to detect all 21 errors. For a reduced rigid body model, introduced by Schwenke et al. [106], the measurement setup is simplified to four LaserTRACER positions using a single reflector. In this case, however, the measurement is only valid for the selected reflector/tool length. The determination of the individual as well as position and orientation errors of rotational axes requires a further measurement setup.

Even if four LaserTRACER are used, the measurement time ranges approximately from 15 minutes up to 45 minutes depending on the size of the machine tool. Naturally this measurement time increases drastically, if only a single LaserTRACER is used. Therefore Wennemer [121] developed a model based approach, that is able to trace back the measured data, spread over time, to specific evaluation times. This method enables indirect volumetric measurements of transient thermo-elastic deviations based on rigid body models. As stated by Brecher et al. [15] the two main advantages of the approach are the consideration of thermo-elastic deviations during measurement time as well as a higher temporal resolution. This results in a higher measurement accuracy of transient thermo-elastic deviations.

Instead of modeling the deviations during the measurement Ibaraki et al. [54] further reduced the measurement time by only measuring 2D square paths. This is possible because it requires the linear positioning error of linear axes to be directly measured a priori, and the tracking interferometer position be estimated separately. The uncertainty caused by the estimation error of the tracking interferometer position can be significant. It is important to note that its influence on the difference between each estimated trajectory in the thermo-mechanical measurement is negligibly small, since the LaserTRACER position is the same during all tests.

The laser tracker/tracer offers a unique possibility to measure 3D grids in the whole working space. In combination with a rigid body model the 21 errors of a 3-axis machine tool can be assessed and a fully volumetric description is possible. Especially for large measurement and machine tools this is the preferable method. If four laserTRACER's are used in parallel a fast measurement of the volumetric thermo-mechanical errors is applicable, especially if used in combination with the modeling method presented by Wennemer [121]. Due to the working space restrictions and the high costs of such a measurement tool, several researchers presented approaches to overcome the economical drawbacks of such a system. Those novel approaches always come with compromises, either by increasing the measurement time, the uncertainty or by focusing on a specific segment of the machine tool.

### Test Pieces

To detect position and orientation errors and error motions under machining conditions, different test pieces have been developed. Examples of test pieces for NC machine tools are given in ISO 10791-7 [59]. Features of these workpieces are e.g. cylinders, cones and planes. Besides ISO other societies like the German NC Gesellschaft [91] or the Association of German Engineers (VDI) [112] developed test pieces for machine tools. With these proposed test pieces the behavior of the machine tool regarding geometrical accuracy under load conditions is investigated. Known test-pieces and corresponding manufacturing processes do not enable a unique distinction between geometrical and thermal machine tool errors. Current research concentrates on the design of new test pieces which are able to capture the thermal errors of 5-axis machine tools. Ibaraki and Ota [50] extended a previous design of a geometrical test piece for the measurement of thermally induced error motions of rotary axes. Three different test pieces are manufactured every 25 min in order to measure thermal effects. The features characterizing the thermal deviations are measured with a touch probe system directly on the machine, under the assumption that the linear axes have small volumetric errors in comparison to the rotary axes. Neidhardt et al. [92] present the idea of a compact test piece for the evaluation of the thermally induced translational displacements of the TCP. The test piece consists of several reference surfaces manufactured at the beginning of the test cycle and several measurement surfaces used as comparison to the initial states.

## 2.3 Modeling and Compensation of Thermo-Mechanical Errors of Machine Tools

Wegener et al. [119] state, that the expenses for the improvements of machines, driven by the accuracy requirements of machine tool applications, by mechanical means are becoming more and more expensive. Therefore apart from design measures to avoid thermo-mechanical deformations of machine tools, e.g. by making use of thermal symmetry planes or systematic cooling and/or isolation of heat sources, numerous compensation methods have been developed. The basis for any successful compensation of a measurement or machine tool is described by Wegener et al. [117] as:

- Availability of reliable geometric measurements
- Understanding of behavior, directly linked to modeling
- Repeatability of the system

Especially the property of being repeatable cannot be underestimated and is one of the most critical properties that enables a model based compensation. Computational models in order to estimate the behavior of a system are commonly used in many areas of engineering and science. In the field of design and control of complex mechatronic systems, researchers prove that it is feasible to predict the thermal behavior and the associated mechanical displacements through the use of thermo-mechanical models. In these approaches the displacements at the TCP are compensated either by direct measurements or by indirect derivations of the displacements. Generally, those models can be divided in two main classes, empirical models and physical models.

Empirical models use correlations between input values and an output values. Experiments are carried out at different loads and the results over time are approximated by a regression model. Also methods using artificial neuronal networks (ANN), fuzzy logic (FL) or transfer functions (TF) belong to this group of procedures. On the other hand physical models are based on the heat transfer and elasticity equations. Those models can be used for the computation of the temperature distribution using thermal load data, and the calculation of the distortions in order to determine mechanical deviations. This approach enables extrapolation so that any thermal load can be considered.

Large subsets of physical models are Finite Element Method (FEM) models and Finite Difference Method (FDM) models. An effective combination of both approaches is the Finite Differences Element Method (FDEM). Especially in the design phase, FEM is a powerful tool to compute different internal and external influences on several machine tool parts. Analyzing a broad spectrum of thermal loads and boundary conditions, the computation with complex FEM models can be very time-consuming due to the large number of degrees of freedom. Ways to reduce this computation effort are researched with different Model Order Reduction (MOR) methods.

These different strategies are summarized in Figure 2.5, where a morphological box for mastering of thermal effects on machine tools is illustrated. The strategies can be divided in three groups, the acquisition of information about the thermal load (Sensor Information), the thermal error model (Modeling) and the possibility of interaction with the machine structure (Actuator Technology).

From each group, one or more technologies can be used, whereas the effort and the engineering knowledge increases from bottom to top. For example, extracting information from an NC-program is straight forward and can be achieved without much programming effort, whereas the measurement of the TCP position is not only difficult to obtain but also coupled with a lot of fundamental understanding of the machine tool in use. Same holds true for the thermal models, the knowledge and the modeling effort is very high for physical models, as material parameters, convection coefficients, thermal elongation coefficients and many more parameters need to be estimated or even measured on a regular basis. For



the actuation the most efficient way of interaction with the existing drive systems can be used, but naturally also auxiliary axes as piezo axes with small strokes and good accuracy are feasible. Cooling and heating today is the dominantly applied technology, but for the sake of energy efficiency, this shall be wherever possible abandoned.

Wegener et al. [117] state that it is observed that with the simplification and reduction of modeling efforts the efforts for parameter identification then rises and it cannot yet be indicated, where the total effort has its minimum.

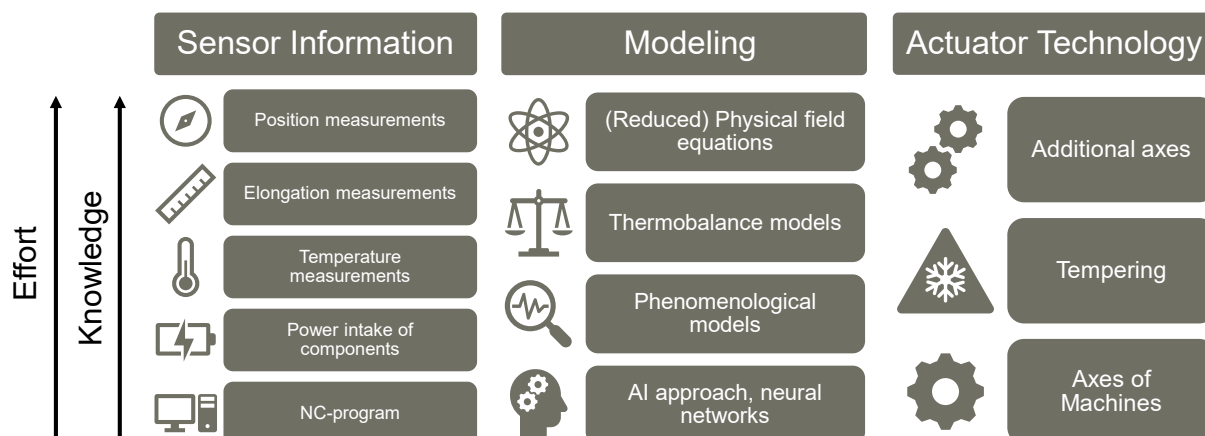


**Figure 2.5:** Morphological box for model based mastering of thermal effects on machine tools, adapted from Wegener et al. [117].

### 2.3.1 Physical Modeling and Compensation of Thermo-Mechanical Errors of Machine Tools

In 1969 Yoshida et al. [128] found, that the variation of the cylindrical error of a workpiece in a longitudinal grinding process is caused by the thermal deformation of the machine tool due to the unbalanced temperature distribution in the machine tool. As it is very difficult to measure the exact distortion of guideways, the same was calculated using simple equations constructed on the basis of temperature distribution and thermal displacement of the machine. The bed of the cylindrical grinding machine was assumed to be a simple beam. Thermal deflections of the beam were calculated under various kinds of temperature gradients.

Jedrzejewski et al. [69] developed in 1992 a 3D thermal model of a machine tool using FEM. This model is extended by the assumption that the amount of energy dissipated in particular components of the kinematic system is a function of the operational conditions. Once the heat sources are identified and the operational parameters like spindle speed, cutting power, ambient temperature, operational time etc. are known, the power loss values

in all components of the drive system as well as temperatures and thermal displacements can be determined.

Mayr [84] developed a FDEM approach in order to efficiently compute the thermal errors of machine tools. Mayr proposed a substructure approach of the system output, reducing the computational effort to compute the TCP-displacements and orientation errors. The thermal errors are calculated for the whole working volume for linear and rotary axes. In addition to the work of Mayr, Ess [30] developed an approach, where different bodies representing the machine tool axes are connected through simplified models of the machine elements. The solution of the thermo-mechanical problem is performed by FEM. In the computation of the TCP-displacement Ess considers the effect of the thermal deformation of the linear glass scales and read heads and developed macro models for important machine elements, such as drive motors, spindles and bearings. Additionally Ess [30] developed a thermal compensation methodology that can directly be derived from such FEM models. It is shown, that up to 75 % of the occurring TCP errors can be reduced.

The computational effort can still be very time-consuming, especially when uncertain boundary conditions and heat transfer coefficients have to be evaluated in multiple iterations. Therefore, Hernández Becerro et al. [44] developed a MOR method for thermo-mechanical error computation. By projecting the full model in a lower dimensional space the computational effort can be drastically reduced. The main advantage of this type of surrogate models is the ability to maintain the dynamical evolution of the system and retaining the system structure, as explained by Benner et al. [5]. Nevertheless, one of the challenges of physical models lies still in an accurate estimation of the boundary conditions and the subsequent heat dissipation mechanisms.

### 2.3.2 Empirical Modeling and Compensation of Thermo-Mechanical Errors of Machine Tools

Correlation is a statistical association, that measures the degree to which a pair of variables are related. The correlation between temperature change and thermal displacement is evident considering the physical phenomena of thermal expansion, Eq. (2.1).

$$\Delta L = \alpha \cdot \Delta T \tag{2.1}$$

where  $\Delta T$  stands for the temperature change,  $\alpha$  for the thermal expansion coefficient and  $\Delta L$  for the corresponding change in length. Using the empirical modeling approach, the more complex physical modeling of the thermo-mechanical errors is avoided and a more generic model is build, that can be applied to a large variety of machines and machining conditions. As summarized by Ramesh et al [96], researchers have investigated different

kinds of strategies to establish thermo-mechanical error models. Popular modeling techniques are, Regression and Artificial Neural Networks.

The goal is to find the optimized thermal error model with high accuracy and robustness as the model determines the correctness and effectiveness of the thermal error compensation subsequently. Weck et al. [116] stated, that the main interest of research activities world wide is directed to the question of how to find an acceptable mathematical model with a minimum of (temperature) sensors within an acceptable time scale.

As stated by Venugopal et al. [113] the deformation of a body at a particular time depends only on the temperature of that body at that particular instant in time. Models based on this assumption aim at building a correlation model between the current temperature measurements and the thermal deformations of the machine. According to Yang and Ni [123] these models are considered a static approach and are widely used for machine tool thermal error modeling. They also state that static models cause a poor robustness, whereas dynamic models are superior in terms of robustness and model accuracy. Therefore this section is divided in static and dynamic models for thermo-mechanical error compensation.

### **Static Models for Thermo-Mechanical Error Compensation**

Most researchers tried to establish a thermo-mechanical model based on several temperature measurements and the deviations at the TCP or of a single component. 1977 Spur and Heisel [109] studied the thermal displacement between the tool and the workpiece on a lathe. They measured the axial spindle elongation and the temperature of the spindle bearing. From the experiment they concluded, that the relation between those values is linear and can be modeled with a linear regression. They also figured, that only one temperature as one independent variable will not be sufficient for different load cases and errors. They extended their approach to a multiple linear regression by taking three or more temperatures into consideration. To on-line compensate the occurring errors on the actual machine tool a software program based on the multiple linear regression equations is implemented in the CNC. With this approach the residual displacement in axial direction is compensated to  $\pm 10 \mu\text{m}$  for different load cases. 11 years later Spur et al. [110] presented an approach where the thermal elongation of a main spindle can be estimated with a resistance thermometer attached to the spindle housing. They found, that the relationship between resistance change and thermal elongation is linear. No compensation based on this model was performed.

Donmez et al. [28] developed a polynomial based regression model. He used a single temperature sensor and a third order polynomial to model the relationship between the cross slide temperature and the spindle tilt drift of a lathe. They also present a methodology for on-line compensation by correction of the axis position of the CNC controller. Never-

theless they did not present any compensation results.

Schellekens et al. [101] developed in a research project a method to model the thermo-mechanical errors of a 5-axis machine tool. Nevertheless they only measured and modeled the zero-point drift in X, Y and Z direction of the tool relative to the workpiece. To model the transient and steady state behavior they used a total of 16 temperature sensors and a linear expansion model. The compensation is implemented in the controller software of the milling machine. The thermal error compensations are computed by an external PC that continuously monitors the thermal state of the machine tool. A developed test piece is used to verify the effectiveness of the error correction. The test-workpiece shows an overall accuracy improvement of up to 69%.

Chen et al. [25] mounted 17 temperature sensors on a machining center after conducting preliminary experiments. One extra sensor was used to measure the ambient temperature. A multiple variable, nonlinear regression model is used to model the thermal errors. The justification to use such a model is given that it is needed to accommodate for the case when a thermal error is affected simultaneously by several machine structures with different time constants. Additionally to the zero-point drifts and the linear thermal displacements, the authors also modeled the position-dependent thermal behavior of linear axes. One of the findings, for the specific machine under investigation, is that although the linear positioning errors varied with temperature, their basic profiles did not change drastically and only the slopes differed. It has been found that this phenomenon also applies to thermal bending errors. A compensation controller was implemented to compensate for the thermal errors. Compensation for the volumetric error was conducted every 10 ms based on the compensation signals received from the controller. A cut workpiece inspected using a coordinate measuring machine (CMM) has also shown that dimension errors have been reduced from  $92.4\ \mu\text{m}$  to  $18.9\ \mu\text{m}$  in a dimension of  $404\ \text{mm} \times 310\ \text{mm}$  and the depth difference of milled surfaces has been reduced from  $196\ \mu\text{m}$  to  $8\ \mu\text{m}$ .

Moriwaki and Zhao [87] stated that the modeling with linear regression models is not satisfactory, as the process of thermal deformation of machine tools is complex. Therefore, they applied an ANN approach to identify the thermal deformations of a 3-axis milling machining center under air cutting conditions based on temperature distribution measurement. Six temperature sensors are attached to the surface of the structure to measure the temperature field of the machine tool. The thermal displacements of the TCP are measured with a precision test bar made of Invar mounted into the spindle, and proximity sensors attached to the frame, also made of Invar, which are mounted on the work table. The investigated thermal load case is the rotation of the main spindle at various speeds. The authors focus on the modeling of the occurring errors and do not show any compensation. In a publication by Chen [26], a thermal error model based on ANN is introduced. The author reasoned the use of such models in a similar manner as in the previous paper, that

due to different thermal time constants of the different components of a machine tool the deviations at the TCP are highly non-linear and different in their warm-up and cool-down behavior. 23 temperature sensors are used to train the ANN. The predicted thermal errors from the ANN models include thermal expansion of ball screws, thermal drifts at spindle head, thermal variation of squareness errors, thermal drift of axis references and thermal bending of the machine structure and spindle. The previously mentioned compensation controller is used to offset the machine tool axes to compensate for the thermal errors. The implemented compensation scheme on a horizontal machining center proved to improve the machine accuracy by one order of magnitude using a laser interferometer and a cutting test.

Hatamura et al. [42] developed a similar ANN as Moriwaki and Zhao [87] with the significant difference of modeling the thermal deformation through deformation sensors which are attached directly to the machine structure and by controlling not the NC axes but thermal actuators that can deform the machine structure by thermal expansion and contraction.

### **Dynamic Models for Thermo-Mechanical Error Compensation**

The widely used static models such as the linear or polynomial based regression models and the ANN models, have good interpolation abilities, but very poor extrapolation capabilities, thus causing the model estimation to be unreliable outside the range of trained working conditions. Yang and Ni [123] indicate that the fundamentals of the thermo-mechanical process are dynamic in nature and that a dynamic model is in fact required to capture the system dynamics, and consequently, improve the model robustness. Therefore several approaches are developed by different researchers to account for this dynamic behavior.

Yang and Ni [123] developed a linear Output Error (OE) model to predict the thermal TCP deviations of a machine tool. The main advantage of the OE model is, that past temperature values are taken into account. This modeling approach describes the non-instantaneous relation between input and output based on the dynamic nature of thermo-mechanical systems. The approach is validated with FEM simulations as well as measurements on a lathe. Up to 80% of the maximum error range of the thermal deformation under varying spindle speeds and working cycles can be predicted.

In most of the above mentioned cases structural and sometimes environmental temperature values are used for calculating the resulting thermal TCP deviations. As pointed out

by Brecher et al. [13] the substantial disadvantage of this strategy, apart from the lack of dynamic modeling methods, is the technical sensor effort and the difficult determination of proper sensor locations for the temperature measurements. Commonly only a few temperature sensors are used so that the real temperature distribution of the whole machine structure cannot be determined with sufficient accuracy. Therefore, the modeling of the thermal deformations on this basis will always remain incomplete. Therefore Brecher et al. [13] introduced a thermal error modeling method that uses mostly only CNC internal data, like the motor current, the speed of the axis or the spindle and additionally the environmental temperature. The behavior between those inputs and the TCP deviations in X, Y and Z direction is modeled by the sum of one first order time delay element (PT1) and one second order time delay element (PT2), as can be seen in:

$$\delta j(i\omega) = \frac{E(i\omega) \cdot K_1}{1 + T_1 \cdot i\omega} + \frac{E(i\omega) \cdot K_2}{(1 + T_2 \cdot i\omega) \cdot (1 + T_3 \cdot i\omega)} \quad (2.2)$$

here  $\delta j(i\omega)$  indicates the displacement in X-,Y- and Z-direction,  $E(i\omega)$  is the load input parameter (speed, change of environmental temperature),  $K_i$  is the gain amplification factor and  $T_i$  the time constant of the time delay elements. To separate the influence of the changing environmental temperature from the load dependent thermal errors, the model of the environmental changes is established first and applied when performing the calibration tests for the spindle and the linear axes. As a load case the main spindle as well as all axis drives are loaded separately with four different load steps ranging from 25 % of the maximum speed up to 100 %. The machine is loaded for a duration of several hours, approximately up to the steady-state condition of the displacements. Afterwards, the machine's motions are switched off and the cool-down phase is recorded over a time of approximately 8 hours. The authors point out, that the amplification and the time constant of the heating- and cooling-phase are different, therefore two separate sets of parameters must be determined. When only considering the translational errors at the TCP of a 3-axis machine tool and the four load cases per axis, 495 parameters need to be determined. Therefore a sufficiently long calibration time of the model is needed, so that in total 17 days of pre-process calibration are necessary. The on-line compensation is performed by counter movements of the linear axes of the machine tool.

In a later publication Brecher and Wissmann [11] present an approach to compensate the thermal behavior of the main spindle of a milling machine. The previously used model of a superposition of PT1 and PT2 is changed to the sum of two PT2 time delay elements. Additionally they developed a stressing unit, so that the speed and the effective spindle power can be used as inputs for the model. To compute the thermal deviations of the TCP in X-, Y- and Z-direction a total of 144 models each with 6 parameters is needed.

The authors do not specify the amount of time necessary to calibrate those models.

In [12] Brecher and Wissmann presented a thermal compensation model for the main spindle based on a third and sixth order delay element. They show, that the third order delay element results in the best compensation quality. A comparison to the previously introduced models based on PT1 and PT2 is missing.

Gebhardt et al. [38] focus on modeling and compensating the rotary axes of 5-axis machine tools. Instead of only measuring the thermal errors at one point in the working space an R-Test measurement of the rotary axis is performed, as explained in Section 2.2.2. The model of the thermal errors is based on several PT1 time delay elements and the drive power is taken as input, but instead of using two separate time constants for the heating-up and cooling-down phase, a linear interpolation is used to reduce the amount of free parameters. A validation measurement is performed, that shows a reduction of the occurring thermal errors of up to 70%. An extension of this approach is presented by Gebhardt et al. in [39], where additionally also the thermal errors of a swiveling axis are modeled in a similar manner. The training phase consists of an arbitrary chosen speed profile for a duration of 75 hours. The authors evaluate that a period of 35 hours is satisfactory for the investigated axes, nevertheless the model is parameterized after 48 hours and improvements in the range of 47% to 85% can be achieved.

Mou and Liu [89] pointed out, that the machining conditions used for model derivation are not identical to the actual conditions during the use phase of the machine tool. Therefore the predicted system behavior is always different from the real one. Additionally statistical uncertainties, assumptions used in modeling and the constantly changing boundary conditions cause the model to deviate after the pre-process calibration and are therefore not necessary accurate in the long term. The authors suggest, that the model accuracy needs to be verified and returned continuously or at least periodically as the machine tool is continually used. An adaptive methodology to monitor and predict the time-varying thermal errors by process-intermittent probing is introduced to enhance the model accuracy and the long-term stability. The thermo-mechanical effects are represented as a dynamic system in state space representation. The state observer technique is used to estimate the full error model, by only measuring a small set of thermal deviations in the working space. Five points on a pre-calibrated workpiece are tracked while moving all the linear axes and rotating the main spindle at arbitrary speeds. The closed-loop state observer model shows a significant reduction of the thermal error affecting these five measurement points.

Yang [124] extended the fundamental ideas of Mou and Liu and developed a dynamical model self-adaptation methodology for improving model estimation under long-term and frequently-changing working conditions based on a Box-Jenkins model and Kalman filter parameter estimation technique enabling a fixed multiple-sampling horizon prediction of thermo-mechanical deviations. The combination of on-machine measurements and the developed model minimizes the intrusion to production while maintaining good model adaptation capabilities.

## **2.4 Discussion of the State of the Art**

In this section, the presented state of the art is discussed and challenged by the barriers that prevent the practical implementation of accurate thermal error compensation in real industrial production, as explained in Chapter 1.

### **Characterization of Thermal TCP Errors is Difficult and Costly**

The deviations at the TCP are a combination of thermal distortions from many machine components with different thermal characteristics. These characteristics are determined by many interacting factors such as environmental temperature, machine working cycles, as spindle speeds, axis feed rates and duty times, cutting conditions, coolant applications, etc. Therefore, the characterization process requires the consideration of all these conditions in order to excite all the different modes of the machine thermo-mechanical system. In the reviewed literature there is no indication of optimally chosen characterization for thermal error identification.

### **Lack of Efficient Thermal Error Measurement Methodology**

The thermally induced errors of a machine tool vary spatially over the entire machine working zone under each specific temperature status. They are not only thermally but also position dependent. Most of the reviewed publications only consider one or more discrete positions in the working space to establish a thermal error model. Indirect measurement methods enable the fast evaluation of several machine components at the same time, if used in combination with process intermittent probing, the effect on the productivity of the machine tool can further be reduced.



## **Insufficient Accuracy and Robustness of Thermal Error Estimation Models**

The robustness of the thermal error model under various working conditions depends on the thoroughness of the training process, which is again related to the length and variability of the characterization time. It also depends on thermal sensor placement and model structure selection. A model trained under one working condition may not be accurate enough under different working conditions. Yang and Ni [123] showed that a dynamical model is needed to estimate the thermo-mechanical deviations accurately without the extensive need of temperature sensors. Nevertheless, the experimental results do not show any supremacy compared to the static models. Additionally the investigation of drastically changing boundary conditions as well as long-term stability are missing.

## **Lack of Model Self-Adaptation Capability under Working Condition Changes**

The pre-calibrated thermal error models have to be used for on-line application because no adequate in-situ sensing technology for thermal error measurement is available. However, due to limited resources and time, model training conditions usually cannot cover all real working conditions, especially for small batch productions, where the sequence of manufacturing processes changes frequently as do the direction and rate of change of thermal effects. Thus, the pre-trained model may not be suitable for long-term application. A model adaptation mechanism needs to be developed in order to refine the thermal error model according to continuous changes of operation status based on arbitrary performed process-intermittent measurements under tight work-cycle requirements. This capability of adaptation is missing in the existing research but is strongly needed in regard of the current Industry 4.0 respectively Industrie 2025 efforts which lead to digitized production processes and products. To this end, it is essential to have smart monitoring systems to optimize the response of manufacturing processes on the line itself, to ensure product quality, to shorten production cycles and to reduce other associated costs.

## **2.5 Research Gap**

The goal of this thesis is to develop an on-machine measurement cycle, that captures the dominant thermal errors in a timely manner and to build an adaptive thermal error modeling methodology, which is based on the system identification theory, in order to resolve the aforementioned problems, including model inaccuracy, non-robustness and long-term instability, model calibration difficulties, lengthy experiments and model adaptation prob-

lems. To achieve this ultimate research goal, the following tasks are proposed as the direct objectives:

- To develop a thermal error calibration methodology for machine tools using an on-machine probing system. In order to fulfill the fast measurement requirement of dynamic thermal-error modeling and model adaptation, the error identification method uses the advantages of indirect measurement methods to obtain a spatial error description.
- To propose an innovative methodology for machine tool thermal error modeling. By taking into consideration the dynamic characteristics of the thermo-mechanical process. A special focus lays on the long-term stability and the robustness in situations with fast changing boundary conditions.
- To propose, setup and validate a model adaptation methodology. Since the initial thermal error estimation model may not be accurate and robust enough in the long-term, an adaptive self-learning model needs to be developed in order to continuously update the estimation model based on irregular process-intermittent measurements with as little as possible intrusions in the production process.

The key contributions of this thesis include the theoretical analysis of the thermo-mechanical process from a system theory viewpoint, introduction of the system identification theory for building the dynamic thermal error models, as well as the development of a process intermittent on-machine thermal-error measurement and adaptive self-learning methodologies.

## 2.6 Outline of the Thesis

This thesis is structured in five main parts, starting with the fundamentals of the dynamics of thermo-mechanical systems and its identification strategy presented in Chapter 3. Based on these findings the modeling methods of the dynamics of thermal errors is explained in Chapter 4. A method for on-machine measurements of thermal errors of rotary axes is presented in Chapter 5. The adaptive learning control for thermal error compensation with dynamic adjustments of measurement intervals is introduced in Chapter 6. The developed self-learning model is tested on a workpiece specially designed for thermal error visualization in Chapter 7. The thesis closes with final conclusions of the key contributions and an outlook for future research.

## Chapter 3

# Fundamentals of Dynamics of Thermo-Mechanical Systems

For a better understanding of the underlying physical phenomena of heat conduction and thermo-mechanical deformations a fundamental analysis of the dynamics of a thermo-mechanical system is performed. The profound understanding of these processes supports the modeling process and provides assistance in comprehending of certain assumptions.

The dynamics of thermal deformations in response to heat inputs are composed of two processes, the heat transfer process and the thermo-mechanical process. The thermo-mechanical process has a much smaller time constant compared to the heat transfer process, and it stabilizes much faster in response to the change of temperature distributions. Therefore, only the thermo-mechanical process in steady state needs to be considered and can directly be mapped by the temperature distribution. The thermal deformation estimation based on this static assumption undergoes certain restrictions. Firstly the whole temperature distribution is needed to uniquely define the thermal deformations of a solid, as explained by Fraser and Osman [35]. However, if only a limited number of temperature measurement points is available, only a subset of the entire temperature distribution can be measured, the mapping from the discrete temperature measurements to thermal deformation is incomplete. Secondly thermal effects have the characteristics of memory of previous loads.

Yang [127] calls these dynamic characteristics "pseudo-hysteresis" effect. He states that this effect originates from the lumped parameter approximation of the thermo-mechanical process and that this effect is the reason that a static modeling approach tends to be less accurate and robust.

Section 3.1 deals with the derivation of the 1D heat equation of a thin rod. The following Section 3.2 elaborates on the thermal elongation caused by a periodically changing temperature boundary condition and explains the concept of the "pseudo-hysteresis" in more detail. The chapter closes with an explanation of discrete time-series modeling of such a thermo-mechanical system.

### 3.1 The 1D Heat Equation

In order to analyze the dynamics of a thermo-mechanical system, a longitudinal one-dimensional rod is considered. The uniform rod with length  $L$  is lying on the  $x$ -axis from  $x = 0$  to  $x = L$ . The density  $\rho$ , the specific heat capacity  $c$  and the thermal conductivity  $k$  are assumed to be constant. Additionally the following is assumed:

- The cross-sectional area of the rod is constant
- There is no heat source within the rod
- The lateral surface of the rod is insulated and only the ends are exposed to heat transfer
- The radial temperature field is uniform
- The rod is mechanically fixed at one side ( $x=0$ )

Therefore the simplified heat equation is given by:

$$\frac{\partial u}{\partial t} = \kappa \frac{\partial^2 u}{\partial x^2}, \quad 0 < x < L \quad \text{with} \quad \kappa = \frac{k}{\rho c} \quad (3.1)$$

In Equation (3.1) the variable  $u$  depicts the temperature distribution,  $t$  the time and  $x$  the spatial variable.

#### 3.1.1 Non-dimensionalization

To make the solution more generic, the physical constants are made dimensionless. The characteristic length, time and temperature are denoted as  $L_*$ ,  $T_*$  and  $U_*$ , respectively. The dimensionless variables are introduced as:

$$\hat{x} = \frac{x}{L_*}, \quad \hat{t} = \frac{t}{T_*}, \quad \hat{u}(\hat{x}, \hat{t}) = \frac{u(x, t)}{U_*} \quad (3.2)$$

Substituting the dimensionless variables from Equation (3.2) in the heat equation (3.1), it follows:

$$\frac{\partial u}{\partial t} = \kappa \frac{\partial^2 u}{\partial x^2} \quad \Rightarrow \quad \frac{\partial \hat{u}}{\partial \hat{t}} = \frac{T_* \kappa}{L_*^2} \frac{\partial^2 \hat{u}}{\partial \hat{x}^2} \quad (3.3)$$

To further simplify the partial differential equation (PDE), characteristic time scale is chosen as  $T_* = L_*^2/\kappa = L^2/\kappa$ , so that:

$$\frac{\partial \hat{u}}{\partial \hat{t}} = \frac{\partial^2 \hat{u}}{\partial \hat{x}^2}, \quad 0 < \hat{x} < 1, \quad \hat{t} > 0 \quad (3.4)$$

### 3.1.2 Periodic Boundary Conditions

The boundary conditions (BC) are defined as a periodically changing temperature at the end of the rod ( $\hat{x} = 0$ ) and a constant temperature of zero degree at the other end ( $\hat{x} = 1$ ). The initial condition (IC) is described as a function of the spatial variable  $x$ . For practical reasons the hats are not shown furthermore, even though a dimensionless problem is solved. The full problem description is as follows:

$$\left. \begin{aligned} u_t &= u_{,xx}, & 0 < x < 1 \\ u(0, t) &= A \cos(\omega t + \varphi), & u(1, t) = 0, & t > 0 \\ u(x, 0) &= f(x), & 0 < x < 1 \end{aligned} \right\} \quad (3.5)$$

$$\text{with } u_t = \frac{\partial u}{\partial t} \quad \text{and} \quad u_{,xx} = \frac{\partial^2 u}{\partial x^2}$$

### 3.1.3 Solution of Heat Equation

The solution is not expected to be independent of time, since the temperature is changing periodically at one end of the rod. However, it is expected that after an initial transient time, the solution will become periodic with angular frequency  $\omega$ . Therefore a solution like this can be expected:

$$u(x, t) = v(x, t) + A(x) \cos(\omega t + \phi(x)) \quad (3.6)$$

where  $v(x, t) \rightarrow 0$  as  $t \rightarrow \infty$  corresponds to the transient part,  $A(x) \cos(\omega t + \phi(x))$  stands for the quasi-steady state part,  $A(x)$  and  $\phi(x)$  are the amplitude and phase of the quasi steady state.

### Quasi-Steady State Solution

The notation  $\text{Re}\{z\}$ ,  $\text{Im}\{z\}$  is used to denote the real and imaginary parts of a complex number  $z$ . The quasi-steady solution from Equation (3.5) is rewritten in terms of complex exponentials.

$$u_{SS}(x, t) = A(x) \cos(\omega t + \phi(x)) = \text{Re} \{ A(x) e^{i\phi(x)} e^{i\omega t} \} = \text{Re} \{ U(x) e^{i\omega t} \} \quad (3.7)$$

for convenience  $A(x) e^{i\phi(x)}$  is replaced by the complex function  $U(x)$ . The quasi-steady state part  $u_{SS}(x, t)$  can be expanded to:

$$u_{SS}(x, t) = \text{Re} \{ U(x) e^{i\omega t} \} = \frac{1}{2} (U(x) e^{i\omega t} + U^*(x) e^{-i\omega t}) \quad (3.8)$$

where the asterisks denote the complex conjugate ( $(x + iy)^* = x - iy$ ). Substituting Equation (3.8) for  $u(x, t)$  into the PDE in Equation (3.5) results in:

$$(i\omega U(x) - U''(x)) e^{i\omega t} + (-i\omega U^*(x) - U''^*(x)) e^{-i\omega t} = 0, \quad 0 < x < 1, \quad t > 0 \quad (3.9)$$

**Lemma** [Zero sum of complex exponentials] If, for two complex constants  $a, b$ ,

$$a e^{i\omega t} + b e^{-i\omega t} = 0 \quad (3.10)$$

then for all times  $t$  in the open interval, it holds true that  $a = b = 0$ .

#### Proof of Lemma:

Differentiation of Equation (3.10) leads to:

$$\frac{\partial}{\partial t} (a e^{i\omega t} + b e^{-i\omega t}) = i\omega (a e^{i\omega t} - b e^{-i\omega t}) = 0 \quad (3.11)$$

Adding Equation (3.10) to Equation (3.11) divided by  $i\omega$  yields:

$$2a e^{i\omega t} = 0 \quad (3.12)$$

Since  $e^{i\omega t}$  is never zero ( $|e^{i\omega t}| = 1$ ), follows, that  $a = 0$ . From Equation (3.11) follows therefore that  $b e^{-i\omega t} = 0$  and hence  $b = 0$

■

Applying the Lemma to Equation (3.9) results in:

$$i\omega U(x) - U''(x) = 0 = -i\omega U^*(x) - U''^*(x) \quad (3.13)$$

Substituting Equation (3.8) into the BCs in Equation (3.5) and applying the Lemma gives for  $t > 0$ :

$$U(0) = A e^{i\varphi}, \quad U(1) = 0 \quad (3.14)$$

From Equation (3.13) and (3.14) the problem for the complex amplitude  $U(x)$  of the quasi-steady state  $u_{SS}(x, t)$  can be summarized to the following ordinary differential equation (ODE) with BCs:

$$U''(x) - i\omega U(x) = 0; \quad U(0) = Ae^{i\varphi}, \quad U(1) = 0 \quad (3.15)$$

The solution to this ODE is:

$$U(x) = C_1 e^{(-Bx)} + C_2 e^{(Bx)} \quad \text{with} \quad B = \sqrt{i\omega} \quad (3.16)$$

where  $C_1, C_2$  are integration constants. Imposing the BCs results in:

$$\begin{aligned} C_1 &= Ae^{i\varphi} \frac{e^B}{e^B - e^{-B}} \\ C_2 &= Ae^{i\varphi} - C_1 = -Ae^{i\varphi} \frac{e^{-B}}{e^B - e^{-B}} \end{aligned} \quad (3.17)$$

Therefore, the quasi-steady-state solution to the heat problem is:

$$u_{SS}(x, t) = \text{Re} \left\{ \frac{e^{B(1-x)} - e^{-B(1-x)}}{e^B - e^{-B}} Ae^{i\varphi} e^{i\omega t} \right\} \quad (3.18)$$

### Transient Solution

Solving for the transient part  $v(x, t)$ , as defined in Equation (3.6):

$$v(x, t) = u(x, t) - u_{SS}(x, t) \quad (3.19)$$

Substituting Equation (3.19) into the heat problem, see Equation (3.5), given that  $u_{SS}(x, t)$  satisfies the PDE and BCs in Equation (3.5), results in the following problem for  $v(x, t)$ :

$$\left. \begin{aligned} v_t &= v_{xx}, & 0 < x < 1 \\ v(0, t) &= 0, \quad v(1, t) = 0, & t > 0 \\ v(x, 0) &= f_2(x), & 0 < x < 1 \end{aligned} \right\} \quad (3.20)$$

where the initial condition  $f_2(x)$  is given by:

$$\begin{aligned} f_2(x) &= u(x, 0) - u_{SS}(x, 0) \\ &= f(x) - \text{Re} \left\{ \frac{e^{B(1-x)} - e^{-B(1-x)}}{e^B - e^{-B}} Ae^{i\varphi} \right\} \end{aligned} \quad (3.21)$$

The problem for  $v(x, t)$  is the basic Heat Problem whose solution is given by:

$$v(x, t) = \sum_{n=1}^{\infty} B_n \sin(n\pi x) e^{-n^2\pi^2 t}, \quad B_n = 2 \int_0^1 f_2(x) \sin(n\pi x) dx \quad (3.22)$$

### Full Solution

It results, that the full solution to the problem is:

$$u(x, t) = \operatorname{Re} \left\{ \frac{e^{B(1-x)} - e^{-B(1-x)}}{e^B - e^{-B}} A e^{i\varphi} e^{i\omega t} \right\} + \sum_{n=1}^{\infty} B_n \sin(n\pi x) e^{-n^2\pi^2 t} \quad (3.23)$$

The first term is the quasi-steady state, and the second one is the transient part that decays exponentially as  $t \rightarrow \infty$ . Considering Equation (3.22), the estimation of IC  $f_2(x)$  that fulfills the BCs is non-trivial. Therefore and based on the declining amplitude of the transient part over time, hereafter only the quasi-steady state part of the solution is considered.

$$u(x, t) = \operatorname{Re} \left\{ \frac{e^{B(1-x)} - e^{-B(1-x)}}{e^B - e^{-B}} A e^{i\varphi} e^{i\omega t} \right\} \quad \text{with} \quad B = \sqrt{i\omega} \quad (3.24)$$

for  $0 < x < 1, \quad t > 0$

The solution of Equation (3.24) is visualized in Figure 3.1 with an excitation frequency  $\omega = 4\pi$  and a phase angle  $\varphi = 0$ . It can be seen, that the BC of Equation (3.5) hold and that the different regions of the rod are exposed to variant amplitudes of temperature changes.

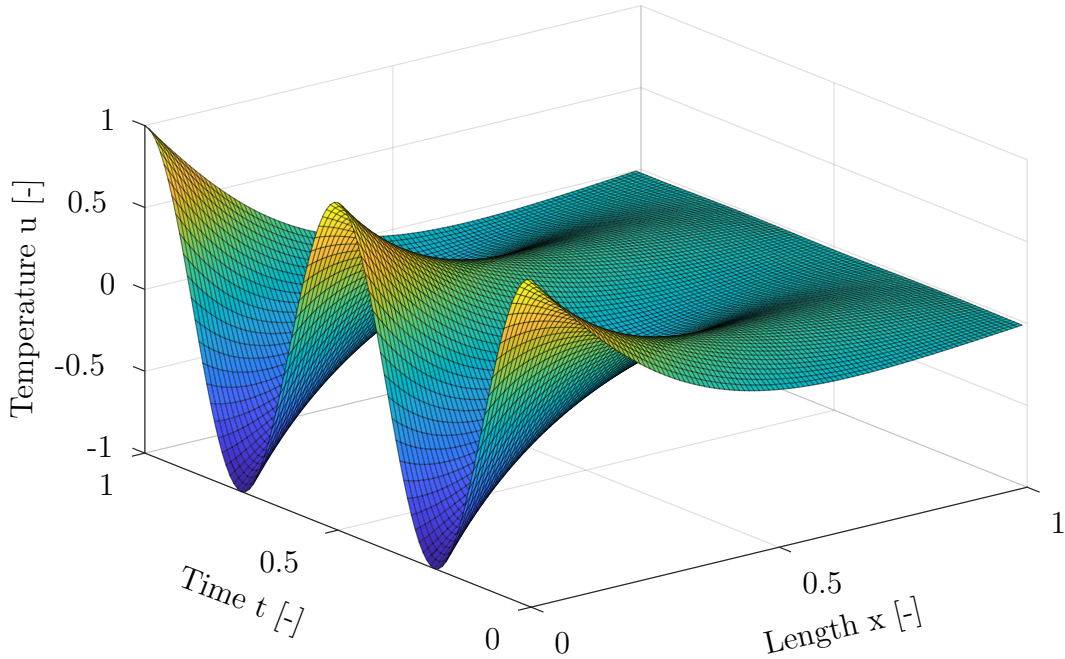


**Figure 3.1:** Dimensionless temperature profile  $u(x, t)$  for a long and thin rod with a periodically changing temperature at one end of the rod with  $\omega = 4\pi$ ,  $\varphi = 0$  and a fixed temperature at the other end.



### 3.1.4 Analysis of the Heat Equation Solution

As stated in Equation (3.7), the quasi-steady state solution can be written as:

$$u(x, t) = A(x) \cos(\omega t + \phi(x)) = \operatorname{Re} \{ A(x) e^{i\phi(x)} e^{i\omega t} \} = \operatorname{Re} \{ U(x) e^{i\omega t} \}$$

with

$$U(x) = \frac{e^{B(1-x)} - e^{-B(1-x)}}{e^B - e^{-B}} A e^{i\varphi}, \quad B = \sqrt{i\omega} \quad (3.25)$$

$U(x)$  has an amplitude of  $A(x) = |U(x)|$  and a phase of  $\phi(x) = \arctan\left(\frac{\operatorname{Im}\{U(x)\}}{\operatorname{Re}\{U(x)\}}\right)$ . The phase  $\phi(x)$  delays the effects of what is happening at the affected end of the rod. If the end is heated at time  $t = t_1$ , the effect is not felt at the center,  $x = 1/2$ , until a later time  $t = \phi(1/2)/\omega + t_1$ . Figure 3.2 shows the spatial relationship of the temperature  $u(x, t)$  at three different positions of the rod for a periodicity of  $2\pi$ . The phase lag and decay in amplitude along the rod are clearly visible.

This effect is also strongly dependent on the oscillation frequency  $\omega$  of the heat source. As illustrated in Figure 3.3, the phase  $\phi(x)$  of  $U(x)$  is negative and decreases along the rod, when the frequency of the periodically changing temperature at the end of the rod is increased. This indicates a delay between what happens at a point  $x$  on the rod and what happens at the fixed end with varying BC.

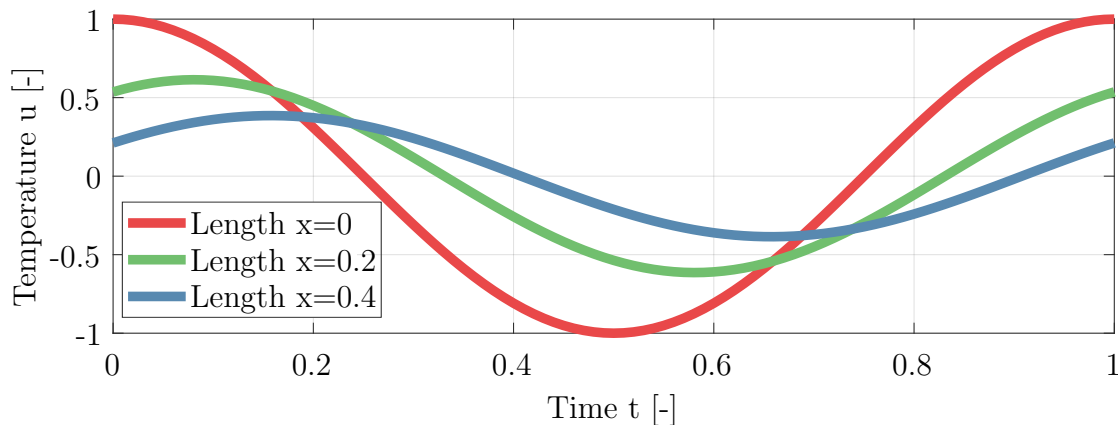


**Figure 3.2:** Dimensionless temperature  $u(x, t)$  at different positions of a long and thin rod with a periodically changing temperature at one end of the rod with  $\omega = 2\pi$ ,  $\varphi = 0$  and a fixed temperature at the other end.

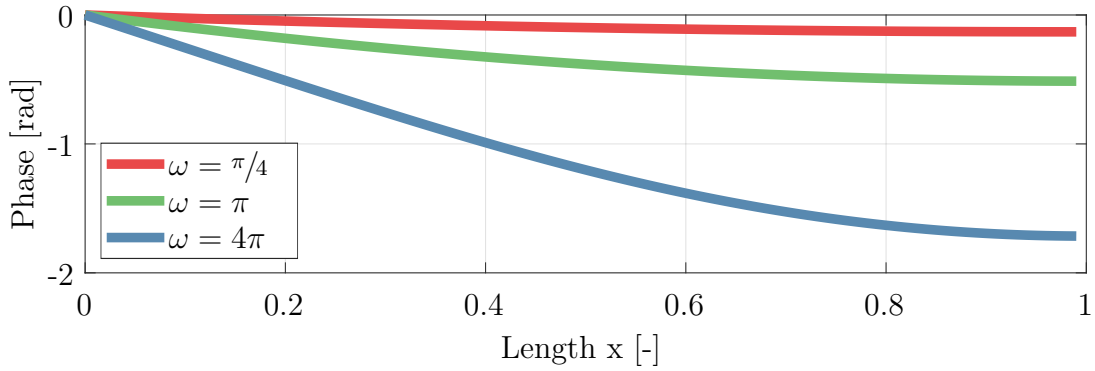


**Figure 3.3:** Illustration of the phase  $\phi(x)$  along the rod for different oscillation periodicities of the changing temperature BC with  $\varphi = 0$ .

The temperature response at two distinct positions  $x_1$  and  $x_2$  with  $x_1 > x_2$  is represented by the following equations:

$$\begin{aligned} u(x_1, t) &= A(x_1) \cos(\omega t + \phi(x_1)) \\ u(x_2, t) &= A(x_2) \cos(\omega t + \phi(x_2)) \end{aligned} \quad (3.26)$$

The temperature at position  $x_2$  can be reformulated in the following way:

$$\begin{aligned} u(x_2, t) &= \gamma(x_1, x_2) \cdot u(x_1, t - \delta(x_1, x_2)) \\ \text{with} & \\ \gamma(x_1, x_2) &= \frac{A(x_2)}{A(x_1)} \quad \text{and} \quad \delta(x_1, x_2) = \frac{\phi(x_1) - \phi(x_2)}{\omega} \end{aligned} \quad (3.27)$$

The parameter  $\gamma$  in Equation (3.27) represents the amplitude decay coefficient between the position  $x_1$  and  $x_2$  and  $\delta$  the propagation time lag of temperature between  $x_1$  and  $x_2$ . Assuming the temperature time response at the fixed end position  $x_0$  is known, the temperature distribution at other points  $x_1, x_2, x_3 \dots$  can be represented by  $u(x_0, t)$ :

$$\begin{aligned} u(x_1, t) &= \gamma(x_0, x_1) \cdot u(x_0, t - \delta(x_0, x_1)) \\ u(x_2, t) &= \gamma(x_0, x_2) \cdot u(x_0, t - \delta(x_0, x_2)) \\ &\vdots \\ &\vdots \\ &\vdots \\ u(x_n, t) &= \gamma(x_0, x_n) \cdot u(x_0, t - \delta(x_0, x_n)) \end{aligned} \quad (3.28)$$

## 3.2 The 1D Thermal Elongation

After the determination of the heat equation along the rod, the numerical integration of the temperature distributions can be used to calculate the 1D thermal elongation of the rod:

$$E(t) = \int_0^L \alpha_E u(x,t) dx \quad (3.29)$$

$$\approx \alpha_E \cdot [\Delta L_0 u(x_0, t) + \Delta L_1 u(x_1, t) + \Delta L_2 u(x_2, t) + \dots + \Delta L_n u(x_n, t)]$$

where  $\alpha_E$  is the expansion coefficient which is assumed constant along the rod,  $\Delta L_i$  is the segment length for a lumped parameter model. Figure 3.4 illustrates the elongation  $E(t)$  of the rod evaluated at the free end for different oscillation periodicities of the temperature of the mechanically fixed end of the rod. The declining amplitude and the phase shift as a function of the oscillation frequency are apparent.

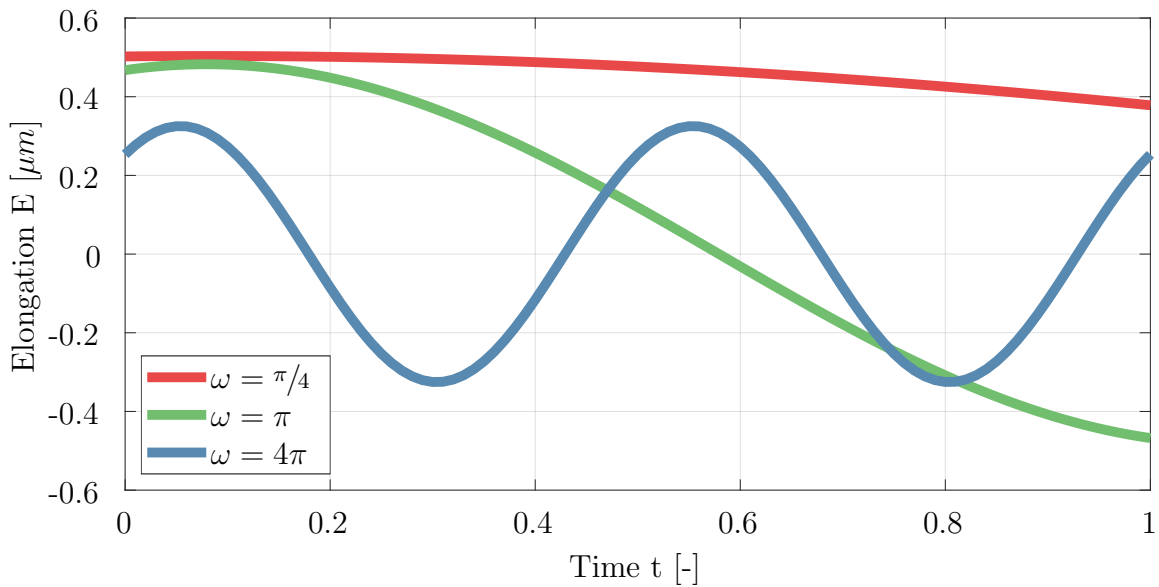


**Figure 3.4:** Illustration of the elongation  $E$  of a rod for different oscillation periodicities of the changing temperature BC with  $\varphi = 0$  and the thermal expansion coefficient  $\alpha_E = 1 \mu\text{m}/\text{K}$ .

### 3.2.1 The Pseudo-Hysteresis Effect

As shown in the previous section, each temperature at a discrete point along the rod shows a phase lag compared to the excitation frequency. According to Equation (3.29) the elongation at the free end of the rod is a summation of all the lumped temperatures with their phase shifts. Therefore the elongation shows also a different amplitude and phase

shift as the excitation. The relationship of the time-varying temperature at discrete points versus the occurring elongation is illustrated as scatter plot in Figure 3.5. A scatter plot can be used to illustrate the degree of correlation between two variables. It is apparent that a position dependent correlation exists. For the shown excitation frequency  $\omega = 4\pi$  only one position along the rod ( $x = 0.27$ ) shows an unique relationship of the occurring temperature to the elongation of the rod and therefore a linear correlation.

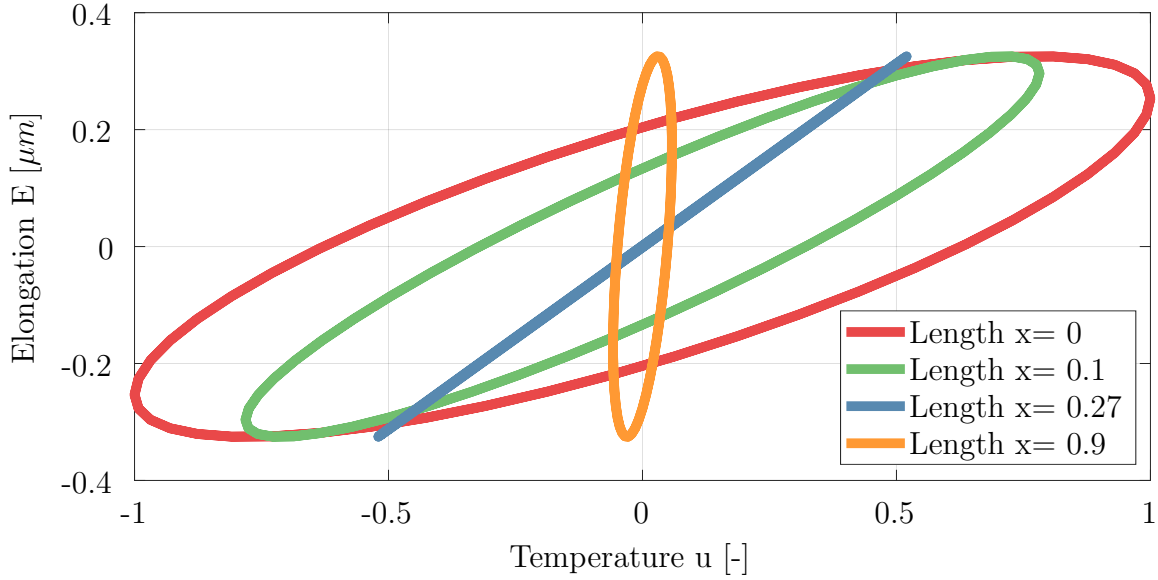


**Figure 3.5:** Illustration of the pseudo-hysteresis effect for different temperature measurement positions  $x$  along the rod and the total expansion  $E$  of the rod. The periodicity of the excitation is  $\omega = 4\pi$ , the phase shift  $\varphi = 0$  and the thermal expansion coefficient  $\alpha_E = 1 \mu m/K$ .

For this specific load case one can reason that a static description of the thermo-mechanical system can be performed by correlating the temperature  $u$  at the position  $x = 0.27$  to the total elongation of the rod, since Figure 3.5 shows a linear relationship between those variables. The feasibility of determining this temperature location is hindered by the dependence of the excitation frequency. To quantify the linearity of the correlation of two variables the Pearson correlation coefficient  $r_{xy}$  can be used.

$$r_{xy} = \frac{\sum_{i=1}^n (x_i - \bar{x})(y_i - \bar{y})}{\sqrt{\sum_{i=1}^n (x_i - \bar{x})^2} \sqrt{\sum_{i=1}^n (y_i - \bar{y})^2}} \quad (3.30)$$

Equation (3.30) shows the definition of the Pearson correlation coefficient  $r_{xy}$ , where  $n$  is the sample size,  $x_i$  respectively  $y_i$  are the individual sample points and  $\bar{x}$  respectively  $\bar{y}$  are the corresponding mean of the sample. The coefficient  $r_{xy}$  has a value between +1 and -1, where 1 is total positive linear correlation, 0 is no linear correlation, and -1 is a total negative linear correlation.

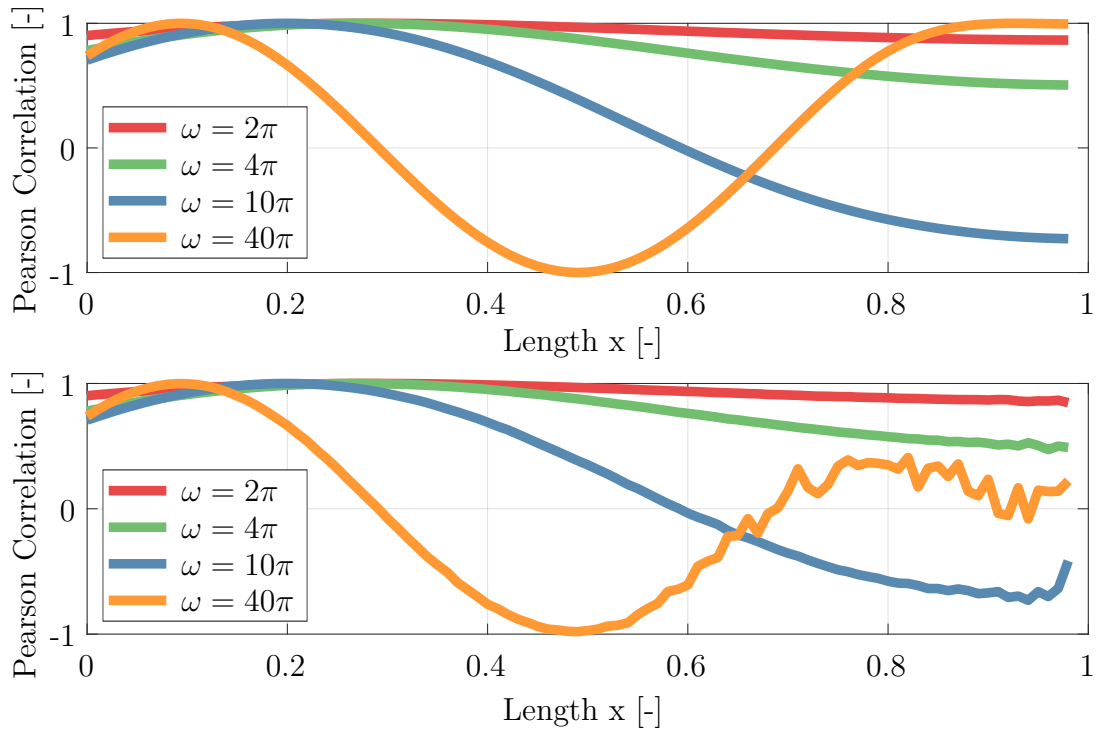


**Figure 3.6:** Illustration of the Pearson correlation coefficient for the temperature along a rod in relation with the occurring elongation of the rod. The periodicity of the excitation is varied and the phase shift is kept constant at  $\varphi = 0$ . Top: without noise, Bottom: with random noise of maximum amplitude 0.01 for the temperature as well as the elongation.

For each discrete position along the rod a Pearson correlation coefficient (PCC) can be calculated according to Equation (3.30). Figure 3.6 shows the PCC along the rod for different oscillation frequencies of the excitation. In the top half the theoretical PCC is depicted. It can be seen, that for different frequencies, one or more position(s) can be found, where the temperature correlates linearly to the elongation. The faster the oscillation of temperature, the closer to the heat source lays this point. The bottom half of Figure 3.6 shows the influence of measurement noise on the estimation of the PCC. Since the amplitude of the temperature is decreasing in function of the distance from the excitation, the influence of noise is increasing and a linear correlation is not apparent anymore.

The pseudo-hysteresis effect originates from the lumped parameter approximation of the thermo-mechanical process. Thus the correlation of discrete temperature measurements to the occurring elongation is inadequate. As a result, the static models such as the multi-variable linear regression or the ANN are deficient since the time variable is not considered. The pseudo-hysteresis phenomenon is one of the major factors causing static modeling approaches lack of robustness.

### 3.2.2 Discrete Time-Series Modeling

Replacing the temperature terms in Equation (3.29) with the relationship of Equation (3.28) results in the following expression for the thermal expansion of the rod:

$$E(t) = \alpha_E \cdot [\Delta L_0 u(x_0, t) + \Delta L_1 \gamma(x_0, x_1) \cdot u(x_0, t - \delta(x_0, x_1)) \\ + \Delta L_2 \gamma(x_0, x_2) \cdot u(x_0, t - \delta(x_0, x_2)) + \cdots + \Delta L_n \gamma(x_0, x_n) \cdot u(x_0, t - \delta(x_0, x_n))] \quad (3.31)$$

Uniform sampling can be represented by substituting the time delay elements in Equation (3.31) with the following expression:

$$\delta(x_0, x_1) = \Delta D, \quad \delta(x_0, x_2) = 2\Delta D, \quad \cdots, \quad \delta(x_0, x_n) = n\Delta D \quad (3.32)$$

Rewriting Equation (3.31) using the uniform sampling interval  $\Delta D$ , yields:

$$E(t) = \alpha_E \cdot [\Delta L_0 u(x_0, t) + \Delta L_1 \gamma(x_0, x_1) \cdot u(x_0, t - \Delta D) + \Delta L_2 \gamma(x_0, x_2) \cdot u(x_0, t - 2\Delta D) \\ + \cdots + \Delta L_n \gamma(x_0, x_n) \cdot u(x_0, t - n\Delta D)] \quad (3.33)$$

After discretization of the time-continuous Equation (3.33) for the sake of suitable numerical computation it follows:

$$E[k] = \alpha_E \cdot (\Delta L_0 u_0[k] + \Delta L_1 \gamma(x_0, x_1) \cdot u_0[k - 1] + \cdots + \Delta L_n \gamma(x_0, x_n) \cdot u_0[k - n])$$

with

$$u_0[k - i] = u[x_0, t - i \cdot \Delta D] \quad i = 0 \dots n \quad (3.34)$$

Therefore, the dynamic thermo-mechanical model bears the discrete time series form:

$$E[k] = b_0 u_0[k] + b_1 u_0[k - 1] + b_2 u_0[k - 2] + \cdots + b_n u_0[k - n] \\ = \sum_{i=0}^n b_i \cdot u_0[k - i] \quad (3.35)$$

with

$$b_0 = \alpha_E \Delta L_0$$

and

$$b_i = \alpha_E \Delta L_i \gamma(x_0, x_i) \quad i = 1 \dots n$$

Equation (3.35) is the Finite Impulse Response (FIR) model of the thermo-mechanical system, see Ljung [77]. The main statement of this equation is that the thermal deformation

---

at the free end of the rod can be evaluated by using the current and previous temperature measurements at the position  $x_0$  only. Because of the inherent dynamics associated with the thermo-mechanical process, the time history of temperature measurements can be used as inputs to formulate the dynamic model to estimate the present value of the thermal deformation.





## Chapter 4

# Dynamic Thermal Error Modeling Methodology for Machine Tools

In this chapter a time series modeling approach of thermal errors based on the system identification theory is presented. System identification is the subject of constructing or selecting models of dynamical systems to serve certain purposes. This modeling approach is capable of describing the non-instantaneous relationship of input and output based on the dynamic nature of thermo-mechanical systems. The aim of the model is to predict thermally induced errors of machine tools in dependency of varying thermal loads.

Firstly modeling of time-invariant systems is introduced, with a special focus on autoregressive models with exogenous inputs for thermo-mechanical system description. The superiority of those models compared to static models and simpler dynamic models is then validated with an FEM based simulation.

### 4.1 Models of Time-Invariant Systems

As shown in Chapter 3 the relationship between temperature data  $u$  and the thermal position and orientation errors at the TCP can be described by a linear time-invariant dynamic system. As explained by Tangirala [111], the output of such systems can be expressed as weighted sum of a finite number of past inputs  $u$  and outputs  $y$  as well as a disturbance term  $e$ . The additive disturbance term  $e$  is introduced to describe modeling uncertainties, such as, modeling approximation, unrecognized and not modeled inputs, and noise-corrupted measurements. According to Ljung [77] a linear time-invariant system can

be written in a general form as follows:

$$A(q)y[k] = \frac{B(q)}{F(q)}u[k] + \frac{C(q)}{D(q)}e[k] \quad (4.1)$$

where  $A(q)$ ,  $B(q)$ ,  $C(q)$ ,  $D(q)$  and  $F(q)$  denote five different polynomials influencing the input  $u[k]$ , the output  $y[k]$  as well as the disturbance term  $e[k]$ . With the use of different combinations of these five polynomials, 32 unique model sets can be created. The structure of Equation (4.1) is of general acceptance and can be constricted for most practical purposes. One or several of the five polynomials can be fixed to unity in most applications.

#### 4.1.1 Autoregressive Model with Exogenous Inputs

As shown in Equation (3.35), the linear system FIR model maps the past system inputs into the present output and ignores the dynamic information in the lagged system outputs. While the linear difference Equation (4.1) maps the past input and output data into the current output and provides a parsimonious system description. Therefore Equation (3.35) can be rearranged as follows:

$$\sum_{i=0}^{n_a} a_i E[k-i] = \sum_{i=0}^{n+n_a} b_i u[k-i] \quad \text{with} \quad a_0 = 1 \quad (4.2)$$

Expressed as a linear difference equation with finite order, the system can be represented as follows:

$$\begin{aligned} E[k] + a_1 \cdot E[k-1] + \dots + a_{n_a} \cdot E[k-n_a] \\ = b_0 \cdot u[k] + b_1 \cdot u[k-1] + \dots + b_{n_b} \cdot u[k-n_b] + e[k] \end{aligned} \quad (4.3)$$

The general difference equation is of order  $n_a$ , which refers to the number of samples the output is directly influenced by its own past values. The length of the input memory is defined by  $n_b$ . Since the noise term  $e[k]$  enters as a direct error in the difference equation, the model is sometimes called an equation error model. The adjustable parameters of this equation are:

$$\underline{\theta} = \left[ a_1 \quad a_2 \quad \dots \quad a_{n_a} \quad b_0 \quad \dots \quad b_{n_b} \right]^T \quad (4.4)$$

For the sake of simplicity the time-shift operator  $q$  is introduced as:

$$qu[k] = u[k+1] \quad \text{and} \quad q^{-1}u[k] = u[k-1] \quad (4.5)$$

Therefore Equation (4.3) can be simplified to:

$$\left. \begin{array}{l} A(q)E[k] = B(q)u[k] + e[k] \\ \text{with} \\ A(q) = 1 + a_1q^{-1} + \dots + a_{n_a}q^{-n_a} \\ \text{and} \\ B(q) = b_1q^{-1} + \dots + b_{n_b}q^{-n_b} \end{array} \right\} \quad (4.6)$$

Such a model is called ARX, where AR refers to the autoregressive part  $A(q)E[k]$  and X to the extra input  $B(q)u[k]$ , also called the exogenous input.

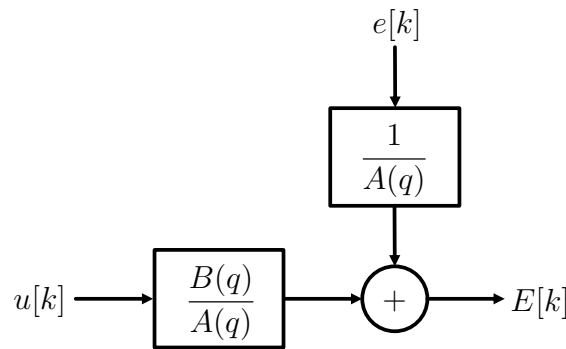


**Figure 4.1:** Illustration of the ARX model structure, where  $u[k]$  is the input,  $E[k]$  the output and  $e[k]$  the disturbance.  $A(q)$  and  $B(q)$  represent time shift polynomials. Adapted from Ljung [77].

The signal flow can be depicted as in Figure 4.1. From that picture one can see that the model from Equation (4.6) is perhaps not the most natural one from a physical point of view, the white noise is assumed to go through the denominator dynamics of the system before being added to the output. Nevertheless, the equation error model set has a very important property that makes it a prime choice, namely the predictor defines a linear regression, what is discussed in the following section.

### 4.1.2 Linear Regression of ARX Models

To derive the linear regression predictor of an ARX model, a system description of the following form is assumed:

$$y[k] = G(q)u[k] + H(q)e[k] \quad (4.7)$$

It is assumed that the disturbance term  $v[k]$  is stable, that is:

$$v[k] = H(q)e[k] = \sum_{i=0}^{\infty} h(i)e[k-i] \quad \text{and} \quad \sum_{i=0}^{\infty} |h(i)| < \infty \quad (4.8)$$

A crucial property of Equation (4.8), which needs to be imposed, is that it should be invertible; that is, if  $v[k]$ ,  $k \leq t$ , are known, then it is possible to compute  $e[k]$  as:

$$e[k] = H^{-1}(q)v[k] = \sum_{i=0}^{\infty} \tilde{h}(i)e[k-i] \quad (4.9)$$

The one-step ahead predictor  $\hat{v}[k|k-1]$  is defined as the prediction of the value  $v$  at sampling instance  $k$  based on all previous events up until  $k-1$ . Therefore the one-step ahead predictor  $\hat{v}[k|k-1]$  can be expressed as:

$$\begin{aligned} \hat{v}[k|k-1] &= \sum_{i=1}^{\infty} h(i)e[k-i] = \left[ \sum_{i=1}^{\infty} h(i)q^{-i} \right] e[k] = [H(q) - 1]e[k] \\ &= \frac{H(q) - 1}{H(q)}v[k] = [1 - H^{-1}(q)]v[k] = \sum_{i=1}^{\infty} -\tilde{h}(i)v[t-i] \end{aligned} \quad (4.10)$$

Applying  $H(q)$  to both sides of the equation results in the alternative expression:

$$H(q)\hat{v}[k|k-1] = [H(q) - q]v[k] = \sum_{i=1}^{\infty} h(i)v[t-i] \quad (4.11)$$

To calculate the one-step ahead predictor for  $y[k]$  Equation (4.7) and the definition of Equation (4.8) can be combined to formulate the following expression for  $s \leq t-1$ :

$$v[s] = y[s] - G(q)u[s] \quad (4.12)$$

The one-step ahead prediction of  $y[k]$  is therefore given by:

$$\begin{aligned} \hat{y}[k|k-1] &= G(q)u[k] + \hat{v}[k|k-1] \\ &= G(q)u[k] + [1 - H^{-1}(q)]v[k] \\ &= G(q)u[k] + [1 - H^{-1}(q)][y[k] - G(q)u[k]] \\ &= H^{-1}(q)G(q)u[k] + [1 - H^{-1}(q)]y[k] \end{aligned} \quad (4.13)$$

Therefore the predictor of  $E[k]$  of Equation (4.6) is based on the adjustable parameter vector  $\underline{\theta}$  of Equation (4.4) and can be expressed by:

$$\hat{E}[k|\underline{\theta}] = B(q)u[k] + [1 - A(q)]E[k] \quad (4.14)$$

For the purpose of simplification the vector  $\underline{\varphi}$  is introduced:

$$\underline{\varphi}[k] = [-E[k-1] \cdots -E[k-n_a] \quad u[k-1] \cdots u[k-n_b]]^T \quad (4.15)$$

Therefore Equation (4.14) can be rewritten as:

$$\hat{E}[k|\underline{\theta}] = \underline{\theta}^T \underline{\varphi}[k] = \underline{\varphi}^T[k] \underline{\theta} \quad (4.16)$$

The predictor is a scalar product between a known data vector  $\underline{\varphi}[k]$  and the parameter vector  $\underline{\theta}$ . Such a model is called a linear regression in statistics, and the vector  $\underline{\varphi}[k]$  is known as the regression vector. It is of importance since powerful and simple estimation methods can be applied for the determination of  $\underline{\theta}$ , namely linear regression.

With Equation (4.16) the predictor error can be calculated as:

$$\epsilon[k, \underline{\theta}] = E[k] - \underline{\varphi}^T[k]\underline{\theta} \quad (4.17)$$

Therefore the quadratic loss function can be derived as follows:

$$V_N(\underline{\theta}) = \sum_{k=1}^N [E[k] - \underline{\varphi}^T[k]\underline{\theta}]^2 \quad (4.18)$$

The unique feature of this function, developed from the linear parametrization and the quadratic characteristic, is that it is a quadratic function in  $\underline{\theta}$ . Therefore, it can be minimized analytically, which results, provided the indicated inverse exists, in the least-squares estimate (LSE):

$$\hat{\underline{\theta}}_N^{\text{LS}} = \arg \min_{\underline{\theta}} V_N(\underline{\theta}) = \left[ \sum_{k=1}^N \underline{\varphi}[k]\underline{\varphi}^T[k] \right]^{-1} \sum_{k=1}^N \underline{\varphi}[k]E[k] \quad (4.19)$$

Another benefit of the LSE is the possibility to assign different weights  $W[k]$  to the different measurements  $E[k]$ , this results in the weighted least-squares estimate (WLSE):

$$\hat{\underline{\theta}}_N^{\text{WLS}} = \arg \min_{\underline{\theta}} V_N(\underline{\theta}) = \left[ \sum_{k=1}^N W[k]\underline{\varphi}[k]\underline{\varphi}^T[k] \right]^{-1} \sum_{k=1}^N W[k]\underline{\varphi}[k]E[k] \quad (4.20)$$

### 4.1.3 MIMO System Identification

The parametric ARX model shown in Equation (4.6) can be extended to a multivariable model with an arbitrary number of inputs. For a 3-axis machining center, ISO 230-1 [62] defines 9 position and orientation errors,  $E_{X0X}$ ,  $E_{B0X}$ ,  $E_{C0X}$ ,  $E_{Y0Y}$ ,  $E_{A0Y}$ ,  $E_{C0Y}$ ,  $E_{Z0Z}$ ,  $E_{A0Z}$ ,  $E_{B0Z}$ , the spindle not included. For a 5-axis machine tool the number of errors increases to 19, with the additional errors, for e.g. a machine with an A- and C-axis,  $E_{Y0A}$ ,  $E_{Z0A}$ ,  $E_{A0A}$ ,  $E_{B0A}$ ,  $E_{C0A}$ ,  $E_{X0C}$ ,  $E_{Y0C}$ ,  $E_{A0C}$ ,  $E_{B0C}$ ,  $E_{C0C}$ . All of these errors can potentially change due to thermal influences. Therefore, a multiple input multiple output (MIMO) system must be considered, that has  $n$  discrete inputs and  $m$  thermal error outputs.

The main MIMO structure is usually very complex to directly identify, since too many

parameters need to be determined. In order to simplify the model structure determination and model identification, the main model is partitioned into several independent submodels, which are multiple input single output (MISO) systems respectively. This approach is similar to the one presented by Yang [127], with the difference of having undefined numbers of inputs and outputs. An illustration of the division in submodels is depicted in Figure 4.2. The vectors  $\hat{u}_{1\dots m}$  in this illustration stand for potential subsets of the inputs  $u_{1\dots n}$ . Correlation analysis, physical relevance or empirical observations can be used to group the most relevant inputs into these subsets specific for each thermal error output.

The MISO equivalent of Equation (4.6) with  $n$  inputs and  $m$  independent outputs is therefore:

$$A_m(q)E_m[k] = B_{m,1}(q)\hat{u}_{m,1}[k] + \dots + B_{m,n}(q)\hat{u}_{m,r}[k] + e[k] \quad (4.21)$$

In Equation (4.21) the variable  $r$  indicates the number of inputs for a specific submodel, this number can change for each submodel. Therefore  $\hat{u}_{m,r}$  stands for the  $m^{\text{th}}$  subset of inputs corresponding to output  $E_m$  and the  $r^{\text{th}}$  input in that specific subset.

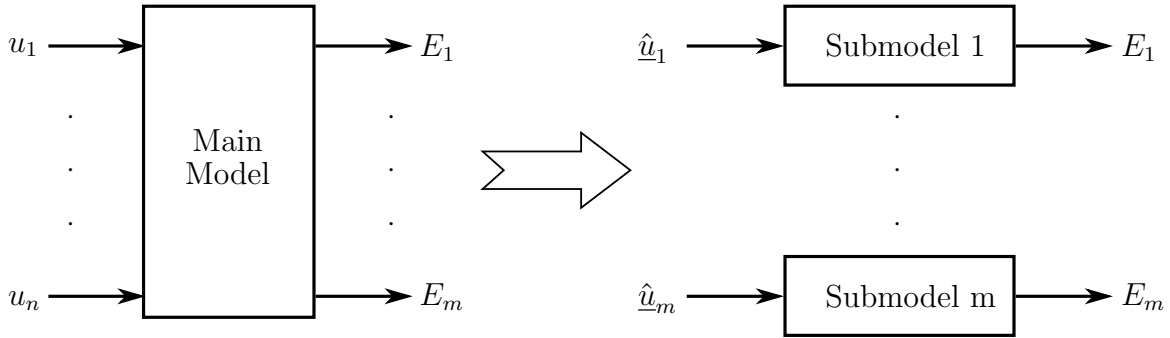


**Figure 4.2:** Partition of the main MIMO model into MISO submodels, where  $u_{1\dots n}$  stands for the inputs,  $E_{1\dots m}$  for the outputs and the vectors  $\hat{u}_{1\dots m}$  for subsets of inputs. Illustration adapted from Yang [127].

## 4.2 Simulation

The temperature field of the machine tool structure changes constantly in response to external and internal heat changes, as do the thermal deviations at the TCP. As pointed out in the previous chapter, the unmodeled dynamic characteristics of temperature variables and thermal errors are the major causes of inaccurate and non-robust thermal error modeling using a static modeling approach.

In this section, a comparison of different static and dynamic modeling methods are used to verify the conclusion of the previous chapter. With the use of a simulation framework

the performance of the different models are compared. A three dimensional FEM model of a simplified machine tool structure is built as shown in Figure 4.3. The modeled machine consists of three bodies, base, column and spindle. All bodies are modeled with the same material. The FEM model is used to simulate both the transient temperature field as well as the thermo-mechanical deviations using the commercial software MORE [86].

The FE-model has two independent heat sources. Heat source Q1 is located at the front end of the base, the heat source Q2 is located at the top of the spindle body. In order to monitor the heat flux inputs of the two independent heat sources, two virtual temperature sensors S1 and S2 are located close to the heat sources. The relative drift between the points T and W is considered as the three dimensional thermal deformation, in X, Y and Z direction, of this machine structure.

The FE-model parameters and material properties are shown in Table 4.1. All material property coefficients are considered temperature independent, since the range of temperature is small.

Thermal conductivity	$k$	60.5 W/mK
Specific heat capacity	$c$	434 J/kgK
Thermal expansion coefficient	$\alpha$	12 $\mu\text{m}/\text{mK}$
Convection coefficient	$h$	5 W/m <sup>2</sup> K
Environmental temperature	$T_{Env}$	20 °C
Density	$\rho$	7850 kg/m <sup>3</sup>
Length	$D_L$	1 m
Width	$D_W$	0.8 m
Height	$D_H$	1.4 m

**Table 4.1:** Material properties and model parameters of FE-model.

To excite a broad spectrum of dynamics of the system, the heat flux data is generated in a random pattern for a total of 48 hours. Two sets of input data for the two heat sources are generated, as shown in Figure 4.4. One is used for thermal error model training, while the other is used for model validation. To simplify the problem, the heat loads are switched and scaled for the validation data set, as can be seen in Figure 4.4.

The corresponding temperature values of the two virtual measurement points S1 and S2 are shown in Figure 4.5. These temperatures will be used in the following sections to model the thermal deviations. In Figure 4.3 the points T and W depict the location of the surfaces used to evaluate the relative deviation between tool and workpiece. The deviations in X-, Y- and Z-direction are depicted in Figure 4.6. The thermally induced deviations in X-direction are neglectable small, due to the symmetry of the modeled machine in the

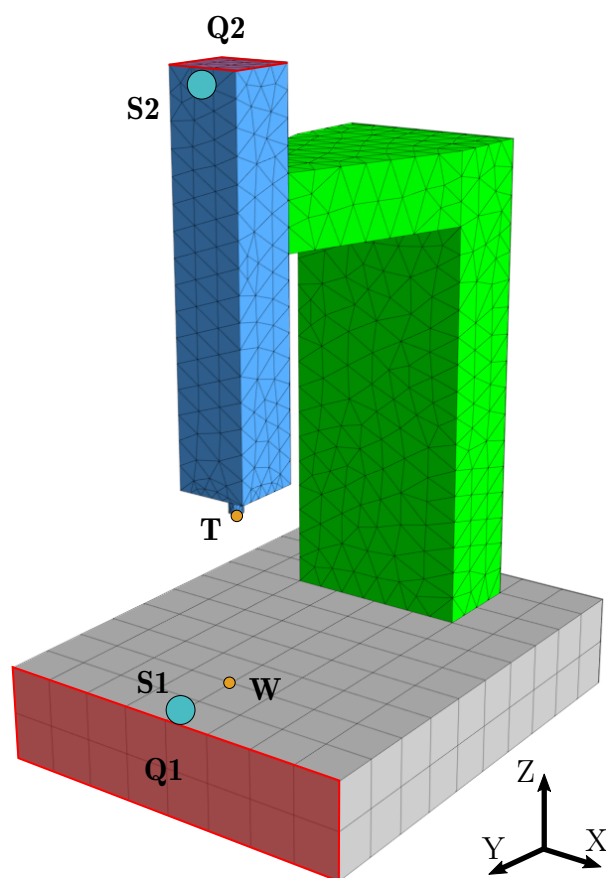


**Figure 4.3:** 3D FE-model of simplified machine tool structure. Indication of heat sources, Q1 and Q2, temperature recording spots, S1 and S2, as well as thermal deviation measurement points, T and W.

YZ-plane. A negative deviation in Z-direction occurs, when the distance between T and W is reduced, as it happens, when for example the spindle body is heated up.

### 4.2.1 Static Modeling

As stated in Chapter 2 the static modeling approach is widely used in industry to compensate thermal deviations of machine tools. The approach is based on the assumption of direct correlation between the structural temperatures and the occurring deviations at the TCP. As shown in the previous chapter, the phenomena of pseudo-hysteresis can have a negative effect on the robustness and the compensation quality of such static models. To further proof these difficulties a static thermal error model based on FEM simulations of the simplified machine tool is computed.



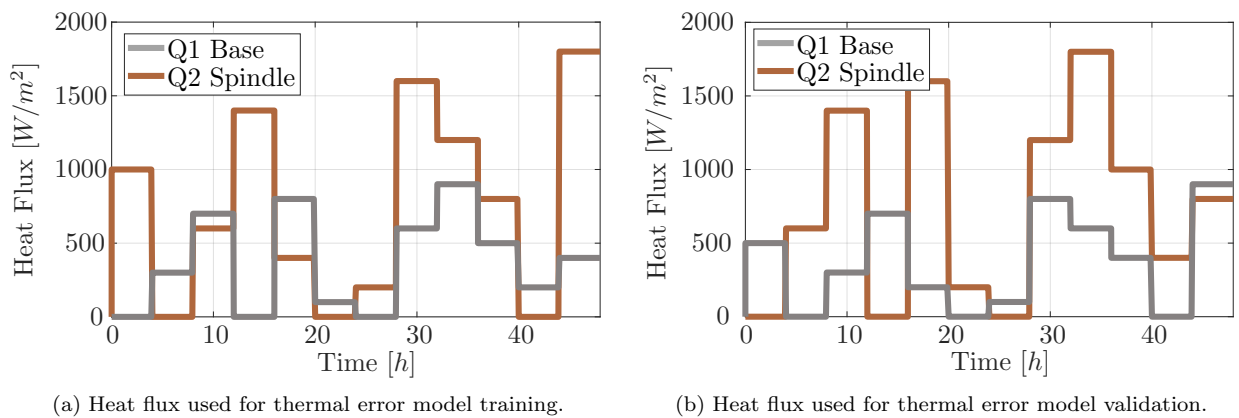


**Figure 4.4:** Heat flux input data for (a) thermal error model training (b) thermal error model validation.

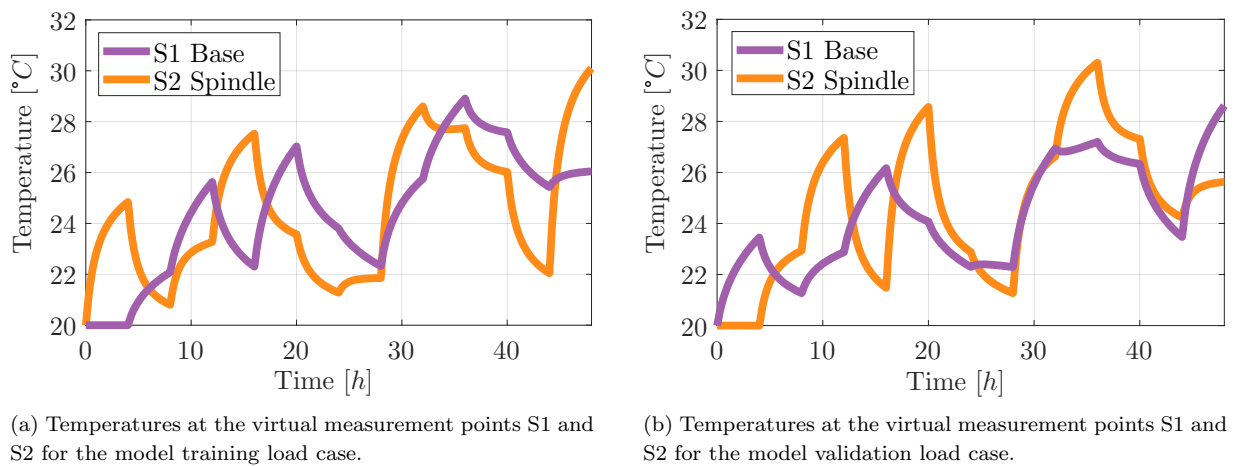


**Figure 4.5:** Temperature data for (a) model training (b) model validation.

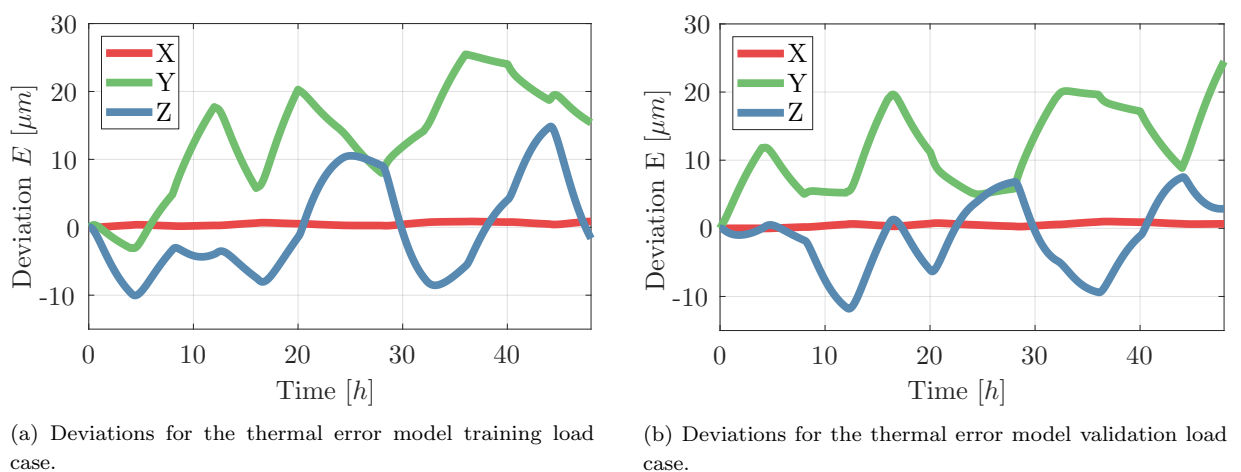


**Figure 4.6:** Relative deviations between T and W for (a) thermal error model training (b) thermal error model validation.

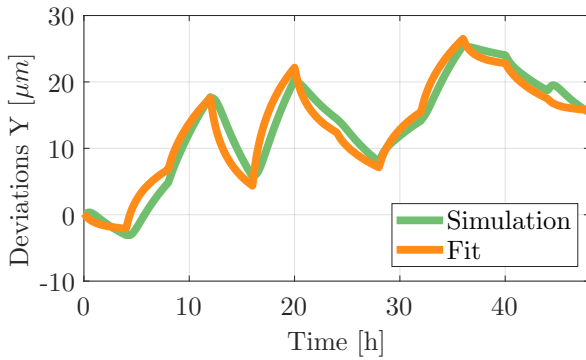
As seen in Figure 4.6 the deviations in X-directions are neglectable small and will not be considered for the modeling process. Therefore only the deviations in Y- and Z-direction are modeled. As inputs for the regression model the virtually measured temperatures close to the two heat sources are used. Using the concept of submodels, presented in Section 4.1.3, this 2-input 2-output MIMO system can be partitioned into two 2-inputs 1-output MISO systems. The parameter estimation is performed on the training data set with the linear least-squares criterion and results in the following equation:

$$\begin{aligned} E_Y[\mu m] &= 0.2 + 3.4 \cdot \Delta T_{S1}[K] - 0.5 \cdot \Delta T_{S2}[K] \\ E_Z[\mu m] &= 1.1 + 1.2 \cdot \Delta T_{S1}[K] - 1.4 \cdot \Delta T_{S2}[K] \end{aligned} \quad (4.22)$$

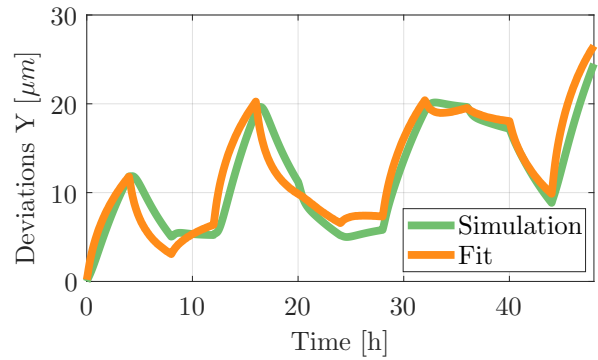
The estimation model of each direction consist of two temperature differences as inputs,  $\Delta T_{S1}$  and  $\Delta T_{S2}$ , as well as the corresponding weighting parameters and the intercept term. The temperature differences  $\Delta T_{S1}$  and  $\Delta T_{S2}$  correspond to the difference to the initial temperature. Figure 4.7 shows the simulated and the modeled deviations of the FE-model in Y-direction. One can see, that the fit for the training as well as for the validation data set is satisfactory. The limitations of the static modeling method are obvious, when comparing the modeled and simulated deviations in Z-direction. Figure 4.8 shows that the thermal error model is not capable of capturing the delayed thermal behavior in Z-direction, neither in the training nor in the validation data set. This can be explained by the underlying physical phenomenon that leads to this deviation in Z-direction. The heat conduction into the column of the machine has a significant influence on the deviation but is due to the time delay of the thermal conduction not covered by the static modeling approach. Therefore the static thermal error model can capture the fast and direct thermal responses of the system, but lacks of robustness when it comes to time delayed effects. Therefore the thermal expansion of the base structure in Z-direction is well predicted by the static model, but structural deformations not in close proximity to the temperature measurement points can not be modeled by this approach.

### 4.2.2 Dynamic Modeling

Since thermo-mechanical deviations show a time dependent behavior with certain time delay effects a dynamic modeling approach is investigated in more detail. In Section 4.1 it is shown, that the thermo-mechanical effect can be described as a linear time-invariant system and that especially the FIR and ARX model seem very promising due to their analytical description and similarity to the physical description of the thermal elongation and the underlying heat conduction process. Therefore those approaches are chosen in the following to model the thermal deviations from the FE-model.

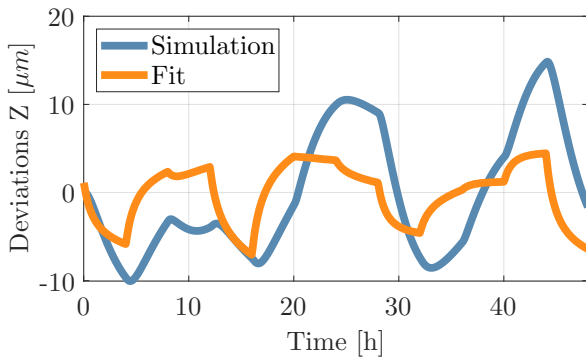


(a) Deviations and fit for the model training load case.

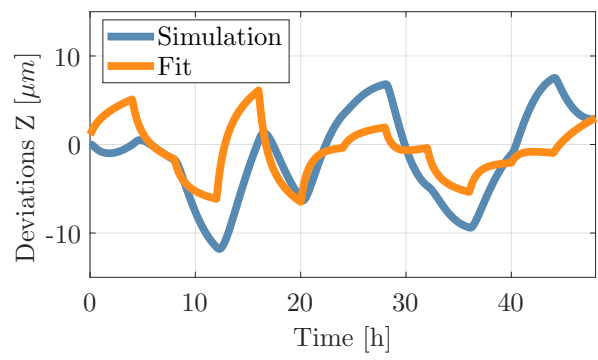


(b) Deviations and fit for the model validation load case.

**Figure 4.7:** Simulated deviations and estimation for Y-direction using a static multivariable regression method for (a) model training (b) model validation.



(a) Deviations and fit for the model training load case.



(b) Deviations and fit for the model validation load case.

**Figure 4.8:** Simulated deviations and estimation for Z-direction using a static multivariable regression method for (a) model training (b) model validation.

### FIR Model

The only difference between the FIR and the static multiple regression model is, that also past inputs are considered to compute the occurring thermal deviation. In the following the time-shift operator  $q$  is used, where for example  $q^{-2}$  denotes that the input is shifted by two sample time instances. For the post-processing of the FE-model a sampling time of 5 minutes is chosen. Since the amount of considered past inputs is strongly influencing the prediction accuracy and the robustness, an optimum has to be found. This can be done with the Minimum Description Length (MDL) criterion introduced by Rissanen [99]. The MDL criterion evaluates the prediction quality and penalizes high model orders. Therefore an overfitting of the training data can be avoided and the model order is kept as small as possible. Therefore each combination of input and output model order is used to compute a thermal error model. The model with the best fit, evaluated with root mean square error  $E_{RMS}$  (see Section 4.2.3), and the smallest model order is chosen. The formula for

the adjustment of the fit quality according to the amount of model parameters is,

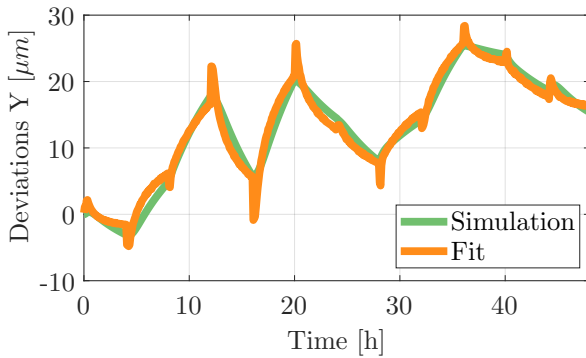
$$V = E_{RMS} \cdot \left(1 + \frac{\log(N)}{N}\right) \quad (4.23)$$

where  $N$  is the sum of the output order  $n_a$  and all the input orders  $n_{b,i}$ . The model with the smallest  $V$  is chosen as optimum selection of the model order.

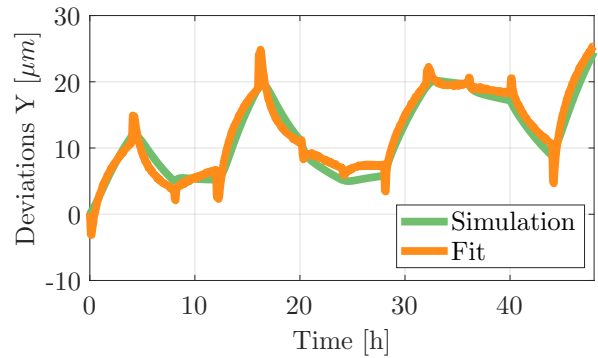
The optimal input order for the deviations in Y-directions for the training load case is found to be  $n_{b,S1} = 2$  and  $n_{b,S2} = 4$ . Therefore the resulting regression model equation, that correlates the inputs  $T_{S1}$  and  $T_{S2}$  to deviations in Y-direction, can be expressed as follows:

$$E_Y[\mu m] = 0.2 + (-20.5 + 23.9q^{-1}) \cdot \Delta T_{S1}[K] + (2.8 - 4.3q^{-1} + 5.9q^{-2} - 4.9q^{-3}) \cdot \Delta T_{S2}[K] \quad (4.24)$$

The optimal input order for the FIR model, chosen by the MDL criterion, of the deviations in Z-direction is  $n_{b,S1} = 10$  and  $n_{b,S2} = 10$ , the model equation representation is omitted here. Based on the fact, that the order of  $n_b$  is limited to 10, the fit quality would improve even more, for higher orders of  $n_b$ . Since the number of considered past inputs is influencing the number of total modeling parameters, the variable  $n_b$  has to be limited to shorten the amount of data needed for training of the model. The limitation of  $n_b$  is discussed in more detail in Chapter 6.



(a) Deviations and fit for the model training load case.



(b) Deviations and fit for the model validation load case.

**Figure 4.9:** Simulated deviations and estimation for Y-direction using dynamic FIR method,  $n_{b,S1} = 2$  and  $n_{b,S2} = 4$ , for (a) model training (b) model validation.

The resulting thermal error model estimation for the training and the validation data sets are depicted in Figure 4.9 and Figure 4.10. The estimation quality in Y-direction is satisfactory, both in the training as well as in the validation data set. The fit shows peaks at instances where the heat load drastically changes.

The model estimation for the deviations in Z-direction show an increased quality compared

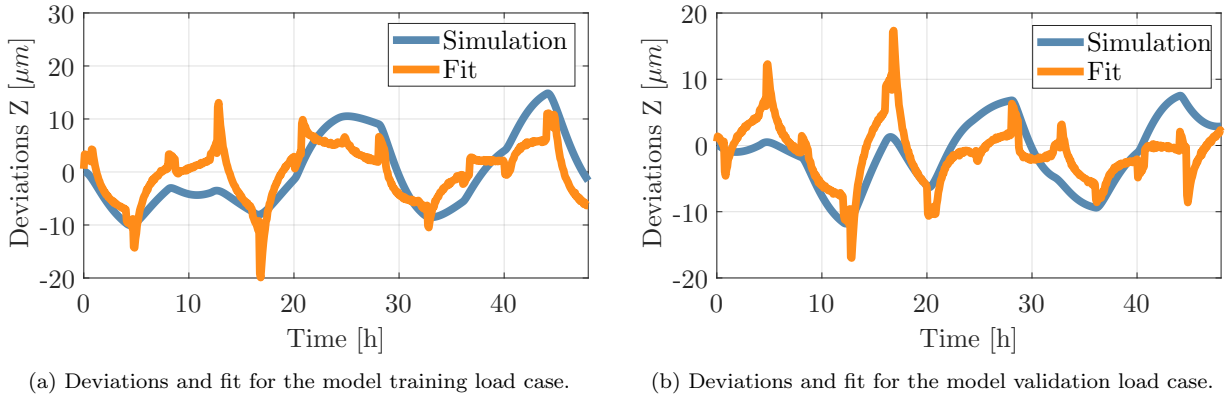


**Figure 4.10:** Simulated deviations and estimation for Z-direction using dynamic FIR method,  $n_{b,S1} = 10$  and  $n_{b,S2} = 10$ , for (a) model training (b) model validation.

to the static model, see Figure 4.8. It can be seen, that the goodness of fit decreases from the training to the validation data set and that in both cases distinct peaks after load changes appear in the model results that are not found in the FE-model data. Additionally, certain dynamics are not captured by the FIR model.

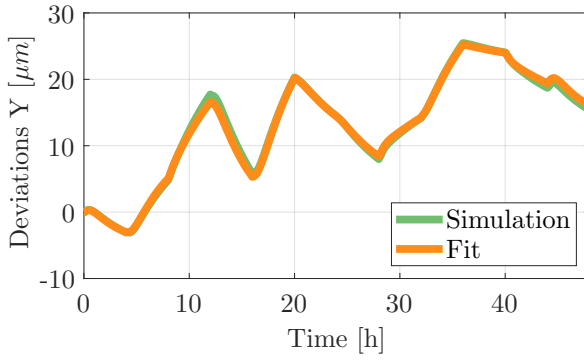
### ARX Model

The ARX model considers past and present system inputs as well as past system outputs to compute the prediction for the current system output. According to Equation (4.3) a system with one input and a feedback loop of the outputs can be described as follows:

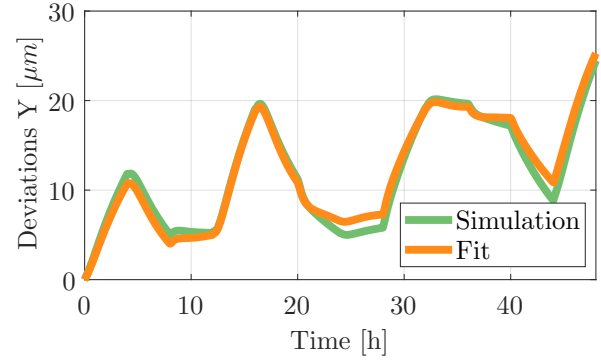
$$\begin{aligned}
 E[k] = & -a_1 \cdot E[k-1] - \dots - a_{n_a} \cdot E[k-n_a] \\
 & + b_0 \cdot u[k] + b_1 \cdot u[k-1] + \dots + b_{n_b} \cdot u[k-n_b] + e[k]
 \end{aligned}
 \tag{4.25}$$

For the ARX model parameter estimation during the training phase the TCP measurement is fed back and used as an additional input. Since in an industrial application the relative TCP deviation cannot be measured in the same frequency as the used sample rate of 5 minutes, not the real deviations but the predicted ones are fed back into Equation (4.25) during the validation phase. So past predictions are used in combinations with temperature measurements to predict the current deviations. The use of real measurement data instead of past predictions can be utilized to further increase the modeling accuracy, this concept is discussed in detail in Chapter 6.

To model the Y- and Z-deviations with an ARX model an order ( $n_a$ ) for the considered past outputs is necessary. For the sake of simplicity and also practical reasons, see Chapter 6, an order  $n_a = 1$  is chosen. The optimal input order for the deviations in Y-directions are the same as for the FIR model,  $n_{b,S1} = 2$  and  $n_{b,S2} = 4$ . By solving Equation (4.19) for the chosen inputs and the deviations in Y-direction the resulting ARX model equation

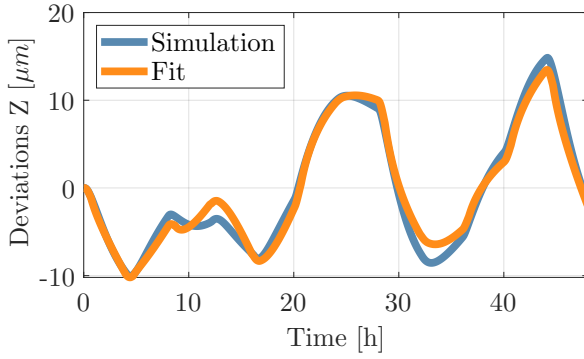


(a) Deviations and fit for the model training load case.

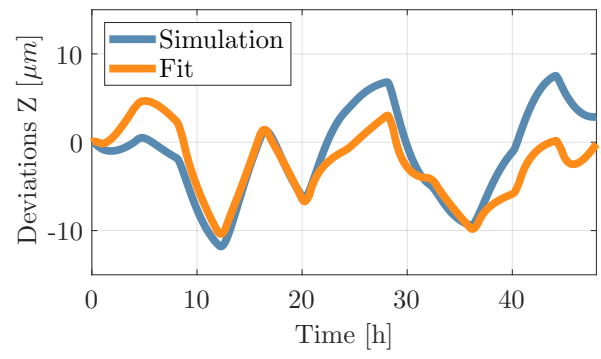


(b) Deviations and fit for the model validation load case.

**Figure 4.11:** Simulated deviations and estimation for Y-direction using dynamic ARX method,  $n_a = 1$ ,  $n_{b,S1} = 2$  and  $n_{b,S2} = 4$ , for (a) model training (b) model validation.



(a) Deviations and fit for the model training load case.



(b) Deviations and fit for the model validation load case.

**Figure 4.12:** Simulated deviations and estimation for Z-direction using dynamic ARX method,  $n_a = 1$ ,  $n_{b,S1} = 10$  and  $n_{b,S2} = 10$ , for (a) model training (b) model validation.

is as follows:

$$E_Y [\mu m] = -0.9q^{-1} \cdot E_Y [\mu m] + (1 - 0.7q^{-1}) \cdot \Delta T_{S1} [K] + (0.1 - 0.1q^{-2} - 0.1q^{-3}) \cdot \Delta T_{S2} [K] \quad (4.26)$$

The corresponding fits for the training and the validation data sets are depicted in Figure 4.11 for the Y-deviations and in Figure 4.12 for the Z-deviations. The fits for both directions in the training data set are nearly perfect. The prediction for the validation data sets are also very satisfactory for both directions.

### 4.2.3 Comparison

A residual analysis of the three models is performed. Figure 4.13 shows the residuals for the models used to model the thermal deviations in Y-direction and Figure 4.14 the residuals for the Z-direction. The superiority of the ARX model over the others is verified by a visual inspection.

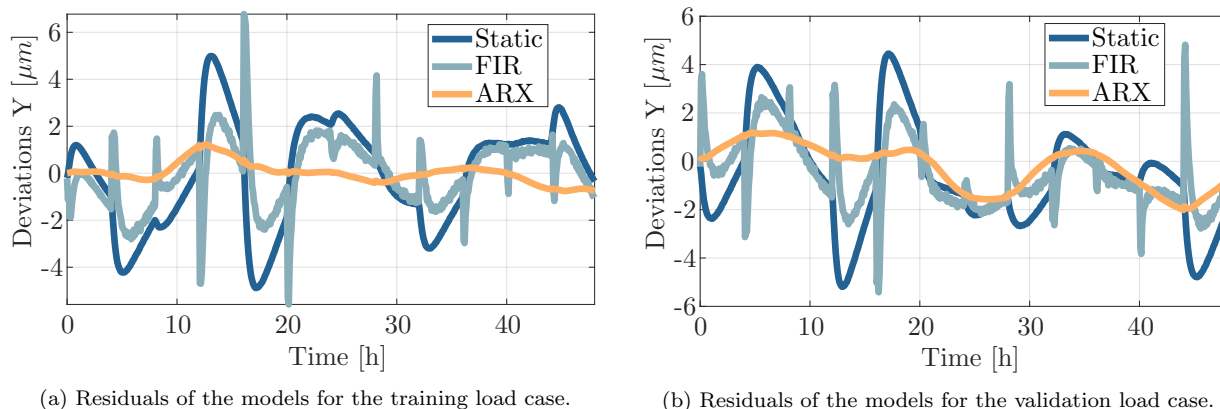


**Figure 4.13:** Residuals of the Y-deviations for the three different modeling approaches, for (a) model training (b) model validation.

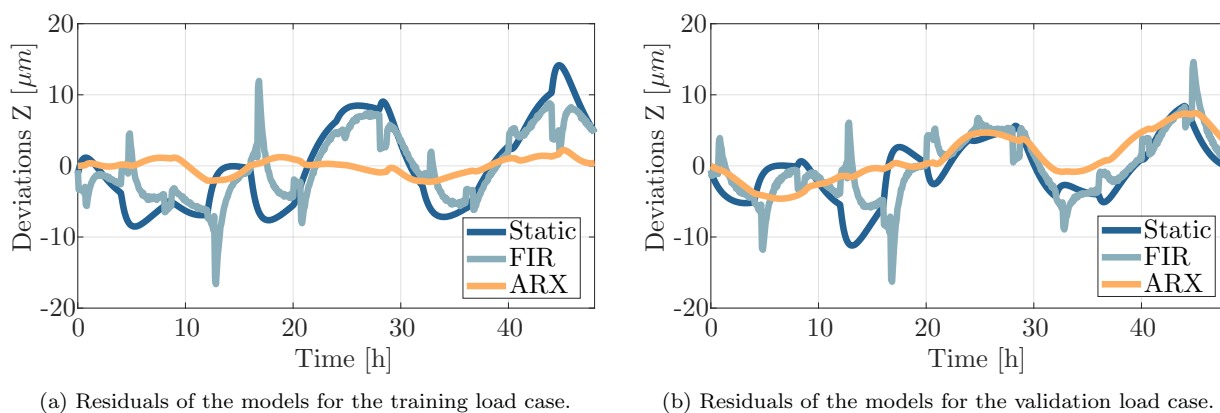


**Figure 4.14:** Residuals of the Z-deviations for the three different modeling approaches, for (a) model training (b) model validation.

For the purpose of a quantitative comparison of the prediction quality of the three models a certain metric is necessary. A literature study performed by Botchkarev [9] showed, that in the field of regression analysis no distinct performance metric is used. Since every measure of the prediction error has its benefits and disadvantages this thesis utilizes the most commonly used prediction metrics and certain additional quality indicators, that have a relation to the actual quality of manufactured workpieces.

In the following sections, the subsequent nomenclature is used. The simulated deviation is

abbreviated with  $E[k]$  for times  $k$  and the fitted deviation with  $\hat{E}[k]$ , the number of total samples is depicted with  $N$ .

### Root Mean Square Error

The root mean square error ( $E_{RMS}$ ) is the square root of the average of squared residuals, see Equation (4.27).

$$E_{RMS} = \sqrt{\frac{\sum_{k=1}^N (E[k] - \hat{E}[k])^2}{N}} \quad (4.27)$$

It is a measure of the difference between samples of the simulated and the predicted deviations.  $E_{RMS}$  is always non-negative and not limited, a value of 0 indicates a perfect fit to the data. In general, a lower  $E_{RMS}$  is better than a higher one. The effect of each error on  $E_{RMS}$  is proportional to the size of the squared error; thus, larger errors have a disproportionately large effect on  $E_{RMS}$ . Consequently,  $E_{RMS}$  strongly penalizes higher differences in the fit from the original data.

### Symmetric Mean Absolute Percentage Error

The symmetric mean absolute percentage error ( $E_{SMAP}$ ) is an accuracy measure based on percentage errors and is calculated as follows:

$$E_{SMAP} = \frac{100}{N} \sum_{k=1}^N \frac{|E[k] - \hat{E}[k]|}{|E[k]| + |\hat{E}[k]|} \quad (4.28)$$

The absolute difference between simulated and predicted value is divided by the sum of absolute values of the actual value  $E[k]$  and the predicted value  $\hat{E}[k]$ .  $E_{SMAP}$  has both a lower bound and an upper bound, so it provides a result between 0% and 100%. A limitation of  $E_{SMAP}$  is that if the actual value or predicted value is 0, the  $E_{SMAP}$  will hit the upper bound, even though the difference between the data and the fit could have been small. Therefore those values are not considered for the further evaluation. Another problem with  $E_{SMAP}$  is that it is not symmetric since over- and under-estimations are not treated equally. Therefore the data is pre-processed before the evaluation by Equation (4.28) and under-estimations are converted in equal distant over-estimations, since both are equally influential on the machine tool precision.



### Peak to Peak

The Peak value  $E_{PV}$  measures the relation between the biggest positive and negative peak of the residuals, Equation (4.29).

$$E_{PV} = \frac{\max(E[k] - \hat{E}[k]) + \left| \min(E[k] - \hat{E}[k]) \right|}{\max(E[k]) + \left| \min(E[k]) \right|} \cdot 100 \quad (4.29)$$

$E_{PV}$  has a lower bound of 0%. It evaluates the biggest outliers, not considering the frequency of occurrence. The smaller the  $E_{PV}$  the better the prediction.

### Percentile

A percentile is a measure indicating the value below which a given percentage of observations in a group of observations falls. For example, the 20th percentile ( $P_{20}$ ) is the value below which 20% of the observations may be found. In this work, the 99<sup>th</sup> percentile ( $P_{99}$ ) is used to describe the residuals according to Equation (4.30). To calculate the  $X^{\text{th}}$  percentile  $PX$  the deviations need to be sorted from lowest to highest. In Equation (4.30)  $R$  corresponds to the absolute residuals  $\left| E[k] - \hat{E}[k] \right|$  and  $\lfloor k \rfloor$  stands for the floor function, whereas  $k\%1$  uses the modulus to represent the remainder of  $k$  after division by 1. Equation (4.31) and Equation (4.32) show the derivation of the sample index  $k$  for the  $X^{\text{th}}$  percentile. The advantage of the percentile is the retaining of the physical basis, so one can directly evaluate the remaining deviation of the residuals.

$$PX = R_{\lfloor k \rfloor} + (k\%1) (R_{\lfloor k \rfloor + 1} - R_{\lfloor k \rfloor}), \forall k \in [1, N] \quad (4.30)$$

$$k = \begin{cases} N \cdot X + \frac{1}{2} & \forall X \in [p_1, p_N] \\ 1 & \forall X \in [0, p_1] \\ N & \forall X \in [p_N, 1] \end{cases} \quad \forall X \in [0, 1] \quad (4.31)$$

$$p_i = \frac{1}{N} \left( i - \frac{1}{2} \right), i \in [1, N] \quad (4.32)$$

## Evaluation

The aforementioned quality indicators are used to quantify thermal error model predictions. Since an evaluation of the training data is biased, only the validation data is used for this evaluation. Table 4.2 shows the results of this analysis. It can be seen, that the ARX model outperforms the other models in all categories. It can also be seen, that the Static and the FIR model both perform similar and that no real improvement is achieved by using only past and present temperature inputs. Only in combination with past measurements the full potential can be tapped. Even though during the validation phase only past predictions are used, the model parameters are based on past measurements during the training phase. In Chapter 6 the combination of past measurements with past predictions is discussed and it can be shown, that the prediction quality significantly increases.

	<b>Y</b>			<b>Z</b>		
	Static	FIR	ARX	Static	FIR	ARX
$E_{RMS}$ [ $\mu m$ ]	2.3	1.6	1.0	4.3	4.5	3.5
$E_{SMAP}$ [%]	9.1	6.9	4.3	48.4	49.8	41.9
$E_{PV}$ [%]	39.4	41.8	13.0	101.8	160.0	62.3
$P99$ [ $\mu m$ ]	5.1	4.1	2.0	10.8	13.2	7.4

**Table 4.2:** Quality indicators for the different prediction models for the validation load case. The smaller the value the better the fit.

## Chapter 5

# On-machine Measurements for Thermal Error Characterization

The thermally induced errors of a machine tool vary spatially over the entire machine working zone. They are not only thermally but also position dependent. Indirect measurement methods enable the fast evaluation of several machine components at the same time, if used in combination with process intermittent probing, the effect on the productivity of the machine tool can further be reduced.

This chapter investigates the feasibility of touch probe measurements for the characterization of thermally induced errors of a vertical rotary axis, the table of a 5-axis machine tool. Firstly, the utilized machine tool and measurement equipment is described. The main principle of the measurement cycle is stated in the second section. In the third section, repeatability of the measurement cycle is validated by experiments. Lastly, the measurement cycle is tested during real measurement conditions to verify the functionality of the procedure.

## 5.1 Utilized machine tool and equipment

For the characterization of the on-machine measurement cycle a touch trigger probe, a 5-axis machine tool and several temperature sensors are used. The following section describes these used devices, their specifications and requirements in more detail.

### 5.1.1 Machine tool

All following experimental investigations are performed on a DMG Mori NMV 5000 DCG, a 5-axis numerically controlled vertical machining center. The machines linear axes are located on the tool side without overhangs. The swiveling axis B and the rotary axis C are located on the workpiece side as shown in Figure 5.1. Detailed axis specifications of the machine are listed in Table 5.1. The optional turning function of the C-axis with a maximum rotation speed of 1200 rpm qualifies this machine tool especially for the investigation of thermal errors of rotary axes. Additionally, the environmental temperature of the shop floor, where the machine is situated in, is not controlled and therefore fluctuations over the course of the day can be observed. The machine tool is also strongly influenced by a hall door that is located right next to the machine.

The axis configuration according to ISO 10791-1:2015 [57] adopted for machining centers with vertical spindles can be described with:

$$V[w \ C2' \ B' \ b \ [Y1 \ Y2] \ X \ [Z1 \ Z2] \ (C1) \ t]$$

The distinctiveness of this machine is a box-in-box design as well as a Drive in Center of Gravity (DCG) system. Additionally, this machine has two separate cooling circuits. One for the linear drives and the spindle and an additional one for the rotary and swiveling axes. The outlet temperature of both circuits is controlled to the bed temperature of the machine.

### 5.1.2 Touch probe

For the on-machine measurements an OMP60 touch trigger probe from the company Renishaw is used. It is clamped with an HSK A63 tool holder into the main spindle. To allow for a high ease of movement, the data is transmitted via infrared technology to the

Axis	Travel distance	Maximum feed rate / rotation speed without AI Contour Control	Command resolution
X	730 mm	6000 mm/min	1 $\mu\text{m}$
Y	510 mm	6000 mm/min	1 $\mu\text{m}$
Z	510 mm	6000 mm/min	1 $\mu\text{m}$
B	$-180^\circ - 160^\circ$	5.55 rpm	0.001 $^\circ$
C	$>360^\circ$	1200 rpm (turning mode) 16.66 rpm (milling mode)	0.001 $^\circ$
Spindle	$>360^\circ$	12 000 rpm	-

**Table 5.1:** Axis specifications of DMG Mori NMV 5000 DCG [27]

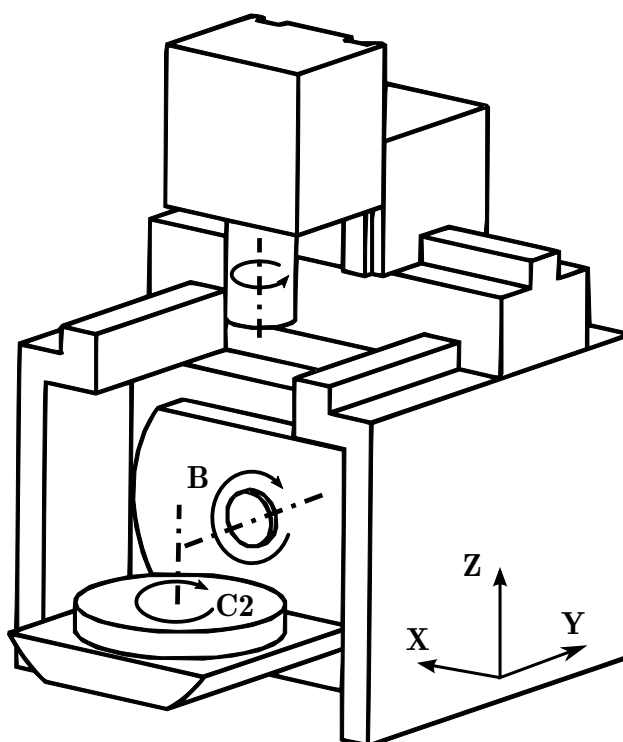


**Figure 5.1:** Schematic of the DMG Mori NMV 5000 DCG.

machine's control and from there transmitted via Ethernet to a PC that is used for data acquisition. The manufacturer guarantees a repeatability of  $1\ \mu\text{m}$  [97]. The system is a 2.5D touch probe, since the probe can only trigger a contact point along the Z-axis in negative direction of travel.

### 5.1.3 Temperature sensors

For temperature logging, the PC temperature measuring system Hygrosense TLOG-USB20 is used, in connection with DALLAS temperature sensors. The Hygrosense TLOG-USB20 is a temperature measurement system, which offers an interface between the measurement computer and the temperature sensors. The sensors are connected to the PC via a USB module, consisting of a microcontroller, which identifies each sensor by their serial number. In addition, the microcontroller controls the USB bus, manages the serial numbers and cyclically records the temperatures of all connected sensors. The current measured values are output as an ASCII string via the USB interface to the connected PC. The temperature measuring system allows a connection to up to 20 temperature sensors, these can be as far off as 100 m [4]. The utilized DALLAS temperature sensors DS 1820 are waterproof and can be used in harsh environments and under MWF influence without any restrictions. The absolute accuracy at  $23\ ^\circ\text{C}$  is stated as  $\pm 0.5\ \text{K}$  [47].

## 5.2 On-machine Measurement Cycle

To measure the thermal position and orientation errors of a rotary axis, a specially designed measurement cycle with a touch probe system, clamped into the spindle, measuring the center of a reference sphere, mounted on the table, is used. The procedure is derived from Weikert's [120] R-Test measurement which is introduced for thermal machine tool measurements by Ess et al. [29]. The X-, Y- and Z-positions of the reference sphere are identified in five given indexed positions of the C-axis, as shown in Figure 5.2. In each specific rotary axis position, the sphere location is identified by the procedure depicted in Figure 5.3. When investigating thermal machine tool errors, the measurement time has to be minimized to maximize the productivity and to reduce the thermal effects during the measurement itself. Thus, the measurement cycle is time optimized by minimizing the single axes movements and increasing the axes feed rates during non-probing movements.

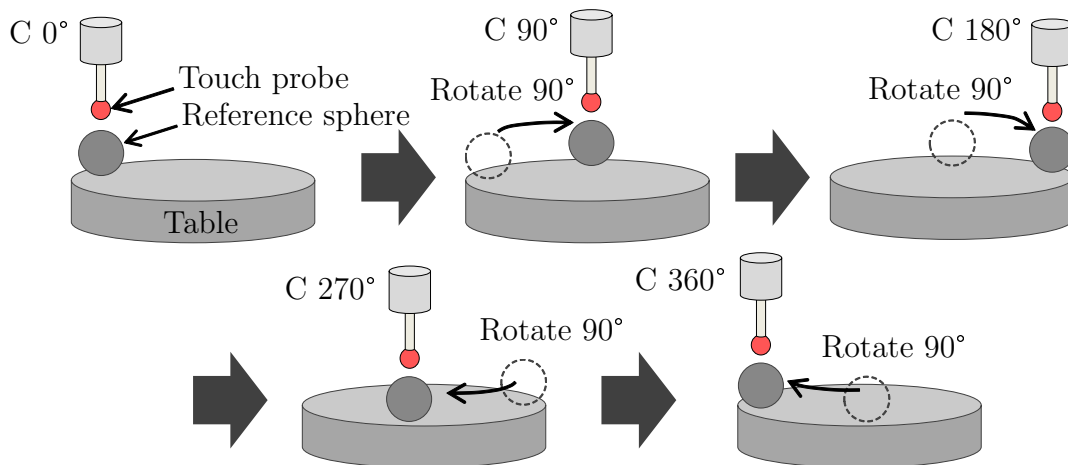


**Figure 5.2:** Procedure for measuring thermal position and orientation errors of the rotary axis C with a touch probe.

During the measurements on the machine tool, the reference sphere is eccentrically mounted on the table in a distance as far away as possible from the axis center of rotation. The sphere is firstly positioned at the nominal position  $p_{nom_1} = 0^\circ$ . The touch probe mounted in the spindle is then used to detect the position  $p_{act_1} = 0^\circ$ . Afterwards, the analyzed axis is rotated by  $90^\circ$ , the sphere is positioned at the position  $p_{nom_2}$  and the actual position of the sphere  $p_{act_2}$  is measured. This procedure is carried out for  $k = 5$  nominal positions. Therefore each nominal and actual position is represented by x, y and z, which are the

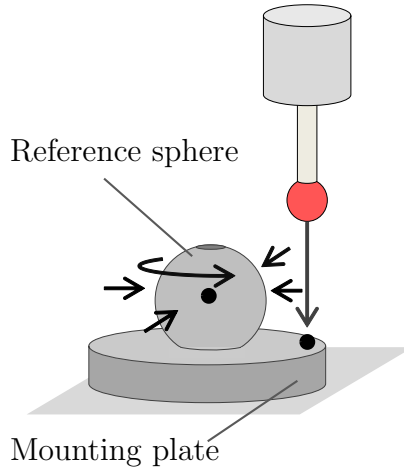


**Figure 5.3:** Detailed illustration of the measurement cycle in each C-axis position

coordinates of the sphere in the machine tool coordinate system.

$$\underline{p}_{nom_k} = \begin{pmatrix} x_{nom_k} \\ y_{nom_k} \\ z_{nom_k} \end{pmatrix} \quad \underline{p}_{act_k} = \begin{pmatrix} x_{act_k} \\ y_{act_k} \\ z_{act_k} \end{pmatrix} \quad (5.1)$$

To analyze the thermal behavior of a rotary axis over a certain period of time the procedure introduced by Gebhardt [40] is adopted to be used with a touch probe. The measurement cycle is carried out  $i$  times with a time gap  $\Delta t$  between the end of one measurement and the start of the next measurement. This generates a matrix  $P$  of measurement values  $\underline{p}_{act_{i,k}}$  where the first index identifies the time step number and the second index the measurement position.

$$\underline{P}_{act} = \begin{bmatrix} \underline{p}_{act_{1,1}} & \underline{p}_{act_{2,1}} & \cdots & \underline{p}_{act_{N,1}} \\ \underline{p}_{act_{1,2}} & \underline{p}_{act_{2,2}} & \cdots & \underline{p}_{act_{N,2}} \\ \vdots & \vdots & \ddots & \vdots \\ \underline{p}_{act_{1,5}} & \underline{p}_{act_{2,5}} & \cdots & \underline{p}_{act_{N,5}} \end{bmatrix} \quad (5.2)$$

The redundant measurement position  $\underline{p}_{nom_1} = \underline{p}_{nom_5}$ , is used as an indicator for the repeatability of the measurement. For the evaluation of the thermal errors it is not needed. The matrix  $P$  is therefore reduced to the necessary measuring data for the evaluation of all thermal errors of a single measurement cycle  $i$  to:

$$\underline{P}_{act} = \begin{bmatrix} \underline{p}_{act_{1,1}} & \underline{p}_{act_{2,1}} & \cdots & \underline{p}_{act_{N,1}} \\ \underline{p}_{act_{1,2}} & \underline{p}_{act_{2,2}} & \cdots & \underline{p}_{act_{N,2}} \\ \underline{p}_{act_{1,3}} & \underline{p}_{act_{2,3}} & \cdots & \underline{p}_{act_{N,3}} \\ \underline{p}_{act_{1,4}} & \underline{p}_{act_{2,4}} & \cdots & \underline{p}_{act_{N,4}} \end{bmatrix} \quad (5.3)$$

The initial measurement ( $i = 1$ ) is used as reference for the following thermal measurements ( $i = 2 \dots N$ ), to mathematically eliminate the influences of the geometrical errors of the machine tool and only consider the time-variant errors.

According to Gebhardt [40] the position and orientation errors listed in Table 5.2 can be derived with this measurement procedure by utilizing the following formulas:

$$E_{X0C_i} = \frac{1}{4} \sum_{k=1}^4 \underline{p}_{act_{i,k}} \underline{e}_x - \frac{1}{4} \sum_{k=1}^4 \underline{p}_{act_{1,k}} \underline{e}_x \quad (5.4)$$

$$E_{Y0C_i} = \frac{1}{4} \sum_{k=1}^4 \underline{p}_{act_{i,k}} \underline{e}_y - \frac{1}{4} \sum_{k=1}^4 \underline{p}_{act_{1,k}} \underline{e}_y \quad (5.5)$$

$$E_{Z0T_i} = \frac{1}{4} \sum_{k=1}^4 \underline{p}_{act_{i,k}} \underline{e}_z - \frac{1}{4} \sum_{k=1}^4 \underline{p}_{act_{1,k}} \underline{e}_z \quad (5.6)$$

$$E_{ROT_i} = \frac{1}{4} \left( \underline{p}_{act_{i,3}} \underline{e}_x + \underline{p}_{act_{i,2}} \underline{e}_y - \underline{p}_{act_{i,1}} \underline{e}_x - \underline{p}_{act_{i,4}} \underline{e}_y \right) - \frac{1}{4} \left( \underline{p}_{act_{1,3}} \underline{e}_x + \underline{p}_{act_{1,2}} \underline{e}_y - \underline{p}_{act_{1,1}} \underline{e}_x - \underline{p}_{act_{1,4}} \underline{e}_y \right) \quad (5.7)$$

$$E_{A0C_i} = \frac{1}{d} \left( \underline{p}_{act_{i,2}} \underline{e}_z - \underline{p}_{act_{i,4}} \underline{e}_z \right) - \frac{1}{d} \left( \underline{p}_{act_{1,2}} \underline{e}_z - \underline{p}_{act_{1,4}} \underline{e}_z \right) \quad (5.8)$$

$$E_{B0C_i} = \frac{1}{d} \left( \underline{p}_{act_{i,1}} \underline{e}_z - \underline{p}_{act_{i,3}} \underline{e}_z \right) - \frac{1}{d} \left( \underline{p}_{act_{1,1}} \underline{e}_z - \underline{p}_{act_{1,3}} \underline{e}_z \right) \quad (5.9)$$

$$E_{C0C_i} = \frac{1}{2d} \left( \underline{p}_{act_{i,1}} \underline{e}_y + \underline{p}_{act_{i,2}} \underline{e}_x - \underline{p}_{act_{i,3}} \underline{e}_y - \underline{p}_{act_{i,4}} \underline{e}_x \right) - \frac{1}{2d} \left( \underline{p}_{act_{1,1}} \underline{e}_y + \underline{p}_{act_{1,2}} \underline{e}_x - \underline{p}_{act_{1,3}} \underline{e}_y - \underline{p}_{act_{1,4}} \underline{e}_x \right) \quad (5.10)$$

In the Equations 5.4 - 5.10  $\underline{e}_x$  is the unity vector in X-direction and  $\underline{e}_y$ ,  $\underline{e}_z$  accordingly in Y- and Z-direction. The eccentric distance between the sphere and the center of rotation of the C-axis is expressed as  $d/2$ .

As stated by Gebhardt [40] it is necessary to measure in four positions during a full  $360^\circ$  movement, in order to be able to evaluate all errors. The Equations 5.4 - 5.10 can only be used if the starting point intersects with the X-axis, otherwise the indexes have to be shifted accordingly.



The advantage of using a touch probe compared to an R-Test device is the high availability in industrial workshops, due to the fact that it is usually used to setup a new workpiece or to probe some special features before or after manufacturing. Additionally the possibility to not only probe a precision sphere but also be able to trace a feature of the table, a corner for example, or a feature of the clamping device or the workpiece itself is a clear benefit of the touch probe. The disadvantage is clearly the measuring time, since five points in each rotary axis position has to be probed. An increase of the measurement time of approximately 30 % have to be accounted for.

<b>Error</b>	<b>Description</b>
$E_{X0C}$	Error of the position of C in X-axis direction
$E_{Y0C}$	Error of the position of C in Y-axis direction
$E_{Z0T}$	Position error of the table surface in Z-axis direction
$E_{R0T}$	Radial error of the functional surface table
$E_{A0C}$	Error of the orientation of C in A-axis direction; squareness of C to Y
$E_{B0C}$	Error of the orientation of C in B-axis direction; squareness of C to X
$E_{C0C}$	Zero position error of C-axis

**Table 5.2:** Position and orientation errors of a rotary axis C according to ISO 230-7 [67] with the additional errors of the functional surface table according to Gebhardt [40].

## 5.3 Uncertainty of On-machine Measurement Cycle

In this section, the functionality of the thermal error measurements with a touch probe is investigated for the later use for long term thermal error characterization of a rotary axis of a 5-axis machine tool. First, repeatability of the sphere measurement itself is investigated. Then, repeatability of the whole touch probe measurement cycle, which is introduced in the previous section, is analyzed.

### 5.3.1 Uncertainty of a Sphere Measurement

To investigate the repeatability of the touch probe itself, the measurement procedure shown in Figure 5.3 is repeated at the position  $C_{nom} = 0^\circ$  for 100 times continuously. Figure 5.4 shows two results of repeatability measurements. The resolution of the measured coordinates of the sphere is  $1 \mu\text{m}$ , due to the limited resolution of the used machine tool. The two experiments differ in the fact, that for the measurements shown in Figure 5.4a the touch probe was continuously clamped in the spindle whereas for the experiment shown

in Figure 5.4b an automated tool change (ATC) is performed. An ATC consists of automatically emptying the spindle and storing the touch probe in the tool magazine, then rotating the tool magazine for one whole round and putting the touch probe back into the spindle. The duration of the experiment without ATC is about 1 hour and approximately 1.5 hours for the one with ATC. Before each experiment is performed, the machine was warmed up with different axes movements for approximately 20 minutes. According to the guide to the expression of uncertainty in measurement (GUM) [68] the standard uncertainty can be expressed as the repeatability of independent repeated observations and is calculated by evaluating the experimental standard deviation of the mean. The results of this analysis are shown in Table 5.3 for all three coordinate directions and as extended uncertainty in 3D. The probability distribution is assumed to be normal and a confidence interval of approximately 95 % ( $k=2$ ) is chosen.

Since this measurement is performed by moving the machine tool axes not only the uncertainty of the touch probe but of the whole system sphere, machine tool and touch probe is evaluated and cannot be separated. Since the thermal influence on the measurement setup over the whole duration of the experiment cannot be avoided. Therefore, the values listed in Table 5.3 represent a rough estimation of the measurement uncertainty and can be treated as worst case values.

The influence of the ATC is mainly visible in the Z-direction, where the extended uncertainty  $U$  increases by more than  $1 \mu\text{m}$ .

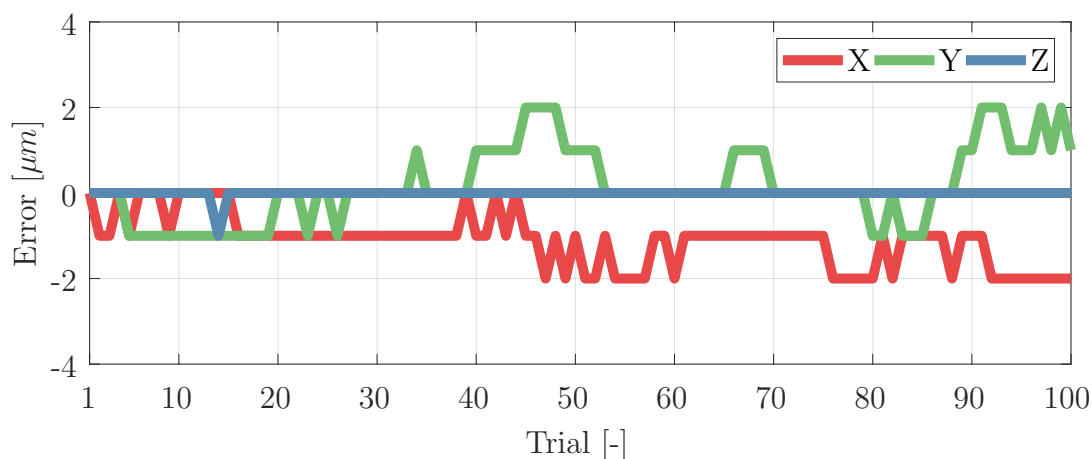
Direction	Extended uncertainty $U$ ( $k=2$ )	
	without ATC	with ATC
X	$1.2 \mu\text{m}$	$1.2 \mu\text{m}$
Y	$1.8 \mu\text{m}$	$1.7 \mu\text{m}$
Z	$0.2 \mu\text{m}$	$1.5 \mu\text{m}$
3D	$2.2 \mu\text{m}$	$2.6 \mu\text{m}$

**Table 5.3:** Uncertainty of the touch probe measurement of a sphere, evaluated with the experimental standard deviation of the mean according to GUM [68].

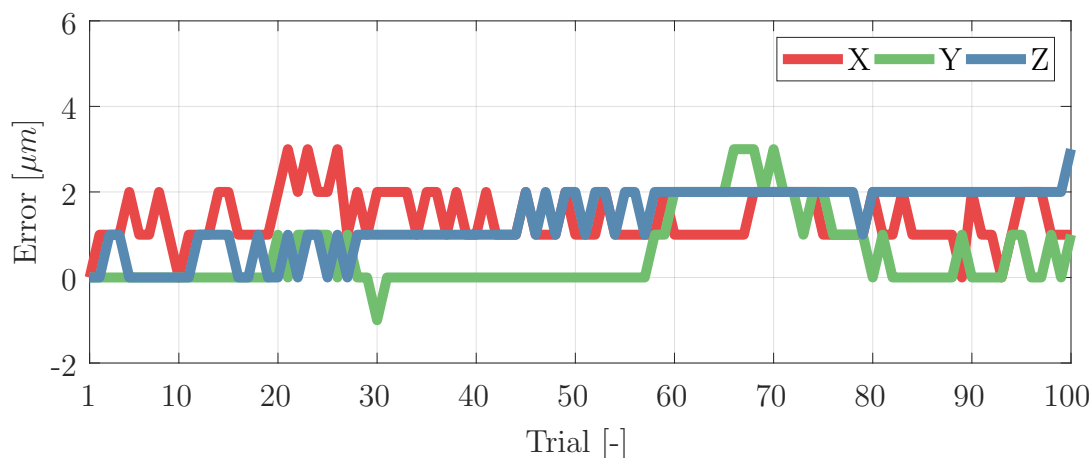
### 5.3.2 Uncertainty of Thermal Error Measurement Cycle

To identify the uncertainty of the designed measurement cycle, described in Section 5.2 and shown in Figure 5.2, the procedure is repeated 100 times with interruptions of an ATC after each cycle. The sphere is positioned  $0.16 \text{ m}$  eccentric of the center of rotation.

The results of this experiment are shown in Figure 5.5. The feed rates of the axes are reduced, to minimize the induced heat load by the motors. Therefore, the investigation



(a) Repeated measurement of the relative position change of a sphere without ATC



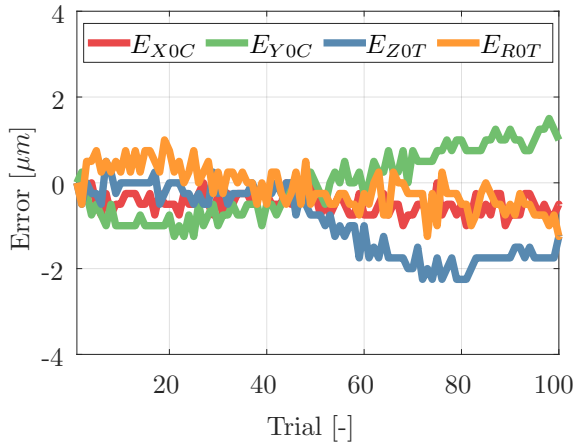
(b) Repeated measurement of the relative position change of a sphere with ATC

**Figure 5.4:** Repeated measurement of the relative position change of a sphere with a touch probe, for (a) without ATC and (b) with ATC.

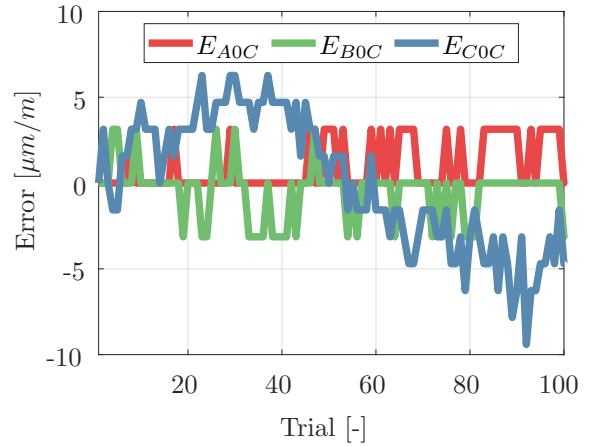
took approximately 8 hours. Because of the long measurement time, long-term drifts are observed in the measurement data. It can be assumed that the root of cause is a thermal drift of the machine tool induced by the changing environmental conditions. Thus, to remove this thermal effect, each error is filtered with a high-pass filter with a cutoff frequency of 0.000278 Hz. Therefore changes slower than  $1 \text{ h}^{-1}$  are filtered out. With this limit the slow changes of the day/night cycle of the environment are filtered out and the slowly reacting internal heat sources can be damped. The results of this filtering technique are shown in Figure 5.5c and 5.5d. The extended uncertainty of each error is calculated from these results and listed in Table 5.4. Theoretical measurement resolutions are also calculated from the machine axes resolutions and the sphere position  $d = 0.32 \text{ m}$  according to the Equations 5.4 - 5.10 and listed in Table 5.4.

Error	Extended uncertainty U (k=2)	Measurement resolution
$E_{X0C}$	$0.4 \mu\text{m}$	$0.25 \mu\text{m}$
$E_{Y0C}$	$0.5 \mu\text{m}$	$0.25 \mu\text{m}$
$E_{Z0T}$	$0.4 \mu\text{m}$	$0.25 \mu\text{m}$
$E_{R0T}$	$0.6 \mu\text{m}$	$0.25 \mu\text{m}$
$E_{A0C}$	$2.3 \mu\text{m/m}$	$3.125 \mu\text{m/m}$
$E_{B0C}$	$2.5 \mu\text{m/m}$	$3.125 \mu\text{m/m}$
$E_{C0C}$	$2.6 \mu\text{m/m}$	$1.5625 \mu\text{m/m}$

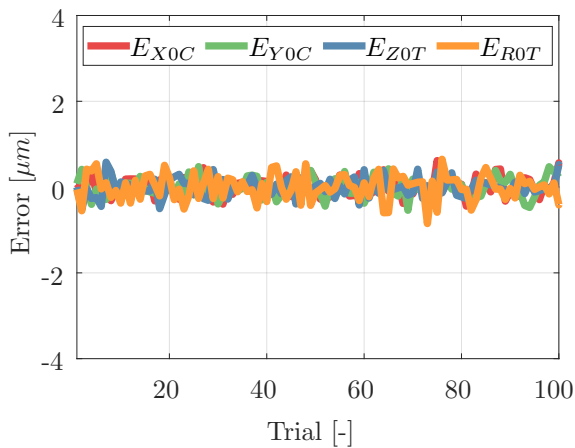
**Table 5.4:** Extended uncertainties and resolutions for the measurement of position and orientation errors of a C-axis with a touch probe. The sphere is located 0.16 m from the center of rotation.



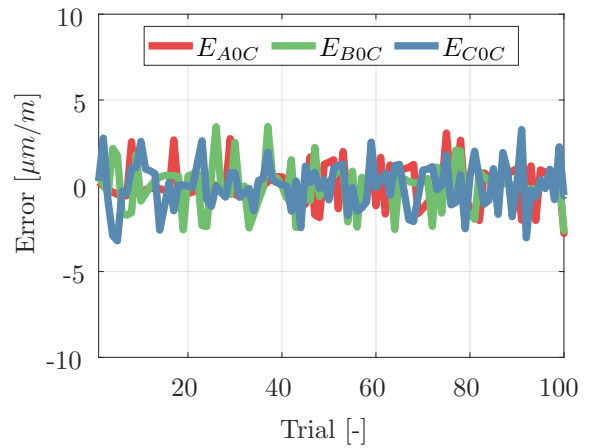
(a) Repeated measurement of linear thermal errors.



(b) Repeated measurement of angular thermal errors.



(c) High-pass filtered measurement of linear thermal errors.



(d) High-pass filtered measurement of angular thermal errors.

**Figure 5.5:** Repeated touch probe measurements of the relative position and orientation error of the rotary axis C with ATC. No filter in (a) & (b), High-pass filter in (c) & (d).

## 5.4 Thermal Error Measurement with On-machine Measurement Cycle

To test the on-machine measurement cycle during machining conditions and to verify the functionality of the measurement procedure two experiments are performed. In each experiment randomly generated rotation speeds of the rotary axis C are used to generate a fluctuation of the internal heat source. The experiments lasted for approximately 72 hours, where every 5 minutes a measurement of the five sphere positions is performed. The schematic of the measurement procedure is shown in Figure 5.6. The difference between both experiments is, that one is run without MWF and one is with MWF. The fluid is delivered through articulated tubes onto the machine table, where it covers a large share of the body of the rotary and swiveling axes. The whole on-machine procedure is time and accuracy optimized, so that the measurement cycle, illustrated in Figure 5.2, takes only 95 s including two ATC's of the touch probe. Additionally to the plots of the position and orientation errors also three representative temperatures are shown. The environmental temperature, the workspace or the MWF temperature and the temperature difference between inlet and outlet of the coolant for the rotary axis unit. These three temperatures characterize all the main heat sources, C-axis motor, environment and MWF. The results

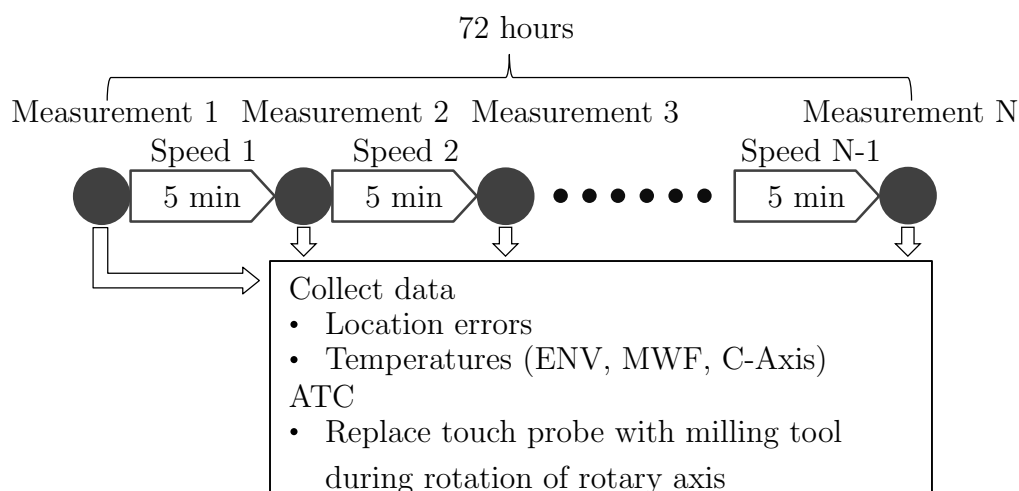


**Figure 5.6:** Schematic of the measurement procedure for thermal error measurement with on-machine measurement cycle.

of the two measurements are shown in Figure 5.7 without MWF and in Figure 5.8 with MWF.

Since the touch probe and the R-Test cannot be mounted simultaneously in the machine tool a sequential analysis has to be performed. Due to different environmental and starting conditions only a qualitative assessment is performed. In comparison with previous mea-

measurements performed by Mayr et al. [81] on the same machine tool with an R-Test device a similar behavior in both magnitude as well as rate and direction of change of the position and orientation errors is observed. Additionally no measurable influence of the MWF on the repeatability of the measurement is detected. Therefore, it can be concluded that the on-machine touch probe measurement system designed in this chapter is functional for the measurement of thermally induced position and orientation errors of a rotary axis.

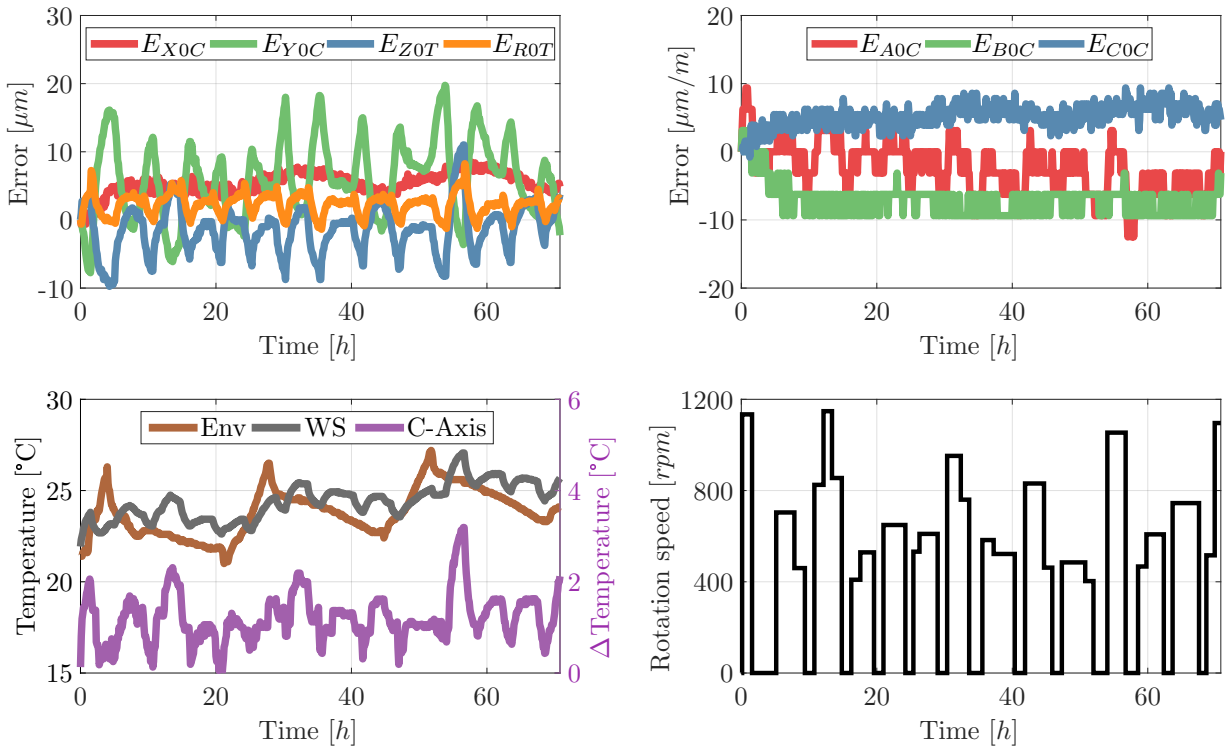


**Figure 5.7:** Measured thermal position and orientation errors of a C-axis with a touch trigger probe with corresponding rotational speed of the rotary axis and measured temperatures (Env: Environment, WS: Working space, C-axis: Difference Inlet/Outlet). Measurement interval: 5 min.

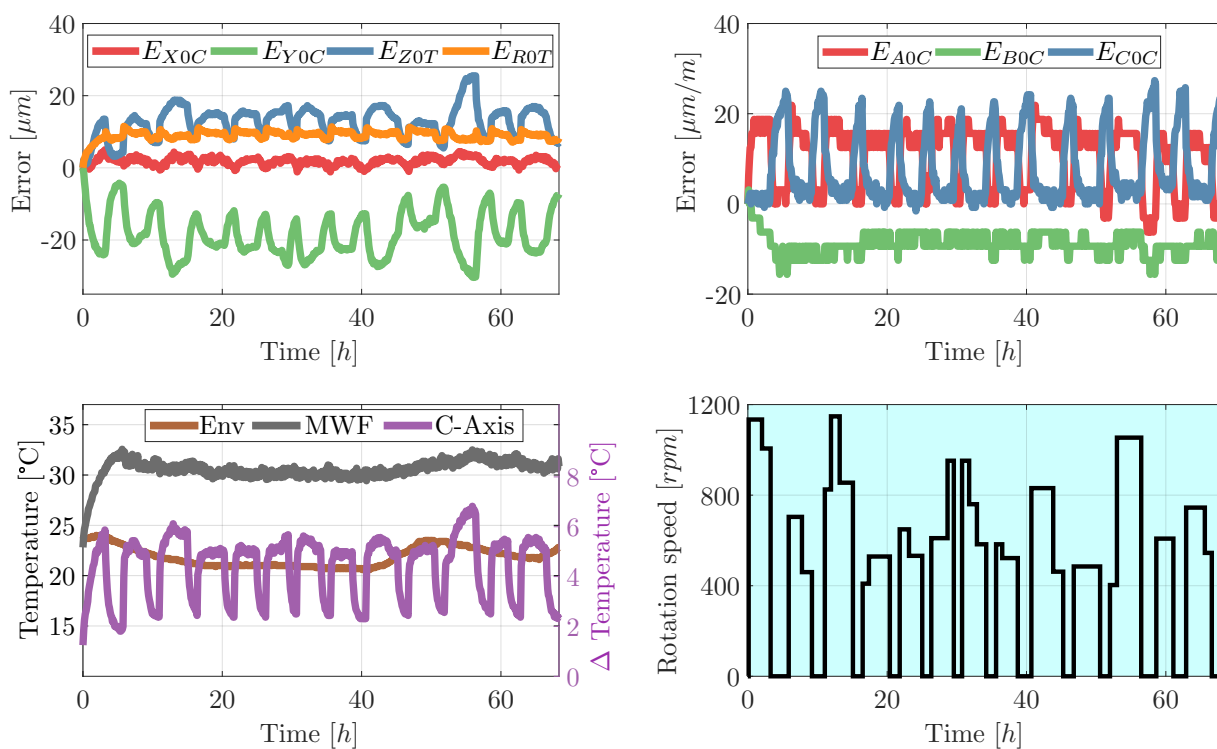


**Figure 5.8:** Measured thermal position and orientation errors of a C-axis under the influence of MWF with a touch trigger probe with corresponding rotational speed of the rotary axis and measured temperatures (Env: Environment, MWF: Metal working fluid, C-axis: Difference inlet/outlet). Measurement interval: 5 min.





## Chapter 6

# Thermal Adaptive Learning Control

In this Chapter the ARX modeling approach presented in Chapter 4 and the on-machine measurement cycle introduced in Chapter 5 are combined to predict and compensate the occurring thermal errors of a 5-axis machine tool.

Ideally the residual errors between the ARX model and the actual machine tool will approach zero. However, the predicted system behavior is always different from the real one. At the same time, the actual machining conditions may not be identical to the machining conditions used to derive the ARX model, which leads to model uncertainties. This can cause problems especially for small batch productions, where the sequence of manufacturing processes changes frequently as do the direction and rate of change of thermal effects. Due to statistical uncertainties, assumptions in the model and the constantly changing boundary conditions, the error models derived from pre-process calibration are not necessarily accurate enough in the long term. They need to be verified and updated iteratively as the machine tool is continually used. The approach presented in this Chapter consists of a newly developed thermal adaptive learning control (TALC) to predict and compensate time and load-varying thermal errors. By adopting current boundary and machining conditions obtained from various sensors, the parameters of the error model can be adapted to the present state.

In the first two sections of this chapter the TALC methodology and the ARX model estimation are introduced. In the third section a sensitivity analysis of the pre-defined measurement and modeling parameters is performed to find the most influential ones and to optimize the TALC approach to achieve good accuracy results while maintaining a sufficiently high productivity rate. In the last section two experiments are presented, that show the results of a compensation with TALC on a real 5-axis machine tool. One experiment validates the long-term robustness under varying heat loads, while the second experiment shows the capability of the TALC approach to learn and adapt under the influence of fast changing boundary conditions.

## 6.1 Methodology

The goal of TALC is to reduce the thermally induced TCP deviations and to enhance the long-term accuracy of the machine tool in both material removal as well as on-machine inspections. The presented procedure is capable of adapting its model parameters to changes in the process and boundary conditions. This methodology is also able to adjust the on-machine measurement time intervals according to a predefined limit to ensure a high productivity at a controlled uncertainty rate of the ARX model.

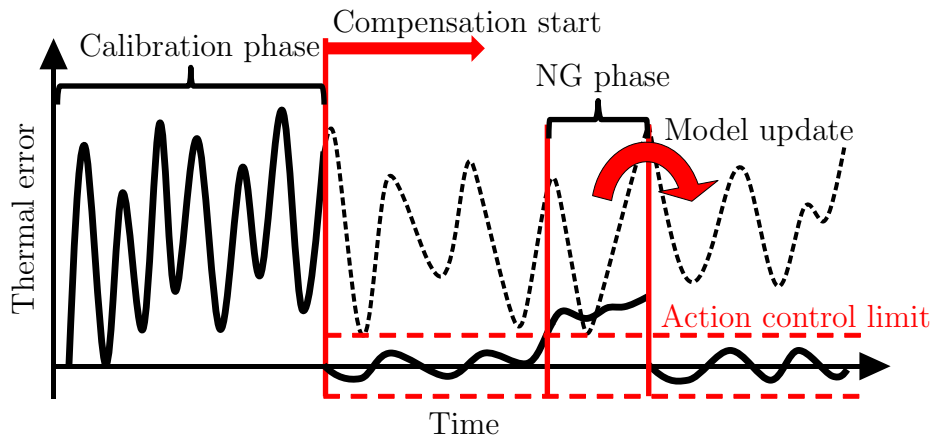


**Figure 6.1:** Illustration of the TALC methodology.

Figure 6.1 shows an illustration of the methodology of the TALC approach. An initial calibration phase at the beginning of the measurement, where thermal TCP deviations and relevant thermal related sensor information is captured, is used to obtain the first set of parameters for the ARX model of the machine tool. To measure the TCP deviations, the on-machine measurement cycle, introduced in Chapter 5, is used. This step is just required once, afterwards the already existing compensation model can be used, when starting the production run. After the calibration phase the frequency of the on-machine measurements is drastically reduced since the model is capable of predicting the thermal deviations and compensate them on the machine tool in real-time. Every time an on-machine measurement is performed, the residual thermal errors are compared to a defined action control limit. If one error exceeds this threshold the No-Good (NG) phase is entered and the measurement frequency is increased for a certain time followed by an update of the model parameters. To update the ARX model, the obtained data since a specified point in time is used.

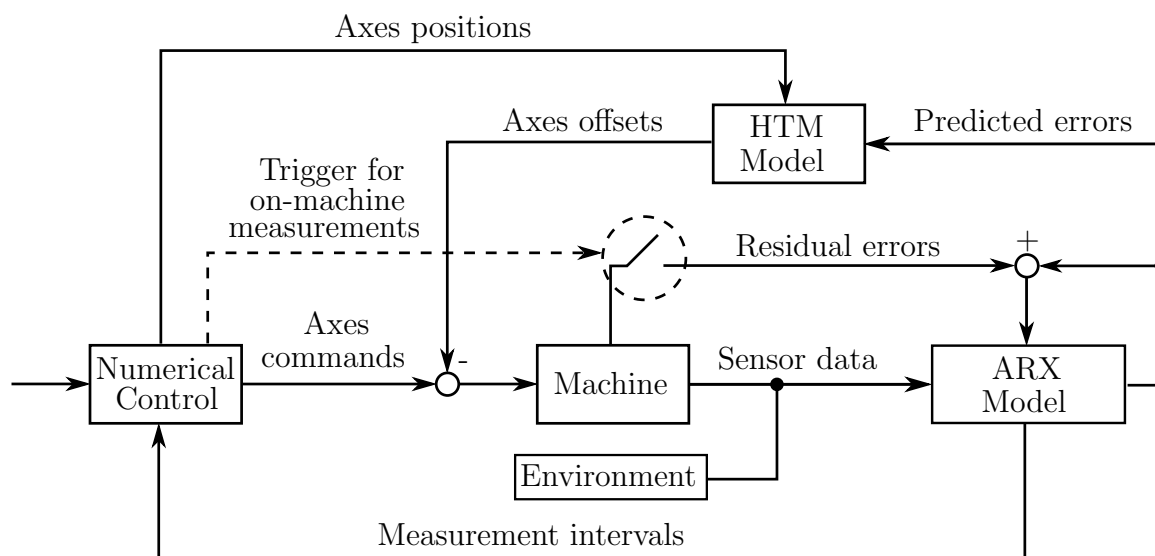


**Figure 6.2:** Schematic of the TALC information flow. The dashed line represents the trigger for on-machine measurements, which give access to the residual thermal errors only at discrete times. The measurement intervals are adaptively adjusted by the ARX model

Figure 6.2 shows a schematic diagram of the ARX methodology. To predict the thermal errors, the ARX model is capable of using multiple temperatures on and around the machine structure as well as control data of the NC to compute the occurring position and orientation errors. The outputs of the ARX model, the predicted errors, are compared with the on-machine measurements obtained by the touch probe at discrete points in time. This comparison is used to periodically update the parameters of the thermal error model. To adapt to changing working conditions the approach is capable of modifying the NC-Code, to adjust the time intervals between on-machine measurements. This allows to dynamically adapt the amount of measurements to maximize the productivity at a stable level of accuracy. To transfer the obtained thermal position and orientation errors of the C-axis into movements of the linear axes an axis error model is used based on the rigid body assumption and the use of homogeneous transformation matrices (HTM), see Section 6.4 for detailed information. The inputs of the HTM model are the predicted errors and the axis position of the machine tool and the outputs are offset that shift the axis origin in the opposite direction of the occurring thermal error.

The computation of both models is carried out on a PC, which is connected via Ethernet with the CNC of the machine tool. The communication between PC and CNC is realized via FOCAS2 (Fanuc Open CNC API Specification Version 2), which is a transmission protocol provided by the CNC manufacturer FANUC [73]. It allows to access the CNC by

a PC. Thereby, many parameters allocated by the CNC can be processed on the PC in near-real time and coordinate offsets can be returned from the PC to the CNC for each axis. This feature is used in this thesis to read the current nominal axis positions  $\hat{X}$ ,  $\hat{Y}$ ,  $\hat{Z}$  and  $\hat{B}$ . These positions are necessary for the compensation of position dependent errors as well as for the coordinate transformation for the swiveling axis B. Additional information as for example the drive power or the MWF state can be used as inputs for the ARX model. The temperature data is directly processed on the PC and therefore independent from the communication with the CNC.

## 6.2 Adaptive ARX Model Estimation

As illustrated in Figure 6.1, the TALC procedure starts with a calibration phase, where on-machine measurements are performed at a defined time interval. After the calibration phase, the compensation starts and the process intermittent probing frequency is reduced, until the predefined control action limit is surpassed, then the frequency is increased. Due to the possibility to adapt the measurement intervals, the identified ARX model structure, needs to be capable of handling a large amount of different sample rates. Ljung [77] described systems with non-constant sample rates as time-varying systems. For such time-varying systems the ARX model structure, as introduced in Section 4.1, cannot be used. Advantageously, the ARX structure has many useful specifications and shows a robust modeling approach for thermal errors of machine tools. Therefore, an extension of the approach presented in Chapter 4 is developed that is able to deal with changing sample rates using an ARX model structure.

### 6.2.1 Calibration Phase

Before an ARX model can be generated information about the system has to be gathered. Therefore the initial set of parameters is calculated after the calibration phase, as indicated in Figure 6.1. The amount of data needed to estimate the ARX model parameters is dependent on the amount of used inputs as well as on the order of past in- and outputs. Therefore it is crucial to limit the initial number of inputs and the maximum model order for each in- and output. To calculate the minimum time span of the calibration phase the sum of all the maximum model orders is used. As an example, if 2 inputs with an order of  $n_{b1} = 5$  and  $n_{b2} = 10$  are chosen and the output is fed back with a time shift of  $n_a = 1$  this results in a minimum calibration time of 16 times the measurement time interval during the calibration phase, so with a usual interval of 5 minutes a minimum of 80 minutes is necessary. Since this is only the mathematical minimum to solve the system

of equations and the LSE is based on a statistical approach, the goodness of fit can be of lower quality. Therefore a second criteria is introduced. For each error it is checked if the matrix of time shifted in- and outputs has full rank. The rank of the matrix is calculated with the method of single value decomposition. The rank of the matrix is computed as the number of singular values that are larger than a set tolerance. By default, the tolerance is a function of the size of the matrix and the relative floating-point accuracy for the 2-norm of the matrix.

### 6.2.2 Start of Compensation

As explained in Section 4.1 the parameters of the ARX model are estimated with the LSE. For the first parameter calculation after the calibration phase the input data and error measurements are used. To avoid an over-fitting the data is separated in training and validation sets by a ratio of 60 % to 40 %. Since the TCP measurement is performed at a constant sample rate the estimated model shows a robust and accurate description of the thermal deformation of the TCP. After the first parameter estimation, a prediction of the occurring error is performed in the same time interval as the measurements during the calibration phase. Every prediction is saved and used as a shifted input for the estimation of the next thermal deviation. Every time an on-machine measurement is performed, the measured errors are saved instead of the predictions.

### 6.2.3 No-Good Phase

Following the calibration phase, the ARX model estimates the occurring thermal errors and sends the axes offsets to the machine tool, see Figure 6.2. The on-machine measurement interval is drastically decreased to increase the productivity of the machine tool. For each position and orientation error a predefined action control limit can be chosen that is checked after every on-machine measurement. If one residual error exceeds the set threshold the NG phase is entered. In the NG phase the measurement frequency is increased for a defined number of measurements. The purpose of this phase is the gathering of a set of up-to-date TCP measurements and the corresponding information of the environment and the machine tool.

The duration of this phase is either set statically or can be defined as dynamic parameter, that adapts depending on the amount of previous measurements since the last ARX model parameter update.

### 6.2.4 ARX Model Parameter Update

Each NG phase is followed by an immediate parameter update of the ARX model. It is also possible to define a time limit for the parameter update interval, just to guarantee an accurate estimation of the current thermal deviations. Since the amount of gathered data has increased since the first estimation of the model parameters the possibility of raising the maximum input order ( $n_b$ ) exists. Therefore a bigger time-shift of the different inputs is possible and thermal effects with slower time constants can be modeled. The model accuracy increases with each parameter update.

Since the sampling time of the on-machine measurements and the model prediction are significantly different, the amount of predictions surpasses the amount of measurements shortly after the start of the compensation. A new set of parameters should be computed on the basis of measurements and not on predictions. By solving the LSE with utilizing mainly predictions, the model parameter estimation would result in the same or a very similar set of parameters that the previous predictions are based on. It is therefore desirable, that data with only predicted errors have less influence in the LSE problem. This is approached with the method of WLSE instead of ordinary LSE. The WLSE criterion is defined in Equation (4.20). An additional benefit of this procedure is the elimination of drift effects since the prediction of new thermal errors depends on past system outputs and therefore replacing a predicted value by the corresponding measured data results in a state update of the model. The WLSE approach also offers the possibility to assign smaller weights to measurements that lay further in the past. This ensures the model reacts accurately to the prevailing situation and avoids an averaging effect over time.

## 6.3 Sensitivity Analysis

As pointed out in the previous section the performance of the TALC is highly dependent on a multitude of parameters. In this section an analytical investigation of those parameters is performed. Table 6.1 shows a list of the nine most influential parameters for the thermal compensation with TALC. As specified in the previous sections over the duration of an experiment the TALC approach can be divided in three phases, the calibration phase (CP), the compensation phase (Post CP) and the No-Good phase (NG).

For the sensitivity analysis, five out of these nine parameters are closer investigated, the ranges of the examined values are listed in Table 6.1. All logical combinations of those parameters are studied and therefore for one load case a total of 2'191 numerical simulation experiments need to be performed.

To handle the big amount of simulations a virtual experiment simulator is programmed

Parameter	Values
Calibration Phase (CP)	8.5/12/16/24/36/48/60 [h]
Measurement Interval (CP)	5 min
Measurement Interval (Post CP)	1/2/3/4/5/6/7/8/9/10/11/12/24/Inf [h]
Measurement Interval (NG)	5/10/15/20/25/30/Inf [min]
Action Control Limit	5 $\mu\text{m}$ resp. 15 $\mu\text{m}/\text{m}$
Nr. of measurements in NG	6/12/18/24/Inf [meas.]
Parameter Update Interval	8/16/24/32/40/48/56/64/72/80/88/96/Inf [h]
Maximum Output Order ( $n_a$ )	1
Maximum Input Order ( $n_b$ )	10

**Table 6.1:** Influential parameters for the TALC and the corresponding range for the sensitivity analysis.

that is able to perform a TALC analysis on basis of real machine tool measurements. The inputs for the simulation are the measured position and orientation errors as well as the corresponding influences from the environment and the machine tool. The simulator is capable of running multiple simulations in parallel, to improve the computational performance.

### 6.3.1 Experiments

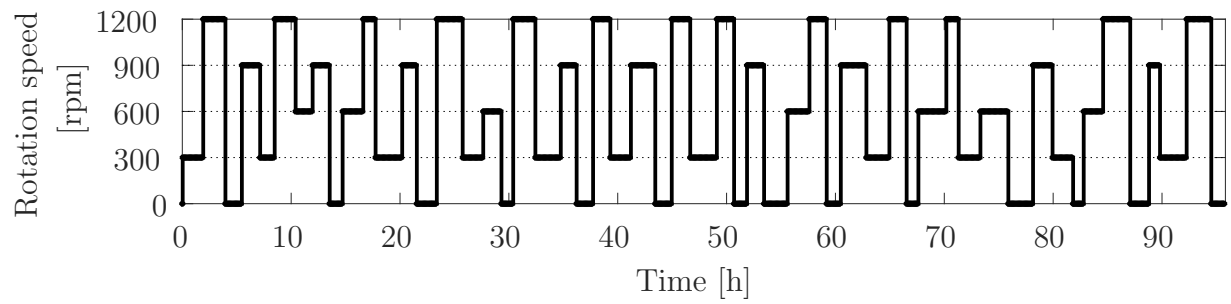
To test the dependability of the compensation quality on different influences, four real experiments are performed on the DMG Mori NMV 5000 DCG 5-axis machine tool. The different load cases (A-D) for the experiments are depicted in Figure 6.3. To induce an alternating thermal load into the machine tool an arbitrary speed profile of the C-axis is performed to simulate a fast changing small batch production. In measurement D in addition to the arbitrary speed profile of the C-axis, the MWF supply through articulated tubes aiming at the working table is switched on and off during different time intervals. In experiment C the first 32 hours consist of an optimized speed pattern. The speed range is divided into steps of 300 rpm from 0 to 1200 rpm. Each possible combination of subsequent speeds is performed for a duration of 1.5 hours. This optimized pattern is followed by an arbitrary speed profile for a total of 104 hours.

The used inputs to model the thermal errors for the load cases A-C are chosen empirically based on previous measurements on this machine tool, see Mayr et al. [82]. The three chosen inputs are the change of the environmental temperature since the start of the experiment, the change of the working space temperature and the change of the temperature difference between the in- and outlet of the coolant for the C-axis. For the load case D the MWF temperature at the outlet of the nozzle is used instead of the working space temper-

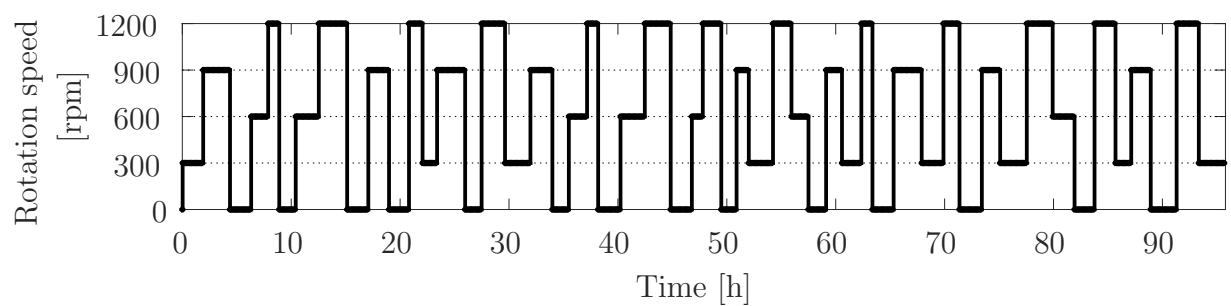
ature. During the phases, where no MWF is introduced in the working space, the sensor measures the working space temperature. The recorded temperature changes during the four experiments are shown in Figure 6.4.

The most dominant thermal errors of the machine tool under investigation for these specific load cases are the error of the position of the C-axis in Y-direction  $E_{Y0C}$ , the position error of the functional table surface in Z-axis direction  $E_{Z0T}$  and the radial error of the functional surface table  $E_{R0T}$ . These three thermal errors are shown in Figure 6.5 for each load case A-D.

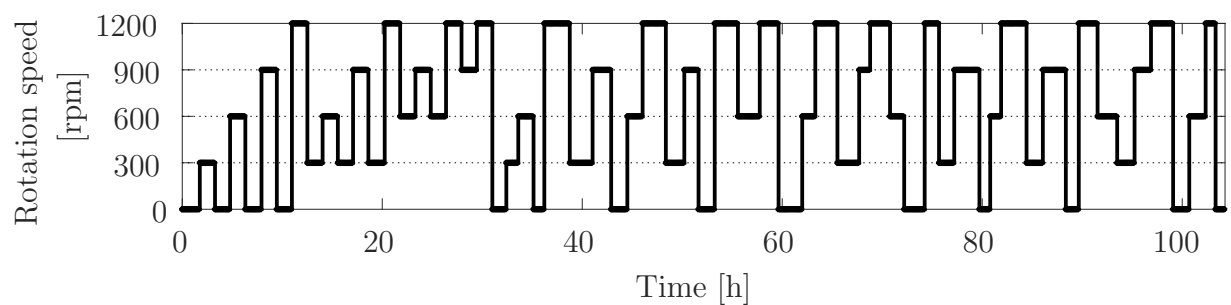




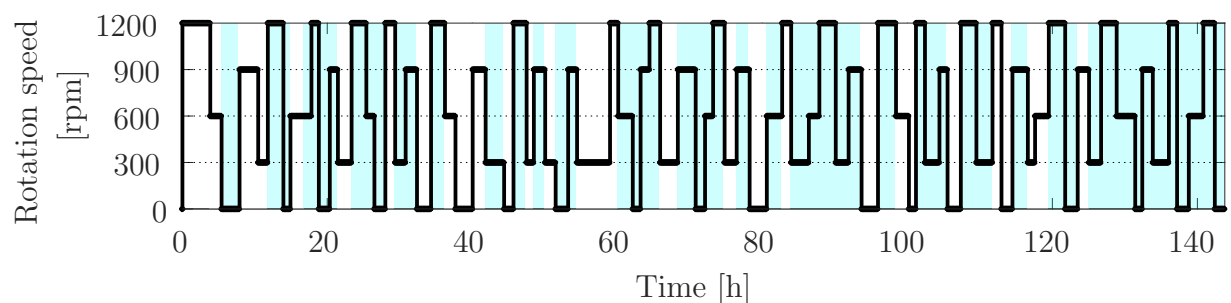
(a) Random speed pattern of the C-axis for a duration of 96 hours. No MWF.



(b) Random speed pattern of the C-axis for a duration of 96 hours. No MWF.

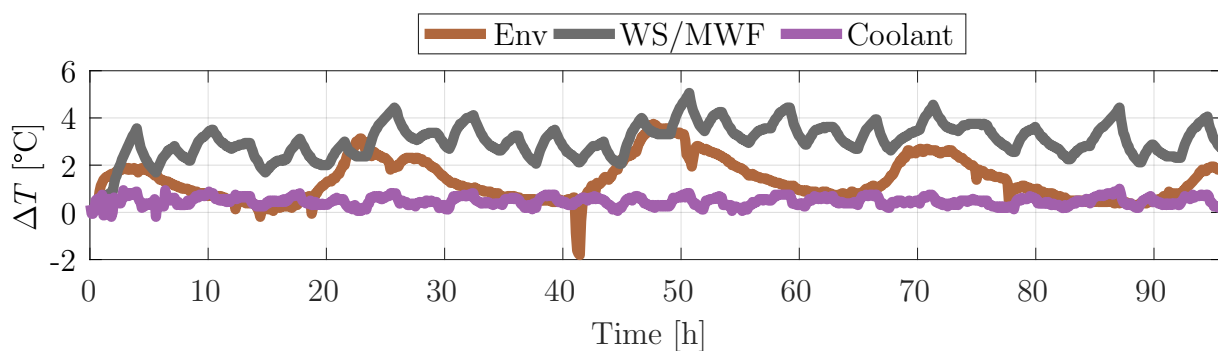


(c) Random speed pattern of the C-axis for a duration of 104 hours. No MWF.

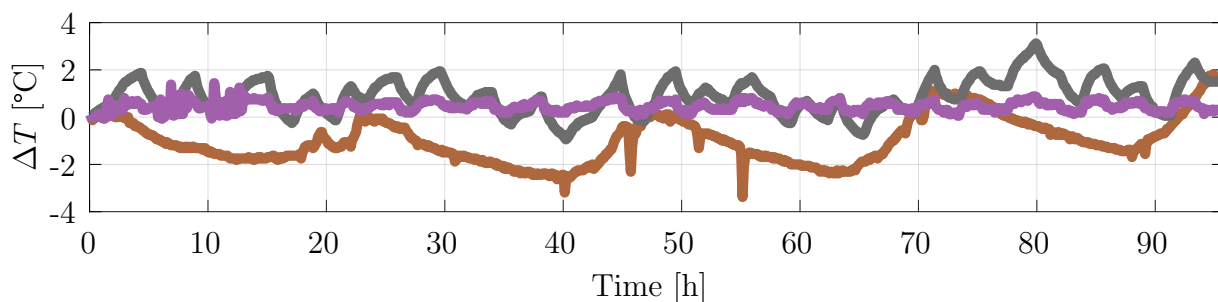


(d) Random speed pattern of the C-axis for a duration of 144 hours. With MWF supply times (cyan).

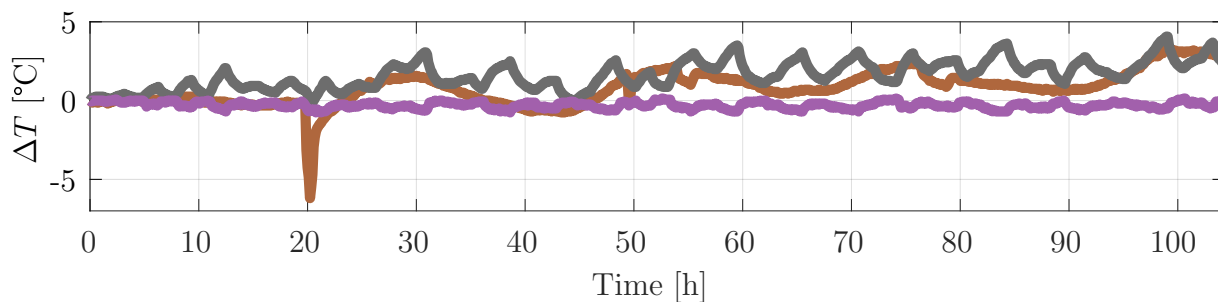
**Figure 6.3:** Four different load cases with varying rotational speed of the C-axis and changes of MWF states. The cyan areas depict the time intervals of switched on MWF supply.



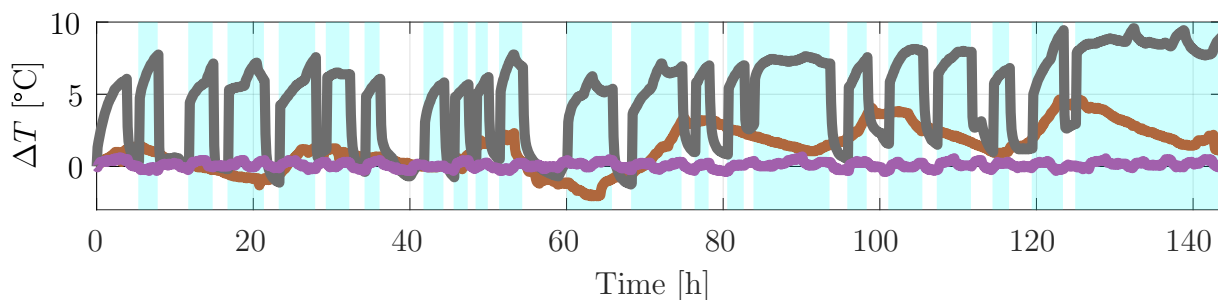
(a) Relative temperature change for load case A for a duration of 96 hours. No MWF.



(b) Relative temperature change for load case B for a duration of 96 hours. No MWF.

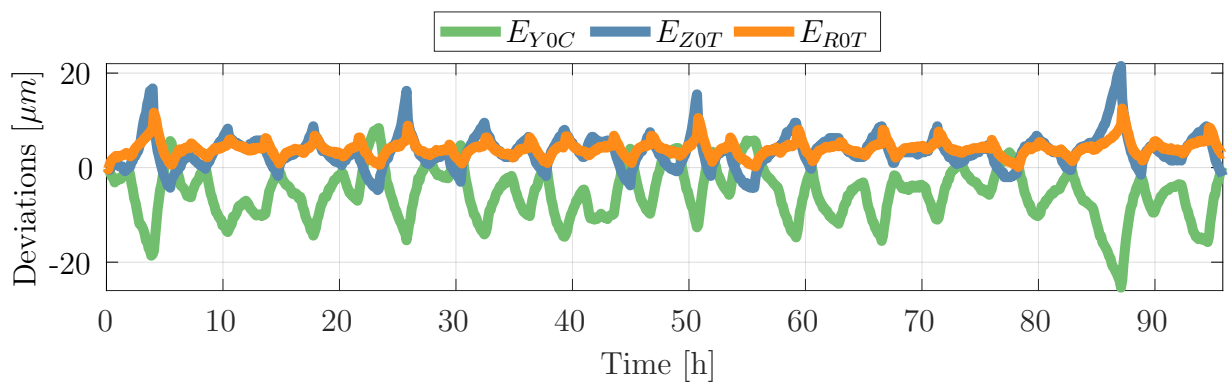


(c) Relative temperature change for load case C for a duration of 104 hours. No MWF.

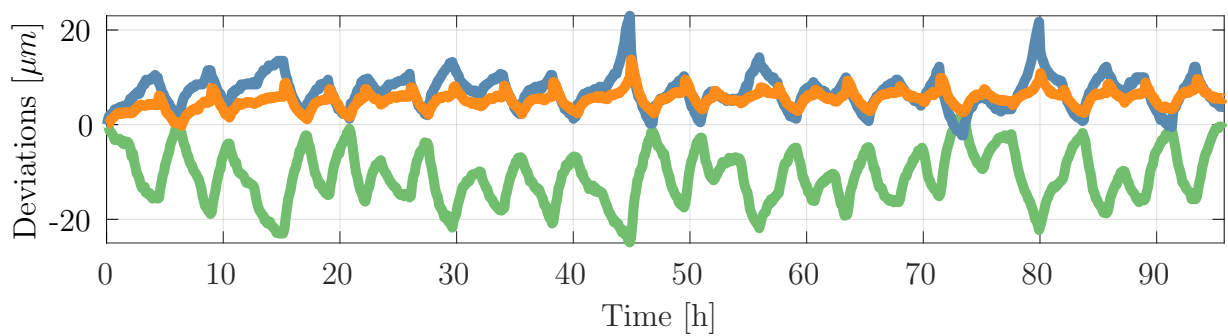


(d) Relative temperature change for load case D for a duration of 144 hours. With MWF supply times (cyan).

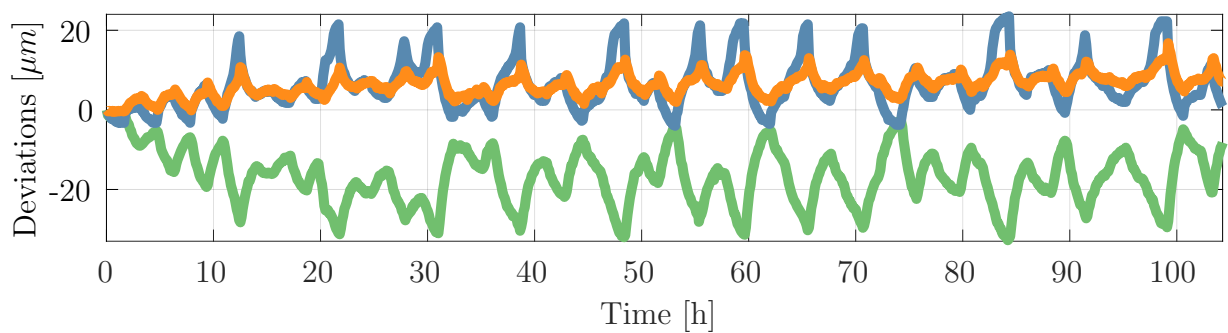
**Figure 6.4:** Temperature changes of the environment (Env), the workspace (WS) respectively the metal working fluid (MWF) and the difference of the inlet and outlet of the C-axis coolant due to the corresponding load cases. The cyan areas depict the time intervals, where the MWF supply is switched on.



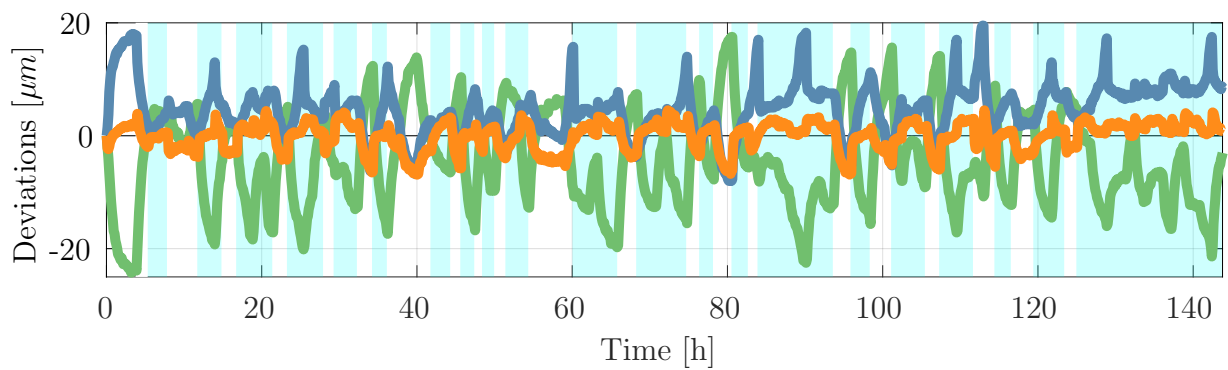
(a) Dominant linear thermal errors for load case A for a duration of 96 hours. No MWF.



(b) Dominant linear thermal errors for load case B for a duration of 96 hours. No MWF.



(c) Dominant linear thermal errors for load case C for a duration of 104 hours. No MWF.



(d) Dominant linear thermal errors for load case D for a duration of 144 hours. With MWF supply times (cyan).

**Figure 6.5:** Most dominant linear thermal errors due to the corresponding load cases. The cyan areas depict the time intervals, where the MWF supply is switched on.

### 6.3.2 Quality Indicators

To evaluate the performance of the ARX model five different indicators are used, to compare the fit to the occurring thermal errors. The four indicators introduced in Section 4.2.3 to compare the different model structures are again utilized to analyze the parameter sensitivity. In addition the time consumed by on-machine measurements in relation to the duration of the experiment is used as an indicator for the productivity of the machine tool. This measure is  $Q_{Prod}$  and calculated as follows:

$$Q_{Prod} = \left(1 - \frac{N \cdot t_M}{t_{total}}\right) \cdot 100\% \quad (6.1)$$

where  $t_M$  stands for the measurement time of a single on-machine measurement, which takes 95 seconds for the machine tool under investigation and the on-machine measurement cycle introduced in Chapter 5.  $t_{total}$  stands for the total duration of the experiment and  $N$  corresponds to the total amounts of measurements performed. All the parameters listed in Table 6.1 are directly influencing the amount of measurements  $N$ . The quality indicator  $Q_{Prod}$  used here is no real measure of machine productivity, since a 100% availability is assumed. In reality the on-machine measurements can also be performed during non-productive times, as for example shift changes, operator breaks, between setups, etc.

### 6.3.3 Results

Based on the four load cases A-D and the combinations of TALC parameters, see Table 6.1, a total of 8'764 simulations are performed. The outputs of each simulation are the fits of the seven measured thermal position and orientation errors of the C-axis. These seven errors are further grouped in linear and angular errors, whereas linear errors are  $E_{X0C}$ ,  $E_{Y0C}$ ,  $E_{Z0T}$  and  $E_{R0T}$ , the angular errors are  $E_{A0C}$ ,  $E_{B0C}$  and  $E_{C0C}$ . For every thermal error the five quality indicators are evaluated. In combination with all the varied parameters, this results in too many degrees of freedom for visual inspection in a single plot. Therefore, in this section, a sequential analysis of the different influences is shown.

To analyze the influence of the length of the calibration phase on the  $E_{SMAP}$  a box plot is shown in Figure 6.6. The figure shows the average  $E_{SMAP}$  of all seven thermal errors. The box plot consists of the median, the 25th respectively 75th quantile as well as outliers above and below the quantiles. It can be seen that the length of the CP has an influence on the  $E_{SMAP}$  and especially on the span of the quantiles. Nevertheless, the impact on the median value is not significant. It is also visible, that the  $E_{SMAP}$  values differ from load case to load case, so that not the same quality of fit can be expected for different thermal

load cases of the machine tool. Especially the load case of changing MWF intervals shows, that this drastic change of boundary conditions is harder to compensate for. It can be concluded, that the length of the CP itself is not the decisive factor for the quality of the fit. Also with short CP's a potential reduction of the thermal errors of more than 70 % can be achieved.

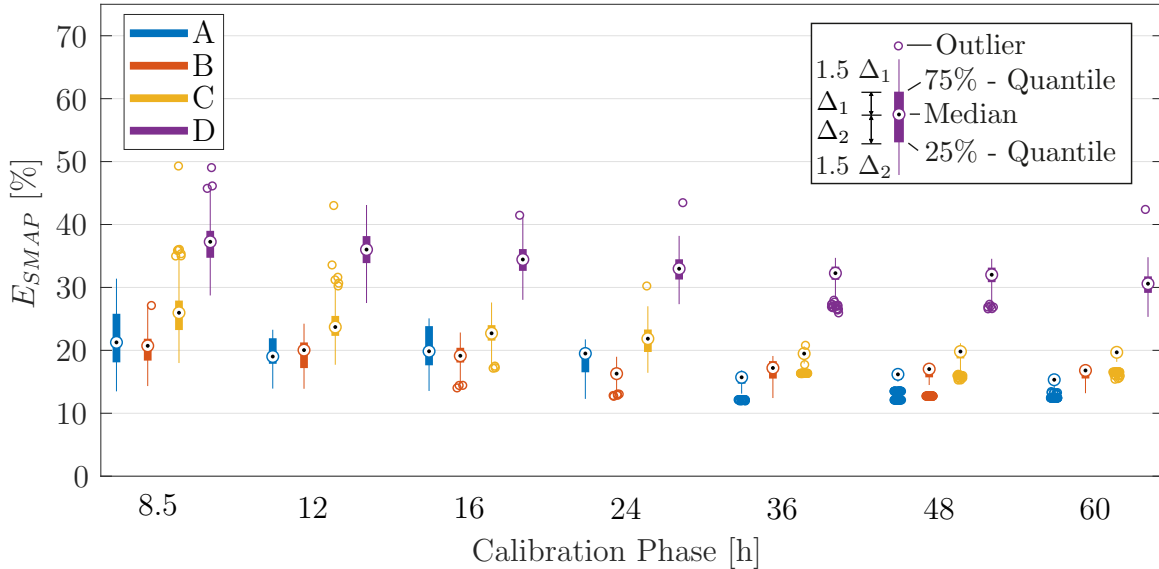


**Figure 6.6:** Boxplot of averaged  $E_{SMAP}$  of the thermal deviations for all load cases versus the length of the calibration phase. The letter A, B, C and D correspond to the load cases in Figure 6.4 and Figure 6.5.

For a quantitative comparison the quality criteria 99<sup>th</sup> Percentile (P99) for the different CP lengths is illustrated in Figure 6.7. Whereas a separate evaluation of the linear and angular thermal position and orientation errors is performed, due to the physical unit mismatch. The plots show that 99 % of the residual errors lay under  $10 \mu\text{m}$  respectively  $10 \mu\text{m}/\text{m}$  for a length of the CP of 24 hours or longer. For shorter CP's the variance is drastically increasing, especially for the linear errors. Another observation that the evaluation with  $E_{SNAP}$  does not show, is the fact, that in load case C the short CP's can lead to big residual errors. This can be explained by the nature of the speed profile used for the load case C. In the first 32 hours each possible combination of subsequent speeds is performed, see Figure 6.3c. Therefore the statistical variability of the induced excitation is not big enough for the generation a robust model for short CP phases. Also for longer CP's the load case C does not show a superior fitting behavior, therefore it can be concluded, that this artificial speed profile does not have any advantages over the arbitrary speed profile approach used in the other load cases.

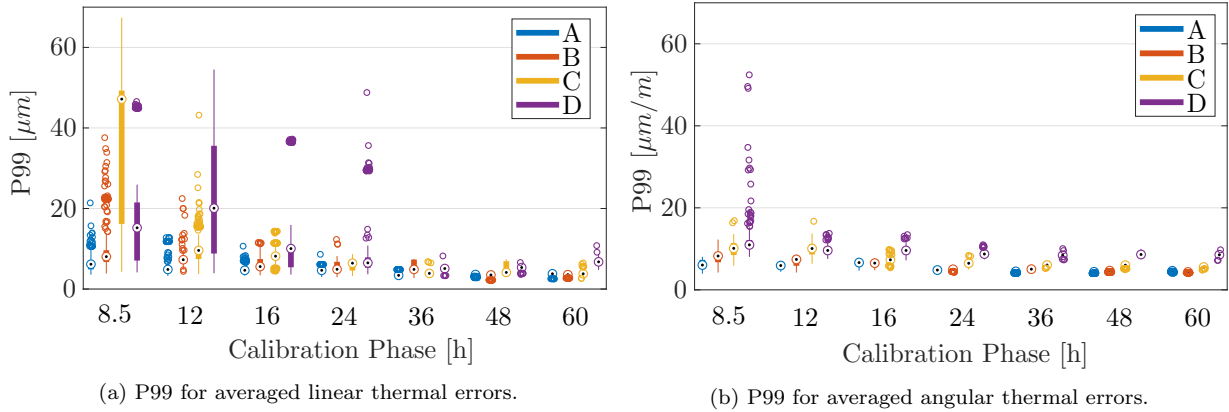


**Figure 6.7:** Box plot of averaged 99<sup>th</sup> Percentile (P99) of the thermal deviations for all load cases versus the length of the calibration phase. The averaged linear thermal errors are represented in (a) and the angular thermal errors in (b).

For all of the performed simulations during the CP every 5 minutes an on-machine measurement is performed until the first set of model parameters is calculated. Following this phase the measurement frequency is drastically decreased to increase the productivity. Therefore long measurement intervals would be beneficial for high volume productions. In Figure 6.8 the influence of the measurement interval after the CP on the  $E_{RMS}$  is illustrated by a box plot for all four load cases. Once again the median value is mainly not influenced by this parameter. The variance on the other hand decreases with increased measurement frequency and therefore reduces the influence of the other parameters. This can be explained when looking at the combination of short CP and long measurement interval, which will lead to an insufficient amount of data to compute a robust model, but if the CP is chosen already sufficiently long, than additional measurements may not influence the result as much. Therefore the relation between CP length and measurement interval has to be investigated more thoroughly.

All the parameters listed in Table 6.1 have not only an influence on the estimation capability but also on the productivity  $Q_{Prod}$ . Therefore a detailed analysis of the impact of  $Q_{Prod}$  on the 99<sup>th</sup> percentile is shown in Figure 6.9. The scatter plot shows that with increasing  $Q_{Prod}$  the variation of the P99 is growing drastically. A higher  $Q_{Prod}$  corresponds to fewer measurements over time and thereby fewer information for the TALC. It is also visible, that there is a remarkable difference in the four experiments and between the linear and the angular errors. It appears that for the angular errors sufficient fit quality can be achieved even when performing less measurements, whereas for the linear errors a certain amount of measurements need to be performed. Nevertheless the figure also shows, that with the right combination of parameters a low residual error and a high  $Q_{Prod}$  can be achieved.

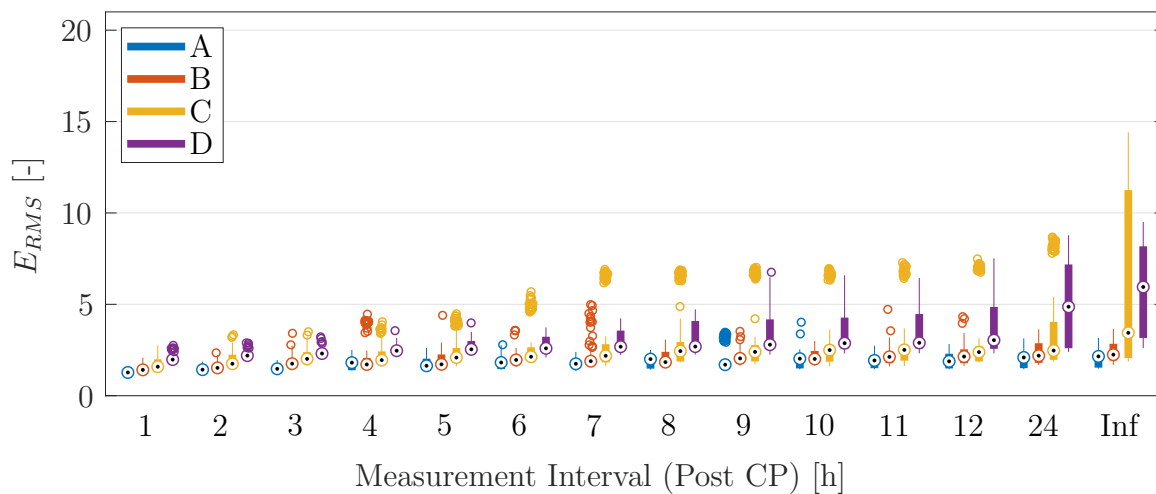


**Figure 6.8:** Box plot of averaged  $E_{RMS}$  of the thermal deviations for all load cases versus the length of the measurement interval after the CP. The interval length "Inf" indicates experiments where no measurements are performed in the Post CP.

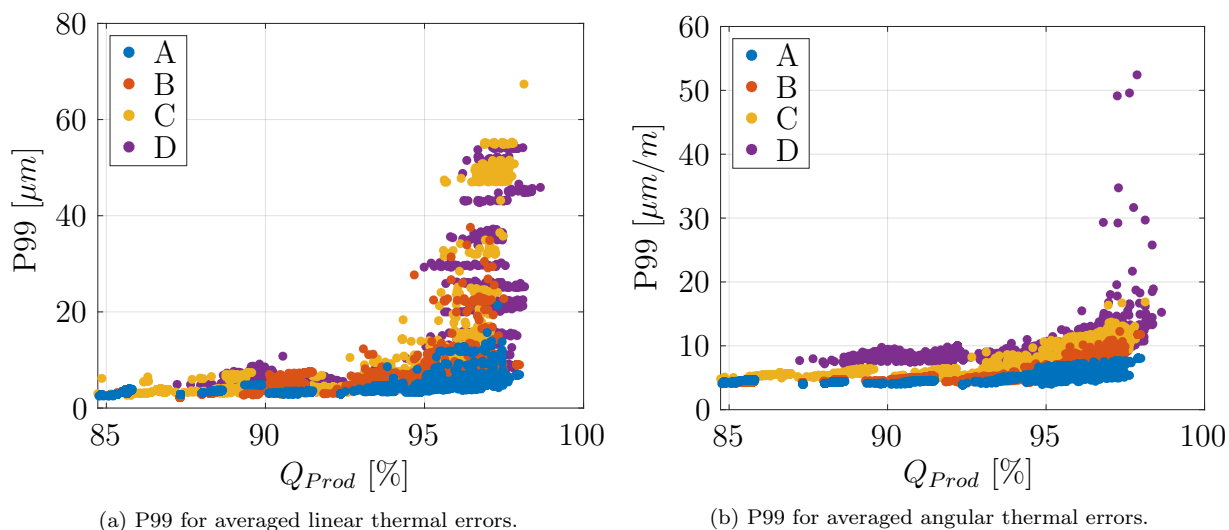


**Figure 6.9:** Scatter plot of averaged 99<sup>th</sup> Percentile  $P99$  of the thermal deviations for all load cases versus the productivity  $Q_{Prod}$ . The averaged linear thermal errors are represented in (a) and the angular thermal errors in (b).

### 6.3.4 Optimal Parameter Estimation

The parameter study showed that especially the quality indicator  $P99$  is very useful since it still contains a physical relation and one can directly relate the corresponding impact on a machined workpiece. Additionally, the reduction of the free parameters to the indicator  $Q_{Prod}$  can simplify the problem and provides a closer industrial indicator for the trade-off between accuracy and productivity. Table 6.2 shows the parameters for the four load

cases that result in the smallest value of  $P99_{lin}$ . As expected the potential fitting quality improves, for long CP's and short measurement intervals, but the  $Q_{Prod}$  is drastically reduced. It can also be seen, that values of  $P99_{lin}$  lower than  $2.23 \mu m$  can not be achieved. This shows the achievable quality of the TALC for this specific machine tool and the chosen on-machine measurement cycle. A possible explanation for this limit is the limited resolution of the machine tool axes as well as the repeatability of the measurement cycle.

Load case	CP	Interval	NG Meas.	NG Interval	$P99_{lin}$	$Q_{Prod}$
	[h]	[h]	[-]	[min]	[ $\mu m$ ]	[%]
A	60	2	24	5	2.52	84.77
B	48	1	12	5	2.23	87.32
C	60	1	6	20	2.64	85.77
D	36	1	6	5	3.28	91.98

**Table 6.2:** Sets of parameters for the load cases A-D, that result in a minimum value of  $P99_{lin}$  for the averaged linear thermal errors.

To find a more balanced set of parameters for the TALC approach the following criterion is introduced:

$$\max(Q_{Prod}) \quad \forall \quad \underline{P99}_{lin} < X \quad (6.2)$$

Equation (6.2) states, that the optimal set of parameters results in a fit, where 99% of the residual linear errors lay below  $X \mu m$  and of those parameters the set with the highest productivity  $Q_{Prod}$  is chosen.

Figure 6.10 shows the resulting maximum  $Q_{Prod}$  for the evaluation of the Equation (6.2) for different  $X$  as limits for the value  $P99_{lin}$ . The figure shows, that for  $P99_{lin}$  bigger than  $6 \mu m$  no drastic increase in  $Q_{Prod}$  is visible. With values for  $P99_{lin}$  smaller than  $6 \mu m$  a productivity  $Q_{Prod}$  of more than 96.7% can be achieved for all four load cases for a set action control limit of  $5 \mu m$ . Also since the CP already reduces the maximum achievable  $Q_{Prod}$  for these load cases with limited experimental duration, values above 97% are not achievable with reasonable fitting qualities, this can also be seen in Figure 6.9.



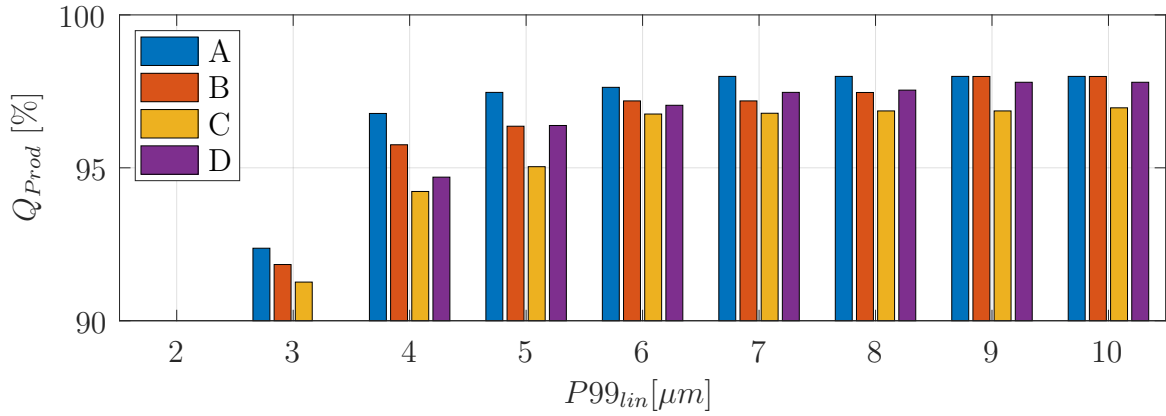


**Figure 6.10:** Evaluation of Equation 6.2 for different limits of  $P99_{lin}$  showing the corresponding maximum achievable productivity  $Q_{Prod}$ .

To obtain reasonable sets of parameters, Equation (6.2) is evaluated with  $X = 5 \mu m$ , since the action control limit for the linear thermal errors is set to the same value. The resulting sets are listed in Table 6.3. For all load cases a different set of parameters is found, that satisfies the preset conditions. The productivity  $Q_{Prod}$  surpasses for all load cases the 95% limit. It is notable; that in three cases the minimal investigated CP of 8.5 hours is sufficient, only in the load case C, where the first 32 hours are not following a random speed pattern, a longer CP is necessary to fulfill the defined criteria.

Load case	CP [h]	Interval [h]	NG Meas. [-]	NG Interval [min]	$P99_{lin}$ [ $\mu m$ ]	$Q_{Prod}$ [%]
A	8.5	10	12	30	4.72	97.47
B	8.5	2	6	30	4.87	96.36
C	12	2	18	5	4.98	95.04
D	8.5	3	12	10	4.93	96.38

**Table 6.3:** Set of parameters for the load cases A-D with  $P99_{lin} < 5 \mu m$  and  $max(Q_{Prod})$ .

### 6.3.5 Discussion

To summarize the findings of the sensitivity analysis it can be concluded, that not a single parameter but the combination of the ones under investigation influence the fitting quality as well as the productivity. It appears that shorter CPs lead to decreased model quality, if not paired with increased measurement frequency and/or longer NG phases. Therefore a machine tool user or builder needs to decide, if a longer CP is feasible and can be e.g. performed over the weekend or it is preferable to have a short CP and more regular

recalibrations of the thermal error model. In the long-term the productivity decrease of long CPs will not affect the overall productivity of the machine tool during its whole lifetime.

## 6.4 Thermal Error Compensation with TALC

To demonstrate the practicability of the TALC, based on an ARX model structure and a WLSQ approach to deal with the arbitrary sets of sample rates on a real 5-axis machine tool, two experiments are performed.

### 6.4.1 Axes Offsets

As illustrated in Figure 6.2 the compensation of the occurring thermal errors is performed by sending axes offsets counteracting the thermal errors to the NC of the machine tool. As stated, the communication between PC and NC is done by Ethernet and the FOCAS2 library. The transformation of the computed thermal errors to axes offsets is done by means of HTM and are listed in Equation (6.3) - (6.5).

$$\begin{aligned}
 X_{\text{Offset}} &= E_{B0C} \cdot \hat{Z} \\
 &+ \left( E_{X0C} + E_{R0T} \cdot \frac{\hat{X}}{d/2} - E_{C0C} \cdot \hat{Y} \right) \cdot \cos \hat{B} \\
 &+ \left( E_{Z0T} + E_{A0C} \cdot \hat{Y} \right) \cdot \sin \hat{B}
 \end{aligned} \tag{6.3}$$

$$\begin{aligned}
 Y_{\text{Offset}} &= E_{Y0C} + E_{R0T} \cdot \frac{\hat{Y}}{d/2} \\
 &+ \left( E_{A0C} \cdot \hat{Z} + E_{C0C} \cdot \hat{X} \right) \cdot \cos \hat{B} \\
 &- \left( E_{A0C} \cdot \hat{X} + E_{C0C} \cdot \hat{Z} \right) \cdot \sin \hat{B}
 \end{aligned} \tag{6.4}$$

$$\begin{aligned}
 Z_{\text{Offset}} &= -E_{B0C} \cdot \hat{X} \\
 &+ \left( E_{Z0T} + E_{A0C} \cdot \hat{Y} \right) \cdot \cos \hat{B} \\
 &+ \left( -E_{X0C} + E_{R0T} \cdot \frac{\hat{Z}}{d/2} + E_{C0C} \cdot \hat{Y} \right) \cdot \sin \hat{B}
 \end{aligned} \tag{6.5}$$

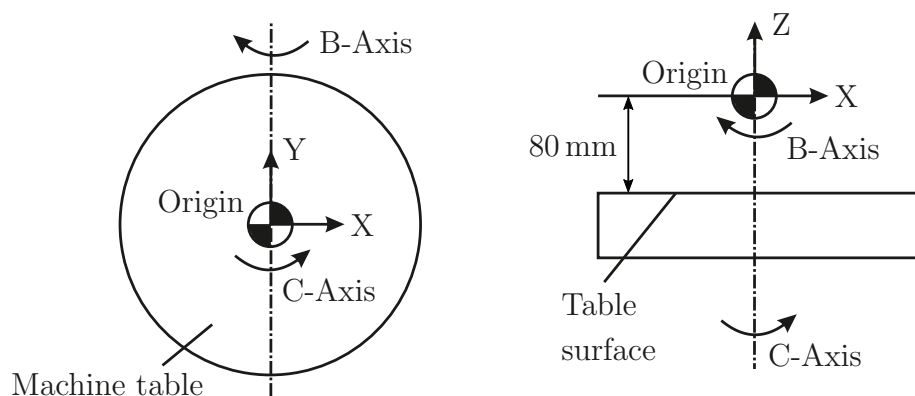


**Figure 6.11:** Origin of machine tool coordinate system during compensation. Axis positions  $\hat{X}$ ,  $\hat{Y}$  and  $\hat{Z}$  read out of the NC are zero in the origin.  $\hat{B}$  is zero when the table surface is parallel to the X-direction, adapted from Gebhardt [40].

The offsets in X, Y and Z-direction are used as parameters in order to adjust the origin of the machine tool coordinate system, see Figure 6.11. The rotary axes B and C of the machine tool are not used for the compensation, because of the limited controllable resolution of  $0.001^\circ$  which corresponds to approximately  $17.5 \mu\text{m}/\text{m}$  and therefore in the same order of magnitudes as the measured angular thermal errors induced by the rotation of the C-axis.

### 6.4.2 Long-Term Compensation

To demonstrate the practicability and the long-term stability of the TALC approach a 178 hour long experiment is performed. The machine tool under investigation is the 5-axis vertical machining center DMG Mori NMV 5000 DCG, described in Section 5.1. The machine tool is located in a not temperature controlled workshop. As internal heat source, the rotary axis C is turning at different speeds and intervals. The objective is to compensate all five position and orientation errors of the rotary axis plus the two errors of the functional surface table, as listed in Table 5.4.

The ARX model uses only three temperatures as inputs to compute all seven thermal errors. The used temperatures and the speed profile of the C-axis are depicted in Figure 6.12.

As pre-defined conditions for the experiment, the parameters in Table 6.4 are used. The duration of the calibration phase is set to as-short-as-possible (ASAP), which corresponds to 6 hours for the chosen maximum model orders. This length is based on the evaluation of the rank of the system matrix, as elaborated in Section 6.2.1. The on-machine measurement interval during the calibration phase is 5 minutes. After the calibration phase and the first model parameter estimation, the measurement interval time is increased to

Parameter	Value
Calibration Phase (CP)	as short as possible (ASAP)
Measurement Interval (CP)	5 min
Measurement Interval (Post CP)	2 h
Measurement Interval (NG)	10 min
Nr. of measurements in NG	12
Action Control Limit	5 $\mu\text{m}$ resp. 15 $\mu\text{m}/\text{m}$
Parameter Update Interval	24 h
Maximum Output Order ( $n_a$ )	5
Maximum Input Order ( $n_b$ )	5

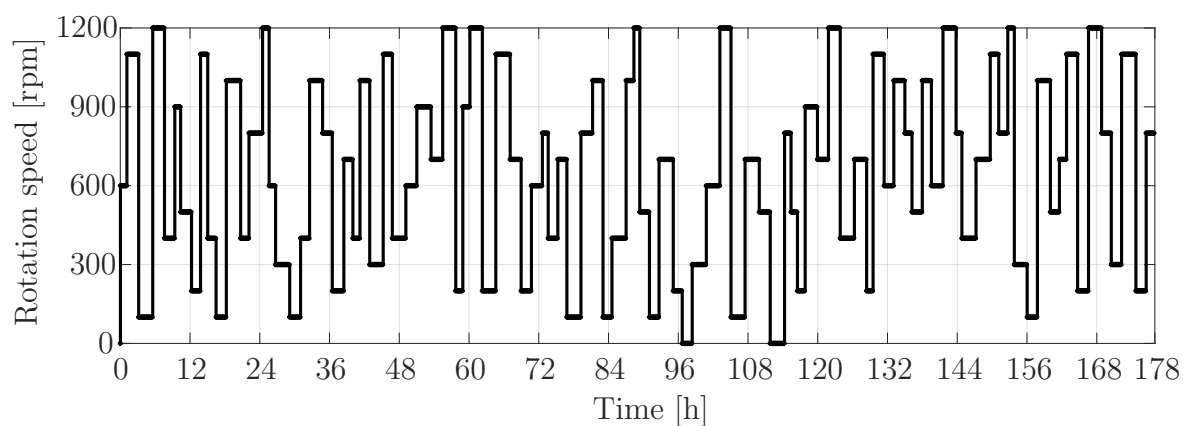
**Table 6.4:** Predefined parameters for the experiment with a duration of 178 hours.

2 hours. The action control limit is set to 5  $\mu\text{m}$  for the linear errors and to 15  $\mu\text{m}/\text{m}$  for the angular errors. If this threshold is surpassed, the No-Good (NG) mode starts, the following 12 measurements are performed every 10 minutes followed by a new parameter update. Apart from the NG mode, a new estimation of the model parameters is performed every 24 hours.

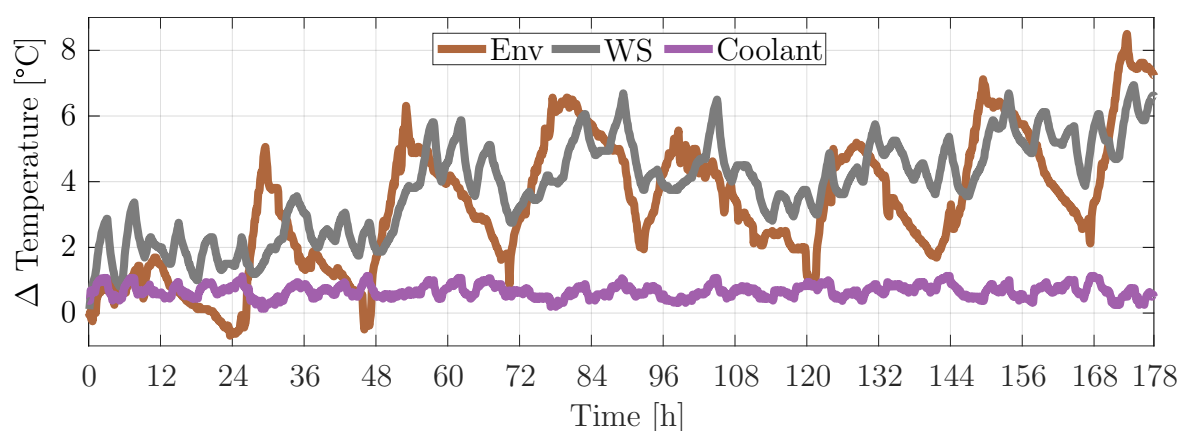
Over the duration of the experiment the environmental temperature is fluctuating by more than 5  $^{\circ}\text{C}$  over the course of 1 day. Additionally a drift of the average daily temperature is visible, see Figure 6.12b. These boundary conditions paired with drastic changes in the heat loads introduced directly into the structure by the C-axis motor result in challenging conditions to validate the TALC approach.

In the following a visual analysis of the compensation of the seven thermal position and orientation errors of the rotary axis C is presented. Each figure shows the specific thermal error with and without compensation. The values for the compensated case are measured directly on the machine tool with the on-machine measurement cycle introduced in Chapter 5. The values for the uncompensated case are reconstructed by superposition of the measured residual errors and the predicted errors calculated by the ARX model. The on-machine cycle is performed every 5 minutes independent from the specified parameters of the TALC approach, see Table 6.4, to clearly visualize the thermal error compensation also during the periods, where no information about the TCP is fed back into the ARX model.

All the following plots have the same span of 40  $\mu\text{m}$  respectively 45  $\mu\text{m}/\text{m}$  for the Y-axis, to ensure the comparability of the amplitudes.



(a) Speed profile of of the C-axis over a duration of 178 hours.



(b) Temperature measurement of the environment (Env), the working space (WS) and the temperature difference of the in- and outlet of the coolant for the rotary axes.

**Figure 6.12:** Speed profile and corresponding measured temperatures during an experiment with a duration of 178 hours.

The thermal position error of the C-axis in X-axis direction  $E_{X0C}$  with and without active TALC compensation is shown in Figure 6.13. Due to the thermo-symmetrical design of the machine tool in the X-Z-plane, see Figure 5.1,  $E_{X0C}$  is small in magnitude compared to other thermal errors and does not show deviations exceeding the set action control limit of  $5 \mu\text{m}$  in the uncompensated state during the whole length of the experiment. The error does not show a direct correlation to the used input temperatures and is also not subject to thermal drift caused by the increasing average environmental temperature. The increased signal-to-noise ratio due to the measurement uncertainty complicates the identification of the ARX model parameters. To quantify the observations the quality criteria P99 is used and it shows a value of  $4.4 \mu\text{m}$  for the uncompensated deviations. The compensation with TALC is able to reduce the P99 to  $2.7 \mu\text{m}$ , which corresponds to a relative reduction of 37.2%, as can be seen in Table 6.5.

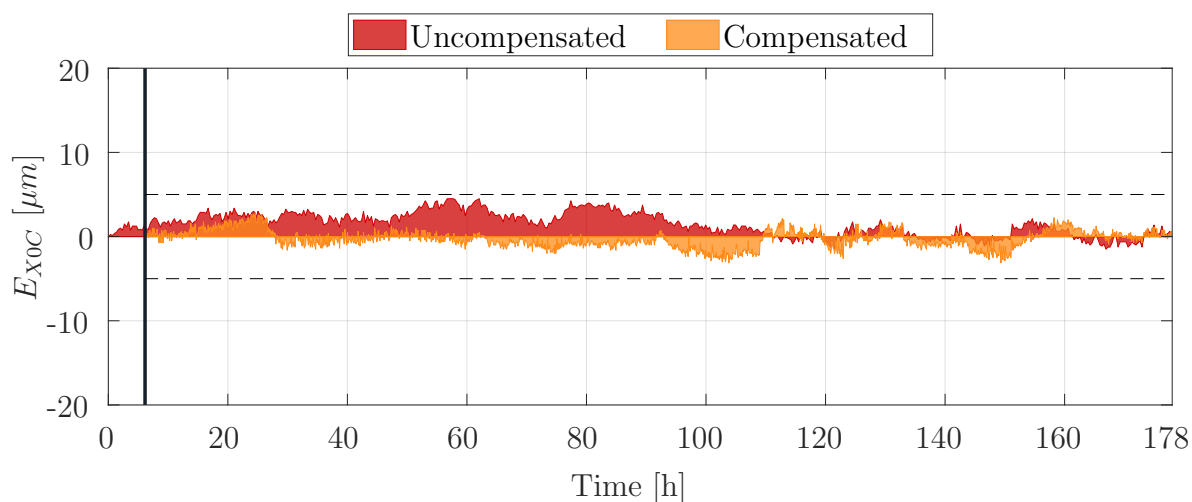


**Figure 6.13:** Experimental result of the compensation with TALC of the thermal position error of the C-axis in X-axis direction  $E_{X0C}$ . The orange area depicts the measured deviations, whereas the red area is reconstructed by the measured and the predicted error. The vertical solid black line represents the start of the compensation after 6 hours. The horizontal black dashed lines illustrate the predefined action control limits of  $\pm 5 \mu\text{m}$ .

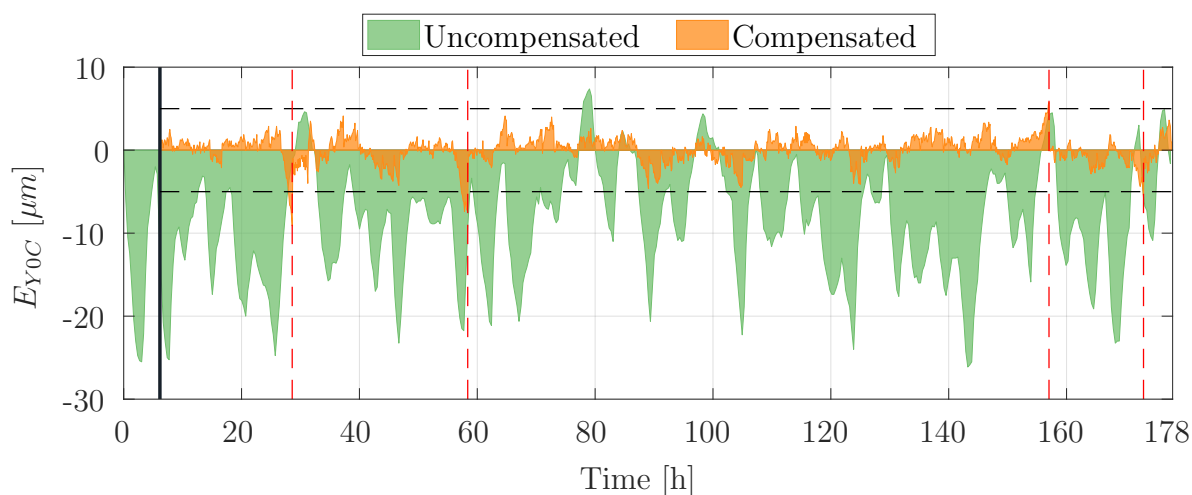


**Figure 6.14:** Experimental result of the compensation with TALC of the thermal position error of the C-axis in Y-axis direction  $E_{Y0C}$ . The orange area depicts the measured deviations, whereas the green area is reconstructed by the measured and the predicted error. The vertical solid black line represents the start of the compensation after 6 hours. The horizontal black dashed lines illustrate the predefined action control limits of  $\pm 5 \mu\text{m}$ . The red vertical lines indicate the moments, when these limits are exceeded and registered.

The thermal position error of the C-axis in Y-axis direction  $E_{Y0C}$  is one of the most significant thermal errors of this machine tool axis for the investigated load case. The results of the compensation with and without TALC are shown in Figure 6.14. The deviations show a P99 value of  $24.4 \mu\text{m}$  for the uncompensated case. With active compensation, this value can drastically be reduced to  $4.9 \mu\text{m}$ , which corresponds to a relative reduction of 79.7%, as can be seen in Table 6.5. Therefore 99% of the occurring thermal deviations can be reduced below the action control limit. The dashed red lines in Figure 6.14 indicate the times, where the residual deviations exceed the set limits and are detected by the on-machine measurements. Over the whole duration of the experiment only four such NG events, caused by the error  $E_{Y0C}$ , can be observed.

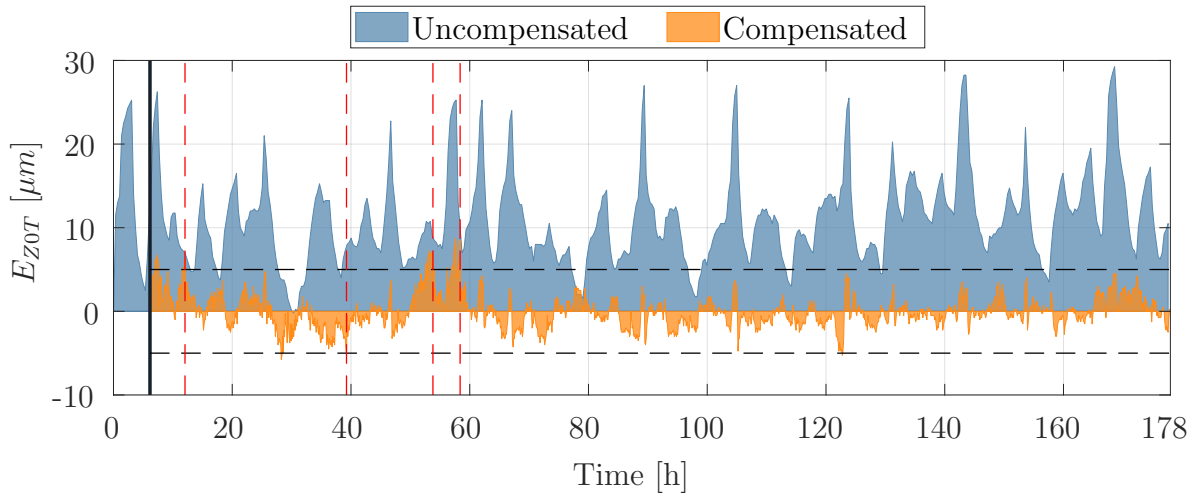


**Figure 6.15:** Experimental result of the compensation with TALC of the thermal position error of the table surface in Z-axis direction  $E_{Z0T}$ . The orange area depicts the measured deviations, whereas the blue area is reconstructed by the measured and the predicted error. The vertical solid black line represents the start of the compensation after 6 hours. The horizontal black dashed lines illustrate the predefined action control limits of  $\pm 5 \mu\text{m}$ . The red dashed lines indicate the moments, when these limits are exceeded and registered.

In Figure 6.15 the thermal position error of the table surface in Z-axis direction  $E_{Z0T}$  is shown. Also this error is one of the most dominant ones. Additionally, this error shows a very dynamic behavior, that results in peak deviations of over  $25 \mu\text{m}$  in magnitude. As fast as the increase is also the decrease of the deviations, if the thermal load is reduced. This fast changing behavior bears a challenge for the modeling and the compensation, since the used temperatures do not show such a dynamic behavior. With the advantages of the dynamic ARX model, discussed in Chapter 4, the error  $E_{Z0T}$  can be reduced by 78%, so that the quality criteria P99 decreases from  $27.5 \mu\text{m}$  down to  $6.1 \mu\text{m}$ . The exceedance of the action control limit of  $5 \mu\text{m}$  is detected four times. All violations of the

limit are registered in the first third of the experiment. During the whole duration of the experiment there are three additional violations that are not detected, since during that short time of exceedance no on-machine measurement is performed. Also the short delays in the registration of the exceedance of the action control limit is caused by the low frequency of Post-CP measurements.

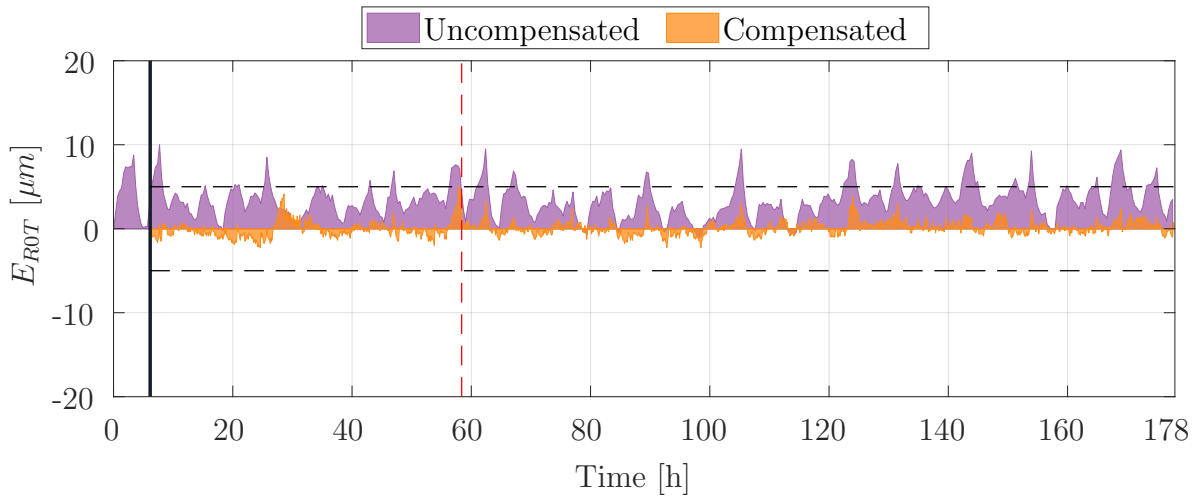


**Figure 6.16:** Experimental result of the compensation with TALC of the thermal radial error of the table surface  $E_{ROT}$ . The orange area depicts the measured deviations, whereas the purple area is reconstructed by the measured and the predicted error. The vertical solid black line represents the start of the compensation after 6 hours. The horizontal black dashed lines illustrate the predefined action control limits of  $\pm 5 \mu\text{m}$ . The red dashed line indicates the moment, when one of these limits is exceeded and registered.

The thermal radial error of the table surface  $E_{ROT}$  is a position dependent error evaluated at the position of the used precision sphere, placed 160 mm away from the axis of rotation of the C-axis. The uncompensated deviations shown in Figure 6.16 show a typical thermal behavior of rotated bodies, where the thermal deformation highly increases, if after fast rotation speeds a period of stand still or very slow rotation follows. This decrease in rotation speed results in a drastic reduction of the airflow around the body and therefore a decrease in the convective heat transfer from the body to the surrounding fluid. This results in an increase in temperature of the body and a corresponding thermo-mechanical expansion. Since the temperature of the rotating table is difficult to measure at these high speeds, the dynamic behavior has to be captured with the help of the ARX model.

As can be seen in Figure 6.16 the error  $E_{ROT}$  can drastically be reduced with the use of TALC. The quality indicator P99 decreases from  $8.5 \mu\text{m}$  to  $2.9 \mu\text{m}$  with active compensation. This results in a relative reduction of 66.2%, see Table 6.5.



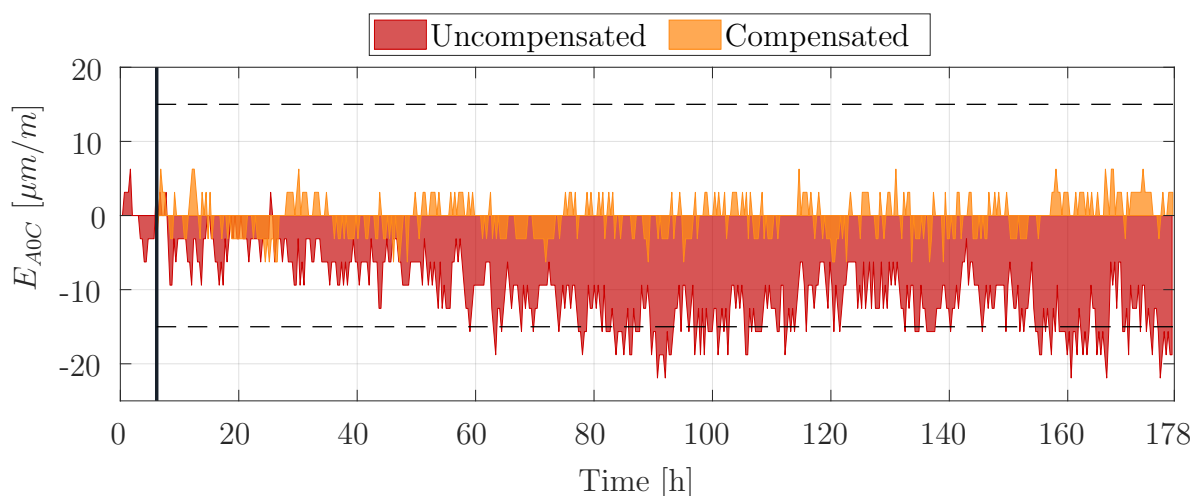


**Figure 6.17:** Experimental result of the compensation with TALC of the thermal squareness error of C-axis to the Y-axis  $E_{A0C}$ . The orange area depicts the measured deviations, whereas the red area is reconstructed by the measured and the predicted error. The vertical solid black line represents the start of the compensation after 6 hours. The horizontal black dashed lines illustrate the predefined action control limits of  $\pm 15 \mu\text{m}/\text{m}$ .

The thermal squareness error of the C-axis to the Y-axis  $E_{A0C}$  is the most dominant angular error on the investigated machine tool. The error shown in Figure 6.17 is mainly influenced by the thermal drift of the environmental temperature of the workshop. The compensation of this rather slow changes are successfully handled by the TALC compensation. The P99 value decreases by 61.7% from  $18.8 \mu\text{m}/\text{m}$  to  $7.2 \mu\text{m}/\text{m}$ , as can be seen in Table 6.5. A further reduction of the error  $E_{A0C}$  is limited by the resolution of the on-machine measurement cycle, see Table 5.4. As for all angular errors the compensated deviations never exceed the set action control limit of  $15 \mu\text{m}/\text{m}$ .

The thermal error  $E_{B0C}$ , squareness error of C-axis to the X-axis, as illustrated in Figure 6.18, is very small in magnitude also due to the thermo-symmetric design of the machine tool. Nevertheless an improvement of 9.8% can be achieved.

Figure 6.19 shows the compensated and uncompensated thermal zero position error of the C-axis  $E_{C0C}$ . This angular error is also rather small in magnitude but shows a fast increase in the deviation at the start of the experiment. This influence is compensated by the TALC method, since regular state updates of the model are performed. The more dynamic part of the error is compensated by the model as well, even though it seems, that the compensation suffers a lack of robustness in the beginning of the experiment, which results in a decreased fitting quality for the first 24 hours of the compensation phase.

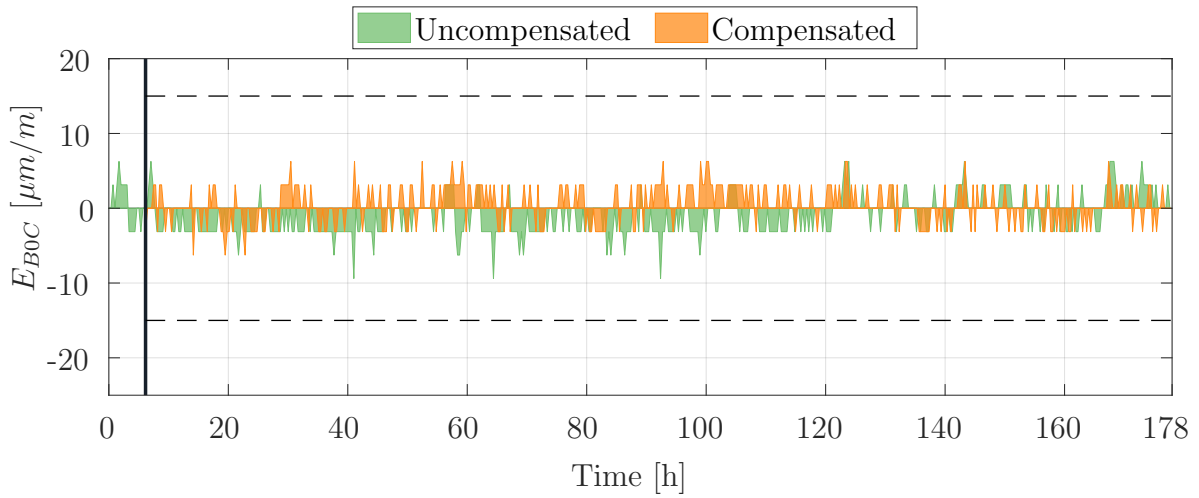


**Figure 6.18:** Experimental result of the compensation with TALC of the thermal squareness error of C-axis to the X-axis  $E_{B0C}$ . The orange area depicts the measured deviations, whereas the green area is reconstructed by the measured and the predicted error. The vertical solid black line represents the start of the compensation after 6 hours. The horizontal black dashed lines illustrate the predefined action control limits of  $\pm 15 \mu\text{m}/\text{m}$ .

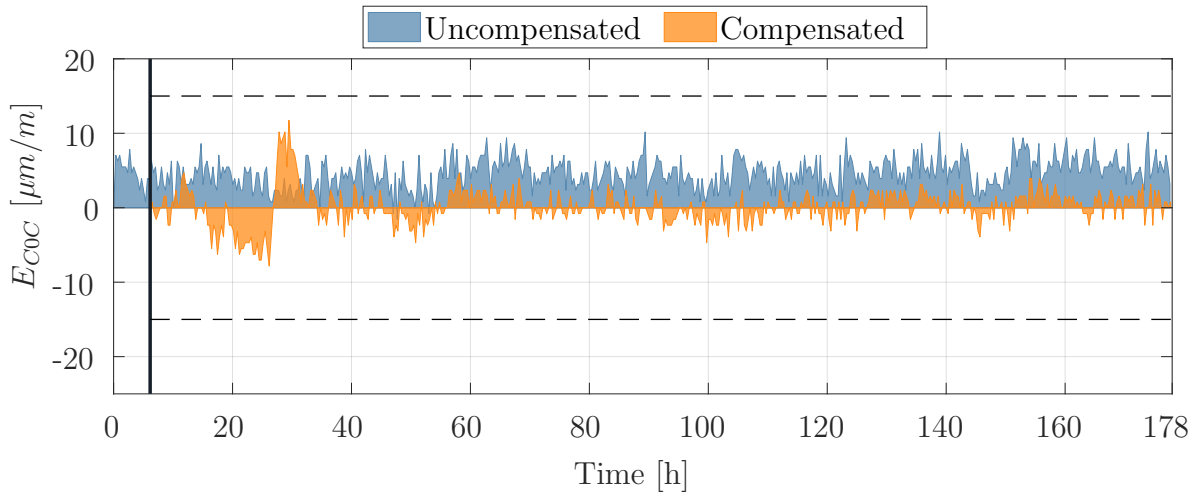


**Figure 6.19:** Experimental result of the compensation with TALC of the thermal zero position error of the C-axis  $E_{C0C}$ . The orange area depicts the measured deviations, whereas the blue area is reconstructed by the measured and the predicted error. The vertical solid black line represents the start of the compensation after 6 hours. The horizontal black dashed lines illustrate the predefined action control limits of  $\pm 15 \mu\text{m}/\text{m}$ .

A significant increase in the prediction quality can be observed after this starting phase of the TALC. This also results in an improvement of the P99 of 25.6%, so a reduction of  $9.4 \mu\text{m}/\text{m}$  to  $7 \mu\text{m}/\text{m}$  is achieved.

Table 6.5 shows a summary of the long-term compensation experiment. Evaluated is the quality indicator P99 for the uncompensated (UC) and the compensated (C) case. It can be seen, that the active TALC compensation reduces 99 % of the values for the thermal position and orientation errors bellow the set action control limit of  $5 \mu\text{m}$  respectively  $15 \mu\text{m}/\text{m}$ , except for the error  $E_{Z0T}$  which lies tightly above the limit. The four most dominant errors  $E_{Y0C}$ ,  $E_{Z0T}$ ,  $E_{R0T}$ , and  $E_{A0C}$  show a reduction of the P99 of 61.7 % up to 79.7 %. The biggest decrease in absolute magnitude shows the error  $E_{Z0T}$ , where a reduction of  $21.4 \mu\text{m}$  is achieved.

	$E_{X0C}$	$E_{Y0C}$	$E_{Z0T}$	$E_{R0T}$	$E_{A0C}$	$E_{B0C}$	$E_{C0C}$
$P99_{UC}$	$4.4 \mu\text{m}$	$24.4 \mu\text{m}$	$27.5 \mu\text{m}$	$8.5 \mu\text{m}$	$18.8 \mu\text{m}/\text{m}$	$6.3 \mu\text{m}/\text{m}$	$9.4 \mu\text{m}/\text{m}$
$P99_C$	$2.7 \mu\text{m}$	$4.9 \mu\text{m}$	$6.1 \mu\text{m}$	$2.9 \mu\text{m}$	$7.2 \mu\text{m}/\text{m}$	$5.6 \mu\text{m}/\text{m}$	$7 \mu\text{m}/\text{m}$
Reduction	37.2 %	79.7 %	78 %	66.2 %	61.7 %	9.8 %	25.6 %

**Table 6.5:** Thermal position and orientation errors, for investigation of rotary axis C for the uncompensated (UC) and compensated (C) machine tool and their relative reduction for the quality criteria 99<sup>th</sup> Percentile (P99). The UC and C values are rounded to  $0.1 \mu\text{m}$  resp.  $0.1 \mu\text{m}/\text{m}$ .

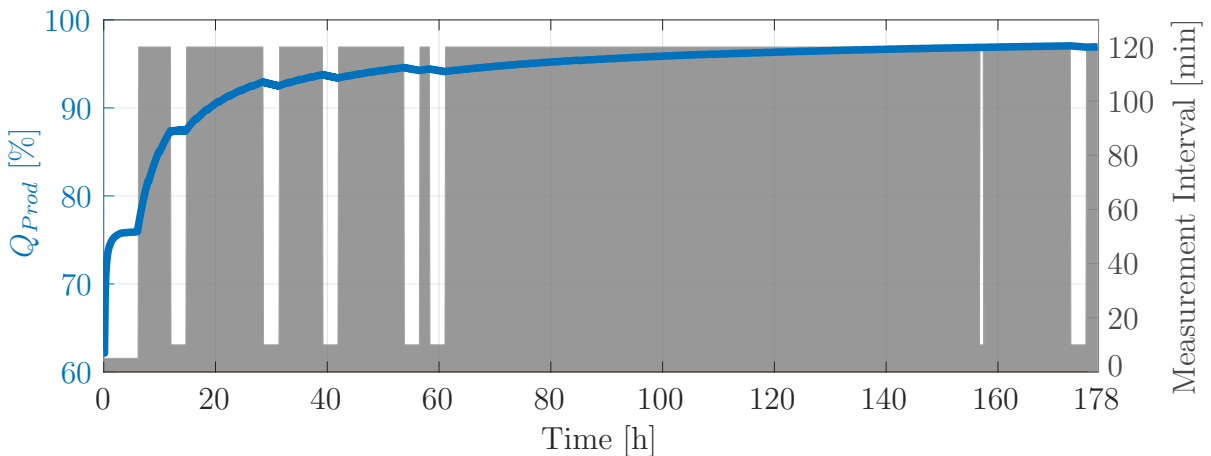


**Figure 6.20:** Illustration of the quality indicator productivity  $Q_{Prod}$  over the duration of the experiment. On the right ordinate the measurement intervals for the on-machine measurements are depicted.

As an additional quality indicator for the compensation with TALC the productivity  $Q_{Prod}$  is introduced in Section 6.3.  $Q_{Prod}$  is a measure of the ratio between time spent for on-machine measurements versus total time of the experiment. Figure 6.20 shows this indicator as a function of time. Additionally, the figure shows the measurement intervals during the duration of the experiment. As stated in Table 6.4 there are three different

intervals used for this experiment, 5 minutes during the CP, 120 minutes after the CP and 10 minutes during the NG phases. The plot illustrates, that the NG phase is entered a total of seven times, whereas the duration of the NG phases depends on the time passed since the last parameter update, since at least every 24 hours an update of the parameters is performed.

At the beginning of the experiment, during the CP, the productivity reaches quickly a stable value of around 75 %. After the CP less measurements are performed and therefore the productivity increases steadily until it reaches its maximum value at about 97 %. The figure also shows, that after 96 hours a productivity of more than 96 % is reached. Therefore the driving parameter for the productivity is the measurement interval time after the CP, even though the measurements during the NG phases lead to a decrease of the  $Q_{Prod}$ , this influence is only marginal and of temporary nature.

### 6.4.3 Compensation of Fast Boundary Condition Changes

For a thermal compensation one of the most challenging scenarios is the sudden change in boundary conditions. Since, especially, the environment acts on a big surface of the machine tool it has a non negligible influence on the thermal behavior. Another common situation for machine tools is the use of MWF, to lubricate and cool the cutting zone and to evacuate the produced chips from the working space. By introducing MWF into the working space, the thermal behavior is drastically changed since the heat removal is, due to the forced convection, strongly increased. Additionally, in most machine tools the MWF is not temperature controlled and therefore subject to temperature fluctuations.

To demonstrate the capability of the TALC approach to adapt to such fast changing conditions and learn from past events, a 144 hour long experiment is performed where the MWF supply is randomly switched on and off during the course of the experiment. The same machine tool as in the previous experiment is used, the DMG Mori NMV 5000 DCG, described in Section 5.1.

As internal heat source, the rotary axis C is turning at different speeds and intervals. The objective is to compensate all five position and orientation errors of the rotary axis plus the two errors of the functional surface of the table, as listed in Table 5.4.

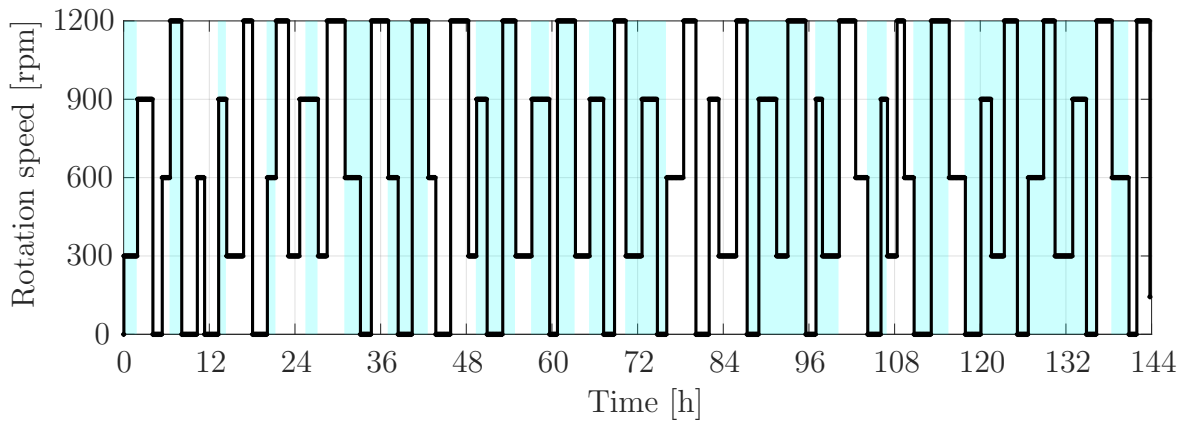
The ARX model uses only three temperatures as inputs to compute all seven thermal errors. The used temperatures and the speed profile of the C-axis are depicted in Figure 6.21 as well as the phases of the active MWF. The MWF is supplied through articulated tubes aiming at the working table and parts of the B-axis corpus.

Parameter	Value
Calibration Phase (CP)	ASAP
Measurement Interval (CP)	5 min
Measurement Interval (Post CP)	2 h
Measurement Interval (NG)	10 min
Nr. of measurements in NG	12
Action Control Limit	5 $\mu\text{m}$ resp. 15 $\mu\text{m}/\text{m}$
Parameter Update Interval	12 h
Maximum Output Order ( $n_a$ )	1
Maximum Input Order ( $n_b$ )	10 resp. 20

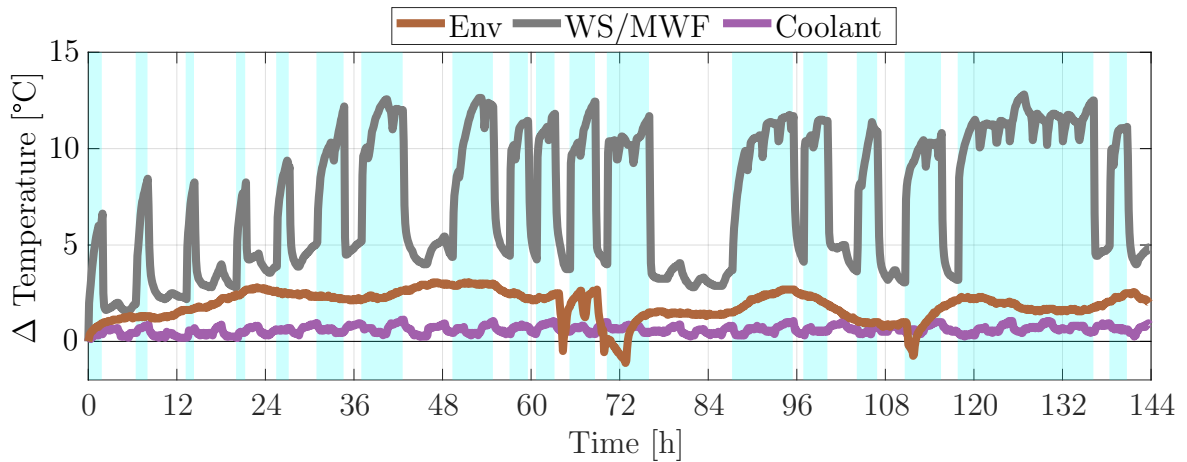
**Table 6.6:** Predefined parameters for the experiment with a duration of 144 hours.

As pre-defined conditions for the experiment, the parameters in Table 6.6 are used. The duration of the calibration phase is set to ASAP, which corresponds to 8.4 hours for the chosen maximum model orders of  $n_a = 1$  and  $n_b = 10$  during the calibration phase. After the calibration phase the maximum input order is increased to  $n_b = 20$  if enough measurement data is gathered. The on-machine measurement interval during the calibration phase is set to 5 minutes. After the calibration phase and the first model parameter estimation, the measurement interval time is increased to 2 hours. The action control limit is set to 5  $\mu\text{m}$  for the linear errors and to 15  $\mu\text{m}/\text{m}$  for the angular errors. If this threshold is surpassed, the NG mode starts, the following 12 measurements are performed every 10 minutes followed by a new parameter update. Apart from the NG mode, a new estimation of the model parameters is performed every 12 hours to ensure an up-to-date compensation model.

Figure 6.21 shows the randomly generated speed profile for the C-axis and the phases of MWF supplied to the working space. As illustrated in Figure 6.21b, over the course of the experiment the biggest temperature variation is measured by the sensor of the MWF. Since the sensor is measuring the temperature of the MWF at the outlet of one of the articulated tubes, the temperature of the fluid is only measured when the supply is switched on. During phases where no MWF is supplied to the working space, the temperature of the working space itself is measured, as in the previous measurement, see Figure 6.21b. The environmental temperature is only slightly fluctuating over the course of 1 day since the experiment is performed in winter and the machine hall is actively heated. Contrary, rapid drops in temperatures are measured over the course of the experiment. These drops result from opening the machine hall door situated next to the machine tool. These boundary conditions paired with drastic changes in the heat loads introduced directly into the



(a) Speed profile of of the C-axis over a duration of 144 hours. The cyan regions depict the times where MWF is supplied to the working space.



(b) Temperature measurement of the environment (Env), the working space (WS) respectively the metal working fluid (MWF) and the temperature difference of the in- and outlet of the coolant for the rotary axes. The cyan regions depict the times where MWF is supplied to the working space.

**Figure 6.21:** Speed profile and time segments of active MWF supply and the corresponding measured temperatures during an experiment with a duration of 144 hours.

structure by the C-axis motor result in the most challenging conditions to test the TALC approach.

Similar to the previous section, a visual analysis of the compensation of the seven thermal position and orientation errors of the rotary axis C is presented. Each figure shows the specific thermal error with and without compensation. The values for the compensated case are measured directly on the machine tool with the on-machine measurement cycle introduced in Chapter 5. The values for the uncompensated case are reconstructed by superposition of the measured residual errors and the predicted errors calculated by the ARX model. The on-machine cycle is performed every 5 minutes independent from the

specified parameters of the TALC approach, see Table 6.4, to clearly visualize the thermal error compensation also during the periods, where no information about the TCP is fed back into the ARX model.

All the following plots have the same span of  $60 \mu\text{m}$  respectively  $55 \mu\text{m}/\text{m}$  for the vertical axis, to ensure the comparability of the amplitudes.

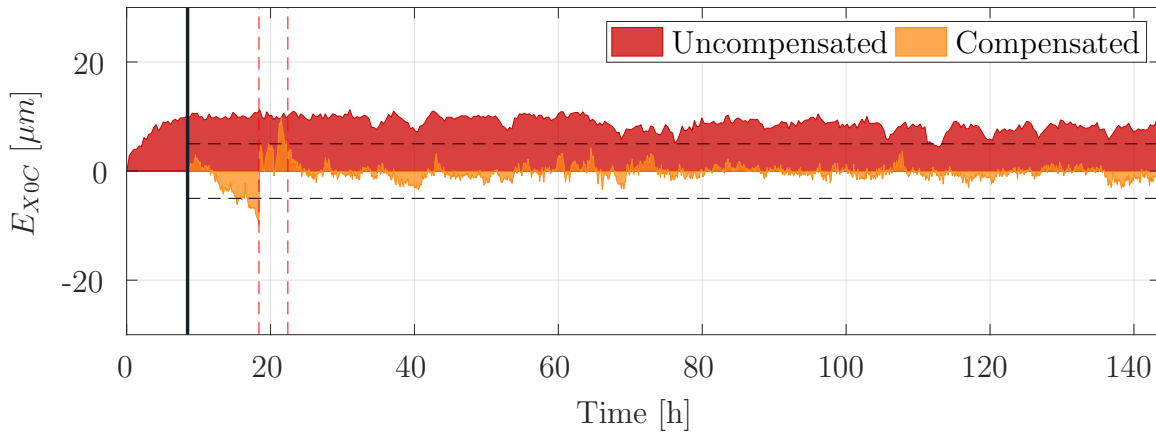


**Figure 6.22:** Experimental result of the compensation with TALC of the thermal position error of the C-axis in X-axis direction  $E_{X0C}$ . The orange area depicts the measured deviations, whereas the red area is reconstructed by the measured and the predicted error. The vertical solid black line represents the start of the compensation after 8.4 hours. The horizontal black dashed lines illustrate the predefined action control limits of  $\pm 5 \mu\text{m}$ . The red dashed lines indicate the moments, when these limits are exceeded and registered.

The thermal position error of the C-axis in X-axis direction  $E_{X0C}$  with and without active TALC compensation is shown in Figure 6.22. Due to the thermo-symmetrical design of the machine tool in the X-Z-plane, see Figure 5.1,  $E_{X0C}$  is small in magnitude compared to other thermal errors. In contrast to the experiment performed without MWF, see Figure 6.13, the uncompensated deviations exceed the set action control limit of  $\pm 5 \mu\text{m}$  almost during the whole duration of the experiment. A possible explanation for this increase in magnitude is the not symmetric supply of the MWF onto the B-axis corpus, due to the manual positioning of the articulated tubes. The error does not show a direct correlation to the used input temperatures. Nevertheless the TALC approach is capable of significantly reducing the occurring thermal errors. The dashed red lines in Figure 6.14 indicate the times, where the residual deviations exceed the set limits and are detected by the on-machine measurements. It can be seen, that shortly after the CP the set action control limit is surpassed and detected twice in a short time span. After the two NG phases the model parameters are updated and the TALC approach is capable of reducing the error

to within its set limits for the next 120 hours until the end of the experiment. To quantify the observations, the quality criteria P99 is used and it shows a value of  $11\ \mu\text{m}$  for the uncompensated deviations. The compensation is able to reduce the P99 to  $6.9\ \mu\text{m}$ , which corresponds to a relative reduction of 37.5%, as can be seen in Table 6.7. This value is mostly dominated by the period where the action control limit is exceeded and drastically decreases after the third parameter update.

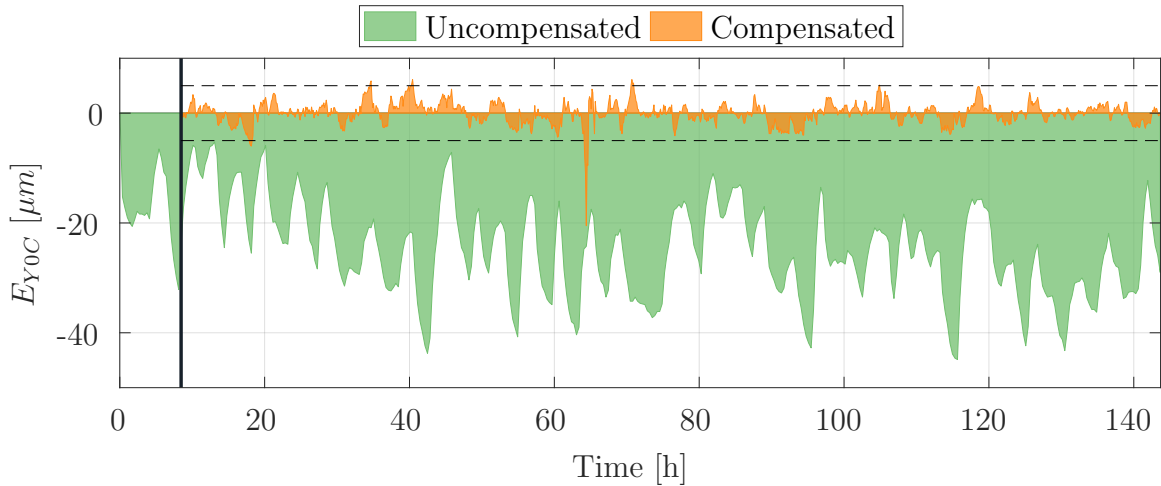


**Figure 6.23:** Experimental result of the compensation with TALC of the thermal position error of the C-axis in Y-axis direction  $E_{Y0C}$ . The orange area depicts the measured deviations, whereas the red area is reconstructed by the measured and the predicted error. The vertical solid black line represents the start of the compensation after 8.4 hours. The horizontal black dashed lines illustrate the predefined action control limits of  $\pm 5\ \mu\text{m}$ .

The thermal position error of the C-axis in Y-axis direction  $E_{Y0C}$  is one of the most significant thermal errors of this machine tool axis also for this investigated load case. The results of the compensation with and without TALC are shown in Figure 6.23. The deviations result in a P99 value of  $43.4\ \mu\text{m}$  for the uncompensated deviations, which is almost double as for the load case without MWF, compare Table 6.5. With active compensation, this value is drastically reduced to  $5.1\ \mu\text{m}$ , which corresponds to a relative reduction of 88.3%, as can be seen in Table 6.7. The set action control limit is surpassed several times but either not detected, since only measurements every 2 hours are considered, or ignored if a NG mode was already triggered beforehand. The biggest drop in the accuracy of the compensation can be observed around 65 hours after the start of the measurement. During that time the environmental temperature drastically drops by  $3\ ^\circ\text{C}$  in less than 30 minutes and keeps fluctuating for the next 9 hours, see Figure 6.21. The exceedance is not captured by the TALC algorithm since the NG mode is already active during that time, compare Figure 6.24. Even though the environmental temperature is fluctuating for several more



hours and a similar drop in temperature is observed around 111 hours into the experiment, the residual error do not show any disturbances in the same magnitude again. This emphasizes the capability of the TALC approach to learn from not previously encountered boundary conditions and proves the high robustness of the compensation method.

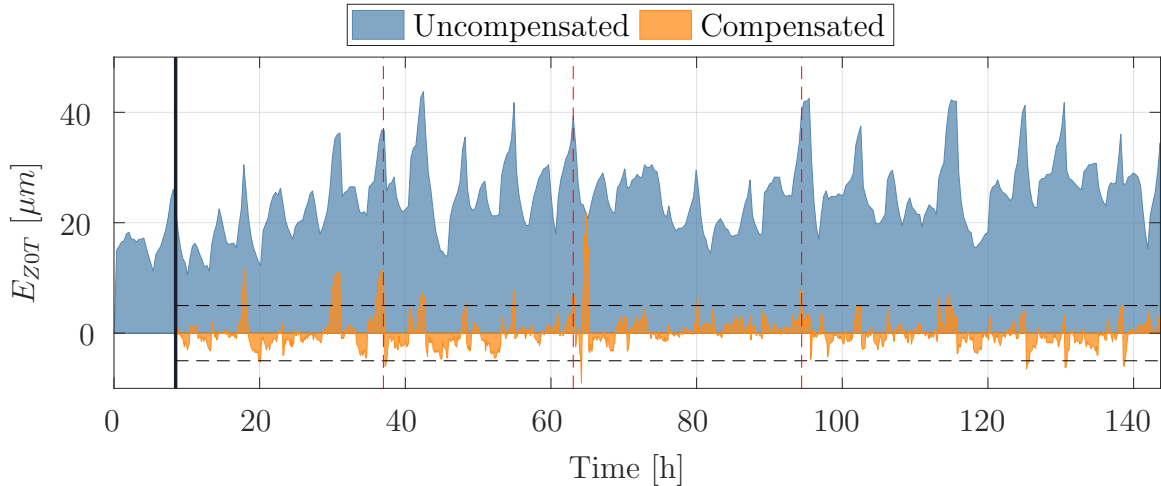


**Figure 6.24:** Experimental result of the compensation with TALC of the thermal position error of the table surface in Z-axis direction  $E_{Z0T}$ . The orange area depicts the measured deviations, whereas the red area is reconstructed by the measured and the predicted error. The vertical solid black line represents the start of the compensation after 8.4 hours. The horizontal black dashed lines illustrate the predefined action control limits of  $\pm 5 \mu\text{m}$ . The red dashed lines indicate the moments, when these limits are exceeded and registered.

In Figure 6.24 the thermal position error of the table surface in Z-axis direction  $E_{Z0T}$  is shown. Also this error is one of the most dominant ones. Additionally, this error shows a very dynamic behavior, that results in peak to valley deviations of over  $25 \mu\text{m}$  in magnitude in less than 4 hours. With the advantages of the dynamic ARX model, discussed in Chapter 4, the error  $E_{Z0T}$  can be reduced by 75.1%, so that the quality criteria P99 decreases from  $42.1 \mu\text{m}$  down to  $10.5 \mu\text{m}$ . The exceedance of the action control limit of  $5 \mu\text{m}$  is detected three times. Two of these violations of the limit are caused by the fast changes of the MWF supply state. The other NG mode is entered because of a combination of the effect of drastic decline of the environmental temperature after 63 hours of the experiment, compare Figure 6.21b, and the switch off of the MWF. The second disturbance in the environmental temperature, at around 112 hours after the start of the experiment, does not cause any visible decrease of the compensation quality.

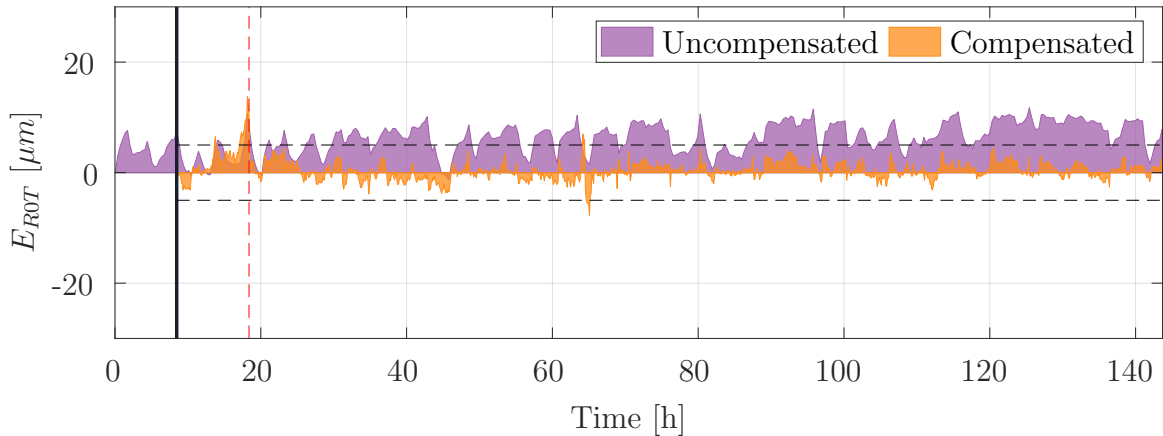


**Figure 6.25:** Experimental result of the compensation with TALC of the thermal radial error of the table surface  $E_{ROT}$ . The orange area depicts the measured deviations, whereas the red area is reconstructed by the measured and the predicted error. The vertical solid black line represents the start of the compensation after 8.4 hours. The horizontal black dashed lines illustrate the predefined action control limits of  $\pm 5 \mu\text{m}$ . The red dashed line indicates the moment, when one of these limits is exceeded and registered.

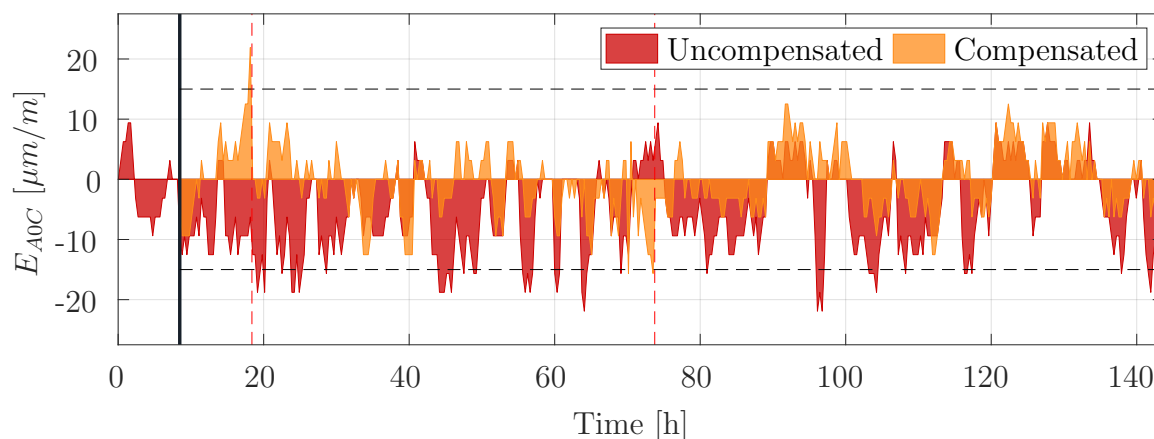
The thermal radial error of the table surface  $E_{ROT}$  is a position dependent error evaluated at the position of the used precision sphere, placed 160 mm eccentric from the axis of rotation of the C-axis. The uncompensated deviations show, that this thermal error is mostly influenced by the MWF supplied directly to the machine tool table as well as the rotational speed of the table itself. As can be seen in Figure 6.25 the error  $E_{ROT}$  can drastically be decreased by 50.3%. The quality indicator P99 decreases from  $10.6 \mu\text{m}$  to  $5.3 \mu\text{m}$  with active compensation, compare Table 6.7.

The exceedance of the action control limit at around 65 hours into the experiment is caused by the fact, that the NG mode is already triggered by another thermal error that exceeded that limit at an earlier point in time.

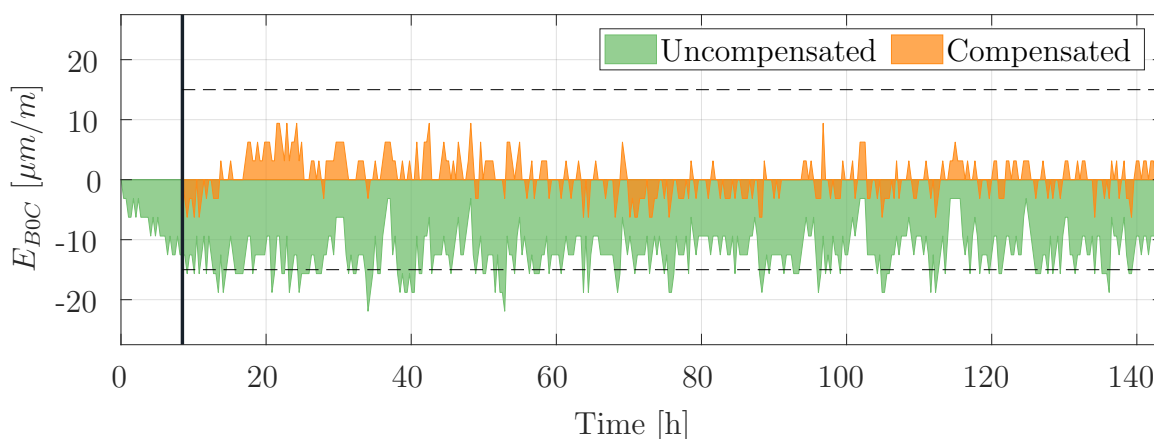
In general the angular errors show a entirely different thermal behavior compared to the long-term experiment performed without MWF, see Chapter 6.4.2.

The thermal squareness error of the C-axis to the Y-axis  $E_{A0C}$  is the most dynamic angular error under the tested circumstances. The error shown in Figure 6.26 is mainly influenced by the MWF supply. The compensation of this very fast changes are mediocly handled by the TALC compensation. The P99 value decreases by 35.4% from  $21.9 \mu\text{m}/\text{m}$  to  $14.2 \mu\text{m}/\text{m}$ , compare Table 6.7.

The thermal error  $E_{B0C}$ , squareness error of C-axis to the X-axis, as illustrated in Figure 6.27, shows a significantly bigger error magnitude in its uncompensated state than in the previous experiment without the use of MWF. This increase can be explained by the fact,

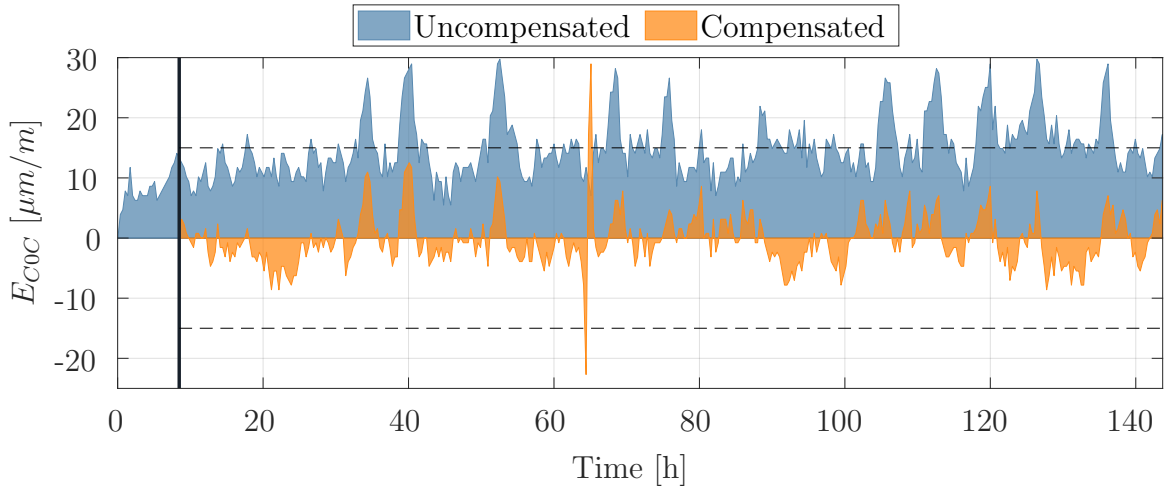


**Figure 6.26:** Experimental result of the compensation with TALC of the thermal squareness error of C-axis to the Y-axis  $E_{A0C}$ . The orange area depicts the measured deviations, whereas the red area is reconstructed by the measured and the predicted error. The vertical solid black line represents the start of the compensation after 8.4 hours. The horizontal black dashed lines illustrate the predefined action control limits of  $\pm 15 \mu\text{m}/\text{m}$ . The red dashed lines indicate the moments, when these limits are exceeded and registered.



**Figure 6.27:** Experimental result of the compensation with TALC of the thermal squareness error of C-axis to the X-axis  $E_{B0C}$ . The orange area depicts the measured deviations, whereas the red area is reconstructed by the measured and the predicted error. The vertical solid black line represents the start of the compensation after 8.4 hours. The horizontal black dashed lines illustrate the predefined action control limits of  $\pm 15 \mu\text{m}/\text{m}$ .

that the MWF supply is purposely aimed asymmetrically at the B-axis body. Nevertheless it can not be fully explained why the deviations do not approach the initial values when no MWF is supplied to the working space over a longer time. The values with active TALC compensation show a reduction of the P99 value from  $18.8 \mu\text{m}/\text{m}$  to  $8.9 \mu\text{m}/\text{m}$ , which corresponds to an improvement of 52.5%.



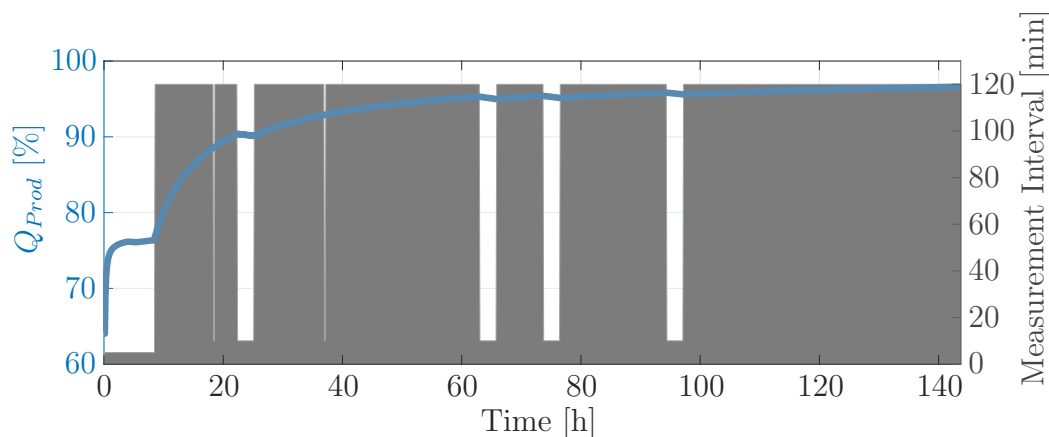
**Figure 6.28:** Experimental result of the compensation with TALC of the thermal zero position error of the C-axis  $E_{C0C}$ . The orange area depicts the measured deviations, whereas the red area is reconstructed by the measured and the predicted error. The vertical solid black line represents the start of the compensation after 8.4 hours. The horizontal black dashed lines illustrate the predefined action control limits of  $\pm 15 \mu\text{m}/\text{m}$ .

Figure 6.28 shows the compensated and uncompensated thermal zero position error of the C-axis  $E_{C0C}$ . This angular error shows a sensitive behavior to the MWF state as well as an increase in the mean deviation over time, that stabilizes after around 24 hours of the start of the experiment. This influence as well as the faster dynamic parts of the error are compensated by the model in a convincing manner. The compensation quality suffers also here from the fluctuations in the environmental temperature after 65 hours. The model then learns to handle those fluctuations, so that in the later state of the experiment the compensation seems insensitive to those fast boundary condition changes. A total reduction of the P99 value of 62.9% can be achieved, so that the P99 value is decreased from  $29.7 \mu\text{m}/\text{m}$  down to  $11 \mu\text{m}/\text{m}$ , see Table 6.7.

	$E_{X0C}$	$E_{Y0C}$	$E_{Z0T}$	$E_{R0T}$	$E_{A0C}$	$E_{B0C}$	$E_{C0C}$
$P99_{UC}$	$11 \mu\text{m}$	$43.4 \mu\text{m}$	$42.1 \mu\text{m}$	$10.6 \mu\text{m}$	$21.9 \mu\text{m}/\text{m}$	$18.8 \mu\text{m}/\text{m}$	$29.7 \mu\text{m}/\text{m}$
$P99_C$	$6.9 \mu\text{m}$	$5.1 \mu\text{m}$	$10.5 \mu\text{m}$	$5.3 \mu\text{m}$	$14.2 \mu\text{m}/\text{m}$	$8.9 \mu\text{m}/\text{m}$	$11 \mu\text{m}/\text{m}$
Reduction	37.5 %	88.3 %	75.1 %	50.3 %	35.4 %	52.5 %	62.9 %

**Table 6.7:** Thermal position and orientation errors, for investigation of rotary axis C for the uncompensated (UC) and compensated (C) machine tool and their relative reduction for the quality criteria 99<sup>th</sup> Percentile (P99). The UC and C values are rounded to  $0.1 \mu\text{m}$  resp.  $0.1 \mu\text{m}/\text{m}$ .

Table 6.7 shows a summary of the TALC compensation of fast boundary condition changes. Evaluated is the quality indicator P99 for the uncompensated (UC) and the compensated (C) case. The three most dominant errors  $E_{Y0C}$ ,  $E_{Z0T}$ , and  $E_{C0C}$  show a reduction of the P99 of 62.9% up to 88.3%. The biggest decrease in absolute magnitude shows the error  $E_{Y0C}$ , where a reduction of 38.3  $\mu\text{m}$  is achieved.



**Figure 6.29:** Illustration of the quality indicator  $Q_{Prod}$  over the duration of the experiment. On the right ordinate the time intervals for the on-machine measurements are depicted.

Figure 6.29 illustrates the quality indicator  $Q_{Prod}$  as a function of time. Additionally, the figure shows the measurement intervals during the duration of the experiment. As stated in Table 6.6 there are three different intervals used for this experiment, 5 minutes during the CP, 120 minutes after the CP and 10 minutes during the NG phases. The plot illustrates, that the NG phase is entered a total of six times, whereas the duration of the NG phase depends on the time passed since the last parameter update, since at least every 12 hours an update of the parameters is performed.

At the beginning of the experiment, during the CP, the productivity reaches quickly a stable value of around 75%. After the CP less measurements are performed and therefore the productivity increases steadily until it reaches its maximum value at about 97%, which is comparable to the case without MWF, see Figure 6.20. The figure also shows, that after 58 hours a productivity of more than 95% is reached. Therefore the driving parameter for the productivity is the measurement interval time after the CP, even though the measurements during the NG phases lead to a decrease of the  $Q_{Prod}$ , this influence is only marginal and of temporarily nature.

In general it can be concluded that the TALC approach enables the compensation of fast changing boundary conditions due to its self-learning and self-adaption capabilities. It enables to manufacture under changing conditions without pre-conditioning and in changing environmental conditions. There is no need to pre-calibrate the parameters, since the approach is learning the different conditions during the use-phase of the machine tool.



## Chapter 7

# Thermal Test Piece

To detect position and orientation errors and error motions under real machining conditions, several test pieces have been developed by many researchers and are adopted by different societies. Examples of test pieces are shown in Chapter 2. In this chapter a newly developed thermal test piece for the evaluation of thermal machine tool errors of 5-axis machine tools is introduced.

The thermal test piece is further used to evaluate the TALC on a 5-axis machine tool, by machining a test piece with and another one without active compensation.

## 7.1 Design of Test Piece

Thermal deviations of machine tools influence the geometrical size of features, e.g. diameter of a cylinder, distances and orientations of functional surfaces, on a machined workpiece. The goal of the design of a thermal test piece is, that thermal position and orientation errors are the main driving source of workpiece errors and that the features can be easily evaluated. As some features may be dimensionally small, the measurement uncertainty surpasses a justifiable limit and the corresponding thermal error cannot be estimated with sufficient accuracy.

The time and energy input dependent changes of the thermal position and orientation errors of the machine tool can be displayed on the surfaces of the thermal test piece and measured by comparing different states to the references machined on the thermal test piece. The reference features are machined in the first cycle before the thermal test of the machine tool starts. To minimize the influence of the geometrical machine tool errors on the machined workpiece errors, the thermal test piece is designed for a production cycle with a minimum set of axis movements, e.g. when testing vertical machining centers the

vertical linear axis is not moved during the thermal test. This procedure avoids imprinting of geometrical errors influenced by positioning and kinematic errors of this axis into the thermal test piece. When machining the features on the thermal test piece, in order to evaluate thermal machine tool errors separately from geometric errors on the workpiece over time, the remaining axes follow a predetermined path repeatedly. This avoids that errors like backlash reproduce on the thermal test piece. The only axis that has to be positioned in different axis positions during the thermal test is the rotary table of the 5-axis machine tool, which is the investigated machine tool axis.

Changing cutting conditions, such as the depth of cut, results in varying cutting forces and leads to geometrical errors on the machined workpieces. The thermal test piece design allows a milling process with constant infeed resulting in constant milling forces. Thus before starting with the evaluation of thermal errors, the thermal test piece is semifinished in a way that the milling forces during finishing are minimized in order to avoid influences of the cutting process distorting the thermal results. A desired cutting thickness of 0.1 mm is considered during the design stage, to achieve good cutting conditions.

The blank that is used for the thermal test piece is shown in Figure 7.1. The blank has a height of 25 mm and a diameter of 203 mm. To avoid influences of asymmetric clamping and resulting geometrical errors on the thermal test piece, three bolt holes are drilled in the blank. The arrangement of the bolt holes is symmetric to the workpiece axis X. The test piece material chosen is aluminum (AlMgSi1). The reasons for choosing aluminum as thermal test piece material is that the material is cheap, available in manufacturing enterprises and the cutting forces are low compared to steel. Nevertheless, the thermal test piece can be machined out of any material that is stiff enough.

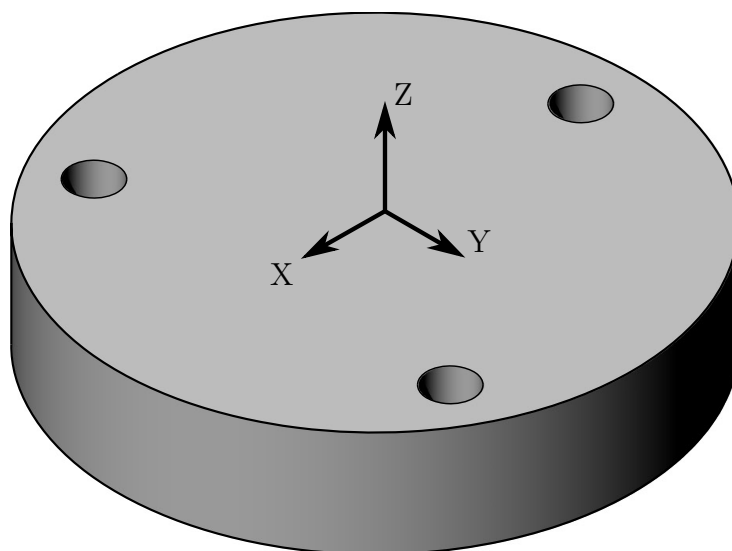


**Figure 7.1:** Thermal test piece blank, 203 mm diameter, height 25 mm.



To mount the thermal test piece on different machine tool tables, an adapter is used, which allows the compensation of different notch distances on different machine tool tables. The material of the adapter is chosen to be the same as the material used for the thermal test piece (AlMgSi1). The decision is made to avoid possible thermal stresses arising, when the temperature of the adapter and thermal test piece is changing. The adapter and the test piece are decoupled by fine ground washers, to achieve a 3-point support for the fixture of the test piece.

Several milling tools and steps are required to manufacture the thermal test piece. For a better understanding the manufacturing sequences are described in more detail in the following sections. All milling operations described are wet cutting. It has to be taken into account, that the MWF influences the thermal behavior of the machine tool, as described by Mayr et al. in [81]. When the thermal errors of the machine tool without the usage of MWF are investigated, the MWF is only supplied during the pre-machining operations.

### 7.1.1 Pre-machining

For the first steps the used tool is a four lips end miller made of high speed steel (HSS) with a diameter of 16 mm. In the beginning the outer circumference of the thermal test piece, which is used later as one of the reference surfaces for evaluation, is circular milled by turning the rotary table. No linear axis is moved, the tool is fixed in one position and only the rotary axis C is moved. With this manufacturing Step 1 it is ensured that the axis of rotation of the test piece is exactly concentric to the rotary axis C of the machine tool. The advantage of this step is that the blank of the thermal test piece has to be positioned only roughly in the center of the machine tool rotary table during the mounting process. The thermal test piece is milled to a diameter of 202 mm. Additionally, three cylindrical measurement surfaces are separated by 5 mm steps in positive Z-direction from 201 mm, 200 mm down to a diameter of 199 mm, as seen in Figure 7.2. The tool position is fixed for two circular surfaces at X0 or Y0 accordingly, for a whole rotation of 360°. The additional surfaces provide an evaluation of the accuracy of the rotary axis C since this is a key factor for the evaluation process. Next the topside of the thermal test piece blank is flattened by face milling with a programmed depth of cut of 1 mm using the same tool.

Since the finished thermal test piece, shown in Figure 7.3, is of strong symmetric design a little mark is engraved in manufacturing Step 2, by an engraving milling tool, identifying one X-sector. This mark is necessary to orient the thermal test piece in subsequent evaluations. In manufacturing Step 3 a 10 mm wide notch is cut in Y-direction of the thermal test piece. The third milling tool used for this operation is a finishing end mill made of solid tungsten carbide with a diameter of 8 mm. This notch is later used for visual in-

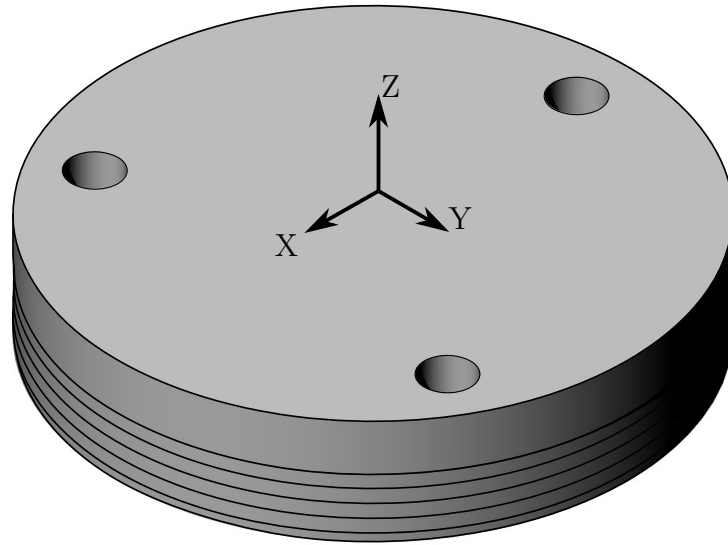


**Figure 7.2:** Thermal test piece after Step 1 of pre-machining with the milled reference cylinder surfaces and a flattened top surface.

spection of the deviations in Z-direction. To avoid a repositioning of the Z-axis during the thermal test, in manufacturing Step 4 the material of a 12 mm depth notch with a width of 106 mm is removed first by a roughing process and afterwards by a finishing process over the whole length of the work-piece in X-direction. The tool used for this process step is the already mentioned tool made of HSS with a diameter of 16 mm. The machined inner XZ-planes, forming the boundary walls of the 12 mm  $\times$  106 mm notch, created by manufacturing Step 4, are used to define the workpiece coordinate system when the workpiece is evaluated on a CMM. By these steps, four segments on the top are created. On the outer diameter of each segment 9 facets with an angle difference of  $6^\circ$  to each other and a machining allowance of 0.1 mm are milled in the fifth and last step. The pre-machining takes approximately 15 min. The semi-finished thermal test piece after manufacturing Step 5 with notches, mark and removed material is illustrated in Figure 7.3.

For all following steps, after manufacturing Step 5, the tool is changed to a finishing cutter. A three lips end-mill made of solid tungsten carbide with a diameter of 12 mm is used for milling the end contour of the thermal test piece. The finished surfaces are machined on the thermal test piece sides and the pre-milled center bottom surface of the large notch (see Figure 7.3). The depth of cut in Z-direction during the thermal test cycle is kept to a minimum of nominal 0.1 mm to avoid influences of the cutting process distorting the evaluation, e.g. by bending of the cutting tool. To avoid positioning errors of the Z-axis the tool is positioned in Z-direction and the axis is afterwards not moved and can be clamped mechanically if there is a clamping unit foreseen on the machine tool. After

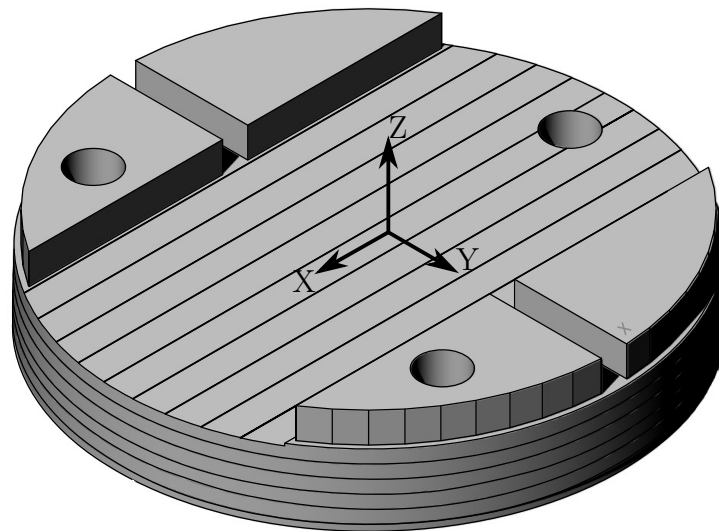


**Figure 7.3:** Thermal test piece after pre-machining.

pre-machining, it is suggested to keep the machine in NC-hold for a defined amount of time, to reduce the thermal influence of the pre-machining steps.

### 7.1.2 Test Cycle

The thermal test piece is designed for a test cycle that is based on eight periods of thermal load changes. For example the day-night cycle of environmental influences over 24 hours can be evaluated by an around-the-clock test with cycle times of four hours. For the experiment presented in this thesis the thermal test piece is used for a four hour warm-up phase followed by a four hour cool-down phase according to ISO 230-3 [64]. During the warm-up phase the rotary table of the investigated machine tool is rotating with maximum speed between the milling steps. During the cool-down phase the rotary table of the investigated machine tool is positioned in NC-hold at  $C = 0$ . For the milling operations during the test-cycle a new finishing end mill, made of solid tungsten carbide with a diameter of 12 mm, is used. Since the removed volume during the test-cycle is very small, the tool wear is assumed to be negligible and is not considered in the evaluation. The following test cycle is used to describe the finishing sequences in detail.

Milling the reference surfaces and facets is followed by milling the measurement surfaces and facets. One full cutting cycle is illustrated in Figure 7.4. The tool is positioned in the waiting position (red square). With the fixed Z-position the tool starts to mill the first Z-line removing material at a nominal depth of cut of 0.1 mm by moving in +X-direction, Step 1 in Figure 7.4. After that the rotary table of the machine tool is positioned, Step 2 in Figure 7.4, so that with a movement in -Y-direction the first facet of the thermal test

piece, the X1-facet, is milled, Step 3 in Figure 7.4. Afterwards the machine tool table is rotated again, Step 7.4 in Figure 7.4, so that with an axis movement in -X-direction the Y1-facet is milled, Step 5 in Figure 7.4. Steps 2-5 are then repeated to mill the facets X2 and Y2. After the milling operation the tool moves back to the waiting position and waits for the next milling cycle, Step 10 in Figure 7.4.

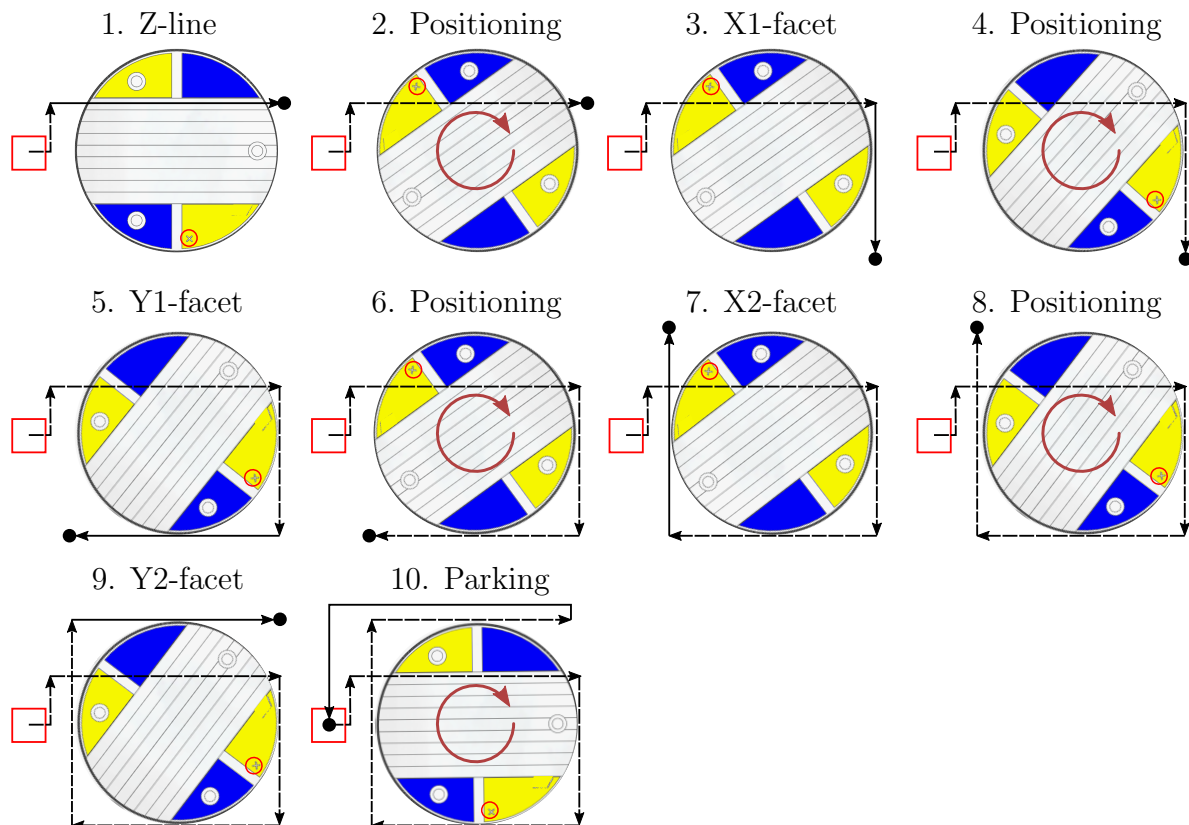


**Figure 7.4:** Illustration of the sequential milling cycle for a set of measurement surface and facets. Due to the design of the cycle a movement of the Z-axis of the machine tool is not necessary.

The test cycle starts with milling the reference surfaces using the cutting cycle illustrated in Figure 7.4, followed by the first warm-up cycle. After one hour warm-up, the first features for measuring the deviations are milled. For this the milling cycle explained in Figure 7.4 is repeated by adding  $6^\circ$  for each cycle to the table rotation when milling the facets for measuring the deviations in X- and Y-direction and shifting the tool path by 12 mm in Y-direction when milling the measurement surface in Z-direction. These steps are repeated for milling all measurements surfaces and facets. Between the milling operations the tool is positioned in the waiting position and after each hour waiting time one measurement surface (Figure 7.5) and four measurement facets (Figure 7.6) are milled according to Figure 7.4.

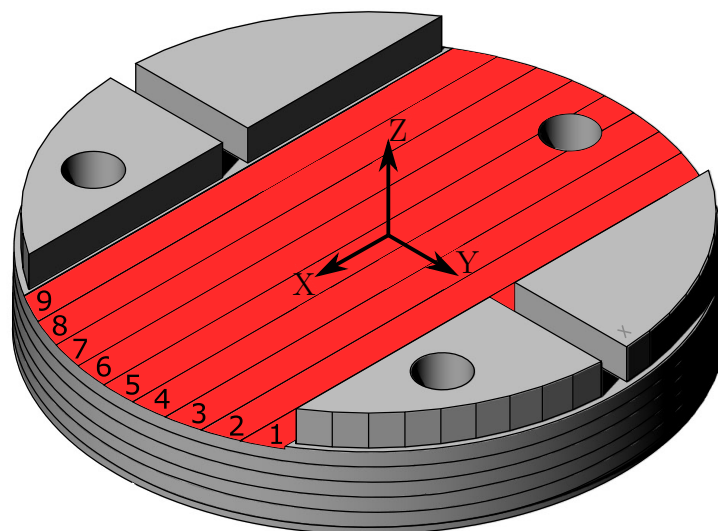


**Figure 7.5:** Surfaces to evaluate the thermal machine tool error in Z-direction, path 5 represents the reference surface, path 1 to 4 and 6 to 9 indicate different stages of the thermal test cycle.

The finished thermal test piece as shown in Figure 7.5 and Figure 7.6 has 45 finished surfaces to detect the thermal machine tool errors. Nine paths are milled in X-direction of the test piece coordinate system. The fifth path, indicated with 5 in Figure 7.5, is milled before starting the thermal error test and is used as reference surface for evaluation. The remaining eight paths, 1 to 4 and 6 to 9, are finished during the different stages of the test cycle. The perpendicular distance between these planes in Z-direction directly indicates the thermal error in Z-direction of the machine tool.

Additional 36 surfaces are milled on the outer circumference of the thermal test piece. Each facet is nominally parallel to a corresponding facet on the opposite side of the thermal test piece. One facet and its opposite for each direction (X and Y) are milled according to Figure 7.4 before starting the thermal error test and are used as reference for evaluation. The remaining eight parallel surfaces are finished during the different stages of the test cycle. The different distances between the parallel facets indicate the thermal machine tool errors in X- and Y-direction. The parallel facets for evaluating the deviations in X- and Y-direction are illustrated in Figure 7.6.

The complete test cycle takes 8 hours and 5 minutes, in which 5 minutes are in total spend for chipping.

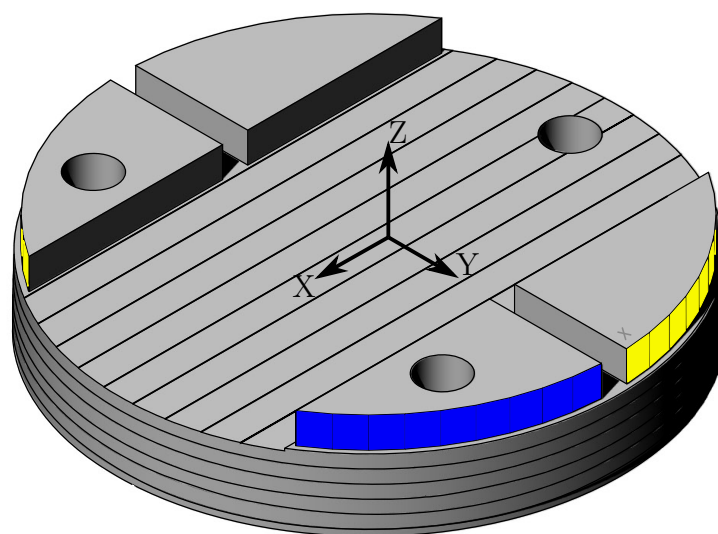


**Figure 7.6:** X-facets (yellow) and Y-facets (blue) for evaluating the thermal machine tool errors in X- and Y-direction. In each direction a set of 9 facets are located on each side of the test piece, so that two facets are nominally parallel aligned. Facet size: 12 mm  $\times$  10.2 mm.

## 7.2 Measurement Procedure

The thermal test piece is designed in a way that it can be evaluated with a CMM, with a touch trigger probe directly on the machine tool for automated inspection, or with measuring equipment usually available in shop floors, for manual inspection.

### 7.2.1 CMM Inspection

For the evaluation of the thermal test piece with a CMM, several features are milled to define the workpiece coordinate system. The surfaces used for definition of the coordinate system are illustrated in Figure 7.7. The top surfaces finished in the first pre-milling step are used to define the X-Y-plane of the coordinate system. The Z-coordinate of the X-Y-surfaces can be determined directly and be used as origin for the coordinate system. The vertical flanks of the large pre-milled notch on the thermal test piece are used to define the orientation of the X-coordinate by building the symmetry line of the opposite flanks. The X- and Y-component of the coordinate system origin are determined by measuring the circular milled top cylindrical surface and by evaluating the center of a least squares circle fit.

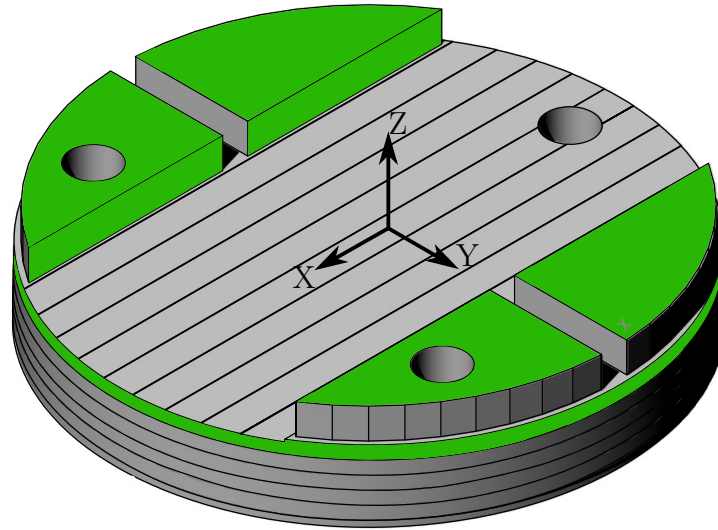


**Figure 7.7:** Illustration of the surfaces (green) to determine the coordinate system of the thermal test piece for inspection on a CMM. Top surface used to define the X-Y-plane, vertical surface to define the X-Z-plane and the circular milled surface to determine the origin of the coordinate system.

To measure the thermal machine tool errors in X- and Y-direction the distance between the nominal parallel facets to the origin of the workpiece coordinate system is measured. The distances of the nominally parallel surfaces milled at the beginning of the test cycle in X-direction  $d_{Xj}(t_0)$  and Y-direction  $d_{Yj}(t_0)$ , with  $j = 1, 2$ , are defining the reference distances for each directions. By comparing the measured distance to the reference distance for each set of facets the thermal error can directly be derived by:

$$E_X(t_i) = \frac{d_{X2}(t_i) - d_{X2}(t_0) - d_{X1}(t_i) - d_{X1}(t_0)}{2}, \quad i = 1 \dots 8 \quad (7.1)$$

$$E_Y(t_i) = \frac{d_{Y2}(t_i) - d_{Y2}(t_0) - d_{Y1}(t_i) - d_{Y1}(t_0)}{2}, \quad i = 1 \dots 8 \quad (7.2)$$

In Equation (7.1) and (7.2) the errors  $E_X$  and  $E_Y$  denote deviations in X- and Y-direction. The values  $d_{Xj}$  and  $d_{Yj}$  are the distances of the nominal parallel facets to the origin of the workpiece coordinate system on the thermal test piece, see Figure 7.7.

During machining the dimension of the workpiece can further change due to thermal expansion. To distinguish this error from the radial growth of the table ( $E_{ROT}$ ) the error  $E_{TTP}$  is introduced, which is measured on the thermal test piece and calculated by:

$$E_{TTP}(t_i) = \frac{l_X(t_i) - l_X(t_0) + l_Y(t_i) - l_Y(t_0)}{2}, \quad i = 1 \dots 8 \quad (7.3)$$

In Equation (7.3)  $l_X(t_i)$  and  $l_Y(t_i)$  are the distances from one facet to its nominal parallel counterpart as illustrated in Figure 7.8.

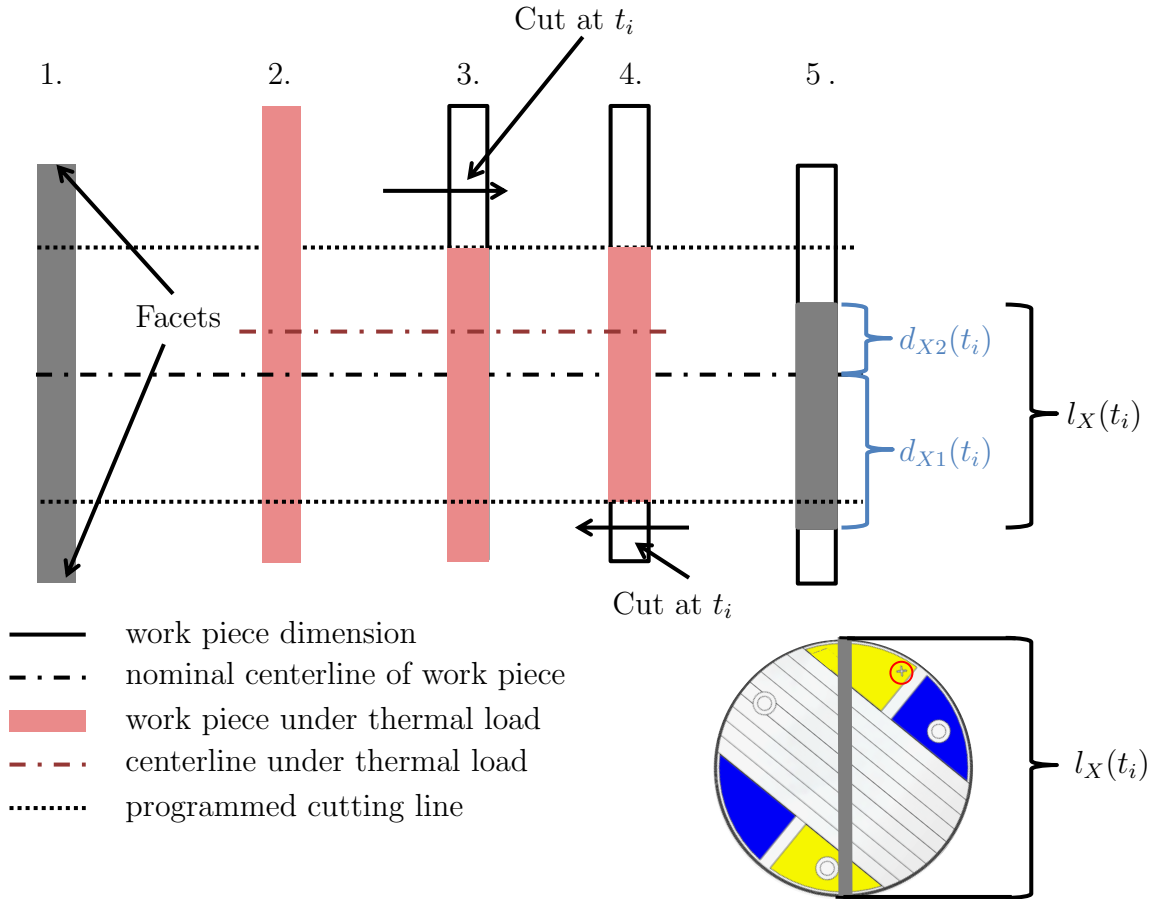


**Figure 7.8:** Milling and evaluation strategy to measure the thermal error in X- and Y-direction as well as the thermal induced radial growth of the test piece. 1. Representation of one pair of facets 2. Machine and workpiece under thermal load 3. and 4. cuts at  $t_i$  on both sides, 5. Evaluation of thermal deviations on the test piece.

Distinguishing directly between table growth  $E_{ROT}$  and the thermal material expansion error of the test piece  $E_{TTP}$  is not possible. The error due to thermal workpiece expansion is mainly influencing  $E_X$  and  $E_Y$ . The X- and Y-facets are milled diametric on opposite sides of the test piece, which allows an evaluation of these effects independently of each other, as seen in Equations (7.1) - (7.3). In the three equations above  $t_i$  is used as the incremental time step between each milling of the measurement surfaces, whereas  $t_0$  is the initial time step and  $t_1$  to  $t_8$  are the subsequent time steps during the thermal test cycle.



Similarly to the X- and Y-deviations, the deviations in Z-direction can be evaluated by

$$E_Z(t_i) = d_Z(t_i) - d_Z(t_0), \quad i = 1 \dots 8 \quad (7.4)$$

In Equation (7.4) the error  $E_Z$  is described as the thermal deviation in Z-direction. The measured lengths  $d_Z$  are the distances from the origin of the coordinate system to the paths for detecting the Z-deviations. In Figure 7.9 an exemplary thermal Z-deviation is illustrated.

Further, the angular deviations in B-direction can be inspected with the thermal test piece. The surfaces perpendicular to the Z-directions are milled by moving the machine tools X-axis only. During the measurement with a CMM a least squares best-fit plane of each measurement surface is computed. Similar to the evaluations in X-, Y- and Z-direction the angular deviations in B can then be evaluated by:

$$E_B(t_i) = \beta(t_i) - \beta(t_0), \quad i = 1 \dots 8 \quad (7.5)$$

where  $\beta(t_i)$  is the angle of the fitted plane in the workpiece coordinate system. The angular deviations in C-direction can theoretically be computed as the angle between two facets at the outer diameter of the thermal test piece is nominally  $6^\circ$ . This evaluation is not implemented as the lengths of the facets are too small for a reasonable analysis. Also the evaluation of the deviation in A-direction is not performed as the cutting tool is slightly inclined to avoid bottom edge cutting effect at the back side of the milling tool. Nevertheless, deviations in A-direction can be evaluated in case of milling the Z-surfaces the workpiece is rotated by  $90^\circ$  and the feed is realized by the Y-axis of the machine tool. In doing so, deviations in B-direction cannot be evaluated.

## 7.2.2 On-Machine Inspection

The on-machine measurements can be performed after the thermal test cycle directly on the machine without unclamping the workpiece from the fixture. A touch trigger probe is used to measure the designed features on the thermal test piece.

The measurement procedure is same to the one used for the inspection on a CMM, except that the rotary table is used to position the test piece for the measurements of the facets. Therefore only a single axis is moved during the measurement with the touch probe and no additional interpolation error of the machine tool is introduced on the measurement result.

The uncertainties of the measurement are comparable to the ones estimated in Chapter 5 and listed in Table 5.3. Due to the symmetric design of the thermal test piece, the evaluation of the thermal errors is possible in a non-air conditioned environment, assuming

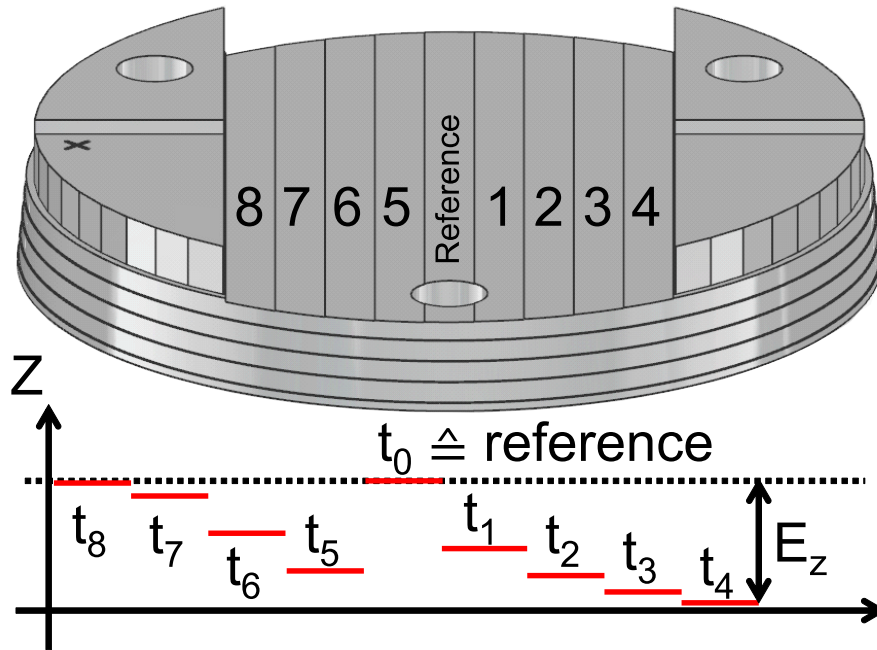


**Figure 7.9:** Illustration of exemplary deviations  $E_Z$  assuming that a negative TCP error in Z-direction is implied during the warm-up phase

that the environmental temperature is sufficiently stable during the measurement of each direction.

### 7.2.3 Manual Inspection

Measurement equipment like precision micrometer gauge, dial gauge, depth gauge or straight edge can be used to analyze the thermal test piece. Also for this form of inspection it is not necessary to evaluate the thermal test piece in air conditioned environment due to the symmetric design of the thermal test piece. It has to be taken into account that the measurement time is increased compared to the on-machine inspection and therefore a stable environmental temperature during the inspection has to be guaranteed. The repetition of a measurement is only marginal influenced by the temperature change between two measurements. Assuming a temperature difference  $\Delta T$  of  $10^\circ\text{C}$  between two evaluations of the aluminum thermal test piece ( $\alpha_{Alu} = 22 \mu\text{m}/\text{mK}$ ) and a measured error  $E_i$  of  $100 \mu\text{m}$ , a measurement deviation assessment  $U_{\Delta T}$  of  $0.022 \mu\text{m}$  can be estimated according to Equation 7.6

$$U_{\Delta T} = \alpha_{Alu} \cdot \Delta T \cdot E_i \quad (7.6)$$

### Manual Inspection on the Machine Tool

After the thermal test, the test piece can be evaluated directly on the machine, by using a dial gauge. To quantify the error  $E_Z$  the dial gauge is mounted in a fixture, so that all paths on the test piece are accessible. By moving the linear axes, the relative distances  $d_Z(t_i)$  between paths and the reference in Z-direction  $d_Z(t_0)$ , can be measured and used to calculate the error  $E_Z$  according to Equation 7.4.

To evaluate the errors  $E_X$ ,  $E_Y$  and  $E_{TTP}$  the dial gauge is fixed close to the machine table, in a way that all facets can be reached by rotating the C-axes of the machine tool. The dial gauge is set to zero at the reference facet. The distance of the facets to the corresponding reference facet in each segment  $g_{Xj}$  respectively  $g_{Yj}$  is measured by rotating the machine table. The acquired distances can be used to solve Equations (7.7) - (7.9).

$$E_X(t_i) = \frac{g_{X2}(t_i) - g_{X1}(t_i)}{2}, \quad i = 1 \dots 8 \quad (7.7)$$

$$E_Y(t_i) = \frac{g_{Y2}(t_i) - g_{Y1}(t_i)}{2}, \quad i = 1 \dots 8 \quad (7.8)$$

$$E_{TTP}(t_i) = \frac{g_{Y2}(t_i) + g_{Y1}(t_i) + g_{X2}(t_i) + g_{X1}(t_i)}{4}, \quad i = 1 \dots 8 \quad (7.9)$$

The measurement duration of a segment takes approximately 5 minutes and in total about 30 minutes. The same measurement procedure can be performed using a touch trigger probe.

### Manual Inspection outside the Machine Tool

Alternatively, the test piece can be removed from the machine tool table and measured outside of the machine tool. It has to be noted, that due to the unclamping of the workpiece additional deformations can be introduced that corrupt the measurement of the thermal deformations. A depth gauge supported at the top surface of the thermal test piece can be used to measure the distances to the milled paths. The Z-deviations can be calculated using Equation 7.4. It is also possible that the Z-deviations are visually inspected for qualitative purposes. A straight edge can be inserted into the milled notch. The thermal errors are usually in the range of several tens of micrometers, therefore the thermal deviations can be seen by naked eye.

Additionally, a micrometer gauge can be used to measure the distances  $l_X(t_i)$  and  $l_Y(t_i)$  of

the nominal parallel facets. With this method only the error  $E_{TTP}$  can be calculated using Equation 7.3. To measure the errors  $E_X$  and  $E_Y$  outside of the machine, a more complex setup is needed. Using a flat surface and a measuring prism to align the test piece, the facets can be measured with a dial gauge, similar as the measurement in the machine. The test piece needs to be rotated by  $6^\circ$ , to measure perpendicular to the facet surface. To the fact, that the rotation is done manually additional measurement errors have to be taken into account.

### 7.3 Validation of Thermal Test Piece

A comparison of thermal measurements of the machine tool and the workpiece deviations is used in this chapter as a validation method for different inspection methods.

The machine tool under investigation is the 5-axis machining center DMG Mori NMV 5000 DCG, described in Section 5.1. The used validation test cycle includes a 4 hour warm up phase and a 4 hour cool down phase, one set of measurement surfaces each hour is milled. The thermal load is induced into the machine structure by the rotary axis of the machine tool. In each hour of the warm up cycle the table rotates at the maximum speed of 1200 rpm. During the cool down phase the machine is in NC-hold.

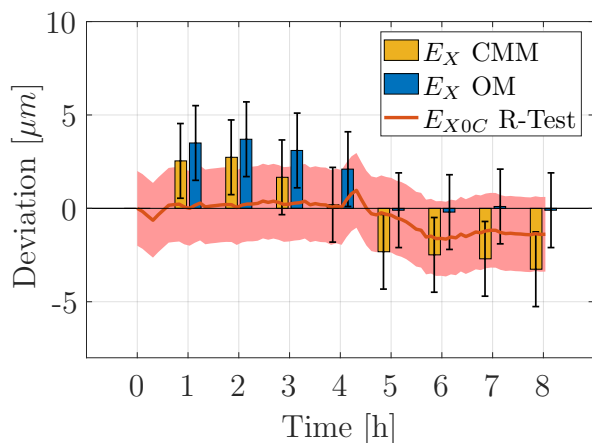
As an independent comparison of the measured thermal errors on the test piece an on-machine measurement, as presented in Chapter 5, is used. It is further referenced as R-Test to distinguish between the on-machine inspection of the test piece.

The CMM used for the evaluation of the results is located in an air conditioned measuring room. The room temperature is controlled to  $20 \pm 0.3^\circ\text{C}$ . The used CMM is specified with a maximal permissible error (MPE) of  $1.2 \mu\text{m} + L/400 \text{ mm}$ , according to ISO 10360-2 [55]. The on-machine (OM) measurements repeatability is guaranteed to be  $1 \mu\text{m}$  at a probing velocity of 480 mm/min by the manufacturer. The measurements are performed with a probing velocity of 200 mm/min, a probe length of 50 mm and a probe tip diameter of 6 mm. In addition to the touch trigger probe the machine repeatability of  $1 \mu\text{m}$  has to be added which results in a total uncertainty of  $2 \mu\text{m}$  for this measurement.

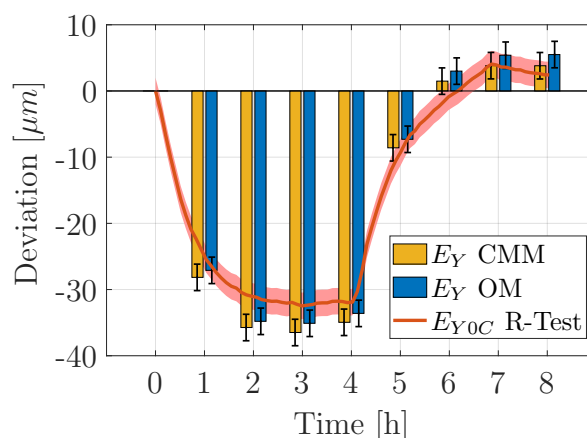
The uncertainties for the R-Test are stated in Chapter 5 and listed in Table 5.3.

Figure 7.10 shows the comparison of the evaluation of the thermal test piece with the inspection method CMM and on-machine (OM). The OM measurements of the test piece are in good agreement compared to the results of the CMM measurements. As a consequence of the thermally symmetric design of the machine tool, the deviations in X-axis direction are negligible small. This can be seen in the measurements of  $E_X$  in Figure 7.10a. The general agreement between CMM and OM measurements is due to the fact that the

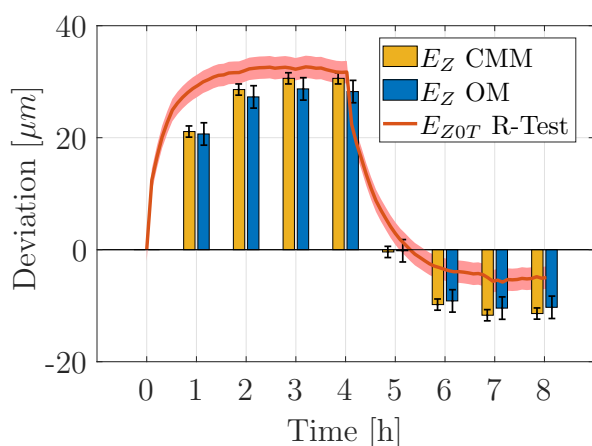
design of the test piece minimizes the influence of the geometrical errors of the machine tool on the on-machine measurement of the test piece. In comparison with the R-Test measurements the test piece inspections show a very similar behavior.



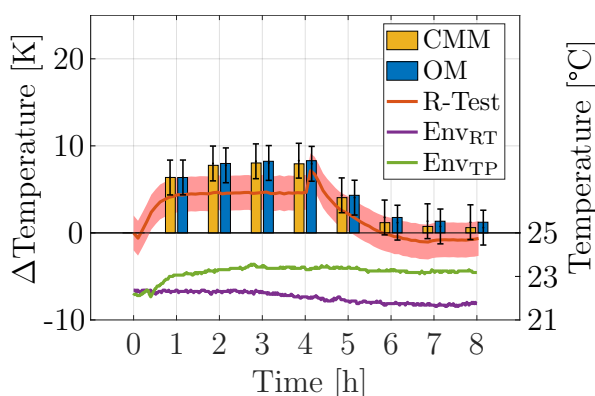
(a) Measured thermal error  $E_X$  on thermal test piece compared with  $E_{X0C}$  measured with R-Test.



(b) Measured thermal error  $E_Y$  on thermal test piece compared with  $E_{Y0C}$  measured with R-Test.



(c) Measured thermal error  $E_Z$  on thermal test piece compared with  $E_{Z0T}$  measured with R-Test.



(d) Calculated test piece and table temperature change, evaluated with CMM, OM and R-Test measurements.

**Figure 7.10:** Evaluation of thermal test piece and R-Test: a) Thermal error  $E_X$  b) Thermal error  $E_Y$  c) Thermal error  $E_Z$  d) Temperature change of the test piece (OM and CMM) as well as the machine table (R-Test). The measurement uncertainty is illustrated by the light red surface and the error bars respectively. Additionally the environmental temperature is illustrated in d).

Since the error  $E_{TTP}$  is evaluating the radial growth of the test piece and the error  $E_{R0T}$ , measured by the R-Test, is measuring the radial growth of the machine table, a direct comparison is not possible since those bodies consist of materials with very different thermal expansion coefficients. Therefore the relative temperature change  $\Delta T$  of the test piece

and the machine table is evaluated. The temperature change can be calculated as follows:

$$\Delta T = \frac{E}{\alpha_{Material} \cdot R} \quad (7.10)$$

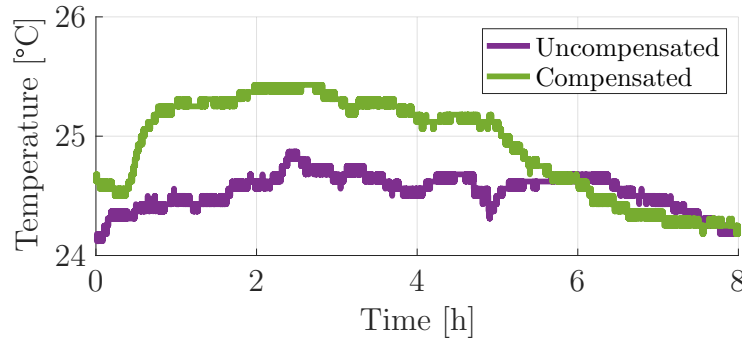
where  $E$  is the thermal radial expansion error of the test pieces  $E_{TTP}$  respectively  $E_{ROT}$  for the machine table.  $\alpha_{Material}$  is either the thermal expansion coefficient of the machine table or the test piece material.  $R$  is defined by the radius of the thermal test piece or the radial position of the precision sphere used for the R-Test.

Figure 7.10d shows the temperature changes  $\Delta T$ , calculated with Equation (7.10), during the test cycle. The material expansion coefficient  $\alpha_{Cast} = 11\mu m/m K$  for the cast iron table and  $\alpha_{Alu} = 22\mu m/m K$  for the aluminum test piece is assumed. The radial position  $R$  of the precision sphere for the R-Test is 160 mm. The radius  $R$  of the test piece is 97.5 mm. This method helps comparing the R-Test and the test piece results. The results show a good comparability between all three measurements. A temperature rise of up to 8 K can be observed. It also shows a peak temperature rise in the R-Test measurement, at the beginning of the cool-down phase, where the forced convection of the table rotation is missing.

## 7.4 Compensation with TALC

To show the capability of the TALC compensation a thermal test piece with and without TALC is manufactured. The thermal load case for both test pieces is chosen similar to the validation experiments. A 4 hour warm up of the C-axis by rotating with a speed of 1200 rpm, is followed by a 4 hour cool down phase where the machine tool is kept in NC-hold. Once every hour five measurement surfaces are machined. Since the machine tool is located in a non-controlled environment and the experiments have to be performed in a sequential order, the ambient conditions for both experiments are slightly different, as shown in Figure 7.11.

Following the cool down phase the thermal test pieces are measured directly on the machine. As shown in the previous section on-machine measurements of the test piece performed with a touch probe are comparable to the CMM results, since the measurements are relative in nature and therefore only influenced by the temperature change during the on-machine measurement of the specific feature. The measurement of one set of features takes approximately 2 minutes. Therefore a constant temperature can be assumed during the measurement time. The resulting thermal deviations measured on the two test pieces are shown in Figure 7.12.



**Figure 7.11:** Measured environmental temperature during the manufacturing of the two test pieces, one with and the other without TALC compensation.

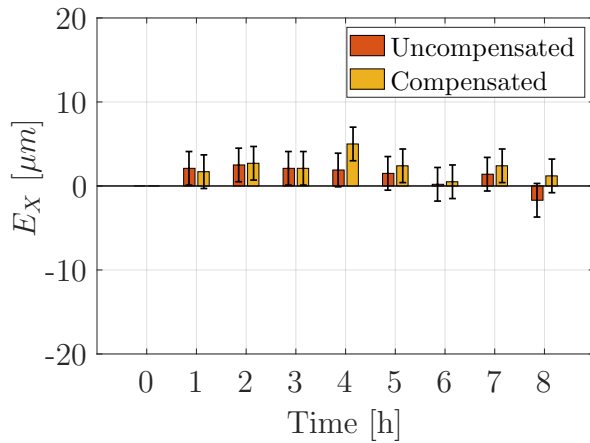
The thermal prediction model for the compensated test piece was trained on load case C, introduced in Section 6.3, with the optimal set of parameters shown in Table 6.3. Before the start of the manufacturing the ARX model parameters are loaded and the compensation starts right away.

The parameters for the compensation during the manufacturing of the test piece are depicted in Table 7.1. For the compensation with TALC an on-machine measurement of the precision sphere is performed every hour, after the machining of the measurement surfaces. Therefore the measurement surfaces of the test piece are milled with a compensation that is running on predictions since 1 hour.

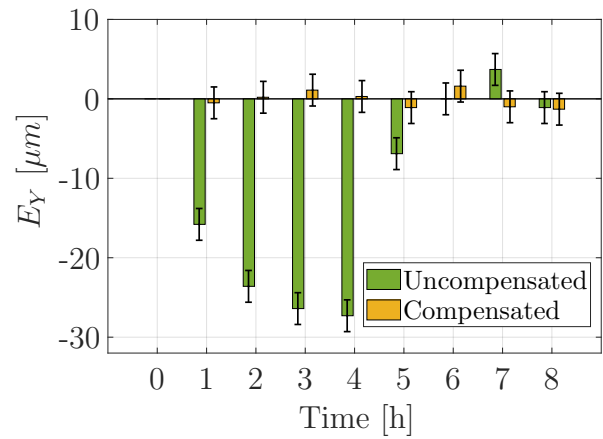
Parameter	Value
Measurement Interval	1 h
Measurement Interval (NG)	5 min
Nr. of measurements in NG	9
Action Control Limit	5 $\mu\text{m}$ resp. 15 $\mu\text{m}/\text{m}$
Parameter Update Interval	8 h
Maximum Output Order ( $n_a$ )	10
Maximum Input Order ( $n_b$ )	10

**Table 7.1:** Parameters used for the manufacturing of the test piece with TALC compensation.

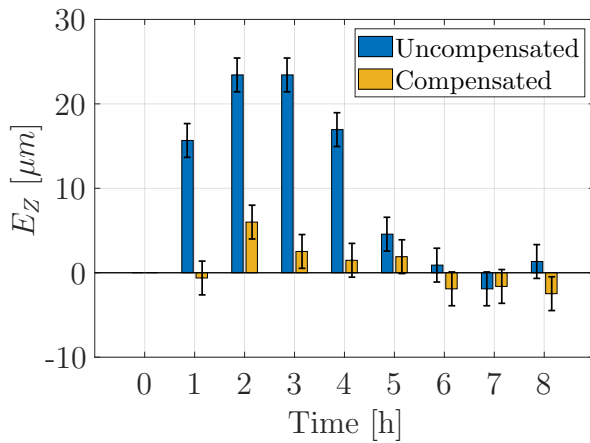
Figure 7.12 shows clearly, that with the TALC compensation the thermal errors of the test piece can be significantly reduced. The biggest remaining errors are  $E_Z$  and  $E_{TTP}$  (Figure 7.12c and 7.12d), this can be explained by the fact, that the TALC is trained to compensate the relative deviations of the machine tool table to the TCP. Not taken into account is the workpiece itself. In the case of the thermal test piece, which consists of



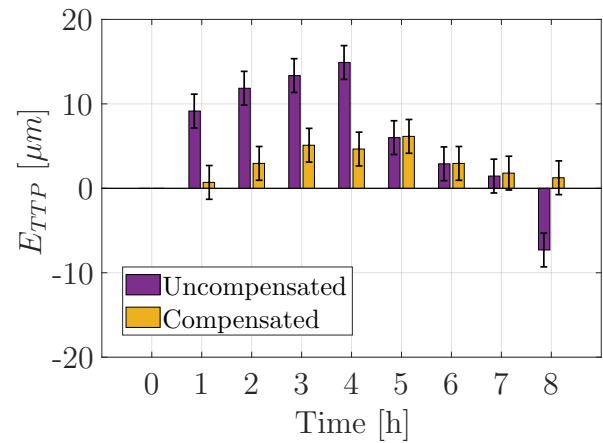
(a) Measured thermal error  $E_X$  on thermal test piece with and without TALC compensation.



(b) Measured thermal error  $E_Y$  on thermal test piece with and without TALC compensation.



(c) Measured thermal error  $E_Z$  on thermal test piece with and without TALC compensation.



(d) Measured thermal error  $E_{TTP}$  on thermal test piece with and without TALC compensation.

**Figure 7.12:** Evaluation of thermal errors with and without TALC compensation shown on a thermal test piece. The load case consists of C-axis rotation with 1200 rpm for 4 hours followed by a 4 hour stand still. The error bars illustrate the measurement uncertainty of the test piece with on-machine measurement ( $U(k=2)=2 \mu m$ ).

aluminum and has approximately double the thermal expansion coefficient as cast iron, the influence is not negligible. The aforementioned errors are directly influenced by the thermal growth of the workpiece and therefore only partially compensated. In the X- and Y-directions which are nearly unaffected by the growth of the workpiece, the errors can be kept close to zero in the range of the measurement uncertainty.

For a quantitative comparison of both test pieces three characteristic values are evaluated. These values are the span of the change of displacement along each axis direction as well as the change of distortion of the test piece, for three distinct time periods. These periods



are the first hour, the first 4 hours and the whole duration of the experiment. Table 7.2 shows the results of this evaluation for both test pieces. It can be seen, that for all evaluated errors on the test piece, except  $E_X$ , a drastic reduction of the span of errors can be achieved. As mentioned the error  $E_X$  is small in magnitude and therefore stronger affected by the measurement uncertainty for the TALC as well as for the evaluation of the test piece.

	$E_X$		$E_Y$		$E_Z$		$E_{TTP}$	
	UC [ $\mu m$ ]	C [ $\mu m$ ]	UC [ $\mu m$ ]	C [ $\mu m$ ]	UC [ $\mu m$ ]	C [ $\mu m$ ]	UC [ $\mu m$ ]	C [ $\mu m$ ]
1h	2.1	1.7	15.8	0.5	15.7	0.6	9.2	0.7
4h	2.5	5	27.3	1.6	23.4	6.6	14.9	5.1
8h	4.2	5	31	2.9	25.3	9.1	22.2	6.2

**Table 7.2:** Evaluation of the span of the changes of displacement for different periods of time for the uncompensated (UC) and the compensated (C) thermal test piece.



## Chapter 8

# Conclusion and Outlook

In this thesis an adaptive learning control for thermal error compensation for machine tools is developed. The presented approach consists of the following parts:

- Dynamic thermal error modeling
- Process-intermittent probing for thermal error estimation
- Adaptive self-learning compensation of thermal errors

In the course of this thesis it is shown, that the underlying phenomena of the thermo-mechanical behavior is of dynamical nature and it is therefore necessary to develop a suitable dynamic model to capture the essence of the physical effects. It is derived, that based on the partial differential equation of heat conduction and thermal elongation of a simple rod with changing heat loads, an ARX model is capable of modeling the thermo-mechanical behavior. The model is compared and validated based on simulations performed on a simple FEM model of a machine tool. The residual analysis confirms the superiority of the ARX model over the others. With the use of past and present inputs as well as past predictions the full potential of the identified model can be assessed.

To complete the implementation of an autonomous thermal error control, an on-machine measurement cycle for thermal error characterization is presented. The cycle is capable of measuring the five thermal position and orientation errors as well as the deviations of the table surface of a rotary axis in a single setup. As a measurement instrument the touch trigger probe can be used, which is present in most modern machining centers. Therefore no additional measurement equipment or complex artifacts need to be purchased nor installed into the machine tool. This measurement cycle enables the fully automated process-intermittent probing and evaluation of the thermal errors during production.

To predict and compensate the occurring thermal errors of 5-axis machine tools, the ARX modeling approach and the on-machine measurement cycle are combined. This newly developed approach is called thermal adaptive learning control (TALC), since it is capable of independently learning the correlation between the chosen inputs and the thermal TCP deviations as well as adapting the measurement intervals based on predefined action control limits. Therefore a long-term stable compensation over the whole use-phase of the machine tool can be ensured. Since the TCP measurements are performed in arbitrary time intervals the approach is extended by the use of a weighted least-squares estimation for the model parameters.

A sensitivity analysis is conducted to identify the most influential parameters for the TALC compensation approach. Since an increased number of on-machine measurements naturally increases the prediction quality of the compensation, but drastically lowers the productivity of the used machine tool, an optimum has to be found, where the quality criteria are still met with the highest possible productivity. It can be concluded, that shorter calibration phases lead to decreased model quality, if not paired with increased measurement frequency and/or longer NG phases. Therefore a machine tool user or builder needs to decide, if a longer calibration phase is feasible and can be e.g. performed over the weekend or it is preferable to have a short calibration phase and more regular recalibrations of the thermal error model. In the long-term the productivity decrease of long calibration phases will not affect the overall productivity of the machine tool during its whole lifetime.

The TALC compensation is validated with two experiments performed on a 5-axis machine tool. The first experiment tests the long-term robustness and adaptability of the approach while turning the C-axis of the machine tool at arbitrary speeds. The experiment showed, that a stable compensation over a duration of 178 hours is achievable and that the robustness of the compensation increases with duration of the experiment, since more data is gathered and the model is continuously updated. A reduction of the thermal error evaluated with the 99<sup>th</sup> Percentile value (P99) of up to 80% is accomplished.

The second experiment aims at testing the model robustness under fast changing boundary conditions. Therefore the cutting fluid supply is switched on and off during arbitrary intervals while rotating the C-axis at different speeds. It is shown, that the TALC is capable of self-learning these sudden changes and adapting the measurement intervals accordingly. The compensation showed a reduction of the P99 value of more than 88% with an absolute reduction of 38.3  $\mu\text{m}$ . Even under these harsh conditions a total productivity rate of 95% is already achieved after 58 hours.

---

To demonstrate the influence of the thermally induced errors on an actual workpiece, a thermal test piece is developed. The test piece offers the possibility to evaluate the thermal deviations in all three spatial directions, one angular deviation, as well as the distortion of the workpiece itself. The workpiece is designed to be measured directly on the machine or on a CMM. It also offers the possibility to use simple handheld gauges or visual inspections for quick checks under workshop conditions.

To validate the thermal test piece, a comparison of the on-machine measurement and the measurement on a CMM with an R-Test is performed. The comparison shows, that the two measurement methods yield comparable results and that the R-Test shows same trends and magnitudes.

For the validation of the TALC on a workpiece, two thermal test pieces are manufactured, one test piece without compensation and one with active TALC compensation. The experiment shows, that the major share of thermally induced workpiece errors can be reduced by the TALC approach. For the compensation with TALC the workpiece distortion itself is not taken into account. Therefore, the directions affected by the thermal growth of the test piece show bigger residual errors than the ones not affected. In the directions not affected by the growth of the test piece, the errors can be kept close to zero for the whole duration of the experiment.

For future developments of thermal compensations of machine tools, it is necessary to extend the on-machine measurement cycle to all the machine tool axes. The challenge hereby lays on the feasibility of developing a fast, precise, robust and mostly artifact free measurement cycle to capture the most dominant thermal errors of 5-axis machine tools. A possible solution is the tracing of a feature of the machine table, the fixture or directly the workpiece. Additionally a robust error separation has to be implemented, so that each error is independent, otherwise the MISO approach is not valid anymore. Due to the increased amount of considered thermal errors additional attention has to be paid to the computational costs for the model estimation since the amount of model parameters is drastically increasing for each added axis.

Furthermore, future work should aim at developing intelligent algorithms to fully automatize the optimal input selection for the TALC compensation, especially when more than one axis is compensated. An optimal set of inputs for each axis respectively each thermal error should be assigned. The static approach of regular measurement intervals after the calibration phase should be substituted with a more intelligent algorithm to dynamically adjust the time between measurements and model parameter updates. An approach based on triggered measurements by out of ordinary input changes seems feasible. Additionally, it is worth considering to develop an algorithm to dynamically adjust the action control limits to the desired precision of the machine tool.

As the results of the test piece show, the thermal distortion of the workpiece itself is not yet considered in the TALC. This can be implemented in the future by taking into account the thermal expansion coefficient and the dimension of the workpiece as additional inputs for the ARX model. The challenge hereby lays in the varieties of different materials, shapes and clamping systems, therefore a suitable approach to find an optimal input signal, as for example a workpiece temperature, is necessary.

Another influence that was not investigated in this work is the process itself, including the elongation of the tool. Since the temperature increase of the tool is highly dependent on the actual cutting conditions, it is also highly variable. As other researchers showed, the influence can be measured with tactile or laser measurements of the tool length paired with measurements of the structure itself. This approach seems very promising but a compensation approach based on such a procedure requires a large database of different tools under varying cutting conditions.

# Bibliography

- [1] M. Abouridouane, F. Klocke, B. Döbbeler, 2016, Analytical temperature prediction for cutting steel, *CIRP Annals - Manufacturing Technology*, 65, pp. 77–80.
- [2] API Services, 2006, XD Laser-Multi-Dimensional Laser Measurement System for CNC Calibration.
- [3] T. Augspurger, M. Brockmann, Y. Frekers, F. Klocke, R. Kneer, 2016, Experimental Investigation of Thermal Boundary Conditions during Metal Cutting, *Procedia CIRP*, 46, pp. 119–122.
- [4] B+B Thermo-Technik GmbH, 2016, Temperature measurement system TLOG20 connections RS232, RS485, USB.
- [5] P. Benner, S. Gugercin, K. Willcox, 2013, A survey of model reduction methods for parametric systems, *MPI Magdeburg Preprints, MPIMD*, pp. 1–36.
- [6] E. Bitar-Nehme, J. R. R. Mayer, 2016, Thermal volumetric effects under axes cycling using an invar R-test device and reference length, *International Journal of Machine Tools and Manufacture*, 105, pp. 14–22.
- [7] F. Bleicher, F. Puschitz, A. Theiner, 2006, Laser based measurement system for calibrating machine tools in 6 DOF, in: *Annals of DAAAM & Proceedings of the International DAAAM Symposium*.
- [8] B. Bossmanns, J. F. Tu, 2001, A Power Flow Model for High Speed Motorized Spindles - Heat Generation Characterization, *Journal of Manufacturing Science and Engineering*, 123, p. 494.
- [9] A. Botchkarev, 2019, Performance Metrics (Error Measures) in Machine Learning Regression, Forecasting and Prognostics: Properties and Typology, *Interdisciplinary Journal of Information, Knowledge, and Management*, 14, pp. 45–76.

- 
- [10] T. Boye, G. Günther, M. Fritz, 2015, Increasing 5-axis accuracy by using a cross-grid encoder for volumetric compensation, in: *Proceedings of Laser Metrology and Machine Performance XI*, pp. 61–70.
- [11] C. Brecher, A. Wissmann, 2009, Optimierung des thermischen Verhaltens von Fräsmaschinen, *ZWF Zeitschrift für wirtschaftlichen Fabrikbetrieb*, 104, pp. 437–441.
- [12] C. Brecher, A. Wissmann, 2011, Compensation of thermo-dependent machine tool deformations due to spindle load: Investigation of the optimal transfer function in consideration of rough machining, *Production Engineering*, 5, pp. 565–574.
- [13] C. Brecher, P. Hirsch, M. Weck, 2004, Compensation of Thermo-elastic Machine Tool Deformation Based on Control internal Data, *CIRP Annals - Manufacturing Technology*, 53, pp. 299–304.
- [14] C. Brecher, M. Fey, M. Wennemer, 2016, The influence of coolant on the thermo-elastic machine tool behavior, in: *Proceedings of the euspen's 16th International Conference & Exhibition*.
- [15] C. Brecher, M. Fey, M. Wennemer, 2016, Volumetric measurement of the transient thermo-elastic machine tool behavior, *Production Engineering*, 10, pp. 345–350.
- [16] C. Brecher, J. Behrens, M. Brozio, T. H. Lee, D. Sensen, 2017, Rapid Geometric Calibration of Five-axis Machine Tool using Dynamic R-test, in: *Proceedings of the 7th International Conference of Asian Society for Precision Engineering and Nanotechnology*.
- [17] C. Brecher, J. Behrens, T. H. Lee, S. Charlier, 2017, Calibration of five-axis machine tool using R- test procedure, in: *Proceedings of the 12th International Conference and Exhibition on Laser Metrology, Machine Tool, CMM and Robotic Performance XII*.
- [18] C. Brecher, R. Spierling, F. du Bois-Reymond, M. Fey, 2017, Thermo-elastic deformation of rotary axes, in: *Proceedings of the 12th International Conference and Exhibition on Laser Metrology, Machine Tool, CMM and Robotic Performance XII*.
- [19] C. Brecher, J. Behrens, M. Klatte, T. H. Lee, F. Tzanetos, 2018, Measurement and analysis of thermo-elastic deviation of five-axis machine tool using dynamic R-test, in: *Procedia CIRP*, volume 77, Elsevier, pp. 521–524.
- [20] B. Bringmann, W. Knapp, 2006, Model-based 'Chase-the-Ball' calibration of a 5-axes machining center, *CIRP Annals - Manufacturing Technology*, 55, pp. 531–534.



- 
- [21] B. Bringmann, 2007, Improving Geometric Calibration Methods for Multi-Axis Machining Centers by Examining Error Interdependencies Effect, Diss., ETH Zürich.
- [22] J. Bryan, 1968, International Status of Thermal Error Research, *Annals of the CIRP*, 16, pp. 203–2015.
- [23] J. Bryan, 1990, International Status of Thermal Error Research, *CIRP Annals - Manufacturing Technology*, 39, pp. 645–656.
- [24] M. A. Chapman, 2003, Limitations of laser diagonal measurements, *Precision Engineering*, 27, pp. 401–406.
- [25] J. S. Chen, J. X. Yuan, J. Ni, S. M. Wu, 1993, Real-time Compensation for Time-variant Volumetric Errors on a Machining Center, *Journal of Engineering for Industry*, 115, pp. 472–479.
- [26] J. S. Chen, 1995, Computer-aided accuracy enhancement for multi-axis CNC machine tool, *International Journal of Machine Tools and Manufacture*, 35, pp. 593–605.
- [27] DMG Mori, 2014, NMV 5000 DCG / NMV 8000 DCG Product Catalogue.
- [28] M. A. Donmez, D. S. Blomquist, R. J. Hocken, C. R. Liu, M. M. Barash, 1986, A general methodology for machine tool accuracy enhancement by error compensation, *Precision Engineering*, 8, pp. 187–196.
- [29] M. Ess, T. Liebrich, W. Knapp, K. Wegener, 2011, Thermal Displacements of Rotary Axes, in: *Proceedings of MTTRF Meeting*.
- [30] M. Ess, 2012, Simulation and Compensation of Thermal Errors of Machine Tools, Diss., ETH Zürich.
- [31] Etalon AG, The LaserTRACER - the Solution to your Accuracy Requirements.
- [32] J. M. Fines, A. Agah, 2008, Machine tool positioning error compensation using artificial neural networks, *Engineering Applications of Artificial Intelligence*, 21, pp. 1013–1026.
- [33] G. H. J. Florussen, F. L. M. Delbressine, P. H. J. Schellekens, 2003, Assessing thermally induced errors of machine tools by 3D length measurements, *CIRP Annals - Manufacturing Technology*, 52, pp. 333–336.
- [34] G. H. J. Florussen, 2002, Accuracy analysis of multi-axis machines by 3D length measurements, Diss., TU Eindhoven.

- [35] S. Fraser, M. Osman, 1998, Modelling, Identification and Control of Thermal Deformation of Machine Tool Structures, Part 1: Concept of Generalized Modelling, *Journal of Manufacturing Science and Engineering*, 120, pp. 623–631.
- [36] M. Fujishima, K. Narimatsu, N. Irino, Y. Ido, 2018, Thermal displacement reduction and compensation of a turning center, *CIRP Journal of Manufacturing Science and Technology*, 22, pp. 111–115.
- [37] M. Gebhardt, P. von Cube, W. Knapp, K. Wegener, 2012, Measurement set-ups and -cycles for thermal characterization of axes of rotation of 5-axis machine tools, in: *Proceedings of the 12th euspen International Conference*.
- [38] M. Gebhardt, M. Ess, S. Weikert, W. Knapp, K. Wegener, 2013, Phenomenological compensation of thermally caused position and orientation errors of rotary axes, *Journal of Manufacturing Processes*, 15, pp. 452–459.
- [39] M. Gebhardt, J. Mayr, N. Furrer, T. Widmer, S. Weikert, W. Knapp, 2014, High precision grey-box model for compensation of thermal errors on five-axis machines, *CIRP Annals - Manufacturing Technology*, 63, pp. 509–512.
- [40] M. Gebhardt, 2014, Thermal behaviour and compensation of rotary axes in 5-axis machine tools, Diss., ETH Zurich.
- [41] E. Gomez-Acedo, A. Olarra, J. Orive, L. N. Lopez De La Calle, 2013, Methodology for the design of a thermal distortion compensation for large machine tools based in state-space representation with Kalman filter, *International Journal of Machine Tools and Manufacture*, 75, pp. 100–108.
- [42] Y. Hatamura, T. Nagao, M. Mitsuishi, K. Kato, S. Taguchi, T. Okumura, G. Nakagawa, H. Sugishita, 1993, Development of an Intelligent Machining Center Incorporating Active Compensation for Thermal Distortion, *CIRP Annals - Manufacturing Technology*, 42, pp. 549–552.
- [43] Heidenhain, Messgeräte zur Abnahme und Kontrolle von Werkzeugmaschinen.
- [44] P. Hernández-Becerro, J. Mayr, P. Blaser, F. Pavliček, K. Wegener, 2018, Model Order Reduction of Thermal Models of Machine Tools with Varying Boundary Conditions, in: *Proceedings of the 1st Conference on Thermal Issues in Machine Tools*.
- [45] O. Horejš, M. Mareš, L. Novotný, 2012, Advanced modelling of thermally induced displacements and its implementation into standard CNC controller of horizontal milling center, *Procedia CIRP*, 4, pp. 67–72.

- [46] E. B. Hughes, A. Wilson, G. N. Peggs, 2000, Design of a high-accuracy CMM based on multi-lateration techniques, *CIRP Annals - Manufacturing Technology*, 49, pp. 391–394.
- [47] HYGROSENSE INSTRUMENTS GmbH, 2006, PC Temperature Measuring System. Description of Calibration.
- [48] S. Ibaraki, T. Hata, 2010, A new formulation of laser step diagonal measurement-three-dimensional case, *Precision Engineering*, 34, pp. 516–525.
- [49] S. Ibaraki, W. Knapp, 2012, Indirect measurement of volumetric accuracy for three-axis and five-axis machine tools: A review, *International Journal of Automation Technology*, 6, pp. 110–124.
- [50] S. Ibaraki, Y. Ota, 2014, A machining test to calibrate rotary axis error motions of five-axis machine tools and its application to thermal deformation test, *International Journal of Machine Tools and Manufacture*, 86, pp. 81–88.
- [51] S. Ibaraki, W. Goto, A. Matsubara, 2006, Issue in laser step diagonal measurement and their remedies, in: *Proceedings of 2006 ISFA*, pp. 26–29.
- [52] S. Ibaraki, T. Hata, A. Matsubara, 2009, A new formulation of laser step-diagonal measurement - two-dimensional case, *Precision Engineering*, 33, pp. 56–64.
- [53] S. Ibaraki, C. Oyama, H. Otsubo, 2011, Construction of an error map of rotary axes on a five-axis machining center by static R-test, *International Journal of Machine Tools and Manufacture*, 51, pp. 190–200.
- [54] S. Ibaraki, P. Blaser, M. Shimoike, N. Takayama, M. Nakaminami, Y. Ido, 2016, Measurement of thermal influence on a two-dimensional motion trajectory using a tracking interferometer, *CIRP Annals - Manufacturing Technology*, 65, pp. 483–486.
- [55] ISO 10360-2, 2009, Geometrical product specifications (GPS) - Acceptance and reverification tests for coordinate measuring machines (CMM) - Part 2: CMMs used for measuring linear dimensions.
- [56] ISO 10791-10, 2007, Test conditions for machining centres - Part 10: Evaluation of thermal distortions.
- [57] ISO 10791-1, 2015, Test conditions for machining centres - Part 1: Geometric tests for machines with horizontal spindle (horizontal Z-axis).
- [58] ISO 10791-6, 2014, Test conditions for machining centres-Part 6: Accuracy of speeds and interpolations.

- 
- [59] ISO 10791-7, 2014, Test conditions for machining centers - Part 7: Accuracy of finished test pieces.
- [60] ISO 1, 2016, Geometrical product specifications (GPS) - Standard reference temperature for the specification of geometrical and dimensional properties.
- [61] ISO 13041-8, 2005, Test conditions for numerically controlled turning machines and turning centres - Part 8: Evaluation of thermal distortions.
- [62] ISO 230-1, 2012, Test code for machine tools - Part 1: Geometric accuracy of machines operating under no-load or quasi-static conditions.
- [63] ISO 230-2, 2014, Test code for machine tools - Part 2: Determination of accuracy and repeatability of positioning of numerically controlled axes.
- [64] ISO 230-3, 2007, Test code for machine tools - Part 3: Determination of thermal effects.
- [65] ISO 230-4, 2005, Test code for machine tools - Part 4: Circular tests for numerically controlled machine tools.
- [66] ISO 230-6, 2002, Test code for machine tools - Part 6: Determination of positioning accuracy on body and face diagonals (Diagonal displacement tests).
- [67] ISO 230-7, 2015, Test code for machine tools-Part 7: Geometric accuracy of axes of rotation.
- [68] JCGM, 2008, Evaluation of measurement data - Guide to the expression of uncertainty in measurement (GUM), International Organization for Standardization Geneva, 50, p. 134.
- [69] J. Jedrzejewski, W. Modrzycki, 1992, A New Approach to Modelling Thermal Behaviour of a Machine Tool under Service Conditions, *CIRP Annals - Manufacturing Technology*, 41, pp. 455–458.
- [70] K.-D. Kim, S.-C. Chung, 2001, Quick identification of spatial-variant thermal errors using on-machine measurement of a 3D artifact, in: *Proceedings of the 29th North American manufacturing research conference*, Gainesville, Florida, pp. 593–600.
- [71] K. D. Kim, S. C. Chung, 2003, On-machine inspection system: Accuracy improvement using an artifact, *Journal of Manufacturing Systems*, 22, pp. 299–308.

- [72] J.-J. Kim, Y. H. Jeong, D.-W. W. Cho, 2004, Thermal behavior of a machine tool equipped with linear motors, *International Journal of Machine Tools and Manufacture*, 44, pp. 749–758.
- [73] W. Klingauf, 2009, Der schnelle Draht zwischen PC und CNC, *WB Werkstatt + Betrieb*, 1, pp. 58–60.
- [74] F. Klocke, M. Brockmann, S. Gierlings, D. Veselovac, 2015, Analytical model of temperature distribution in metal cutting based on Potential Theory, *Mechanical Sciences*, 6, pp. 89–94.
- [75] K. Lau, Y.-Q. Liu, 1997, Five-axis/six-axis laser measuring system (Patent).
- [76] Y. Li, W. Zhao, S. Lan, J. Ni, W. Wu, B. Lu, 2015, A review on spindle thermal error compensation in machine tools, *International Journal of Machine Tools and Manufacture*, 95, pp. 20–38.
- [77] L. Ljung, 1999, *System Identification - Theory for the User*, Prentice Hall PTR.
- [78] J. R. R. Mayer, 2012, Five-axis machine tool calibration by probing a scale enriched reconfigurable uncalibrated master balls artefact, *CIRP Annals - Manufacturing Technology*, 61, pp. 515–518.
- [79] J. Mayr, M. Ess, S. Weikert, K. Wegener, 2009, Calculating thermal location and component errors on machine tools, *Proceedings of the 24th ASPE Annual meeting*, 2000, pp. 2–5.
- [80] J. Mayr, J. Jedrzejewski, E. Uhlmann, M. Alkan Donmez, W. Knapp, F. Härtig, K. Wendt, T. Moriwaki, P. Shore, R. Schmitt, C. Brecher, T. Würz, K. Wegener, 2012, Thermal issues in machine tools, *CIRP Annals - Manufacturing Technology*, 61, pp. 771–791.
- [81] J. Mayr, M. Gebhardt, B. B. Massow, S. Weikert, K. Wegener, 2014, Cutting Fluid Influence on Thermal Behavior of 5-axis Machine Tools, *Procedia CIRP*, 14, pp. 395–400.
- [82] J. Mayr, M. Egeter, S. Weikert, K. Wegener, 2015, Thermal error compensation of rotary axes and main spindles using cooling power as input parameter.
- [83] J. Mayr, W. Knapp, K. Wegener, 2015, Reduction of Thermal Errors of 5-Axis Machine Tools, *Proceedings of MTTRF Meeting*, 1, pp. 53–58.
- [84] J. Mayr, 2009, *Beurteilung und Kompensation des Temperaturganges von Werkzeugmaschinen*, Diss., ETH Zurich.

- [85] P. A. McKeown, 1987, The Role of Precision Engineering in Manufacturing of the Future, *CIRP Annals - Manufacturing Technology*, 36, pp. 495–501.
- [86] MORe Simulations, 2019, [www.more-simulations.ch](http://www.more-simulations.ch).
- [87] T. Moriwaki, C. Zhao, 1992, Neural network approach to identify thermal deformation of machining center, *Human Aspects in Computer Integrated Manufacturing*, , pp. 685–697.
- [88] T. J. Morris, 2001, A new slant on diagonal laser testing, in: *Laser Metrology and Machine Performance V*, volume 34, pp. 29–40.
- [89] J. Mou, C. R. Liu, 1995, An Adaptive Methodology for Machine Tool Error Correction, *Journal of Engineering for Industry*, 117, pp. 389–399.
- [90] J. Mou, C. R. Liu, 1996, An innovative approach to increase the accuracy of multi-axis machines for process-intermittent inspection, *Journal of Manufacturing Science & Engineering*, 118, pp. 585–594.
- [91] NCG, 2005, NCG-Prüfwerkstück für die 5-Achs-Simultan-Fräsbearbeitung, [NCG test piece for 5-axis-simultaneous milling].
- [92] L. Neidhardt, H. Höfer, H. Wiemer, 2017, Prüfwerkstück zum Nachweis von thermisch bedingten Verlagerungen an Fräsmaschinen, *ZWF Zeitschrift für wirtschaftlichen Fabrikbetrieb*, 109, pp. 814–818.
- [93] F. Pavliček, 2019, Parametrierbare Metamodelle zur Berechnung des Wärmeübergangs in Hohlräumen, Diss., TU Chemnitz.
- [94] M. Putz, C. Richter, J. Regel, 2018, Industrial relevance and causes of thermal issues in machine tools, in: *Proceedings of the 1st Conference on Thermal Issues in Machine Tools*, pp. 127–139.
- [95] M. Rahman, J. Heikkala, K. Lappalainen, 2000, Modeling, measurement and error compensation of multi-axis machine tools. Part I: Theory, *International Journal of Machine Tools and Manufacture*, 40, pp. 1535–1546.
- [96] R. Ramesh, M. A. Mannan, A. N. Poo, 2000, Error compensation in machine tools - a review Part II : thermal errors, *International Journal of Machine Tools and Manufacture*, 40, pp. 1257–1284.
- [97] Renishaw, 2014, OMP60 - Messtastersystem mit optischer Signalübertragung.
- [98] Renishaw, 2018, User Guide: XM-60 multi-axis calibrator.

- [99] J. Rissanen, 1983, A Universal Prior for Integers and Estimation by Minimum Description Length, *The Annals of Statistics*, 11, pp. 416–431.
- [100] S. Sartori, G. Zhang, 1995, Geometric Error Measurement and Compensation of Machines, *CIRP Annals*, 44, pp. 599–609.
- [101] P. Schellekens, H. Spaan, J. Soons, E. Trapet, V. Looock, J. Dooms, H. de Ruiter, M. Maisch, 1993, Development of Methods for Numerical Error Correction of Machine Tools, in: *International Progress in Precision Engineering*, Elsevier, pp. 212–223.
- [102] H. Schulz, T. Schmitt, 1994, Model-based determination of heat generation in the mechanical structure of high speed feed drive systems, *Production Engineering*, 1, pp. 89–92.
- [103] H. Schwenke, J. Hannaford, K. Wendt, 2003, Verfahren zur Ermittlung systematischer geometrischer Abweichungen in technischen Mehrkörpersystemen (Patent).
- [104] H. Schwenke, M. Franke, J. Hannaford, H. Kunzmann, 2005, Error mapping of CMMs and machine tools by a single tracking interferometer, *CIRP Annals - Manufacturing Technology*, 54, pp. 475–478.
- [105] H. Schwenke, W. Knapp, H. Haitjema, A. Weckenmann, R. Schmitt, F. Delbressine, 2008, Geometric error measurement and compensation of machines-An update, *CIRP Annals - Manufacturing Technology*, 57, pp. 660–675.
- [106] H. Schwenke, R. Schmitt, P. Jatzkowski, C. Warmann, 2009, On-the-fly calibration of linear and rotary axes of machine tools and CMMs using a tracking interferometer, *CIRP Annals - Manufacturing Technology*, 58, pp. 477–480.
- [107] H. Shi, C. Ma, J. Yang, L. Zhao, X. Mei, G. Gong, 2015, Investigation into effect of thermal expansion on thermally induced error of ball screw feed drive system of precision machine tools, *International Journal of Machine Tools and Manufacture*, 97, pp. 60–71.
- [108] H. A. M. Spaan, 1995, Software error compensation of machine tools Software Error Compensation of, Diss., TU Eindhoven.
- [109] G. Spur, U. Heisel, 1977, Automatic compensation of thermal disturbances in machine tools, in: *Proceedings of the 3rd International Conference on Production Engineering*, Kyoto, Japan, pp. 119–122.

- [110] G. Spur, E. Hoffmann, Z. Paluncic, K. Benzinger, H. Nymoen, 1988, Thermal Behaviour Optimization of Machine Tools, *CIRP Annals - Manufacturing Technology*, 37, pp. 401–405.
- [111] A. K. Tangirala, 2017, Principles of System Identification: Theory and Practice, *IEEE Control Systems*, 37, pp. 181–184.
- [112] VDI/NGQ 5211, 2013, Testing guidelines and testing workpieces for high speed cutting (HSC) - Part 2: Milling machines and machining centres for the 5-axis simultaneous milling.
- [113] R. Venugopal, M. Barash, M. C. Shaw, 1986, Thermal Effects on the Accuracy of Numerically Controlled Machine Tools, *CIRP Annals - Manufacturing Technology*, 35, pp. 255–258.
- [114] C. Wang, 2000, Laser vector measurement technique for the determination and compensation of volumetric positioning errors. Part I: Basic theory, *Review of Scientific Instruments*, 71, pp. 3933–3937.
- [115] C. Wang, 2008, Volumetric Positioning Error Measurement at Various Thermal Conditions, in: *Proceedings of the Measurement Science Conference, Orlando, FL, USA*.
- [116] M. Weck, P. McKeown, R. Bonse, U. Herbst, 1995, Reduction and Compensation of Thermal Errors in Machine Tools, *CIRP Annals - Manufacturing Technology*, 44, pp. 589–598.
- [117] K. Wegener, S. Weikert, J. Mayr, 2015, Age of Compensation - Chance and Challenge for Machine Tool Industry, in: *Proceedings of the 8th International Conference on Leading Edge Manufacturing in 21st Century*, volume 10, pp. 609–623.
- [118] K. Wegener, J. Mayr, M. Merklein, B. A. Behrens, T. Aoyama, M. Sulitka, J. Fleischer, P. Groche, B. Kaftanoglu, N. Jochum, H. C. Möhring, 2017, Fluid elements in machine tools, *CIRP Annals - Manufacturing Technology*, 66, pp. 611–634.
- [119] K. Wegener, T. Gittler, L. Weiss, 2018, Dawn of new machining concepts, *Procedia CIRP*, 77, pp. 1–17.
- [120] S. Weikert, W. Knapp, 2004, R-test, a new device for accuracy measurements on five axis machine tools, *CIRP Annals - Manufacturing Technology*, 53, pp. 429–432.
- [121] M. Wennemer, 2018, Methode zur messtechnischen Analyse und Charakterisierung volumetrischer thermo-elastischer Verlagerungen von Werkzeugmaschinen, Diss., RWTH Aachen.



- 
- [122] M. Yang, J. Lee, 1998, Measurement and prediction of thermal errors of a CNC machining center using two spherical balls, *Journal of Materials Processing Technology*, 75, pp. 180–189.
- [123] H. Yang, J. Ni, 2003, Dynamic Modeling for Machine Tool Thermal Error Compensation, *Journal of Manufacturing Science and Engineering*, 125, p. 245.
- [124] H. Yang, J. Ni, 2005, Adaptive model estimation of machine-tool thermal errors based on recursive dynamic modeling strategy, *International Journal of Machine Tools and Manufacture*, 45, pp. 1–11.
- [125] S. H. Yang, K. H. Kim, Y. K. Park, 2004, Measurement of spindle thermal errors in machine tool using hemispherical ball bar test, *International Journal of Machine Tools and Manufacture*, 44, pp. 333–340.
- [126] S.-H. Yang, H.-H. Lee, K.-I. Lee, 2019, Identification of inherent position-independent geometric errors for three-axis machine tools using a double ballbar with an extension fixture, *The International Journal of Advanced Manufacturing Technology*, 102, pp. 2967–2976.
- [127] H. Yang, 2002, *Dynamic Modeling for Machine Tool Thermal Error Compensation*, Diss., University of Michigan.
- [128] Y. Yoshida, F. Honda, M. Kubota, 1970, Effect of thermal deformation on the cylindrical accuracy in a grinding process, in: *Advances in Machine Tool Design and Research 1969*, Elsevier, pp. 161–170.
- [129] H. Zhang, J. Yang, Y. Zhang, J. Shen, C. Wang, 2011, Measurement and compensation for volumetric positioning errors of CNC machine tools considering thermal effect, *International Journal of Advanced Manufacturing Technology*, 55, pp. 275–283.
- [130] S. Zuest, 2017, *Model Based Optimization of Internal Heat Sources in Machine Tools*, Diss., ETH Zurich.

# Curriculum Vitae

## Personal Data

Name: Philip Blaser  
Date of birth: 12. October 1987  
Place of birth: Burgdorf, Switzerland  
Civil status: married

## School education

1994-2000 Primary school (Primarschule Gsteighof Burgdorf)  
2000-2003 Secondary school (Oberstufe Gsteighof Burgdorf)  
2003-2007 State college of higher educations (Freies Gymnasium Bern)

## Academic studies

2008-2013 BSc Mechanical Engineering, ETH Zurich  
2013-2015 MSc Mechanical Engineering with specialization in Machine Tools and Manufacturing, ETH Zurich  
2015-2020 PhD Student at IWF, ETH Zurich

## Occupation

2014: Intern at DMG Mori / Davis, CA, USA  
2015-2020: Research associate at IWF / ETH Zurich.

# List of Publications

## Conferences

- P. Blaser, M. Gebhardt, W. Knapp, K. Wegener, Automatic Compensation of Thermally Induced Errors on Five-Axis Machine Tools, euspen, SIG: Thermal Issues 2014, Zurich, Switzerland
- M. Gebhardt, J. Mayr, P. Blaser, W. Knapp, K. Wegener, Thermal Compensation for 5-Axis Machine Tools with Physical Model, 14th euspen International Conference, 2014, Dubrovnik, Croatia
- J. Mayr, P. Blaser, W. Knapp, K. Wegener, Compensation of cutting fluid influences on five axis machine tools, MTTRF Annual Meeting, 2016, San Francisco, USA
- F. Pavliček, F. Dietz, P. Blaser, S. Züst, J. Mayr, S. Weikert, K. Wegener, An approach for developing meta models out of fluid simulations in enclosures of precision machine tools, 31st ASPE Annual Meeting, 2016, Portland, Oregon, USA
- P. Hernández Becerro, P. Blaser, J. Mayr, S. Weikert, K. Wegener, Measurement of the effect of the cutting fluid on the thermal response of a five-axis machine tool, Laser Metrology and Machine Performance XII, 2017, Renishaw Innovation Center, Wotton-under-Edge, United Kingdom
- J. Mayr, F. Pavliček, S. Züst, P. Blaser, P. Hernández Becerro, S. Weikert, K. Wegener, Thermal error research, an overview, Laser Metrology and Machine Performance XII, 2017, Renishaw Innovation Center, Wotton under Edge, United Kingdom
- P. Blaser, F. Pavliček, K. Mori, J. Mayr, S. Weikert, K. Wegener, Adaptive Learning Control for Thermal Error Compensation of 5-Axis Machine Tool, NAMRC 45, 2017, Los Angeles, USA
- S. Züst, P. Blaser, J. Mayr, W. Knapp, K. Wegener, Thermo-energetic issues in 5-axis machine tools, MTTRF Annual Meeting, 2017, San Francisco, USA

- P. Blaser, P. Hernández Becerro, J. Mayr, M. Wiessner, K. Wegener, Thermal errors of a large 5-axis machine tool due to cutting fluid influences - evaluation with thermal test piece, American Society for Precision Engineering, 2017, Charlotte, USA
- P. Blaser, J. Mayr, F. Pavliček, P. Hernández Becerro, K. Wegener, Adaptive learning control for thermal error compensation on 5-axis machine tools with sudden boundary condition changes, Conference on Thermal Issues in Machine Tools, 2018, Dresden, Germany
- M. Wiessner, P. Blaser, S. Böhl, J. Mayr, K. Wegener, Evaluation of thermal errors of 5-axis machine tools by on-machine measurements of a thermal test piece, Conference on Thermal Issues in Machine Tools, 2018, Dresden, Germany
- P. Hernández Becerro, J. Mayr, P. Blaser, F. Pavliček, K. Wegener, Model Order Reduction of Thermal Models of Machine Tools with Varying Boundary Conditions, Conference on Thermal Issues in Machine Tools, 2018, Dresden, Germany
- P. Hernández Becerro, N. Zimmermann, F. Pavliček, P. Blaser, W. Knapp, J. Mayr, K. Wegener, Learning Efficient Modeling and Compensation for Thermal Behavior of Machine Tools, MTTRF Annual Meeting, 2018, USA
- J. Mayr, T. Tiziana, P. Blaser, K. Wegener, Thermal error compensation of 5-axis machine tools using a staggered modeling approach, Conference on Thermal Issues in Machine Tools, 2018, Dresden, Germany
- F. Pavliček, D. Pamies, J. Mayr, S. Züst, P. Blaser, P. Hernández Becerro, K. Wegener, Using meta models for enclosures in machine tools, Conference on Thermal Issues in Machine Tools,, 2018, Dresden, Germany
- P. Hernández Becerro, P. Blaser, J. Mayr, K. Wegener, Design improvement of the cutting fluid supply of a large 5-axis machine tool, 33rd ASPE Annual Meeting, 2018, Las Vegas, Nevada, USA
- P. Blaser, C. Hauschel, R. Rüttimann, P. Hernández Becerro, J. Mayr, K. Wegener, Thermal characterization and modeling of a gantry-type machine tool linear axis, 19th euspen International Conference, 2019, Bilbao, Spain
- P. Blaser, J. Mayr, K. Wegener, Long-Term Thermal Compensation of 5-Axis Machine Tools Due To Thermal Adaptive Learning Control, 15th International Conference on High Speed Machining, 2019, Prague, Czech Republic

- P. Blaser, J. Mayr, K. Wegener, Simulation based comparison of thermal error modelling methods for machine tools, euspen, SIG: Thermal Issues, 2020, Aachen, Germany

## Journals

- S. Ibaraki, P. Blaser, M. Shimoike, N. Takayama, M. Nakaminami, Y. Ido, 2016, Measurement of thermal influence on a two-dimensional motion trajectory using a tracking interferometer, CIRP Annals, Vol. 65, Nr. 1, pp. 483-486, DOI: 10.1016/j.cirp.2016.04.067
- P. Blaser, F. Pavliček, K. Mori, J. Mayr, S. Weikert, K. Wegener, 2017, Adaptive learning control for thermal error compensation of 5-axis machine tools, Journal of Manufacturing Systems, USA, Vol. 44, Nr. 2, pp. 302-309, DOI: 10.1016/j.jmsy.2017.04.011
- A. Mohammadi, S. Züst, J. Mayr, P. Blaser, S. Rostgaard, H. Henri, K. Wegener, 2017, A methodology for online visualization of the energy flow in a machine tool, CIRP Journal of Manufacturing Science and Technology, Vol. 19, pp. 138-146, DOI: 10.1016/j.cirpj.2017.08.003
- M. Wiessner, P. Blaser, S. Böhl, J. Mayr, W. Knapp, K. Wegener, 2018, Thermal test piece for 5-axis machine tools, Precision Engineering, Vol. 52, pp. 407-417, DOI: 10.1016/j.precisioneng.2018.01.017
- J. Mayr, P. Blaser, A. Ryser, P. Hernández Becerro, 2018, An adaptive self-learning compensation approach for thermal errors on 5-axis machine tools handling an arbitrary set of sample rates, CIRP Annals, Vol. 67, Nr. 1, pp. 551-554, DOI: 10.1016/j.cirp.2018.04.001
- P. Blaser, J. Mayr, K. Wegener, 2019, Long-Term Thermal Compensation of 5-Axis Machine Tools Due To Thermal Adaptive Learning Control, MM Science Journal, pp. 3164-3171, DOI: 10.17973/MMSJ.2019\_11\_2019066
- N. Zimmermann, S. Lang, P. Blaser, J. Mayr, Adaptive Input Selection for Thermal Error Compensation Models, CIRP Annals, Vol. 68, Nr. 1, *accepted*

**Talks**

- P. Blaser, 2019, Online Machine-Learning für die Reduktion von thermischen Fehlern, 4.F&E-Konferenz zu Industrie 4.0, Rapperswil, Switzerland
- P. Blaser, J. Mayr, K. Wegener, 2018, Online Machine Learning for Thermal Error Compensation - An Applied Example of Self-Optimizing Machine Tools, CWG Self-Optimizing Machining Systems - CIRP General Assembly, Tokyo, Japan
- P. Blaser, P. Hernández Becerro, 2017, Thermische Messtechnik zur Analyse von Werkzeugmaschinen, Fertigungstechnisches Kolloquium, ETH Zurich

## List of Supervised Theses

The following theses (unpublished) were supervised or co-supervised by the author.

- A. Diews, 2018, Automatic Estimation of Optimal Data Inputs for Adaptive Learning Control for Thermal Error Compensation, Master Thesis
- C. Hauschel, 2018, System Identification for Thermal Deviations of Linear Axes for Machine Tools, Bachelor Thesis
- O. Jaussi, 2016, Simulationsunterstützte Optimierung eines Prüfwerkstücks zur Visualisierung von thermomechanischen Abweichungen von Rundachsen, Bachelor Thesis
- K. Mori, 2016, Iterative learning control for thermal error compensation of 5-axis machine tools, Semester Thesis
- R. Rüttimann, 2017, Experimental analysis to evaluate and model the thermal behavior of a linear axis, Bachelor Thesis
- A. Ryser, 2017, Optimization of an Adaptive Learning Control for Thermal Error Compensation of 5-Axis Machine Tools, Semester Thesis
- P. Satz, 2018, Development of volumetric thermal error measurement procedure for validation of thermo-mechanical FEM models of machine tools, Master Thesis
- S. Schmid, 2018, Development of an IoT Wireless Temperature Sensor System for an Industry 4.0 Application, Semester Thesis
- F. Stoop, 2017, Umsetzung von Industrie 4.0 in Werkzeugmaschinen-Baugruppen, Semester Thesis
- V. Widmer, 2016, Messung und Simulation der energetischen Flüsse in einer 5-Achs-Werkzeugmaschine, Bachelor Thesis